

# **Study of Two-Stage Collimation System in Fermilab Booster**

*Fermi National Accelerator Laboratory*

*Written by*

**V.V. Kapin**

*Edited by*

**W.A. Pellico**

*Contributors*

**S.J. Chaurize, V.A. Lebedev, N.M. Mokhov, T.M. Sullivan,  
S.I. Striganov, R.J. Tesarek, A.K. Triplett, I.S. Tropin**

**Date: June 12, 2017**

**Version 20170612**

## Table of Contents

Abstract .....	4
1. Introduction.....	5
2. The Booster Collimation System .....	7
2.1 Fermilab Booster.....	7
2.2 Demands for Booster intensity increase.....	10
2.3. Radiation in Booster Tunnel and Needs for Effective Collimation .....	11
2.4 Overview of the Booster Collimation System Designs .....	14
2.4.1. Original 2001-Design with L-shaped Secondary Collimators .....	14
2.4.2. The 2003-Design with Integrated Secondary Collimators.....	17
2.4.2.1 The design conception and the basic rules.....	17
2.4.2.2 Adopted Integrated Collimator Design .....	17
2.4.2.3 STRUCT & MARS Simulations for New 2003-Design.....	19
2.4.2.4 Commissioning the New Collimation System in 2004.....	21
2.4.2.5 The 2004 Collimator Design Paper with STRUCT results.....	25
2.4.2.6 The Collimator Design with Optimal Primary Foils.....	27
2.5 Details of the Collimation System Hardware .....	29
3. Reassessment of the Booster 2SC system.....	33
3.1 Plans and approaches for reassessments .....	33
3.1.1 Initial plans and motivations at PIP start in 2011 .....	33
3.1.2 Plans by start of new efforts in 2014.....	34
3.1.2.1 Initial Plan for Study Booster Collimation System.....	34
3.2 General Principles of Two-Stage Collimations .....	35
3.2.1 The problems of conventional (one-stage) collimation .....	35
3.2.2 Features and merits of two-stage collimation system .....	38
3.3 Preparation for Numerical Simulations of the Collimation System .....	43
3.3.1 Substituting STRUCT code by MADX code.....	43
3.3.2 Adaptation of MADX code for Booster collimation .....	44
3.3.2.1 Generation of the initial particle distributions .....	44
3.3.2.2 Implementation of the proton scattering on thin-foil .....	45
3.3.2.3 Implementation of the trapezoidal aperture in MADX .....	49
3.3.3 Attaching Regular Apertures to the Booster MADX lattice .....	50
3.3.4 Apertures in Collimation Area for the Booster MADX lattice .....	53
3.3.5 Non-linear fields in the Booster lattice files .....	56
3.4 Peculiarities of the Booster two-stage collimations system.....	58
3.4.2 Analytical evaluations for 2SC in the vertical plane.....	58
3.4.1.1 Definitions of the Collimation Efficiency.....	64
3.4.1.2 Collimation Efficiencies for analytical evaluations of the vertical 2SC.....	64
An example with 400 $\mu$ m Cu foil .....	64
An example with 50 $\mu$ m Cu foil .....	65
An example with 10 $\mu$ m Cu foil .....	65
3.4.1.3 Differences between a "steady" machine vs a rapid synchrotron .....	66
3.4.1.4 Summary of reasons for potentially low collimation efficiency.....	67
3.5 Numerical Simulations.....	70
3.5.1 New Simulation Approaches .....	70
3.5.2 Absorber Model in MARS Code .....	70
3.5.3 Simulations for Single Stage Collimation System.....	71

3.5.4 Simulations for Two Stage Collimation in Vertical Plane.....	73
3.5.4.1 Simulation of 2SC in vertical plane with 1D-configuration .....	73
3.5.4.2 Simulation of 2SC in vertical plane with full 2D-configuration.....	78
3.5.5 Simulations for Two Stage Collimation in Horizontal Plane .....	82
4. Alternative Scheme with Thick Primary Collimator .....	84
Conclusion and outlook .....	91
5. Experimental Studies of the 2SC in Booster.....	92
5.1 Beam Instrumentation in Collimation Region .....	92
5.2 Collimation Tests with Booster Beam for the Vertical Plane .....	93
5.2.1 Initial Configuration of Collimators .....	93
5.2.2 Pre-study for the beam orbits preparations.....	93
5.2.3 Collimation Test Steps and 2SC Configurations Realized .....	95
5.2.4 Post-processing Beam Loss Data.....	97
5.2.5 Conclusions for Vertical Collimation Study.....	99
5.3 Collimation Tests with Booster Beam in Horizontal Plane .....	100
5.3.1 Initial Configuration of Collimators .....	101
5.3.2 Details of the Collimator motion in the Horizontal Plane .....	101
5.3.3 Realized Configurations for 2SC Horizontal Collimation.....	102
5.3.4. Post-Processing Beam Loss Data Study Results.....	102
5.3.5 Conclusions for Horizontal Collimation Study.....	105
6. Conclusion .....	106
Acknowledgements.....	107
References .....	108
Appendix A. RAL Collimation Scheme .....	112
Appendix B Installation of new optimal primary foils .....	113
The first 2014 rejected version of the 381 $\mu$ m Al primary collimators [81].....	113
Appendix C. Collimator Motion Applications and Studies .....	115
Appendix D Beam Instrumentation and ACNET Applications .....	116
Appendix E The Fast Loss Monitors (FLM) .....	117
Appendix F Software Developed for Post-Processing of Study Results .....	118

## **Abstract**

The growth of the Booster proton flux during the last decade leads to an increase of the residual radiation in the collimation area. This report described new efforts started in autumn of 2014 for a possible upgrade of the Booster collimation system installed in 2004, which was designed as a two-stage collimation (2SC) system, but operates in the conventional single stage collimation mode still ensuring a significant reduction in Booster activation.

This report finalizes both theoretical and experimental studies performed for the Booster 2SC system. The original 2004 design is reviewed, and the purpose for 2SC system is reformulated. For numerical simulations of the 2SC, new software combination with the MADX and MARS code has been prepared. The results of numerical simulations for 2SC in both horizontal and vertical planes did not show advantages of the 2SC mode in comparison to conventional 1SC mode.

The analytical evaluations for 2SC in the vertical plane have been performed. They defined peculiarities of the Booster collimation system and have explained reasons for its potentially low collimation efficiency.

Two major experimental beam studies for the collimation in horizontal and vertical planes have been performed. Several configuration of 2SC has been realized. The experimental results did not show any advantages of 2SC operation mode in comparison to 1SC mode.

A new configuration of 2SC system using a rather thick foil relocated into the long straight section before of the first secondary collimator has been suggested and numerically simulated. The collimation efficiency of this single pass collimation system is higher the multi-turn collimation efficiency of existing 2SC system. A possible configuration of new 2SC system is discussed and a two-stage plan for updating the Booster collimation system is proposed.

# 1. Introduction

The Fermilab Booster is a 15Hz rapid cycling synchrotron accelerating protons from 400 MeV to 8 GeV with accelerating efficiency about 90%. Booster optics is based on combined function dipoles and includes 24 equal-length periods. Totally, about 10% of protons are lost during 20,000-turn accelerating cycle. Major fraction of loss happens at the beginning of the accelerating cycle.

The Proton Improvement Plan (PIP) established in 2012 is aimed to double the beam throughput, while maintaining the present residual activation levels. One of 22 PIP tasks is a possible upgrade of the Booster collimation system installed in 2004 at its periods 5, 6 and 7.

The booster collimation system has been designed as a two-stage collimation (2SC) system. In past, shortly after installation, there were some efforts to put the 2SC in regular Booster operation. However, 2SC did not show any advantages in comparison to a conventional 1SC operation. Therefore, only the 1SC operation mode has been used for Booster operation during many years, which was still ensuring a significant reduction in the Booster activation.

The growth of the Booster proton flux during the last decade leads to an increase of the residual activation in the collimation area. It was believed that the effective operation of 2SC mode is mainly prevented by uncontrolled radial orbit variations inherent to the radial cogging used in Booster till 2015. Implementation of new magnetic cogging in 2015 resulted in a stable beam orbit and created favorable conditions for a new implementation of the 2SC, which is aimed to reduce uncontrolled beam losses mostly generated shortly after injection.

New efforts for implementation of 2SC system in the Booster operation have been started in autumn of 2014. This report finalizes both theoretical and experimental studies performed for 2SC system.

The second chapter of this report contains a general description Fermilab Booster, outlines demands for its intensity increase. Overview of a residual radiation in Booster demonstrates a strong need for an effective collimation system. In order to understand basic design principles of the designed 2SC system some relevant details from available publications are presented. A lot of useful information concerning tuning of the installed collimation system has been found in reports about its commissioning works. It was found that the design purpose for 2SC was formulated very softly, assuming 99%-beam loss over up to 25÷50 m region in periods 6, 7 and immediately downstream. It looks that the presently used 1SC mode of operation achieves this purpose. We also present an overview of the hardware of the existing collimation system. The details of shielding in the collimation area are given together with constructions of secondary and primary collimators.

The third chapter overviews the reassessment plans generated at the start of the PIP project and their evolutions during last years. For better understanding of the 2SC problems, its general principles, merits and features are briefly presented. Motivations for transfer from 1SC to 2SC are also discussed. Our efforts to prepare numerical analysis of 2SC are described in full details. They included an adaptation of MADX code, modifying the Booster lattice file and connecting the MARS code for accounting the out-scattering effects.

The presented analytical evaluations for 2SC in the vertical plane have defined peculiarities of the Booster collimation system and have explained reasons for its potentially low collimation efficiency. These evaluations provided an insight on possible simulation tricks increasing the resulting collimation efficiency during multi-turn simulations in the lattice with imperfections. The results of numerical simulations for 2SC in both horizontal and vertical planes are also presented. The absorption efficiency of the secondary collimator (1SC mode) has been calculated with MARS code.

Since the simulation results and experimental studies did not show advantages of 2SC in comparison with 1SC for existing configuration, we proposed a new configuration of 2SC system using a rather thick foil relocated into the long straight section before of the first secondary collimator. The

results of numerical simulations for new proposed 2SC are presented in the fourth chapter. This single pass collimation system does not depend on multi-turn behavior of Booster optics. The collimation efficiency of the new 2SC system is higher than the collimation efficiency of existing 2SC system, and potentially higher of 1SC mode. A possible configuration of new 2SC system is discussed and a two-stage plan for updating the Booster collimation system is proposed.

The results of the experimental studies for the collimation in horizontal and vertical planes are presented in the fifth chapter. The details of the study steps are discussed. Several configuration of 2SC has been realized. The sum of many BLMs reading located around the Booster was used as a figure of merit to compare 1SC and 2SC. The results did not show any advantages of 2SC operation mode in comparison to 1SC mode. Such results are in agreement with our theoretical prediction about low collimation efficiency due to the Booster peculiarities.

## 2. The Booster Collimation System

### 2.1 Fermilab Booster

The Proton Source is an initial part of the Fermilab accelerator complex, which also includes Main Injector (MI), Recycler, and external Beamlines (NuMI, BNB, Switchyard, MTA, etc.). The Fermilab 8 GeV Proton Source consists of 750 keV Pre-Accelerator, 400 MeV Linac, 8 GeV Booster and the beginning part of the MI-8 Line [1]. The Fermilab Booster [2, 3, and 4] is a 15Hz rapid cycling synchrotron accelerating protons from 400 MeV to 8 GeV during 20,000-turn accelerating cycle at a repetition rate of 15 Hz and accelerating efficiency about 90%. Totally, about 10% of protons are lost during accelerating cycle. Major fraction of loss happens at the beginning of the accelerating cycle.

Figure 2.1 shows the Booster enclosure map. The Booster tunnel is a concrete tunnel 8 feet high and 10 feet wide, covered by 15 feet of earth shielding. The Booster circumference along the reference orbit is about 474.2 m. Booster is made up primarily of combined-function magnets and RF cavities and is divided into 24 equal-length periods.

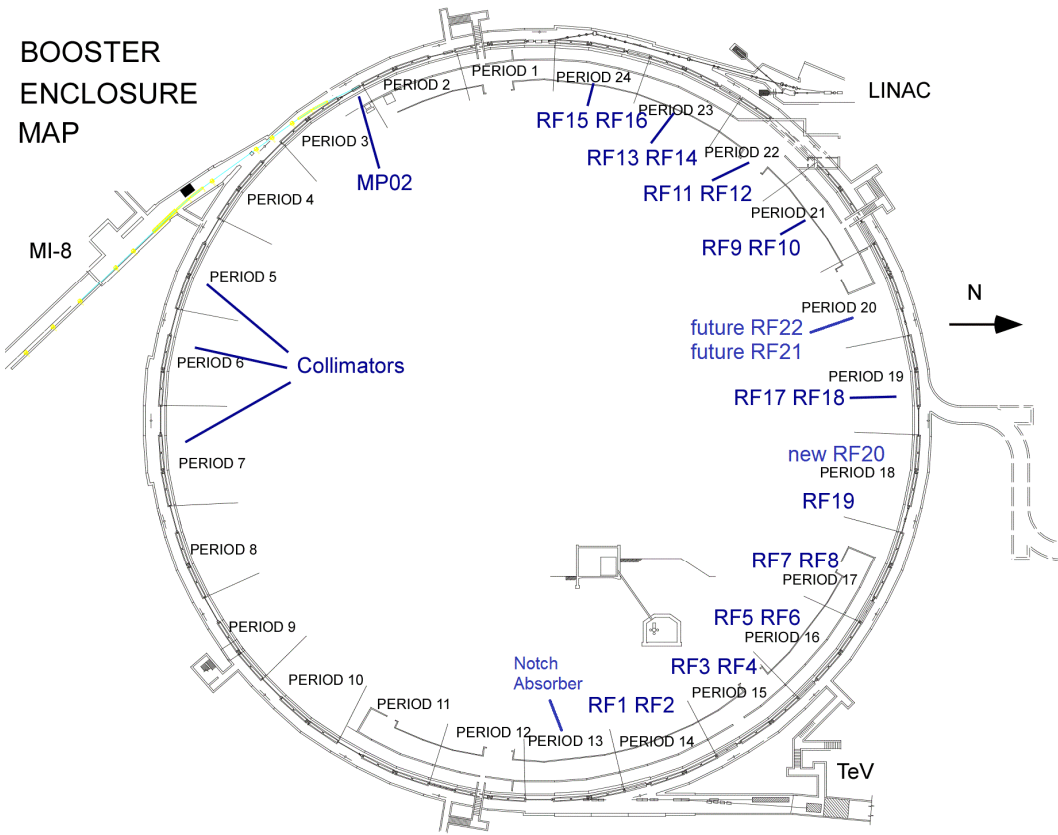


Figure 2.1: Booster Enclosure Map (courtesy of J.M. Fulgham).

The combined-function magnets provide both a dipole field and a quadrupole field. The dipole field bends the beam and the quadrupole field focuses the beam either horizontally or vertically. These magnets are named like regular quadrupoles, "F" for focusing and "D" for defocusing. Figure 2.2 shows the cross sectional view of combined-function magnets [4] and apertures of typical Booster elements. The horizontal widths of so-called "good field" area for "F" and "D" are equal to 4.3" and 3.0", respectively. The vertical widths of "good-field" for both magnets are the same as distances between pole tips, i.e. 1.64" and 2.25" for F and D magnets, respectively. Minimal beam aperture in the

horizontal plane is defined by RF-cavities having the internal diameter of 2.25". In the vertical plane, three smallest apertures have the following elements: "F" magnets with the vertical pole gaps of 1.64"; "D" magnets with the vertical pole gaps of 2.25", and RF-cavities with drift-tubes diameter of 2.25".

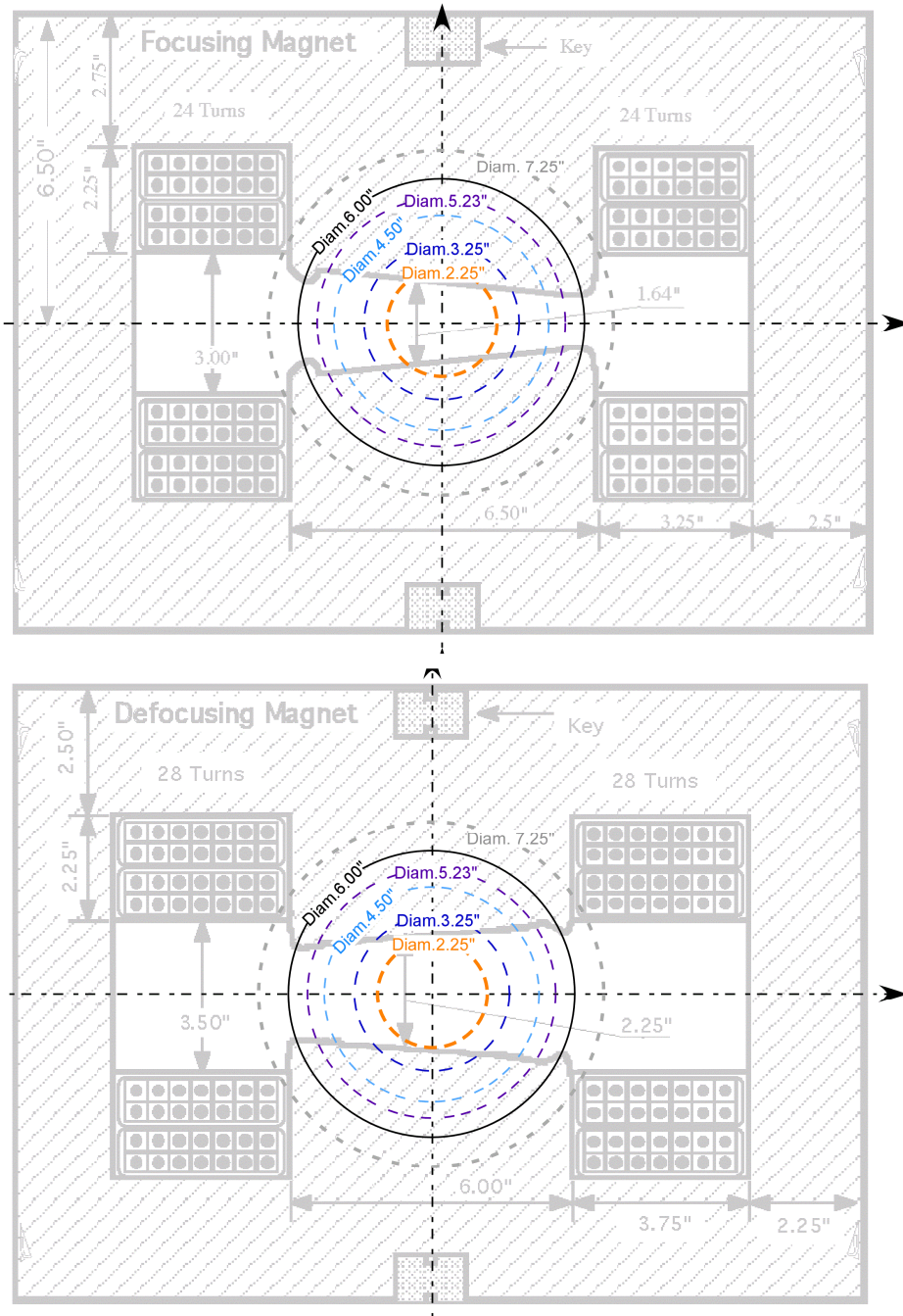


Figure 2.2: Cross Sectional View of a "F" magnet (left) and a "D" magnet [4] overlapped by apertures of some typical Booster elements implying possible aperture restrictions on the beam: a) RF-cavities (Diam. 2.25"); b) regular beam pipes (Diam. 3.25"); c) corrector package (Diam. 4.5"); d) special aperture in short straight 12 (Diam. 5.23" shifted horizontally by 2 cm outwards); e) 0.5 meter pipes between F and magnets (Diam. 6.00"); f) flanges of combined-function magnets (Diam. 7.25").

Each Booster period contains two horizontally focusing magnets ("F-magnet") and two horizontally defocusing magnets ("D-magnet") separated by two straight lines (6.0-meter "long straight" and a 1.2-meter "short straight") and two 0.5-meter short drifts separating F and D magnets (see Fig. 2.3). The standard cell length is 19.76 meters.

Numbering of the lattice periods arbitrarily begins at the injection long straight, designated as "Long 1" (or more shortly, as "L01"). The long straights precede the correspondingly numbered short straights, so the short straight immediately downstream of "Long 1" is labeled "Short 1" (or "S01"). Incidentally, the terms "upstream" (or "US") and "downstream" (or "DS") refer to the direction of beam motion. Beam always travels from upstream to downstream. There are 24 long and 24 short straight sections in Booster for a total of 96 combined-function magnets in the ring.

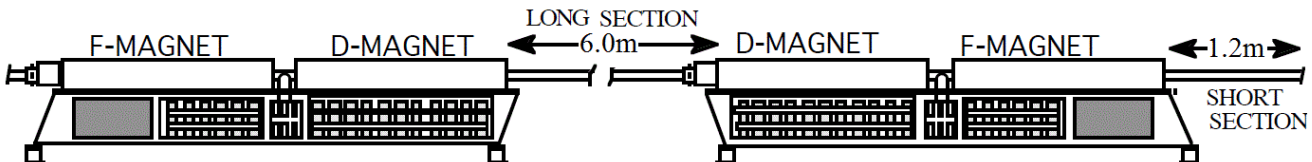


Figure 2.3: Typical Lattice Period of Booster [4].

RF cavities, injection and extraction components, secondary collimators, notch kickers and notch absorber are located in the long straight sections. Beam diagnostics and correction element packages are located in both the long and short straight sections. The correction element packages are made up of six different circuits that generate dipole, quadrupole, and sextupole fields, giving fine control over the beam.

The initial 400 MeV proton beam in the Booster is provided by the Fermilab Linac using multi-turn charge-exchange injection. The 400 MeV H<sup>-</sup> ions exit from the Linac pass through a stripping foil which removes two electrons of H<sup>-</sup> ions. Beam injection into the Booster take place at Long 1. Beam can be extracted from Booster at two locations, depending on its destination. An extraction at long 13 transfers beam to the Booster dump. An extraction at Long 3, initiated by kickers in period 2, transfers beam to the Main Injector via the MI-8 line.

The Booster RF system is composed of about twenty stations<sup>1</sup> that increase the beam energy from 400MeV to 8 GeV. Since Booster is a synchrotron, the cavity resonant frequency sweeps from 37.8 MHz to 52.8 MHz as the beam revolution period decreases from 2.2  $\mu$ s at injection to 1.6  $\mu$ s at extraction. Presently (spring of 2017), twenty RF stations (also called as RF cavities) are located in ten long straight sections of the Booster lattice. As a rule, there are two RF stations per long straight. Every RF cavity contains a drift tube with accelerating gaps at both ends. The drift tube is tapered copper structure with a minimum 2.25" i.d. beam pipe in the center.

The Booster collimation system is located in periods 5, 6, and 7. Figure 2.4 shows layout of the Booster collimation system in its present configuration. It is a two-stage collimation (2SC) system installed in 2003. 2SC general principles used for this design can be found in the paper "Beam Collimation at Hadron Colliders" written by N.V. Mokhov [5]. The design of the collimation system for the Booster is described in several reports [6, 7, 8, 9, 10, and 11].

Note, the enumeration of the combined function magnets shown in Fig. 2.4 corresponds to the magnet labeling in the Booster tunnel, which is not quite consistent with the definition of the Booster period shown in Fig. 2.3. The letters F or D are also added to the numbers to designate focusing and defocusing magnets, respectively. For example, the period 6 includes magnets labeled as 5-3F, 5-4D, 6-1D, and 6-2F, and the period 7 includes magnets labeled as 6-3F, 6-4D, 7-1D, and 7-2F.

<sup>1</sup> Over the years, the total number of RF stations was increased during Booster upgrades from 16 stations in the original designs to 20 in 2017, and to 22 stations planned in a future.

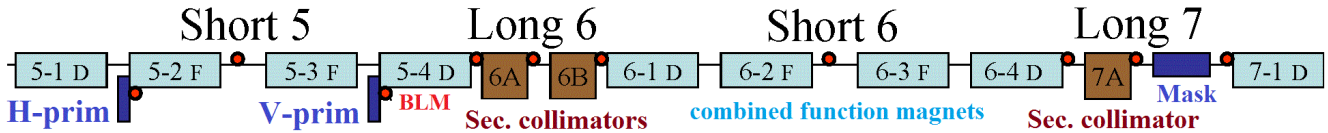


Figure 2.4: Layout of 2SC system in periods 5, 6 and 7.

The Booster 2SC consists of horizontal (H-prim) and vertical (V-prim) primary collimators located in the short drifts nearby of Short-5 and three identical 1.2 m-long secondary collimators (or absorbers) 6A, 6B, and 7A located in Long-6 and Long-7. Each absorber is capable to limit beam aperture in both horizontal and vertical planes. Primary collimators limit the beam aperture only in one plane, *i.e.* H-prim limits horizontal beam aperture, and V-prim limits the vertical beam aperture. The primary collimators are movable thin scattering foils. The absorbers are movable girders with square cross-section with square apertures in the center for beam passage. Originally, the absorbers has been also used the Booster notching system. Recently (~2013), the dedicated Notch Absorber has been installed in period 13.

## 2.2 Demands for Booster intensity increase

The flagship of Fermilab's long term research program is the Deep Underground Neutrino Experiment (DUNE). The staged plan to achieve the multi-megawatt beam power required by the DUNE physics program is outlined in the paper [12]. This plan drives the need for increased proton intensity for the Fermilab accelerator complex. All protons are originated in the 8 GeV Proton Source, which is largely original construction.

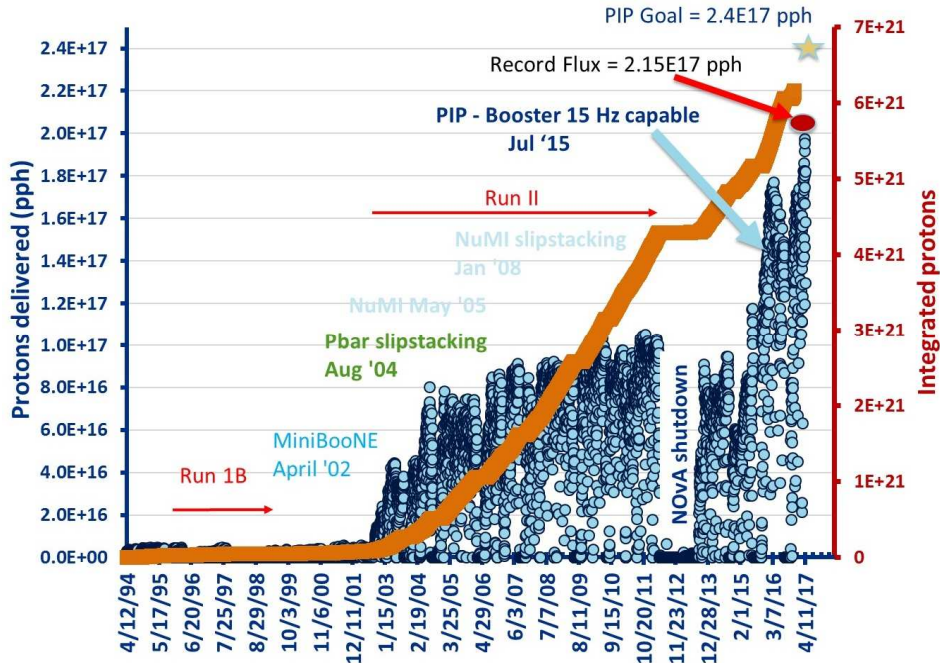


Figure 2.5: Evolution of Booster proton delivery [17].

The lab has adopted a staged approach to increasing the proton intensity for the high energy neutrino program. The Proton Improvement Plan (PIP) [13, 14, 15, and 16] is a campaign to maximize the proton output from the existing Proton Source. The key component is to reduce losses and upgrade

pulsed hardware in the Booster to allow beam to be accelerated on all 15 Hz cycles. This goal has recently been achieved. Figure 2.5 shows the total proton output from the Booster. The goal of the PIP campaign is  $2.4 \cdot 10^{17}$  protons per hour while maintaining 2012 activation levels, ensuring viable operation of the proton source through 2025. This and other upgrades will allow the Main Injector to deliver 700 kW of beam to the NuMI line. On Jan. 24, 2017 the Main Injector has delivered 700 kW proton beam over one hour [17].

In the current configuration, it's unlikely that significantly more beam current could be injected into the Booster. Therefore, in order increase the beam power available for the DUNE from 700 kW to 1.2 kW the Proton Improvement Plan-II (PIP-II) [18] has been established. The key feature of PIP-II is to replace the existing 400 MeV linac with a new superconducting 800 MeV linac. In addition, the Booster rate will be increased from 15 to 20 Hz.

To prepare Fermilab accelerator complex to PIP-II requirements, a new flexible campaign named as PIP-I+ is proposed as follow-on to PIP [17]. This campaign is considered as a bridge between PIP-I and PIP-II. The goal is to get 1 MW beam power to the NuMI line prior to PIP-II. In addition, this transition plan should anticipate a transition to the new PIP-II linac in 2023, with which Booster will be expected to deliver  $4.7E^{17}$  protons per hour at a repetition rate 20 Hz. Such increase in the Booster beam intensity will demand a further reduction of losses in the Booster.

Thus, there is a demand to increase Booster intensity while decreasing the particle losses and maintaining the same residual activation levels in the accelerator components.

### **2.3. Radiation in Booster Tunnel and Needs for Effective Collimation**

Figure 2.6 show the recent (Mar 31, 2017) radiation data at different locations around the Booster<sup>2</sup>. The radiation has been measured at the distance of one foot from the Booster elements. Two plots of the same data with two different vertical scales are presented to facilitate comparison the radiation levels at different areas and view details of distributions within some particular areas.

According to the ACNET application B87, the main Booster parameters within 8 hours before shutdown for the above Mar 31, 2017 radiation data measurements are the following: the Booster up time, the average number of events (or the Booster cycles) per seconds, the average number of protons per event, the average number of protons per hour, the number of protons "out/in" (or the Booster beam transmission efficiency) are equal to 95.8 %, 12.6 ev./s,  $3.8 \cdot 10^{12}$  ppc,  $1.72 \cdot 10^{17}$  pph, 90.9 %, respectively.

Figure 2.6,a demonstrates very high radiation levels at the collimator region in periods 6-7 (up to 700 mrem/hour) and at the extraction region in period 3 (up to 550 mrem/hour). Also the relatively high radiation exists at the injection region in period 1 (up to 200 mrem/hour) and the notching region in periods 12 and 13 (up to 150 mrem/hour).

Figure 2.6,a shows details of radiation distribution in the collimation region. The highest activation levels corresponds to period 6, especially at the following measurement points: 1) "SEC.COL 6A" (up to 700 mrem/hour) located between the absorbers 6A and 6B (see Figure 2.4); 2) "L6" ((up to 400 mrem/hour) located in front of the absorber 6A; 3) "SEC.COL 6B" (up to 300 mrem/hour) located behind of the absorber 6B; 4) "S6" (up to 300 mrem/hour) located in the short straight 6. The activation levels in vicinity of the primary collimators ("HORZ PR IN/OUT", "S6", and "VER IN/OUT") and in the period 7 ("L7" and "L7 DS" located before and after the absorber 7A) are relatively smaller and do not exceed 100 mrem/hour.

Therefore, the collimation region and extraction regions remains a main source of concern since some of the magnets around these regions have seen very high levels of beam loss. The Booster has never lost a gradient magnet due to coil failure [13]. It is expected that if gradient magnet fails due to radiation damage it will happen first in the collimation area. It is also expected that all cabling in this region will eventually have to be replaced.

---

<sup>2</sup> Booster Radiation Reports on Web-page: [http://www-bd.fnal.gov/cgi-booster/rad\\_survey.pl](http://www-bd.fnal.gov/cgi-booster/rad_survey.pl)

If beam losses in the Booster will be increased in a future due to an intensity increase without essential improvement of Booster beam efficiency, then the collimation regions with existing collimation system may experience even higher radiation level. For example, in the “Proton Source Improvement Plan” issued in 2011 [14] it is noted that prompt radiation levels were already a measurable concern in a small number of West Booster Tower offices located above the collimation region, when residual activation levels in the Booster tunnel are up to 1300 mrem/hour at 30 cm on the outside of the shielding in the vicinity of the Booster collimators.

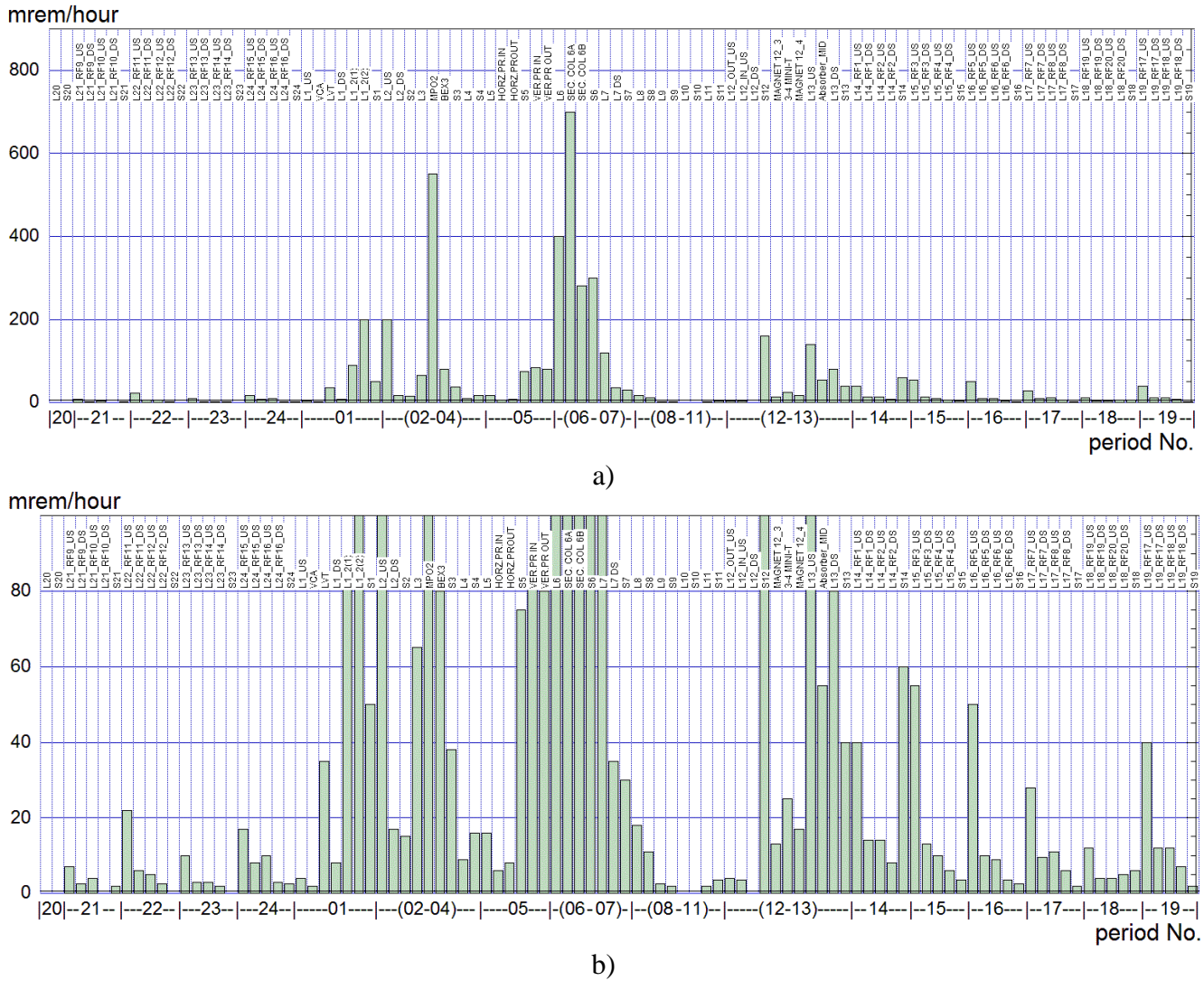


Figure 2.6: Radiation data for Mar 31, 2017 at the distance of one foot at different locations around the Booster for two different vertical scales: a) 900 mrem/hour; b) 100 mrem/hour.

Collimators do a satisfactory work on a reduction of radiation in the most of Booster tunnel. However radiation is already very high in the vicinity of collimators and its further increase does not look as a possible solution. The radiation significantly exceeds the level predicted by simulations performed during the design phase of the Booster collimators [14].

Radiation exposure of maintenance workers is a concern driven by potentially higher equipment activation due to increased proton flux and by the expected higher frequency of maintenance due to increased stress of the equipment. For example, the highest radiation rate at 1 ft of secondary collimator 6A reaches 700 mrem/hour. At Fermilab, the individual checkpoint is set to 50 mrem per

week for 1 person, while the job stop limit is set to 55 mrem. This means that the radiation worker can not remain there more than 4 minutes<sup>3</sup>. These conditions complicate possible maintenance works on accelerator components in vicinity the collimation region. Further worsening of the radiation situation in collimation region will make impossible immediate assess to the collimator area requiring long cool-off periods that can significantly affect the length of Booster downtimes.

Figure 2.6,b allows to view details of radiation distribution in regions with RF stations. Let's remind that RF-cavities have smallest apertures in both horizontal and vertical directions (see the above discussion for Fig. 2.2). The RF stations are located in pairs within the long straights of periods 14÷24, except of the period 20 (see Fig. 2.1).

The radiation measurements are performed at 5 points within those periods, namely 4 points within long straights (upstream and downstream of every of two RF stations) and 1 point at short straight. For example, the period 15 has the 5 measurement points with the following nicknames: 1) "L15\_RF3\_US" and "L15\_RF3\_DS" for the points no. 1 and no. 2 located upstream and downstream of the first RF station "RF3", respectively; 2) "L15\_RF4\_US" and "L15\_RF4\_DS" for the points no. 3 and no. 4 located upstream and downstream of the second RF station "RF4", respectively; 3) "S15" for the point no. 5 located in the short straight 15.

It is seen from Fig. 2.6,b that within long straights of all periods with RF stations, namely periods 14÷19 and 21÷24, the radiation levels are highest for the measurement point no. 1 located upstream of the first RF station. Moreover, within long straights of most periods with RF stations, except of period 19, the radiation levels decrease monotonically with increase of the point number from 1 to 4. Also within the most periods, except of periods 14 and 18, the radiation levels for last point no.5 located at short straights are minimal.

This regularity suggest that every pair of RF stations acts as a sequence of aperture restrictions for incoming beam which size exceeds the drift-tube apertures of RF cavities. Note that this behavior exists in the presence of acting collimator system. This regularity could mean that some considerable part of the beam halo avoids the aperture restrictions in the collimators and directly hit apertures of RF stations. Therefore, up to now the RF stations act in part as collimator system providing a relatively high radiation in their vicinity. Since RF stations require quit frequent, complicated and relatively long maintenance procedures, the reduction of residual activation near RF-stations is very desirable to avoid excessive radiation exposure of maintenance workers. This circumference can also drive the need for an upgrade of existing collimation system or even for designing and building a new one.

---

<sup>3</sup> 50 [mrem]/(700/60) [mrem/min]=4.3 min

## **2.4 Overview of the Booster Collimation System Designs**

Note, that the Booster 2SC systems were the designed for their possible usage at both the injection energy (0.4 GeV) and the top energy (8 GeV). However, the optimal thickness of the primary collimators should be very different at the injection and top energies. It was suggested [6] to use rotating primary collimators constructed as disks of different thickness. Presently, this suggestion is considered to be unpractical. Moreover, since major beam losses happen at injection energy, it was decided to consider the collimation system only for the injection energy.

The 2SC system has been designed using the STRUCT [19] code and the MARS codes [20], which perform two mutually complementary tasks. The STRUCT code simulated multi-turn particle tracking in the accelerator and halo interaction with collimators. The MARS code simulated full-scale Monte Carlo hadronic and electromagnetic shower in the lattice elements, shielding, tunnel and surrounding soil.

### **2.4.1. Original 2001-Design with L-shaped Secondary Collimators**

The original design of the Booster collimation system has been presented in the 2001 paper [6]. Some details and motivations were also reviewed in the paper [7]. Below is the description of the collimator design taken from ref [6].

It was proposed to use straight sections of periods 6 and 7 for collimation because this region is far from the engineering, support and office buildings. It was assumed that 30% of the beam is lost at injection energy (0.4 GeV), and the purpose of the beam halo cleaning system is to localize proton losses in a specially shielded short section, thus to reduce irradiation of the rest of the machine to the acceptable levels.

A 2SC system has been proposed with 0.1 mm thick tungsten (or 0.15 mm thick graphite) horizontal and vertical primary collimators followed by four copper secondary ones. The length of secondary collimators is equal to 0.6 m. The mechanical design of the secondary is based on two pieces of copper welded together in an "L" configuration. The collimator assembly is bolted inside a stainless steel box.

Figure 2.7 shows the layout of the suggested 2SC system and horizontal and vertical  $\beta$ -functions. The principal locations of the primary collimators and 3 of 4 secondary collimators are the same as in the presently existing 2SC system (see the above Fig. 2.4), in which only 3 secondary collimators are used. The 4th secondary collimator named as SV2 in Fig. 2.7 for the 2001 design is absent in the present configuration. In the later designs, the 3rd and the 4th secondary collimators "SH2" and "SV2" shown in Fig. 2.7 were merged in the later design and named as "SHV2".

Note, the collimator names shown in Fig. 2.7 are used in the lattice scripts for STRUCT code. The character "S" means "secondary", and characters "H" and "V" are set for "horizontal" and "vertical" designating the major collimation plane. The number attached to the secondary collimator name designates a function of the collimator in the 2SC scheme. For example, the 2SC scheme for the horizontal plane uses the primary collimator "Pr.H" and two secondary collimators "SH1" and "SH2", and the 2SC scheme for the vertical plane uses the primary collimator "Pr.V" and two secondary collimators "SV1" and "SV2".

There are several different naming conventions used in the lattice scripts and the Booster controlling devices and radiation surveys. Let's list here three naming conventions which can be used for absorbers of the 2SC: 1) Collimator "6A" can be also named as "COL1" or "SH1"; 2) Collimator "6B" can be also named as "COL2" or "SV1"; 3) Collimator "7A" can be also named as "COL3" or "SHV2". By the way the latter name "SHV2" is used for secondary collimator when it works as 2nd secondary collimator in the both horizontal and vertical planes.

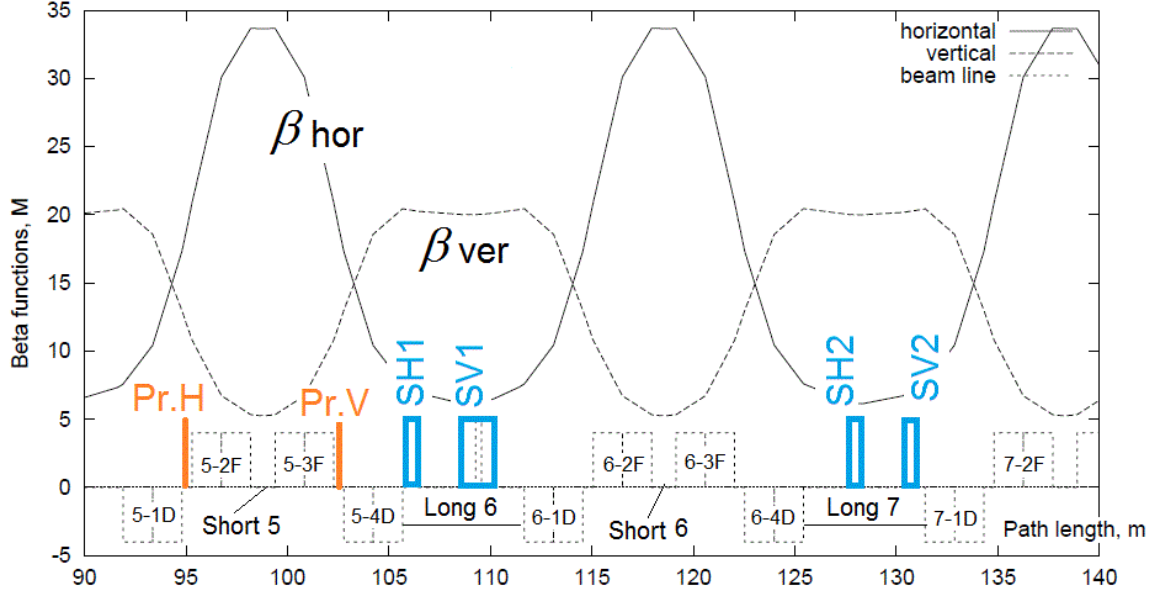


Figure 2.7: Beta functions and the collimator location for 2001 2SC design [6].

Primary collimators are placed at the edge of the circulating beam after injection. Secondary collimators are positioned with  $0.5 \sigma$  offset with respect to the primary ones at phase advances that are optimal to intercept most of particles out-scattered from the primary collimators during the first turn after the halo interaction with the primary collimators. Table 2.1 presents the  $\beta$ -functions and phase advances  $\Delta\mu$  between collimators for the 2001 design [6].

Table 2.1  $\beta$ -functions and phase advances between collimators for the 2001 design [6].

element	$\beta_{\text{hor}}$ , m	$\beta_{\text{ver}}$ , m	$\Delta\mu_{\text{hor}}$ , deg	$\Delta\mu_{\text{ver}}$ , deg
horiz. prim. Pr.H	19.0	11.9	0	-
vert. prim. Pr.V	19.0	11.9	-	0
Secondary SH1	7.4	20.4	37	-
Secondary SV1	6.2	20.0	-	20
Secondary SH2	6.2	20.0	154	-
Secondary SV2	7.1	20.3	-	127

Figure 2.8 shows the beam loss distribution along the accelerator at injection. Below the location of the combined-function magnets and elements of the 2SC system are also shown. The original plot (on the left) is accompanied by the zoom image of the collimation region (on the right) extracted with help of a standard graphical editor (right).

According to Ref. [6], this 2SC system localizes about 99% of beam loss in a 50 m long region. Beam loss in the rest of the machine is on average 0.1 W/m, with several peaks of  $\sim 1$  W/m. The hands-on maintenance limits are 0.25 W/m in the open long beam pipes and 3 W/m in the magnets. We can discern from Fig. 2.8 that this 50 m long region starts from horizontal primary collimator and includes all Booster elements till the middle of the long straight 8, namely periods 6 and 7.

It was also noted in Ref. [6], that the primary collimators produce a very large tail of out-scattered particles in the transverse phase space, and the particles in the tails will be lost on the aperture during the first half of a betatron oscillation. The loss rate in the magnets behind the primary collimators at injection is  $\sim 100$  W/m. This note means that regular Booster aperture restrictions affect on quality of the suggested design.

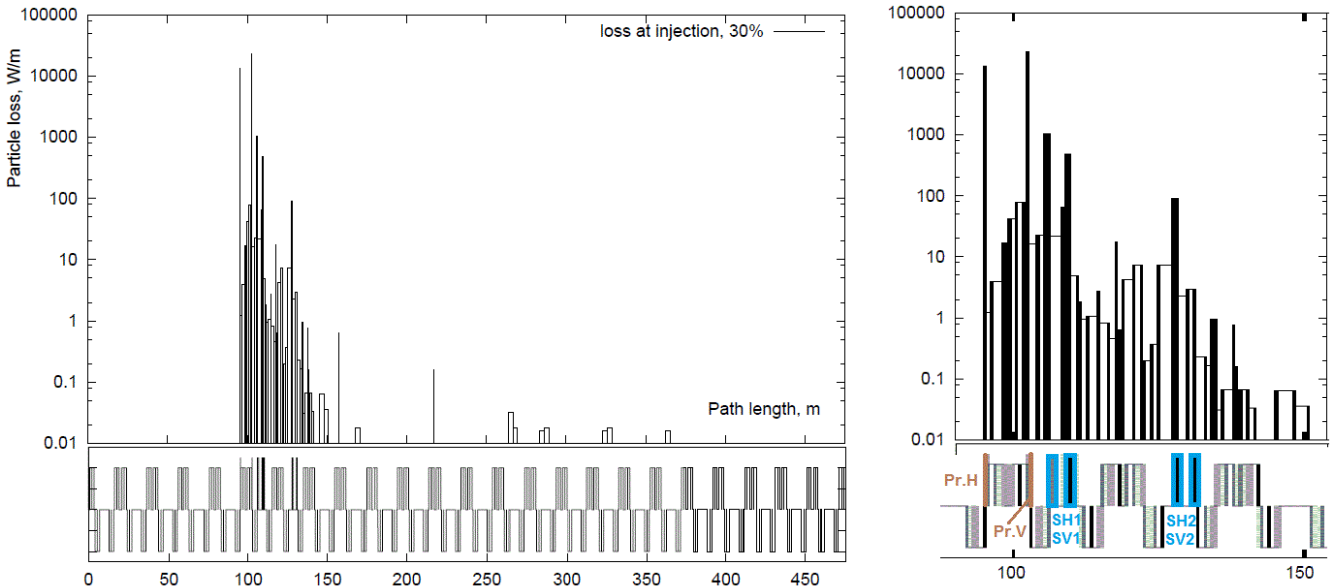


Figure 2.8: Beam loss distribution along the accelerator at injection for the 2001 design [6]: the original plot (on the left) and the zoom image of the collimation region with colored and captioned boxes for primary (brown) and secondary collimators.

Figure 2.9 shows actual layouts of the 2SC with L-shaped absorbers founded in ref [7, 22]. It is seen that the 3rd and the 4th secondary collimators "SH2" and "SV2" shown in Fig. 2.7 were physically merged in one absorber in the installed 2SC system.

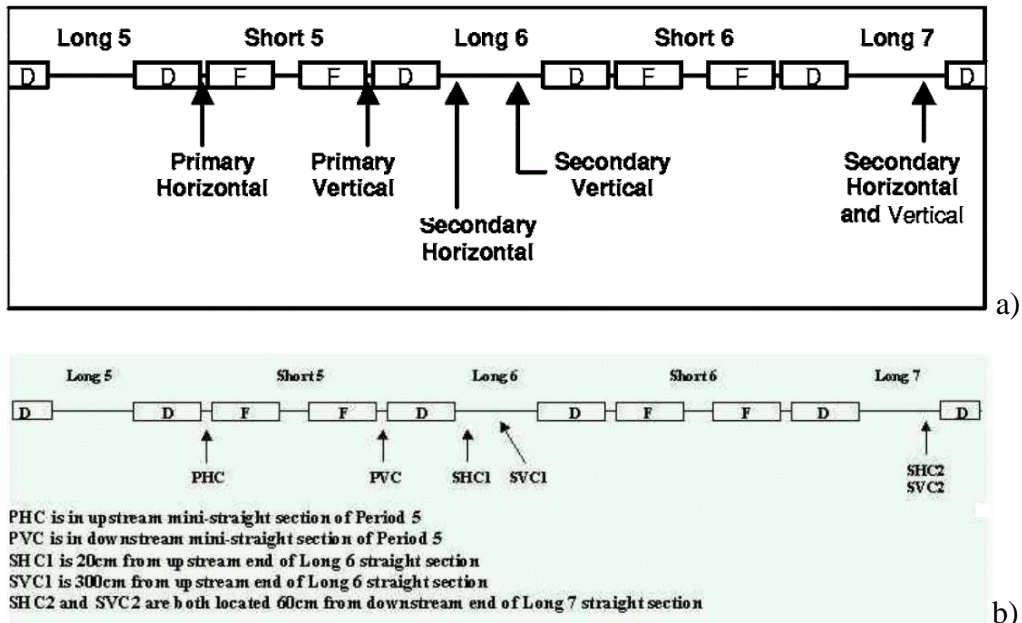


Figure 2.9: Layout of 2SC system with L-shaped absorbers installed in 2002 design : a) [7]; b) [22].

MARS simulations shows that the secondary collimators SH1 and SH2 should be embedded into iron shielding about 60 cm thick transversely (starting at 5 cm from the collimator outer surface) and extended about 60 cm downstream. This 2SC system with copper L-shaped secondary collimators without shielding boxes has been installed in Booster tunnel during the summer of 2002 [7, 21]. All

collimators were movable, they have been exercised. Initial results looked encouraging. A preliminary design of shielding was complete and it was planned to install shielding over the next few months.

The installation of shielding for the three Booster secondary collimators has been planned for the January 2002 shutdown [23], even ~75 tons of steel has been ordered. However, that "Shielding Plan" has been abandoned due to the following reasons [24]:

- a) radiation levels in the area of the collimators meant that it would require several crews to complete the shielding job;
- b) the awkwardness of location made it likely that the beam pipe or bellows would be damaged – particularly if we had multiple crews trying to work quickly;
- c) the existing design did not allow for servicing of the motors, LVDT's, or vacuum flanges without unacceptable radiation exposure;
- d) there was no provision for the eventual removal of the system.

The conclusion was quite categorical: "Remove collimators and do it right". The collimators were removed during the shutdown in January of 2003 result [25]. It was recognized in ref [26] that "previous design scrapped as unworkable".

## 2.4.2. The 2003-Design with Integrated Secondary Collimators

### 2.4.2.1 The design conception and the basic rules

After abandoning the 2001 design with L-shaped collimators surrounded by steel-box shielding, the design conception for new collimators has been suggested [24]:

- a) integrate collimator and enough shielding for at least twice present Booster flux into a movable system which can be assembled externally and installed quickly (~ 1 day)
- b) design must include a clear plan to scale up to the full shielding;
- c) there must be a reasonable method for servicing the motors and LVDTs<sup>4</sup>;
- d) there must be a reasonable plan to remove the central collimation system ("coffin") in the event of a catastrophic failure (e.g. vacuum leak);
- e) there must be a reasonable plan to remove the entire system if a new Booster comes.

Some ground rules have been also listed [24]: no "quick and dirty" temporary solutions; what goes in, stays in; no partial designs; nothing goes in until we have a clear plan for the whole system.

Two basic design choices described in ref. [24] includes: a) movable collimator inside a central coffin, all on rolling cart, around which full shielding could later be placed; b) collimator fixed inside central shielding steel, and entire assembly is moved.

### 2.4.2.2 Adopted Integrated Collimator Design

The secondary collimators with the steel jaws fixed within a movable shielding body were chosen for a new design. Such design principle is also called as the integrated collimator-shielding design. It was designed during winter and summer of 2003 [25]. It was planned to complete the design of the new collimation system by June of 2003 [26]. The mechanical design and fabrication of the new secondary collimator has been ordered to the external company "Bartoszek Engineering" [27].

The 3D model of the new secondary collimator by "Bartoszek Engineering" shown in Fig. 2.10 and example of the MARS-code model had been presented soon in March, 2003 [28]. Those figures had been included also in the poster of the report [10] presented at the PAC'2003 (May, of 2003).

The report [10] describes the new collimation system as the biggest single project to increase the Booster intensity. The collimation principle was described using the same figure as for the previous abandoned 2001-design with L-shaped absorbers (e.g., ref [21, 25]). This means that the collimation

---

<sup>4</sup> the Linear Variable Differential Transformer used for measuring linear displacement of collimators.

principles are the same for both the previous 2001-design and the new 2003-design. The principles were formulated in the following way. High amplitude particles are intercepted by a thin primary foil, and subsequently absorbed by thick stainless steel secondary collimators. Each of the secondary collimators intercepts the beam on one edge in each plane.

The report [10] describes the mechanical assembly of the secondary collimators in the new collimation system design in the following way. The otherwise simple design is complicated by the need for fairly extensive shielding of the secondary collimators. Due to lack of a quantitative model for Booster beam loss, it is assumed that beam losses at injection and extraction energy are equal to 30 % and 2% respectively. This leads to a shielding requirement of about 1.2 m long steel 0.6 m thick around each of the three secondary collimators. To avoid the need for moveable parts or vacuum seals in the extreme radiation environment inside the shielding, we settled on a design in which the secondary collimator jaws are fixed within monolithic steel shielding blocks. Each block is attached to the beam pipe on either end with bellows, allowing the entire assembly to move over the range required by collimator operation.

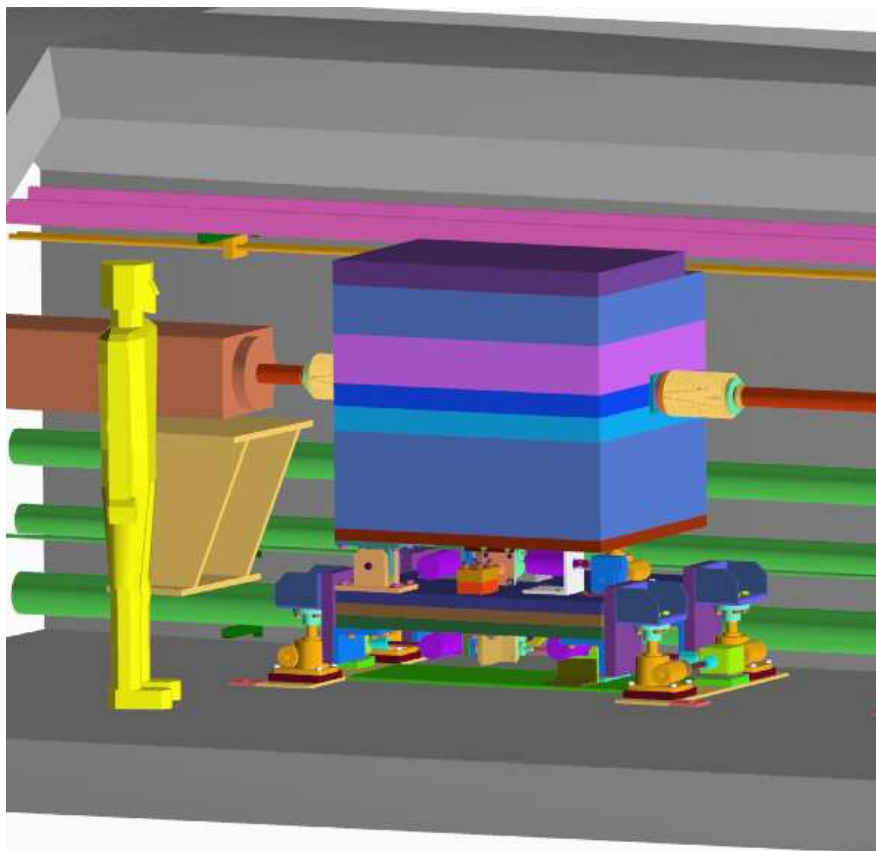


Figure 2.10: The Bartoszek's 3D model of the new secondary collimator in the straight long 6 [27].

Design of three new secondary collimators has been almost complete by May of 2003. They have been assembled and were ready for installation in the 2003 "summer" shutdown [29], namely in September of 2003 [30]. The successful installation of the collimators has been declared on the post-shutdown meeting in October, 2003 [31]. Figure 2.11 shows photos of the installed collimators.



Figure 2.11: The photos of the installed secondary collimators: 6A and 6B in the long straight 6 (on the left) and 7A in the long straight 7 (on the right) [31].

The plan to begin the collimator commissioning during 1-2 month in semi-parasitic mode has been outlined at this meeting [31]. Since this plan is also vital for nowadays experiments with collimation system, it is presented in this report:

- Run secondaries in until the begin to attenuate the beam, then back off slightly;
- Adjust primary positions to minimize (uncontrolled loss)/(transported beam);
- Re-optimize orbit for each collimator setting;
- Measure loss patterns and establish tight limits;
- Integrate collimators into normal operation.

According to December 12, 2003 report [32], the collimation system commissioning has been delayed due to necessity "to have Booster optimized to the new lattice". It was estimated to be about 2 month to bring collimator into standard operation after fixing this issue.

#### 2.4.2.3 STRUCT & MARS Simulations for New 2003-Design

We was able to find only two more or less detailed publications about simulations with STRUCT and MARS codes for the new 2003-design performed before the integrated collimator-shielding secondary collimators has been installed into Booster tunnel in autumn of 2003: the review talk [7] given by N. Mokhov on March 17, 2003 and paper [9] submitted in May of 2003 for PAC'03. Let's consider these publications in details in order to understand basic ideas of this design.

The talk [8] was devoted to physics justification of a new integrated collimator-shielding design of the Booster beam cleaning system. According to the abstract accompanying the report, the system developed will localize 99% of beam loss with low beam loss and radiation levels in the rest of the machine. The collimator-shielding units developed for the ultimate system parameters and optimized via detailed MARS14 simulations as L6A and L6B secondary collimators will provide adequate collimation, shielding and maintenance functionalities, assuring that prompt and residual radiation levels inside the tunnel, in sump water and above dirt shield are below the regulatory limits with a reasonable safety margin.

It is emphasized in the report conclusion that the declared the 99 % localization of beam loss can be reached, if the proposed optimal primary scatterers and secondary collimators in L6 and L7 sections are implemented. Installed two 0.3-mm carbon foils as primary collimators are OK at injection

but too thin at 8 GeV. Installation of only a pair of secondary collimators, L6A and L6B, instead of the optimal four-unit set, would do a reasonable beam cleaning but with a somewhat reduced efficiency.

The pair of STRUCT [19] and the MARS codes [20] has been used for simulation of this new design, while the beam loss analysis has been performed with STRUCT code by A. Drozhdin. Unfortunately, there is some inconsistency in the collimator system models used with the STRUCT code. The model of the 2SC system used with STRUCT code is exactly the 2001-design with four 0.6-m long secondary collimators. Instead the new 2003-design uses three 1.2 m long secondary collimators with 0.2 m long tapered upstream end of jaws [10, 27]. The description of the 2SC system for the presented STRUCT results is accompanied by exactly the same figure and data shown above for the 2001-design (see Fig. 2.7, 2.8 and Table 2.1). The optimal thickness of the primary collimator foil at the injection energy is also exactly the same as for the 2001-design, namely 0.15 mm thick graphite. It was concluded again that such a system would localize about 99% of beam loss in a 50-m long region.

It is also important to mention that the above STRUCT simulations have been performed for the Booster lattice without injection and extraction bumps.

The second part of this talk [8] presents the MARS simulation results. Figure 2.12 shows the MARS model of the used in the simulations. The absorber configuration and sizes corresponds to the integrated collimator-shielding secondary collimator adopted for the new 2003 design [10, 27]. Thus, the MARS calculations presented in this report are based on the beam loss analysis performed by STRUCT code for the old 2001-design. It is not clear how such inconsistency may affect on the declared efficiency of the collimation system.

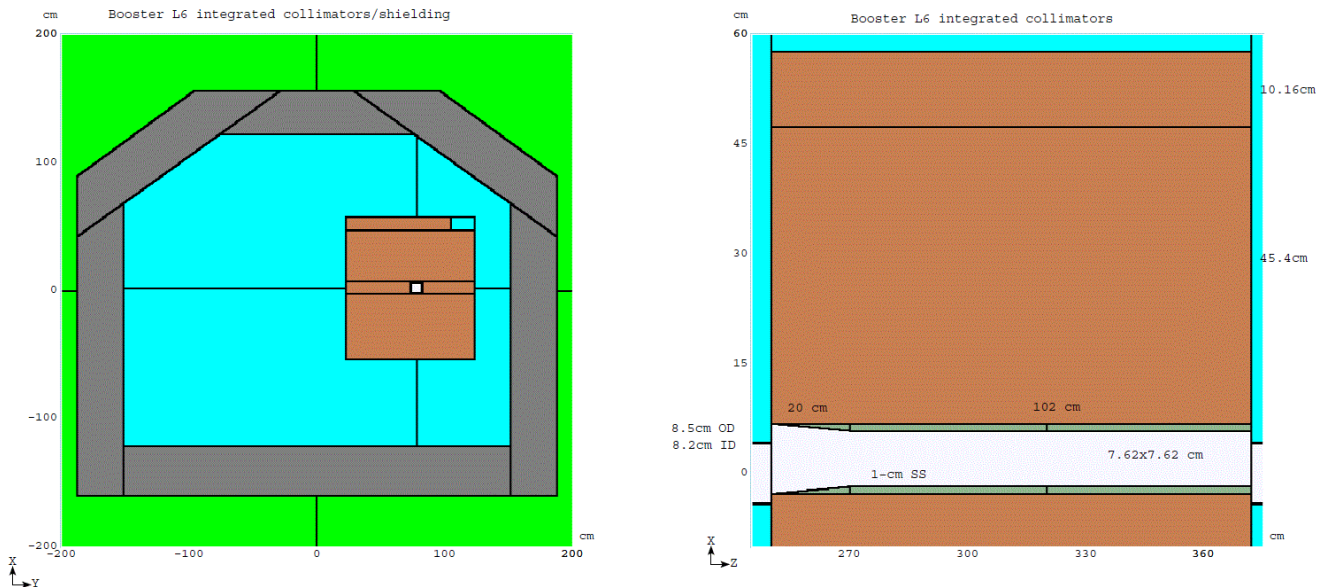


Figure 2.12: The MARS model for the integrated secondary collimator of the new 2003 design [8].

Another paper [9] submitted in May of 2003 for PAC'03 contains more comprehensive information about STRUCT and MARS simulations for the 2SC system. Again as in the recent talk [8], the model used by STRUCT code is based on the old 2001-design and MARS uses model for the new 2003-design with integrated collimator-shielding of system. Thus, one sees again, that the MARS calculations presented in this report are based on the beam loss analysis performed by STRUCT code for the old 2001-design. Also, in comparison with the above talk [8], key conclusions in this paper [9] have some difference, which is important for understanding the collimation system efficiency.

In the abstract of the PAC's paper [9] it is stated that the purpose of a new beam halo cleaning system is to localize proton losses in specially shielded regions, while calculations show that this 2-stage collimation system will localize about 99% of beam loss in straight sections 6 and 7 and immediately downstream. This statement is different from ones presented in the talk [8] and Ref. [6] for the old 2001-design: "such a system would localize about 99% of beam loss in a 50-m long region".

Why the above difference in statements has an importance? The mentioned above the 50 m long region (see Fig. 2.8) includes many unshielded Booster elements (combined function magnets, beam position monitors, vacuum pipes, bellows and pipes between collimators) and the beam losses on these elements will create a high activation around them and could not be considered as desirable or "useful". Only beam losses which happen in specially shielded regions (i.e. on jaws of the secondary collimators without out-scattering of incident protons back to the beam pipe) must be treated as desirable. The straight sections 6 and 7 also include unshielded pipes and bellows between collimators. Therefore beam losses on them must be considered as harmful contributing in high residual activation levels. However, paper [9] treats all losses within periods 6 and 7 as permissible ("useful") because "sections 6 and 7 are far from the engineering, support and office buildings".

Although the 2SC system simulated with STRUCT code and presented in the paper [9] has three secondary collimators (L6A, L6B, L7) as it was adopted for the new 2003-design, the 0.6-m long stainless steel secondary collimators as in the old-2001 design are still considered. Moreover, it directly makes reference to the results published in the 2001 paper [6] for the old 2001-design when the optimal thickness of the primary collimators is discussed.

To evaluate the quality of a 2SC system it is necessary to know what portion of beam losses happens on well-shielded collimator jaws. A good design of the 2SC system must maximize this portion and minimize losses in the rest of machine including losses on all unshielded elements located in the collimation region. Unfortunately, the results presented in the above ref [8,9] does not allow us to evaluate the portion of beam losses on collimator jaws with a total length of ~4 m, while it is not clear how out-scattering of incident protons back to the beam pipe has been treated, if any.

Moreover, it is not clear how and why the beam loss 50-m region [6, 8] was shrunken to (long straight - V.K.) sections 6 and 7 with total length of 12 m. Looking on Fig.2.8 from the referenced 2001 paper [6], one can see that some considerable part of the beam losses spread to outside of collimators including magnets and beam pipes in periods 5, 6 and 7. Therefore, the declared 99% could be essentially less, if "useful" losses are applied only to either straight sections 6 and 7 or collimator jaws.

#### **2.4.2.4 Commissioning the New Collimation System in 2004**

In January of 2003, E. Prebys presented the detailed "Initial Commissioning Plan" [33] which consisted of two parts. The first part of the plan named as "Collimator Position and Angle Registration" contained the following steps:

- Conditions: Turn MiniBooNE off; moderate impact on stacking.
- With pitch and yaw set to zero, move each of the secondary collimators in all directions until beam transmission is reduced by 10-20%. Record transmission vs. location.
- Repeat Horizontal measurements with yaw angle at each extreme.
- Repeat Vertical measurements with pitch angle at each extreme.
- Use information to calculate beam angle at collimators and set pitch and yaw accordingly.
- Move both vertical and horizontal primary collimators in until transmission is reduced by 5-10%. Record transmission vs. location to determine the position of the beam relative to these.

The second part of the plan named as "Performance Studies" contained the following steps:

- Conditions: Reduce MiniBooNE as needed to prevent tripping.

- With the angles established, move each of the secondary collimators individually in the design vertical direction (1 and 2 up, 3 down) until an effect is seen on transmission. Back out until the observed effect disappears. Snapshot beam losses (B136) in each case.
- Begin to run the primary vertical collimator into the beam. As soon as there is any measurable effect on losses or transmission, move the primary collimator into the beam in roughly 1 mm increments, snapshotting losses at each point, until transmission is reduced by 5%.
- Retract and repeat individual collimator studies in the horizontal plane (1 and 2 move out, 3 moves in).
- Repeat measurements in each plane with all three secondary collimators in their operational configuration.

Note the collimation optimization plan included the movement of secondary collimators both horizontally and vertically under different pitch and yaw angles. Both primary collimators were also moved as it required by principles of 2SC systems.

By the E. Prebys's talk given in February of 2004 [34], the two-stage collimation system was in the works a long time, while it was suffered major setbacks, but now in place. Another month or so has been estimated to bring collimators into standard operation. It was also noted that at the time, "primary collimators are not optimized to energy loss profile" and they should be "replaced in upcoming shutdown".

Some successful tuning of collimators has been performed by May of 2004, and the collimators were put for a one week of continuous operation. The Booster radiation has been measured after that week and compared with measurements done a week before when collimators did not operate. Figure 2.13 (E. Prebys's talk [35]) shows improvement in the Booster activation due to collimator operation. It was recognized that this plot provides reasons for optimism [35]. The collimator operation has reduced the radiation almost everywhere around Booster except of the collimation area itself where the radiation was considerably increased.

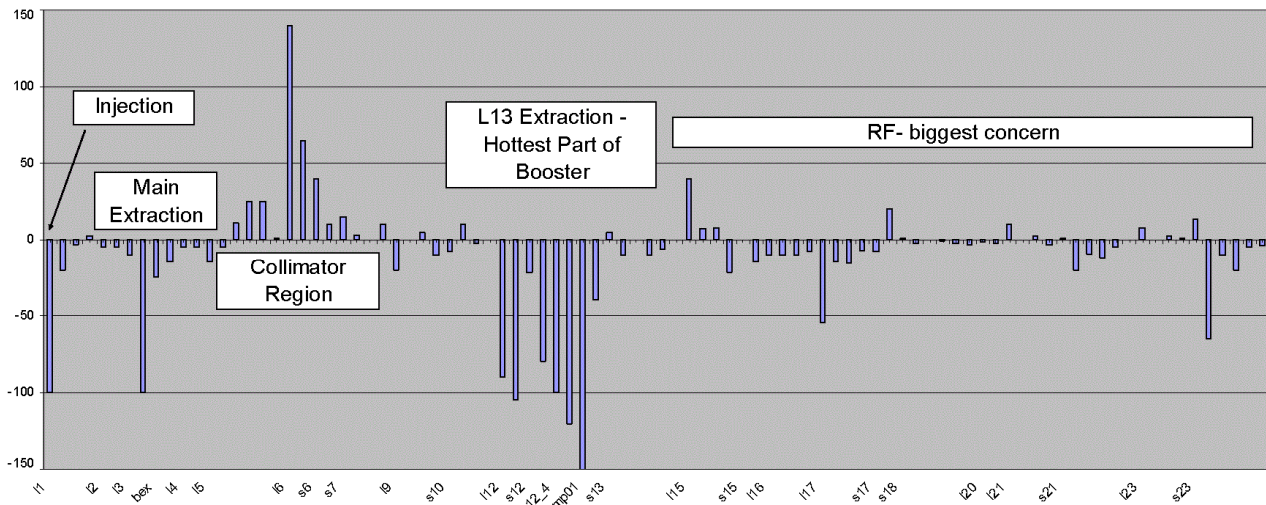


Figure 2.13: Difference in the Booster activation (mrem/hr@1ft) after one week of collimator operation in comparison with the previous week measurements done after operation without collimators [35].

The usage of the collimators in normal Booster operation has been declared in June 2004 [36]. Figure 2.14 shows readouts of Beam Loss monitors (BLM) located around the Booster for two cases: when collimators are off and when collimators are on. BLM readouts are normalized by the alarm (trip) values set individually for every particular BLM.

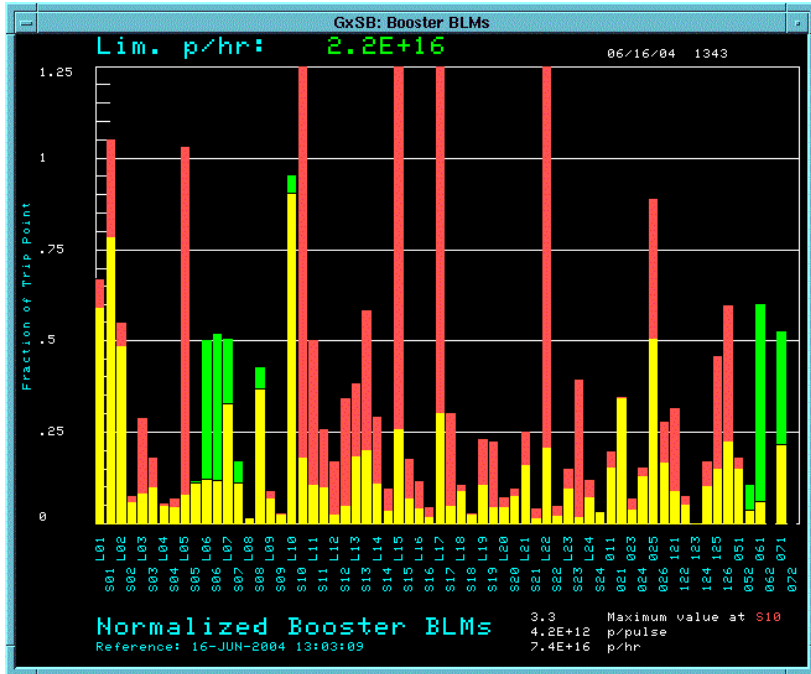


Figure 2.14: The screenshot of the "Fraction of Trip Plot" by ANCET application B88 showing Booster losses via normalized BLM signals: a) losses without collimators as a reference plot (red bars); b) losses with collimators shown as yellow bars, if they less of red bars, and as green bars, if they exceed red bars [36].

One can see that due to usage the collimation system the beam losses registered by BLMs become less almost everywhere around the Booster. However, BLMs located near the primary and secondary collimators, namely in short straight sections 5, 6, and 7, and in long straight sections 6 and 7 have considerably increased values.

Several general principles adopted for operation of Booster collimation system has been presented in ref. [36]: 1) activation was “OK” before collimator implementation; 2) we want to use collimators to increase rate while keeping activation “about the same”.

It was noted that historically, the “watt meter” has been our most reliable indicator of activation, but it works by counting lost protons. Since we can not distinguish protons absorbed on the collimator, now we must rely on individual loss monitors (BLMs) and radiation surveys.

Figure 2.15 shows relative change in the Booster activation in percents since collimators become operational. One can see the reduced activation by 40÷50 % around much of the ring [37], particularly in the extraction regions and in the RF station regions. However, the activation has been increased about 50 % in the Booster period 1 (injection region) and 50÷150 % in the collimators regions and immediately downstream, i.e. in the periods 6, 7, and 8. According to ref. [37], it can be afforded to collimate a little less to mitigate the activity at periods 6÷8 somewhat.

Another interesting suggestion contained in the comments in ref. [37] is the following: “Perhaps try running with reduces (or eliminated) primary collimation????”. Probably, there was not noted a considerable difference between operating the collimation system with the primary collimators, i.e. as a 2SC system, and without primary collimators, i.e. as a single stage collimation (1SC) system. The further activity with collimators has been formulated in ref. [38] as “trying to find and optimum collimator configuration that achieves adequate loss reduction around the ring with the minimum increase near the collimators.” A quite critical evaluation of the collimator operation was given by

E. Prebys in ref [39]: "Helping, but still at least a factor of five away from initial predictions." The Booster shutdown plans to move "pinger" to period 5 and use collimators for extraction pre-notch [39] have further increased the demand for further minimization of beam losses near the collimators.

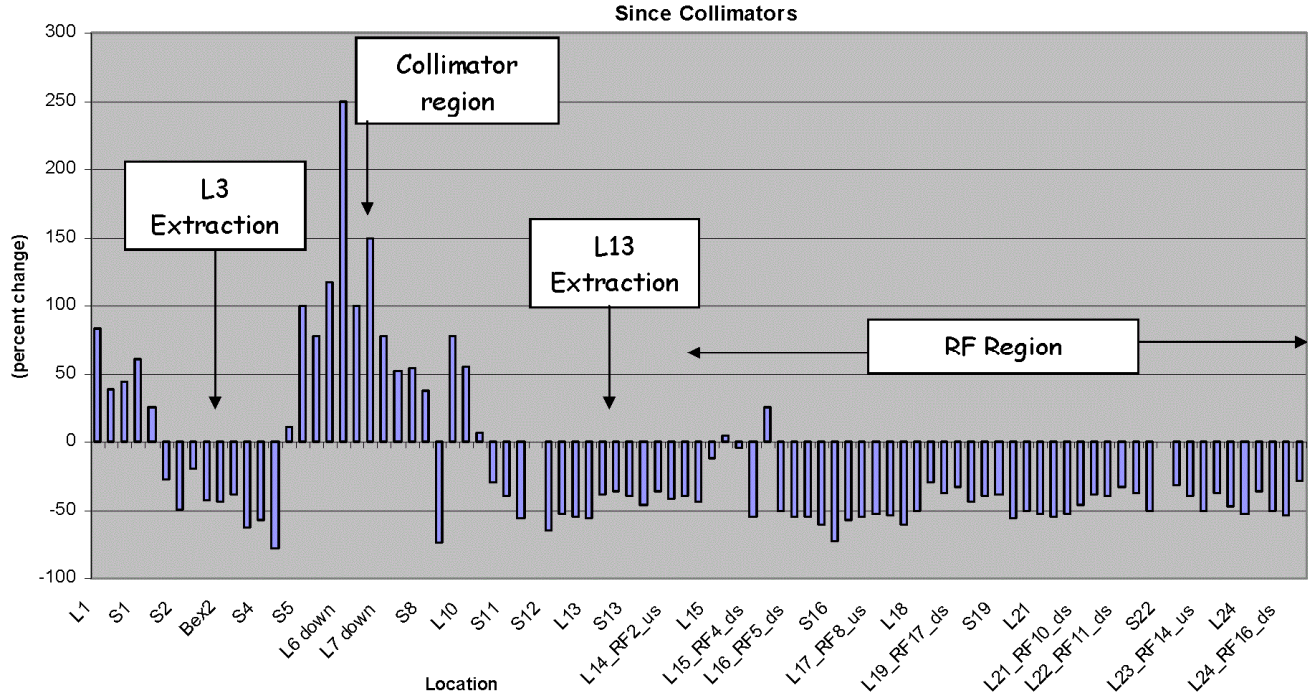


Figure 2.15: Relative change in the Booster activation expressed in percents since collimators become operational [36,37,38].

Comprehensive information on the above commissioning works with the collimators was presented in two talks given in June of 2004 [40] and March of 2005 [41], respectively. The talks contain useful photos and schemes of installed primary and secondary collimators, their mechanical data, motion possibilities and restrictions, overview of new software controlling the collimator motion, examples of measured beam orbits in the collimator regions, procedures for positioning the collimators and many other useful information, e.g. about 0.3 mm copper foil used in the primary collimator. In the conclusion of the 2004 talk, it was cautiously declared that collimators working at some level. The conclusion of the 2005 talk emphasized, that collimators have significantly reduced losses in areas of concern allowing an increase in the maximum extracted proton per hour. Note, the talks [40, 41] presented the Booster collimation system as a two-stage one. However, 2SC operation mode was never used in regular operations. Up to now (2017), only secondary collimators are used for operations in a single-stage collimation mode without any usage of primary collimators.

This talk did not touch any details of collimator simulations and reference to the issued on the next day (June 25, 2004) document [11] by A. Drozhin et al. as a "collimator design paper", which contained the STRUCT code simulation results for the installed 0.3 mm thick copper primary collimators. The only connection of this talk [40] to simulation results is a formulation of the purpose of the collimation system. At the beginning of the talk [40] it has been formulated as a paraphrase of text presented in the abstract of the 2003-design paper [9]: "Their purpose is to clean up the beam halo and localize the proton losses particularly in shielded Booster periods Long 6 Long 7 and immediately downstream." Let's mention, that the "collimator design paper" [11] could not contain any conclusion, since it does not contain any text excepting the single line abstract and figure captions.

### 2.4.2.5 The 2004 Collimator Design Paper with STRUCT results

The mentioned "collimator design paper" [11] contains results of the STRUCT code simulation for primary collimators made of 0.4 mm thick copper, which is quite close to the installed 0.3 mm thick copper foil [40]. Figure 2.16 shows the layout of the STRUCT model of the installed 2SC system and horizontal and vertical  $\beta$ -functions at the injection energy (400 MeV) and at the extraction energy.

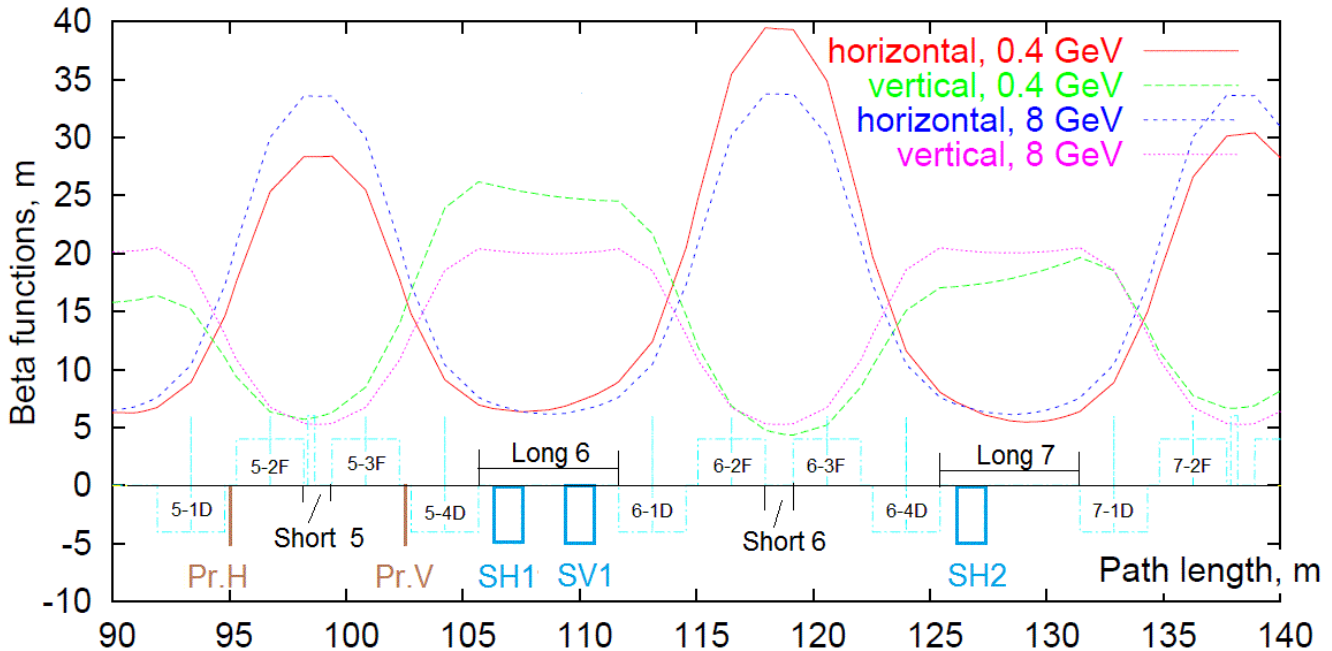


Figure 2.16: Beta functions at the injection and at the top energy in the collimation regions for real location of collimators [11].

In comparison to Fig. 2.7 for the old 2001-design, the locations of primary collimators and two secondary collimators in the long straight section 6 did not change. There is a difference in the long straight section 7. In ref. [11], it contains only one secondary collimator named "SH2" instead of two in the old 2001-design, while this collimator is located closer to the section entrance. Note, that the Booster lattice with nonperiodic  $\beta$ -functions at the injection energy is now used instead the lattice with periodic  $\beta$ -functions for the old 2001-design shown in Fig. 2.7. Figure 2.17 shows the transverse positions of the collimators jaws for collimation in the both horizontal and vertical planes.

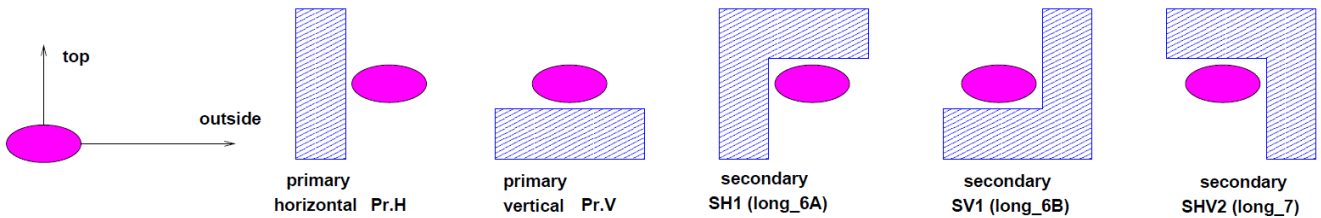


Figure 2.17: Transverse positions of the collimator jaws [11].

The names of the secondary collimators are the same as in the lattice script for STRUCT code. As it was discussed above for Fig. 2.7, the collimator names used in the STRUCT code explain the

collimator function in 2SC scheme. In this "collimator design paper" [11], the 2SC scheme for the horizontal plane uses the primary collimator "Pr.H" and two secondary collimators "SH1" and "SHV2", and the 2SC scheme for the vertical plane uses the primary collimator "Pr.V" and two secondary collimators "SV1" and "SHV2". The collimator "SHV2" (also called either "COL3" or "7A" somewhere else) is used as 2nd secondary collimator in the both horizontal and vertical planes.

Table 2 in [11] lists sizes of the beam envelopes at the collimator locations and the horizontal and vertical collimator positions. According to the caption for Figure 1 in, "95% normalized emittance is  $12\pi \text{ mm}\cdot\text{mrad}$ ". Our reconstructing evaluations showed that the beam envelopes corresponds to  $3\sigma$ -size of the beam. The transverse collimator positions correspond to general rule when primary collimators are placed exactly at the  $3\sigma$ -edge of the beam, and secondary collimators are positioned with 2 mm offset with respect to the beam.

Although, Figure 2.17 shows the vertical position of the collimator "SH1" and the horizontal position of the collimator "SV1" in proximity to the beam, one could realize that these collimators are effectively involved in 2SC schemes for the vertical and horizontal planes, respectively. The phase advances of these collimators do not obey conventional rules (see e.g. ref [4]) adopted for 2SC system, and they could not intercept protons scattered by the primary collimator.

The "collimator design paper" [11] also contains the Table 1 with values of  $\beta$ -functions at collimators and phase advances between collimators. The table 2.2 reproduces the values of these parameters at the injection energy.

Table 2.2  $\beta$ -functions and phase advances between collimators for the 2004 design [11]. The values for the 2001 design [6] are shown in parentheses.

element	$\beta_{\text{hor}}$ , m	$\beta_{\text{ver}}$ , m	$\Delta\mu_{\text{hor}}$ , deg	$\Delta\mu_{\text{ver}}$ , deg
horiz. prim. Pr.H	15.8 (19.0)	10.7 (11.9)	0	-
vert. prim. Pr.V	16.2 (19.0)	14.8 (11.9)	-	0
Secondary SH1	6.5 (7.4)	24.1 (20.4)	53 (37)	-
Secondary SV1	7.9 (6.2)	23.3 (20.0)	-	21 (20)
Secondary SHV2 (SH2)	6.0 (6.2)	18.3 (20.0)	143 (154)	124 (127)

The values listed in the earlier Table 2.1 for the 2001-design are also shown in the table 2.2 in parentheses for comparison purposes. This table demonstrates that changes in the lattice  $\beta$ -functions functions can cause some noticeable changes in beam sizes and phase advances at the collimator locations. The behavior of the  $\beta$ -functions in the Booster is routinely varied and tuned using the correctors. Such corrections are aimed to reach some purposes which are not directly related to the collimation. Therefore, 2SC system in Booster works at conditions of varying beam sizes and phase advances, and must be steady against variations of these parameters.

Although the "collimator design paper" [11] does not formulate the purpose of this 2SC system with version, the presented STRUCT results for primary collimators made of 0.4 mm thick copper allows us to understand them. The first raw in the Table 3 of this document [11] lists the following beam loss values at the injection energy (0.4 GeV)<sup>5</sup>: total losses in the ring are equal to 1439 W, beam loss in the collimation region (92-152 m) are equal to 1412 W, and the beam loss outside the collimation region are equal to 26.14 W.

The first, we can calculate that beam losses in the collimation region are equal to 98 %. The second, the total length of the collimation region considered in the report is equal to 60 m, i.e. about three 20 m Booster periods. Figure reproduces a fragment of Fig.8 from this document [11] showing the beam loss distribution along 35 m long region starting at the position of the horizontal primary collimator "Pr.H" and terminated at the end of the long straight section 7. To facilitate understanding of

<sup>5</sup> As it is written in all figure captions [11], the beam intensity was  $5\cdot10^{12}$  ppp at 15 Hz repetition rate, i.e.  $2.7\cdot10^{17}$  pph.

the collimator positions and to connect them to the beam loss bars, we have slightly edited the original figures via coloring collimators and captioning them with nick names.

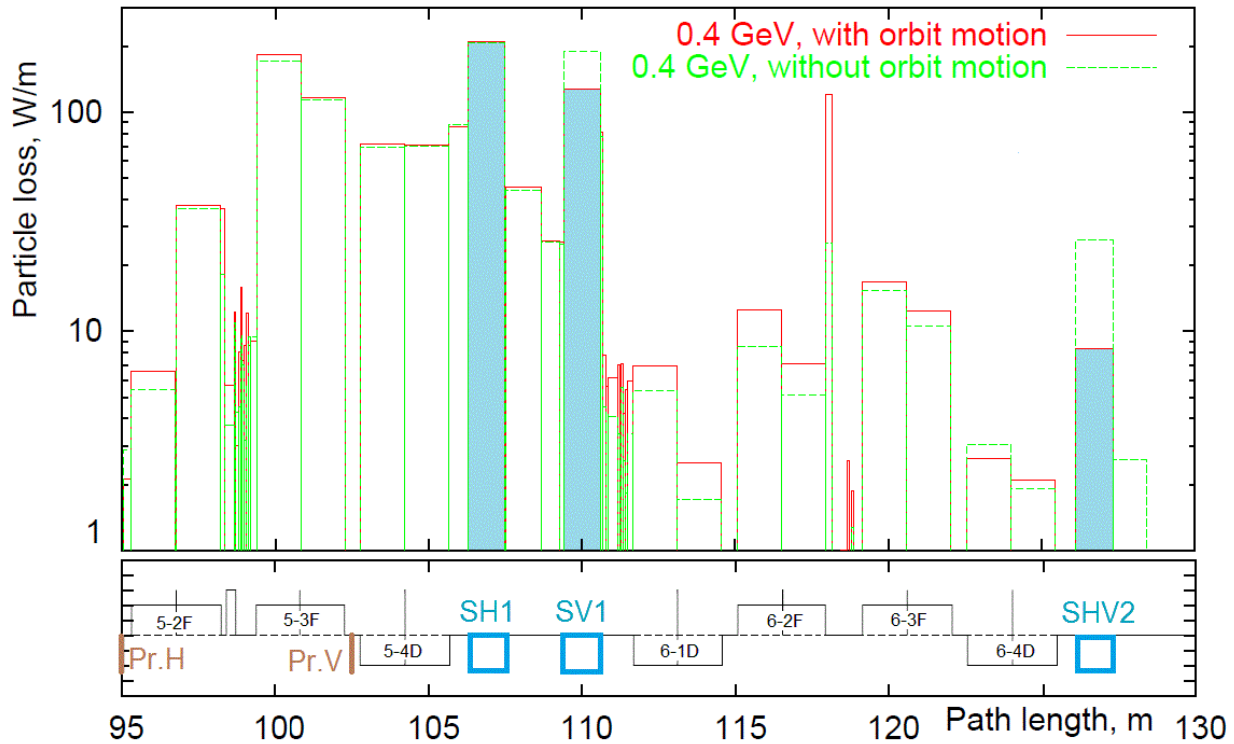


Figure 2.18: Beam loss distribution in the collimation region at the injection energy with (red) and without (green) orbit motion (fig.8 of ref [11]).

One can see that beam losses on the primary collimators are absent. It can be visually seen that the total losses on secondary collimators do not exceed 30 % of total beam losses on the presented 35 m long collimation region. Most of beam losses happen on the combined function magnets and on beam pipes. Since these elements are not shielded, the losses on them could not be considered as desirable (or "useful"), one can conclude that collimation efficiency of the 2SC with 0.4 mm thick copper primary collimator does not exceed 30%.

#### 2.4.2.6 The Collimator Design with Optimal Primary Foils

During years starting from the collimator commissioning in 2003 there was an opinion that the efficiency of the collimation system could be improved if the primary collimators of an optimal thickness will be used instead of really installed 0.3 mm cooper foil. It was declared again in the talk [42] at 2010 Proton Source Workshop that the highest collimation efficiency is achieved and beam loss rate even immediately downstream of the primary collimators can be kept at 1 W/m level if the thickness of primary collimators is equal to 0.003 mm for tungsten and 0.15 mm for carbon at injection energy, and it is equal to 0.1 mm for tungsten and 5.4 mm for carbon at the extraction energy. Thus, the optimal primary collimator thickness must be increased with energy growth. Note the above values of thickness are exactly the same as in the 2001 design paper [6].

The declared purpose [42] of the collimation system is to localize proton losses in a specially shielded section, thus to reduce irradiation of the rest of the machine to the acceptable levels. Straight sections 6 and 7 were chosen because these regions are far from engineering and support buildings. The

collimation system would localize about 99% of beam loss in a 25-m long region. Beam loss in the rest of the machine is on average 0.1 W/m, with several peaks of  $\sim$ 1 W/m.

The talk [42] also presented results of the STRUCT code simulations at the injection energy. The plot with beam loss distribution along Booster for the 0.3 mm thick graphite primary collimator has been presented there. That thickness is two times larger of optimal one for at the extraction energy. The plot demonstrated that the beam losses outside of the collimation region are less 1 W/m even at non-optimal twice-thicker primary collimator.

Another plot of the talk [42] has presented the beam loss distribution in the collimator region for two different primary collimators. The above 0.3 mm thick graphite primary collimator is compared with the 0.1 mm thick tungsten primary collimator. The thickness of the latter one is optimal at the extraction energy. Thus, the beam loss distributions with almost optimal "thin" and non-optimal "thick" primary collimators are compared. Figure 2.19 reproduces than plot, which we have slightly edited via coloring collimators and captioning them with nick names.

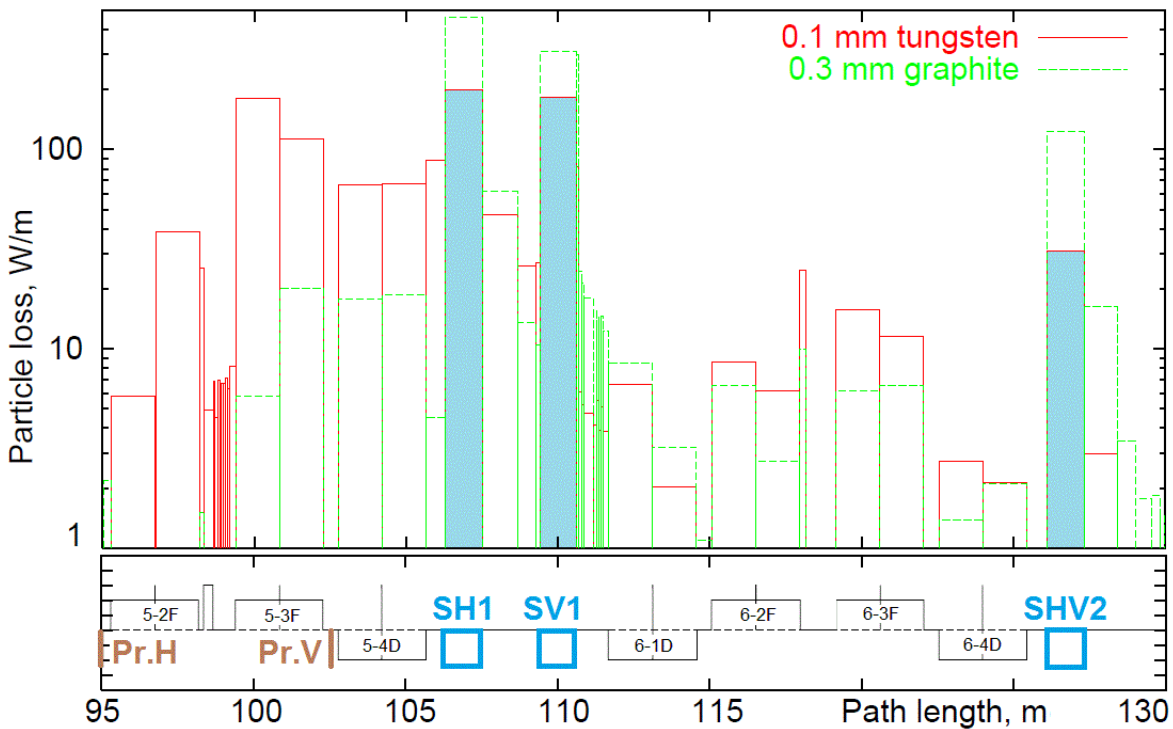


Figure 2.19: Beam loss distribution in the collimation region at the injection energy for 0.3 m thick graphite primary collimators (green) and for 0.1 mm thick tungsten (red) [42,43].

One can see effects of a thicker primary collimator: losses on the secondary collimators are reduced, while losses on other elements are increased. However, total losses on the secondary collimators do not exceed 50 % of total beam losses on the presented 35 m long collimation region even for 0.3 mm thick graphite primary collimator, while the loss power on some unshielded elements (combined function magnets and beam pipes) is rather high reaching 10 $\div$ 50 W/m.

Since about of half losses happen on unshielded elements, one can conclude that collimation efficiency of the 2SC with 0.3 mm thick graphite primary collimator does not exceed 50%. Unfortunately, we was not able to find a plot with beam loss distributions for the optimal primary collimators (neither 0.15 mm C nor 0.003 mm W) in published results of STRUCT code.

## 2.5 Details of the Collimation System Hardware

Three secondary collimators (absorbers) have been designed by "Bartoszek Engineering"[27]. In this design, because of tight integration of the collimator jaws and shielding steel, both the collimator jaws and the surrounding shielding move. The shielding looks like a cubic block. Its weight is 10.6 ton. The absorber has four degrees of freedom. It can be moved horizontally and vertically by  $\pm 1.50$  inches, and it can be yaw and pitch rotated by  $\pm 10$  radians. All three absorbers 6A, 6B, and 7A are identical. Figure 2.20 shows details of the absorber assembly together with sizes important for description of the beam aperture in beam dynamics simulations codes.

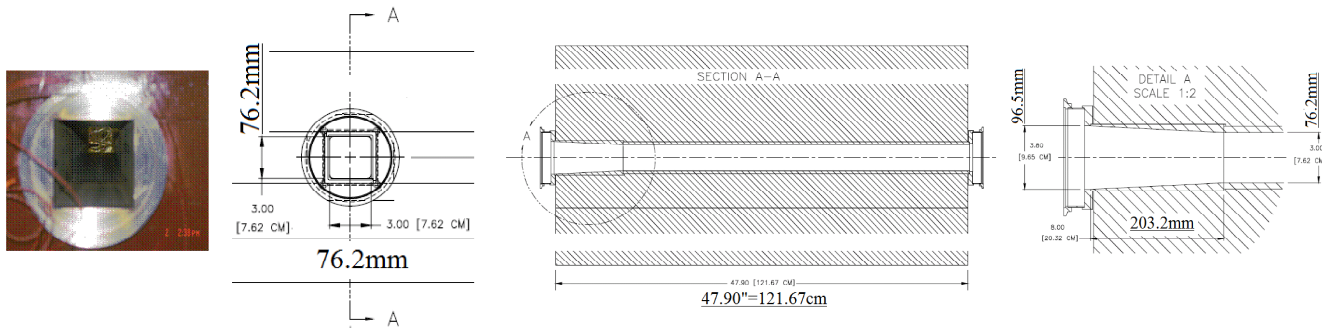


Figure 2.20: Booster absorber assembly (found at AD drawing<sup>6</sup>).

The long vacuum liner with square cross-section serves as the collimators jaws. The liner is surrounded by steel shield with wall thickness  $\sim 0.5$  m. The shielding spreads along the full length of vacuum liner ( $\sim 1.22$  m). To minimize a hot spot at the upstream end of the absorber and to move the radiation further into the shielding volume, the upstream 8 inches of the liner is tapered by 2 cm at vertically and horizontally. When the absorber is centered on the beam they have a 3 inches square aperture. The upstream and downstream ends of every absorber are connected to the neighboring vacuum pipes via usual unshielded bellows, which allow simultaneous horizontal and vertical translation of 1.50 inches each, while a total lateral offset for the bellows is up to 2.12 inches. Figure 2.21 shows the absorber layout in the long straight section 7.

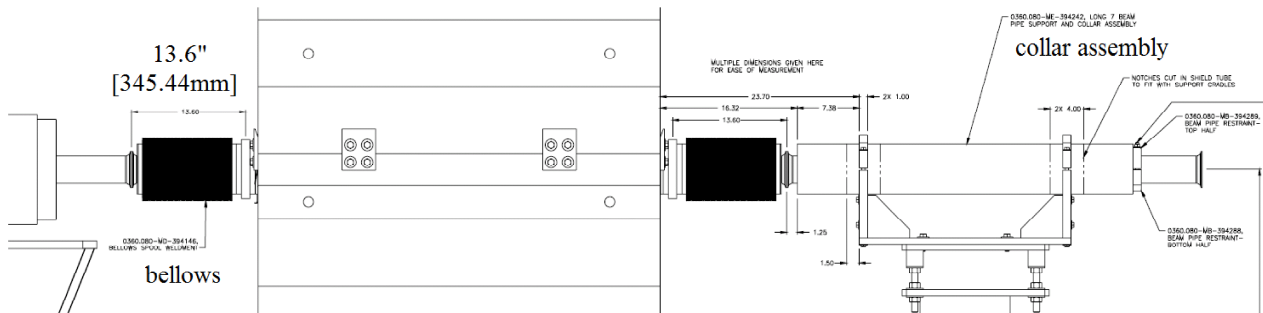
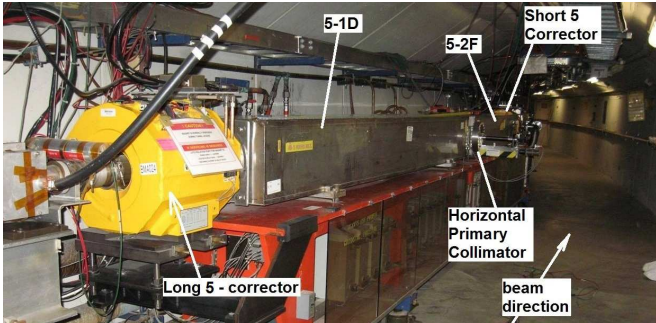
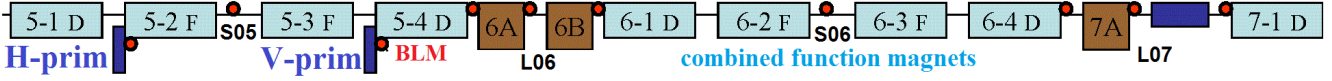


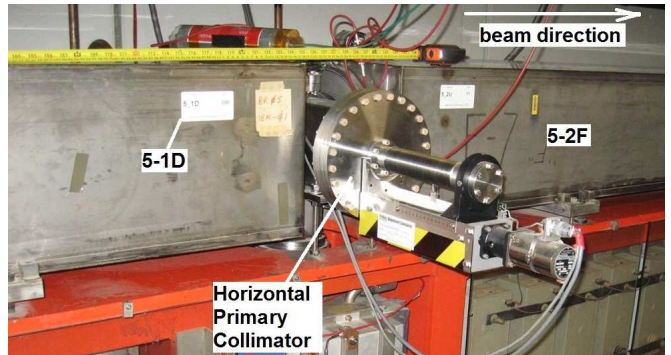
Figure 2.21: Absorber layout in the long straight section 7 (AD drawing, #0360.080-ME-394243").

Figure 2.22 shows 8 photos taken in the collimation area of the Booster tunnel [44]. Booster elements in the photos has been labeled following to designations adopted earlier in Fig.2.4. For a reader convenience the schematic layout of the 2SC system is again shown at the top of Fig. 2.22.

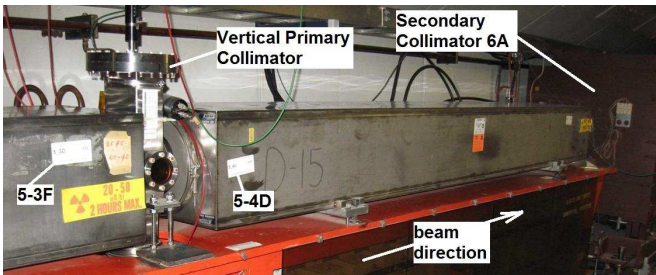
<sup>6</sup> Accelerator Division drawing library at web <http://admscad.fnal.gov>



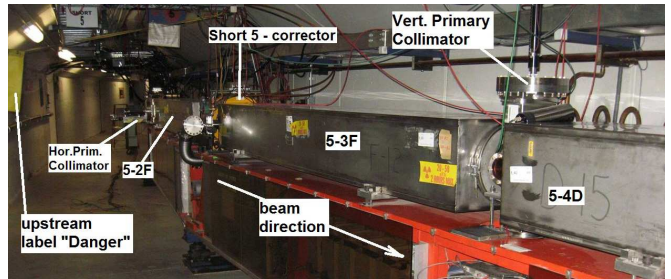
a) downstream view from the end of L05



b) view at horizontal primary collimator



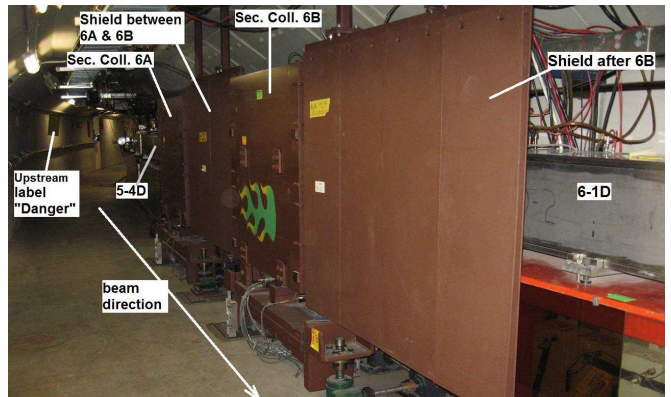
c) downstream from vertical primary collimator



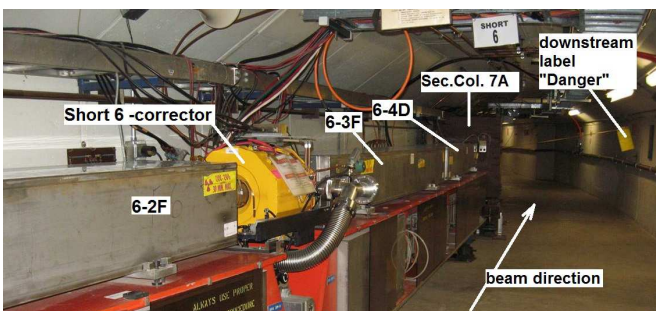
d) upstream from vertical primary collimator



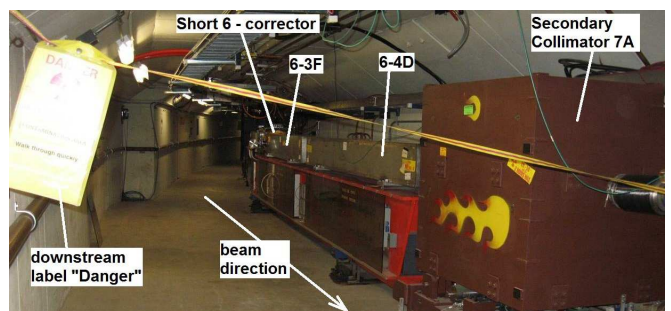
e) downstream view from US end of absorber 6A



f) upstream view from DS end of absorber 6B



g) downstream view from S06



h) upstream view from DS end of absorber 7A

Figure 2.22: Photos in the collimation area of the Booster tunnel (courtesy A.K. Triplet [44]).

Except of the discussed above absorbers, all shown Booster elements, namely combined function magnets, correctors, beam pipes, bellows, and both primary collimators have no any special shielding. There are only two supplementary shielding assemblies. One is located between absorbers 6A and 6B, and another is located after absorber 6B (see Fig. 2.22,e and Fig. 2.22,f). Note that there is no any kind of supplementary shielding at both ends of the absorber 7A, and at the upstream end of the absorber 6A (see Fig. 2.22,e and Fig. 2.22,h).

These supplementary shielding assemblies protect the aisle pass in the Booster tunnel from high residual activation existing at attached to the absorbers unshielded pipes and bellows. Every shielding assembly consists of the several rectangular steel plates hanged up on the hooks. Every plate is not heavy and can be mounted by a single worker.

Within the collimation region there is special area with a high residual activation. Two tablets "Danger" with the text "Contamination area. Walk through quickly" are located at the boundaries of this area. It starts from straight short section 5 (S05) and ends at the downstream end of the secondary collimator 7A (see Fig. 2.22,d and Fig. 2.22,h) occupying length of about one and half of the Booster period, *i.e.* about 30 m. This area includes many unshielded elements (combined function magnets, correctors, beam pipes, bellows). The boundaries of this high activation are set on the base of regular Booster radiation surveys. Example with results of such survey done on March 31, 2017 has been shown earlier in Fig.2.6. According to that survey, the residual activation at 1-foot from Booster elements exceeds 70 mrem/hour within all this 30-m long contamination area. The maximum residual activation exists at 1-foot distance from the absorber 6A.

Let's remind again, that up to now (2017) only secondary collimators are used for operations in a single-stage collimation mode without any usage of primary collimators. However, from time to time some beam tests to check a feasibility of the 2SC mode with usage of the primary collimators has been performed. Several constructions of the primary collimators have been used.

Both primary collimators use similar vacuum enclosures based on wire scanner assemblies allowing for motion control [41]. Two primary collimators are installed in 0.5-m short drifts (see Fig. 2.3), which are located before and after the 1.2-m short straight section 5 (S05). The flanges of the vacuum enclosures of primary collimators are connected to the flanges F and D magnets in a usual way without any special shielding (see Fig. 2.22,b-d).

Initial 2004 design [40] of the primary collimator used two foils attached to opposite sides of rectangular frame of the movable foil holder. Figure 2.23 shows two sides of the same movable foil holder with a 12 mils (0.3mm) carbon foil used at the injection energy and a 15 mils (0.381mm) copper foil used for higher energy collimation testing. That initial double foil configuration has been rejected and replaced by configuration with a single 15 mils copper scattering foil in 2005 [41].

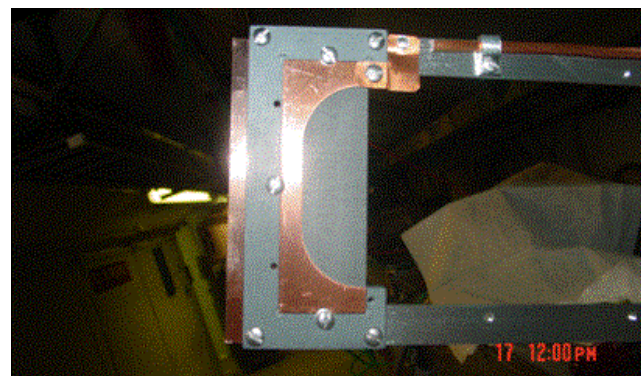


Figure 2.23: Copper (left) and carbon (right) sides of the primary collimator used in 2004 [40].

Figure 2.24 shows some drawings of the vacuum enclosure for the primary collimator, the movable assembly holding the scattering foil, the copper hot sink with 0.381 mm scattering foils, and photo of the primary collimator installed in 2005 [41].

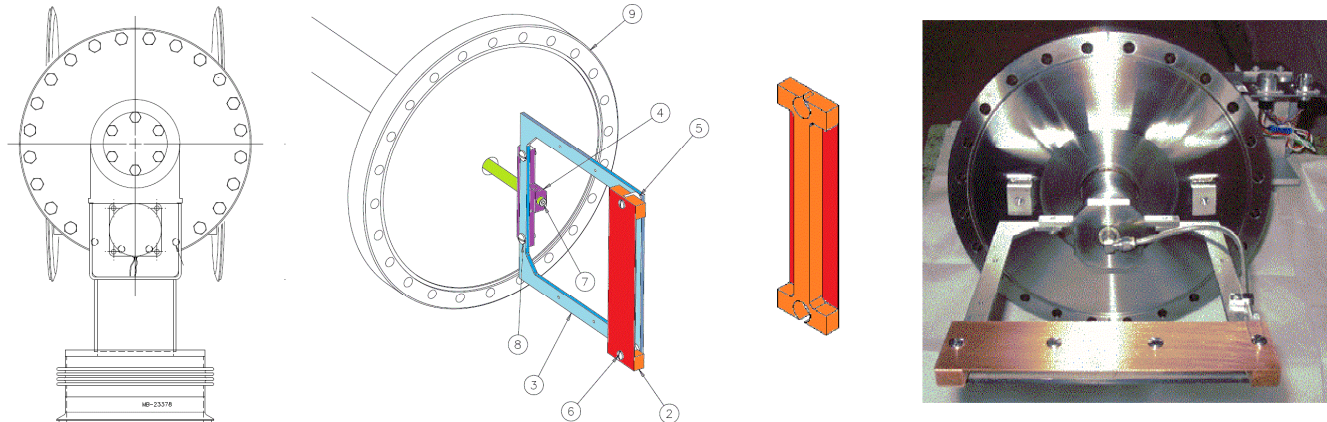


Figure 2.24: The primary collimator [41] (from left to right): drawings of the vacuum enclosure and the movable assembly, the copper hot sink with 0.381 mm scattering foils, and photo of assembly.

As results of our theoretical studies and discussions in 2015-2016, the above primary collimator configuration with the copper hot sink has been replaced by simple uniform aluminum plates with uniform thickness of 15 mils (0.381 mm) on February 2, 2016. With minor mechanical modifications this new aluminum foils was attached to the same the movable assembly shown in Fig. 2.24. To confirm a firmness of this new primary collimator configuration to a thermal load from the proton beam the calculation of deposited beam power and thermal parameters has been also performed [45].

The presented here details of the collimation system hardware demonstrated clear that the most elements of Booster periods 5, 6 and 7 located within the 30-m long collimation have no any dedicated shielding. Only secondary collimators covering a total length of about 4 m have dedicated shielding.

### **3. Reassessment of the Booster 2SC system**

#### ***3.1 Plans and approaches for reassessments***

##### **3.1.1 Initial plans and motivations at PIP start in 2011**

As it was discussed in the 2010 “Proton Task Force Report”, the improvements made to the Booster, have allowed higher throughput while keeping the activation levels less than 1 watt per meter (outside the collimation region) [13]. It was also stated that the areas near the collimators and extraction where the machine components and magnets have been and will continue to receive high doses of radiation will be of greatest concern. However, the Booster has never lost a gradient magnet due to coil failure. It is expected that if gradient magnet fails due to radiation damage it will happen in this area. It is also expected that all cabling in this region will eventually have to be replaced.

There were different ideas to decrease high radiation in the collimation area to allow a further increase of the beam intensity. Let's remind that till recently the Booster notching system had used the secondary collimator 6A as a notch absorber adding extra beam losses in the collimation area. Therefore, the one way to decrease beam losses in the collimator region was to create a dedicated notch absorber in another Booster region instead of usage of the secondary collimators. This way has been accepted and its realization has been started in 2012 as a part of the PIP plan [13,14,15,16,46,47].

Another way to decrease high radiation in the collimation area is a potential improvement of the Booster collimation system. At the start of PIP plan in 2012 [47], a potential improvement in the collimation system in future has been considered to be vital for 15 Hz operation. Although during all years after its installation in 2004 the Booster collimation system operated in a single-stage collimation (1SC) mode using only secondary collimators, the primary collimators were ready for operations in a two-stage collimation (2SC) mode of collimation.

Initial tests during commissioning of the collimation system in 2004 described in the previous chapter did not proved an advantage of the 2SC mode versus 1SC. By the 2012 a low performances of the 2SC system has been related with several issues, e.g. non-optimal thickness of the primary foils and frequent radial orbit variations inherent in the RF cogging scheme. Therefore, a new study on feasibility of 2SC mode has been planed after implementation of the momentum cogging which keep the beam orbit stable [46,47]. The momentum cogging has been implemented in 2014 [48] allowing new beam studies of the Booster collimation system in 2SC mode of operation.

The initial strategy concerning an improvement of the Booster collimation system has been outlined in the “Proton Source Improvement Plan” issued in 2011 [14]. The plan is to reduce radiation problems associated with the present Booster collimation system by reassessing its design, implementation, and operational use in light of present-day Booster operations, which could results in **development a specific collimator improvement plan**. This might result in a proposal for **a new Booster collimation system**. The final scale of this plan element could be known only after completion of beam studies and simulations, but \$3.2M including M&S and burdened labor had been allocated in the initial budget.

It was stated that the radiation significantly exceeds the level predicted by simulations performed during the design phase of the Booster collimators. The following steps are necessary [14]:

1. Perform realistic simulations of the beam loss and radiation levels and compare them with observations in order to learn why present radiation exceeds the expected levels.
2. Depending on the outcome of the previous step, 2 possible scenarios can be expected:
  - a) better machine tuning together with improvements of cogging will be sufficient to address the problem;

- b) a new collimation system or an upgrade of the existing one needs to be elaborated, designed and build.

It was noted that the first outcome looked somewhat less probable. It was recognized to be impossible to put a realistic effort estimate in the case of the second outcome. It was assumed that the worst case scenario can require few years to fully address the problem.

Up to now the above plan formulated in 2011 looks to be actual. It quite correctly outlines our works on the reassessment of the Booster collimation system. Our efforts presented in this report have been started in autumn of 2014.

### **3.1.2 Plans by start of new efforts in 2014**

Initially, the problems with 2SC collimation system have been reduced to quite simple task, which was formulated by N. Mokhov [49] and V. Lebedev. [50]. It was believed that these problems are originated from non-optimal thickness of the primary collimator foils used in the installed hardware [42]. To define an optimal foil thickness it was necessary to repeat simulations of the beam loss following to the approach adopted at the design of the collimation system. Since the STRUCT code became obsolete by 2014, it was necessary to develop a new simulation tool and check new results with the design ones.

Note, our posterior simulation results obtained later in 2016-2017 and presented in this report have brought out many questions and concerns about an applicability of usual simulation approach for the Booster collimation system. Some specific features of the Booster hardware and working parameters have required critical reconsideration of the simulation results and well-developed principles of two-stage collimation systems.

#### **3.1.2.1 Initial Plan for Study Booster Collimation System**

New efforts on the Booster collimation system has been started in autumn of 2014. Initial list with all relevant subjects has been presented by W. Pellico at the meeting on Dec. 17, 2014 [65]. It included the following items:

1. Review present Booster operations
  - a) Running conditions – impact of collimators on present operations
  - b) Orbits and Apertures
  - c) Beam loss profile around the ring
  - d) Present positioning of both primary and secondary collimators w.r.t. beam
2. Review Original Collimator Design
  - a) Primary(s) – have been upgraded several times
  - b) Secondary(s) – Placement
3. Review Present Diagnostics
  - a) BLM placement
  - b) Additional Scintillators – being planned (by R.T. Tesarek)
  - c) Local BPMs (near collimators)
  - d) Determine if upgrades are required
4. Review Present Software
  - a) ACNET software
  - b) Simulations/Optics Modeling Software
    - i. Original software – used to predict activation and ring loss profile
    - ii. Re-generate activation and loss profile
      1. Use MADX
      2. Use Optim

V. Kapin has been appointed to lead and organize an implementation of the above tasks.

Later the above general purposes for study of the existing Booster collimation system have been specified more precisely. It was necessary to understand and demonstrate if operation of collimators in a two-stage mode could be more efficient than its current operation in conventional (single-stage) mode. An optimization of 2SC mode has been tightly related with an optimal choice of the scattering foil for the primary collimators. A common plan to achieve the above purpose has been generated. The main steps of the plan are outlined as the followings:

- a) choose and adjust a computer code for study Booster collimation system
- b) with help of numerical simulations find optimal foil thickness for primary collimators
- c) install a new optimal foil
- d) perform beam study using the Booster collimation system in 2SC mode operation
- e) post-process data of beam study and compare beam loss for 2SC mode with 1SC.
- f) make conclusions if it is reasonable to operate in 2SC mode instead of 1SC mode

## 3.2 General Principles of Two-Stage Collimations

### 3.2.1 The problems of conventional (one-stage) collimation

Various beam physics mechanisms can cause beam emittance growth and formation of a beam halo. The most important causes of emittance growth are the following [51]: nonlinear forces due to magnet errors; beam mismatch causing oscillations of the rms radius; misalignments of the focusing and accelerating elements; nonlinear space-charge forces in beams with non-stationary density; nonlinear single-particle and coupling resonances; random kicks due to rf noise and etc. As result, a small fraction of the particles with large transverse amplitudes may form a “halo” surrounding the beam core. As noted in ref. [51], some details of a halo formation are not yet fully understood.

Particles in a beam halo are a main source of uncontrolled regular beam losses on the aperture restrictions of the machine elements. Uncontrolled beam losses cause various problems such as residual activation of accelerator components, local vacuum degradation and radiation damage of insulation materials. As rule, a beam halo contains future lost particles. The defense against uncontrolled beam losses is a collimation system, which should be the tightest aperture restriction at suitable position in the machine.

The main purpose of a collimation system is to clean beam by removing all halo particles. A proper collimation system should intercept halo particles (or future lost particles) and redirect them inside of well-shielded beam absorbers, while it should be done in well-predefined controllable way which is stable to fluctuations of the machine parameters. Figure 3.1 [52] illustrates concepts of beam core and beam halo, and problem with a conventional beam collimator jaw.

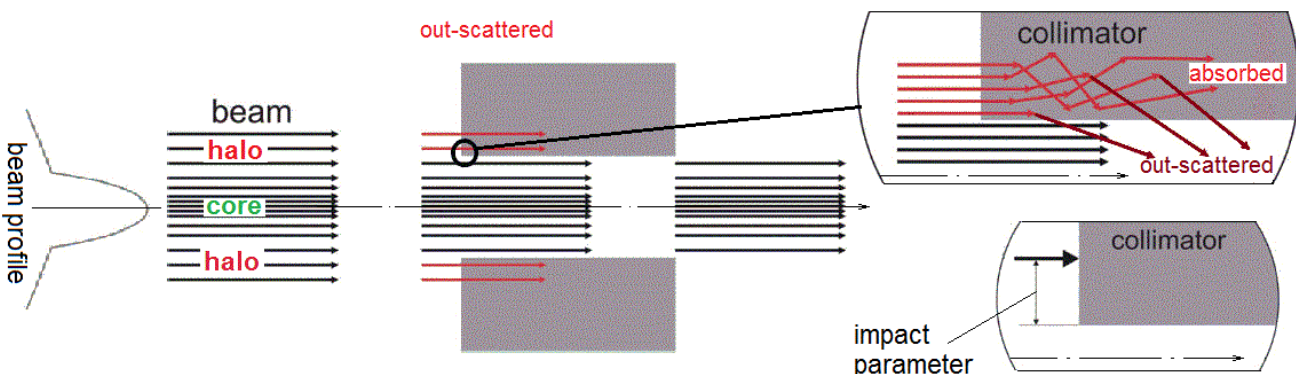


Figure 3.1: Illustration of beam profile, beam core and halo, out-scattered trajectories in a conventional solid block collimator, the impact parameter [52].

As contrasted with a naive idea that all particles touching a conventional beam collimator are stopped inside its body, a considerable portion of the halo particles hitting near collimator edge at small impact parameter is scattered out of such collimator. The impact parameter is the distance from the edge at which the collimator jaw is hit (see Fig 3.1.)

The problems related with usage of conventional solid blocks to define the beam aperture restriction has been understood more than 50 years ago, e.g. in 1969 FNAL reports by L.C. Teng [54, 55]. Figure 3.2,a shows a calculation model for proton out-scattering at edge of the collimator jaw sketched in ref. [54]. The systematic description of drawbacks related to the conventional (or single-stage) collimation has been presented in many papers, e.g. in ref. [56, 57, 58].

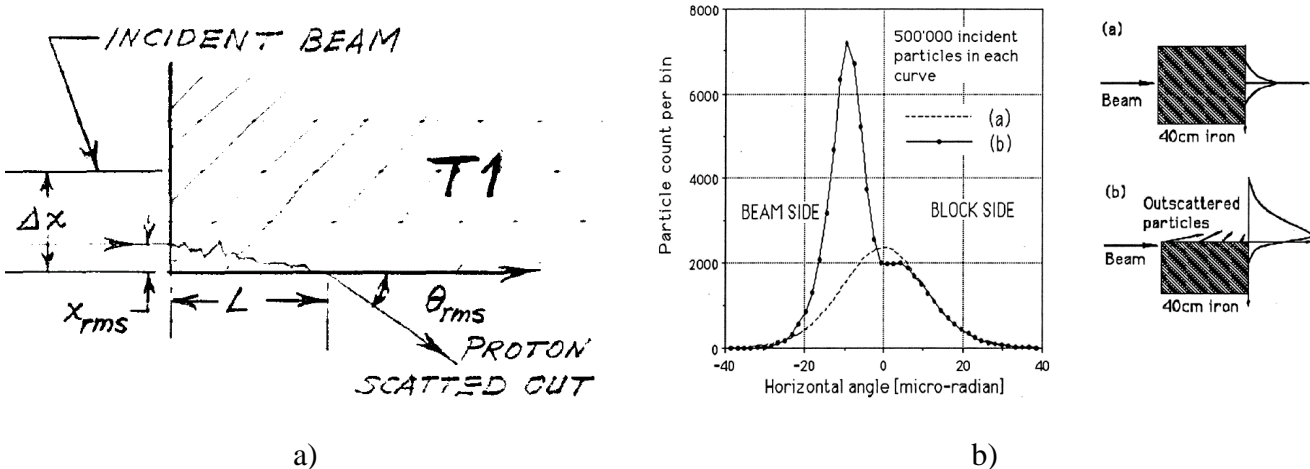


Figure 3.2: Proton out-scattering in a conventional collimator: a) scheme by L.C. Teng [54]; b) projected angular distributions of elastically scattered particles in ref [56].

Let's follow description presented in ref. [56]. The most direct way of collimating a beam of particles is conventional solid-block aperture. Depending upon the material and thickness, a certain fraction of the intercepted beam will survive, either by traversing the whole length of the block or by being scattered out of the side against the beam.

Figure 3.2,b shows two calculations for a 40cm-long iron block. Curve "a" corresponds to the surviving particles that entered the block far enough from the edge not to be affected by out-scattering. They leave the downstream end with a Gaussian-type distribution peaked in the forward direction. Curve "b" corresponds to particles that are intercepted at 1  $\mu\text{m}$  from the edge of the block. The right-hand side of their distribution ('Block side') is essentially unchanged compared to curve "a", whereas the left-hand side ('Beam side') is enhanced by a tall peak of particles scattering out of the block. The particles traversing the whole block (curve "a") can be suppressed by using a longer block or a 'denser' material. Suppressing the out-scattered peak in curve "b" is more difficult. The out-scattered particles may have increased amplitude and essentially lower energy, and therefore, they are very likely to be lost in an aperture restriction in the machine before returning to the collimation section.

Although specific examples have been taken in Figure 3.2,b the form of the curves is characteristic. See for example, very similar curves for SSLC collimators [58] by A. Drozhdin et al. For a given material of the collimator, the position and width of the peak of the out-scattered particles in curve (b) depends upon the impact parameter and upon the energy. The smaller the impact parameter and the higher the energy, the narrower the peak becomes and the closer it moves to the zero-angle position. When using a single block to collimate a beam, the absorption efficiency of the block is the first concern.

For a given material of the absorber, the absorption efficiency  $\varepsilon_{\text{abs}}$  depends on good alignment of the absorber jaw. It can be defined as ratio of the absorbed particles  $N_{\text{abs}}$  to total number of particles entering into the collimator  $N_{\text{tot}}$ , i.e.  $\varepsilon_{\text{abs}} = N_{\text{abs}} / N_{\text{tot}}$ . If the number of incident particles which are out-scattered from the collimator is designated as  $N_{\text{out}} = N_{\text{tot}} - N_{\text{abs}}$ , then one can define the out-scattering efficiency as  $\varepsilon_{\text{out}} = N_{\text{out}} / N_{\text{tot}} = (1 - \varepsilon_{\text{abs}})$ .

The dependence of out-scattering efficiency  $\varepsilon_{\text{out}}$  on an alignment angle  $\alpha_{\text{col}}$  for single solid-block collimator jaw has been simulated by M. Seidel at DESY [57]. Figure 3.3 shows the out-scattering efficiency  $\varepsilon_{\text{out}}$  (or probability) as a function of alignment angle for two different average impact parameters  $\langle b \rangle$ . In the simulation, the collimator jaw has a simple rectangular cross-section.

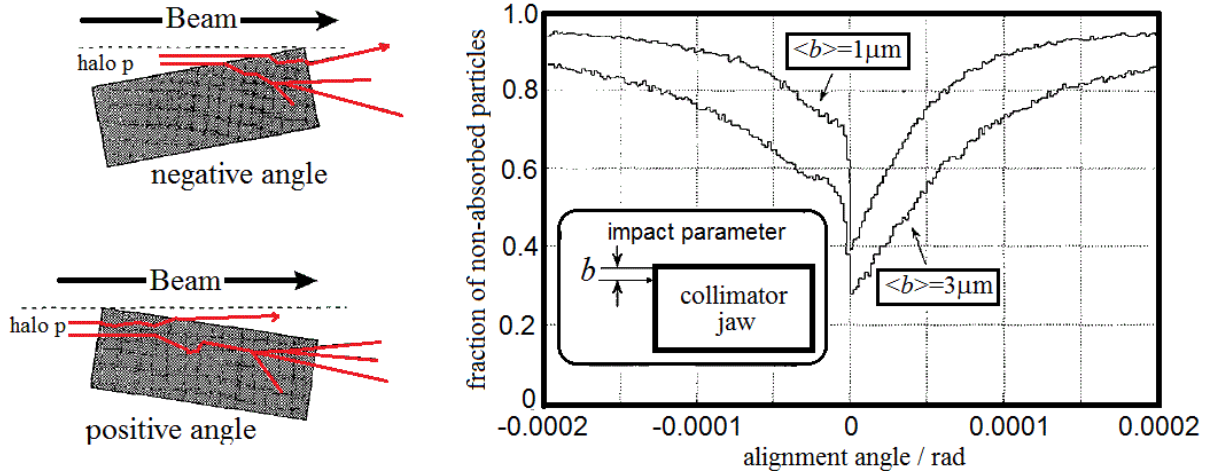


Figure 3.3: The out-scattering probability as a function of alignment angle for two different average impact parameters  $\langle b \rangle$  [57].

The impact parameter strongly influences the absorption efficiency of a single collimator jaw. In the case of the perfect alignment ( $\alpha_{\text{col}} = 0$ ), the absorption efficiency  $\varepsilon_{\text{abs}}$  is up to 60 % and 70 % for the impact parameters  $\langle b \rangle = 1 \mu\text{m}$  and  $\langle b \rangle = 1 \mu\text{m}$ , respectively. The most important result is the strong dependence of the absorption efficiency on the angular alignment of the collimator jaw. If the jaw is misaligned as depicted in Fig. 3.3 (left side), the effective collimator length is reduced. With misalignment of  $\pm 0.1 \text{ mrad}$ ,  $\varepsilon_{\text{abs}}$  drops to 10 % and 30 % for  $\langle b \rangle = 1 \mu\text{m}$  and  $\langle b \rangle = 1 \mu\text{m}$ , respectively.

Note, a sharp drop of  $\varepsilon_{\text{abs}}$  at small negative angles ( $\alpha_{\text{col}} < 0$ ). For example, at the alignment angle ( $\alpha_{\text{col}} = -0.01 \text{ mrad}$ )  $\varepsilon_{\text{abs}}$  drops down to 30 % and 50% for  $\langle b \rangle = 1 \mu\text{m}$  and  $\langle b \rangle = 1 \mu\text{m}$ , respectively. The dependence  $\varepsilon_{\text{abs}}$  on  $\alpha_{\text{col}}$  for positive alignment angles is quite smooth. Probably, the difference between  $\varepsilon_{\text{out}}(\alpha_{\text{col}})$ -curves for small positive and negative angles is originated from the fact that at a small positive  $\alpha_{\text{col}}$  particles enter into the collimator perpendicular to its surface, while at a small negative  $\alpha_{\text{col}}$  particles enter into the collimator tangentially to its surface. Therefore a small positive misalignment angles are preferable in a practice. Nevertheless, the total angle width of the maximal absorption efficiency does not exceed several tens of  $\mu\text{rad}$ , which is far below of usual mechanical possibilities for bulky collimators.

Thus, there is a non-negligible chance that a particle that hits a collimator reenters the beam aperture as a result of multiple scattering in the material. The absorption efficiency strongly depends on the angular alignment of the collimator jaw. Theoretically maximal values of the absorption efficiency are located within a narrow interval of the alignment angles (about several tens of  $\mu\text{rad}$ ). Due to edge scattering the absorption efficiency of a single collimator turns out to be insufficient [57]. Note, that small misalignments within  $\pm 0.1 \text{ mrad}$  could be partly cured with steering the beam orbit.

### 3.2.2 Features and merits of two-stage collimation system

The particle out-scattering in the conventional (or single-stage) collimation is uncontrollable and harmful process, which can create high residual activation in areas nearby and downstream of the collimator. However, it can be converted into a useful mechanism, if additional collimators (so-called secondary collimators) can be added downstream after the conventional collimator, which is called in such two-stage scheme as primary collimator. In this scheme, the major function of the primary collimators is to scatter a primary beam, while major function of the secondary collimators is the interception and absorption of particles which were scattered by the primary collimators. Therefore, the primary collimator can be transformed from thick solid block to thin scattering foil passing most of incident particles. Such primary collimators are also called as targets or scrappers. The secondary collimators must have dedicated shielding and the aperture of these secondary collimators must of course be such that they never interfere with particles which have not touched a primary collimators.

It is convenient and customary [55, 56, 59, and 60] to use normalized variables when analyzing the action of the two-stage collimation system. The transformation from un-normalized to normalized coordinates reduces the betatron oscillations to simple harmonic motion. Let's use throughout this report the following formulae for dimensionless normalized coordinates (capital letters) for some transverse plane (either horizontal or vertical) [60]:

$$X = x/\sigma; \quad X' = (\alpha/\sigma)x + (\beta/\sigma)x', \quad \sigma = \sqrt{\varepsilon\beta} \quad (3.1)$$

where  $x$  and  $x'$  are non-normalized coordinates,  $\alpha$  and  $\beta$  are the Twiss parameters and  $\varepsilon$  is the beam emittance,  $\sigma$  is the rms beam size. Figure 3.4 taken from lecture [52] illustrates transformation from un-normalized to normalized coordinates.

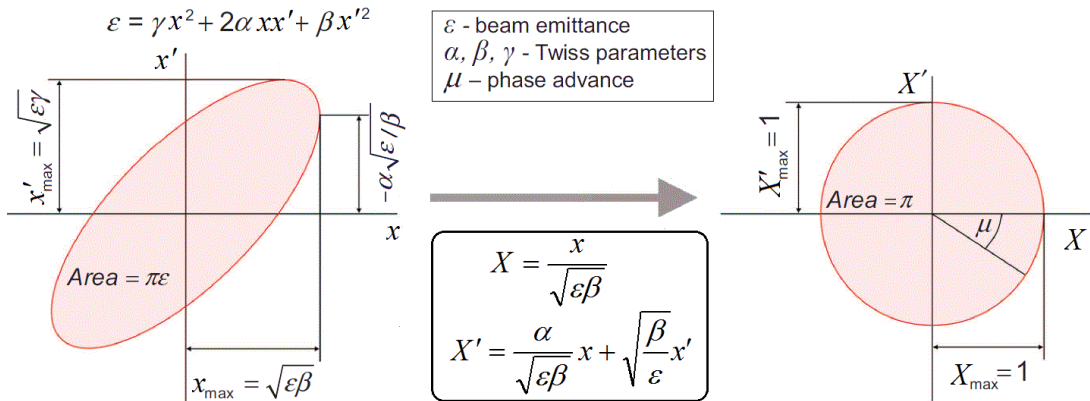


Figure 3.4: Conversion from un-normalized phase space (left) to normalized phase space (right) [52].

Note, that Figure 3.4 illustrates a simple case of the linear motion. During multi-turn motion all particles stay exactly on their elliptic trajectories for the non-normalized phase. With the above linear transformation formulae the ellipses are converted to circles, and all particles stay on their circle trajectories in the normalized phase. However, the above ideal elliptical and circle trajectories will be destroyed in the case of non-linear motion, which is always realized in all real machines where particles are affected by nonlinear components of both the magnetic field (sextupoles, octupoles, etc) and the space-charge field of beam with non-uniform distribution of the charge density.

Let's illustrate the case of the non-linear motion by the MADX code examples for its symplectic tracking module PTC-TRACK [53] created by V.K. and F. Schmidt in 2005. Figure 3.5 shows the

phase-space coordinates of several particles during 1000 turns in a non-linear test lattice for un-normalized phase-space and four cases of the normalized phase space, which differ between each other by the order of the normal-forms given by parameter "norm\_no".

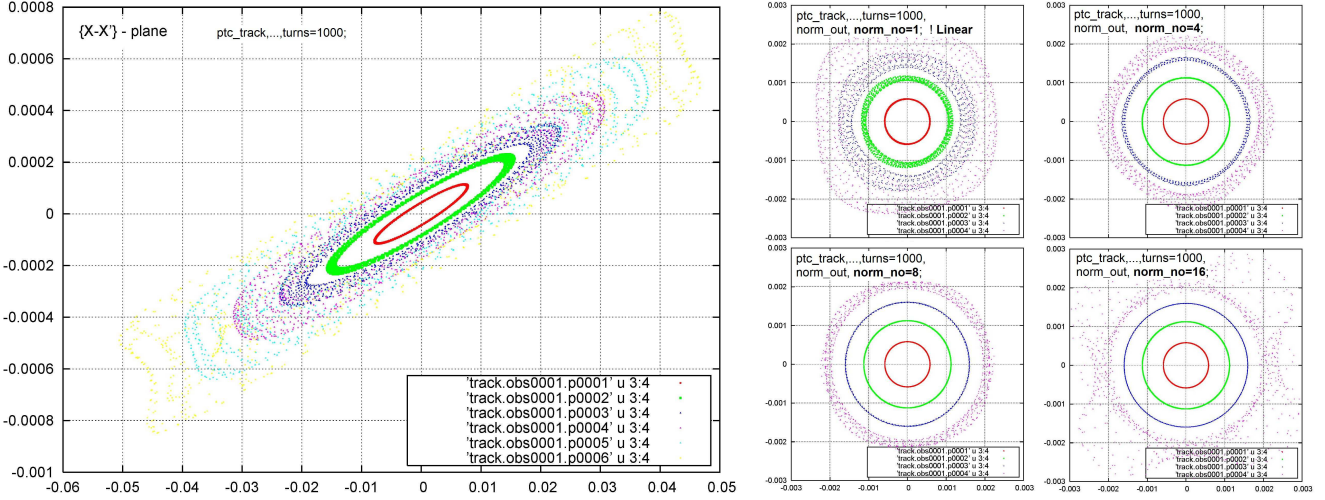


Figure 3.5: Example of nonlinear normal-form conversion from un-normalized phase space (left) to normalized phase space (right) at 4 different normal-form orders [53, examples for MADX code].

The un-normalized phase-space contains the phase-space coordinates of six particles, which differ by values of the initial amplitudes. The particles are enumerated in terms of their initial amplitudes in increasing order. Points representing output coordinates of six particles after every turn form images of tilted ellipses. The first (red) particle with smallest initial amplitude forms an ideal tilted ellipse with a thin boundary. The second (green) particle forms a tilted ellipse with a thicker boundary. The third (blue) particle forms a cloud looking as a tilted ellipse with a smeared boundary. Next particles form some smeared clouds reminding ellipses.

The normalized phase-spaces on the right part of Fig. 3.5 show the phase-space coordinates of first four particles with smallest amplitudes. The left-up plot shows results of the linear conversion ("norm\_no=1"), which corresponds to "ellipse-to-circle" conversion formulae presented in Fig. 3.4. The right-up plot shows results of the 4th order the normal form ("norm\_no=4"), and the bottom plots show results the 8th and 16th orders of the normal forms on the left and right plots, respectively.

The linear normal form ("norm\_no=1") demonstrates a perfect transformation of the red ellipse into the red circle representing the 1st particle with the smallest amplitude, while next particles forms the circles with thick boundaries, which is distorted and smeared with the amplitude increasing. To suppress such distortions for first three particles at least the 16th order normal forms should be used.

The above discussion has a direct impact on an analysis of a two-stage collimation system with help of ideal phase-space circles and straight lines in the normalized coordinates. It is necessary to realize that the initially perfect shapes on the phase plane will be essentially distorted after a number of turns in real machine having non-linear fields. For example, a thin straight line on the initial phase space may finally look as a cloud of particles smeared around a bended line. This smearing means that phase-space coordinates of particles coming to the collimator location will deviate from coordinates prescribed by collimation design. As result, some particles may even avoid the collimator.

Figure 3.6 shows the schematic layout of a conventional two-stage collimation system [56] consisting of primary collimator (thin foil) which scatters the halo particles, and two secondary collimators (solid blocks) absorbing the scattered particles. The half aperture set by the primary collimator is  $n_{\text{prim}}$  in normalized coordinates and the secondary collimators are stepped-back from the

beam by a distance  $\delta$ , also in normalized coordinates, i.e. the distance between the secondary collimators and the beam axis is equal to  $n_{\text{sec}} = n_{\text{prim}} + \delta$ . After passing through the primary collimator scattering foil the particles have an angular spread, which enables many of them to be intercepted by the secondary collimators placed at optimal positions later in the lattice.

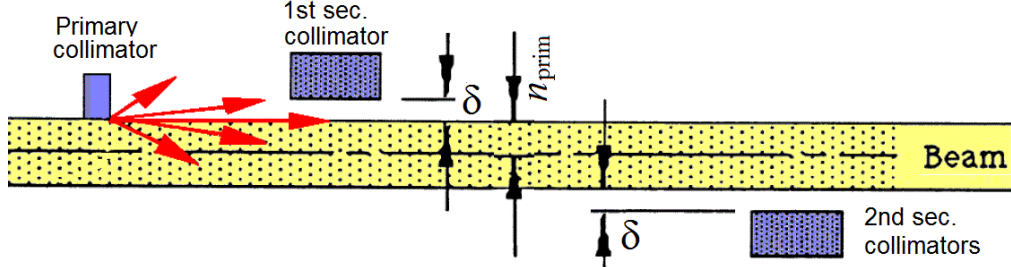


Figure 3.6: Layout of two-stage collimation scheme [56].

Figure 3.7 shows example of three characteristic particle trajectories in this system ( $n_{\text{prim}}=1$ ) [61]. The first trajectory (in red color) shows particle scattered outwards of the beam and passes through the first secondary collimator. This particle can be absorbed by this first secondary collimator. The second trajectory (in green color) belongs to particle which passed through the primary collimator without getting any angle kick. This undisturbed particle will continue motion inside the beam envelope. The third trajectory (in red color) shows particle scattered inward to the beam axis and passes through the second secondary collimator. This particle can be absorbed by this second secondary collimator.

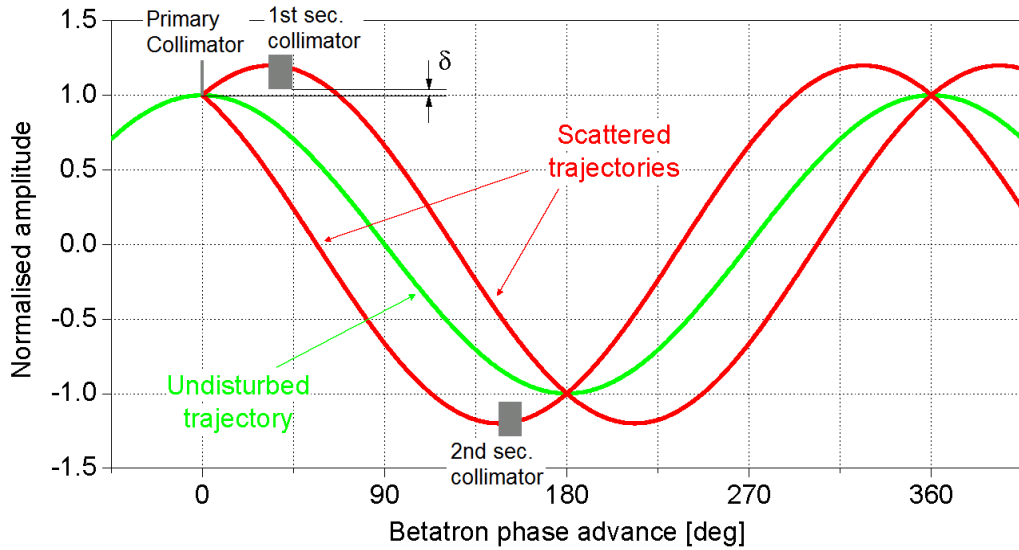


Figure 3.7: Particle trajectories in the two-stage collimation system [61].

Particles may have a small impact parameter on the primary collimator. However, the impact parameter of the scattered particles at the secondary collimator is significantly enlarged. This leads to reduced leakage of the particles due to out-scattering effect from the secondary collimators. A minimization of the out-scattering effect in solid bulky collimators is main merit of the two-stage collimation system in comparison to a conventional single-stage collimation. As result, residual activation around the absorbers included two-stage collimation system should be lower than for absorbers operating as conventional (single-stage) collimators.

As it was noted by P. Braynt in CERN Accelerator school lecture [59], the principle for positioning the secondary have been first given in the 1969 FNAL report [55] by L.C. Teng. It was also independently developed at CERN. Figure 3.8 shows main features of two-stage collimation scheme.

The scheme uses a primary collimator (or scattered) followed by two secondary collimators that are optimized to intercept particles that are scattered by the primary collimator. Figure 3.8,A shows the case of optimal phase shifts  $\mu_1$  and  $\mu_2$  for the most efficient interception of the scattered tails. It is assumed that energy loss suffered by these scattered particles in the primary collimator is negligible.

The situation "a" in Fig. 3.8,A shows phase space at a moment when particles located on the boundary of the beam envelope were scattered by the primary collimator. The normalized particle coordinates at the primary collimator before scattering are  $X=n_{\text{prim}}$  and  $X'=0$ , or non-normalized coordinates are

$$x_{\text{prim}} = n_{\text{prim}} \sigma, \quad x'_{\text{prim}} = -(\alpha/\beta)x_{\text{prim}}. \quad (3.2)$$

These scattered particles suffer essentially an angular deflection. Furthermore, the scattered protons populate a vertical straight line (red) including particles scattered at both positive and negative angle relatively the beam. The density of the particle distribution along the line is well described by Gaussian distribution centered at  $X'=0$ , where the particle density has maximum values. The rms angles of the Gaussian distribution in the normal coordinates  $\theta_n$  are shown in Fig. 3.8,A as two green dots with coordinates  $X'_{1,2}=(n_{\text{prim}}, \pm \theta_n)$ . Their non-normalized coordinates are  $x'_{1,2} = x'_{\text{prim}} \pm \theta_0$ . The rms angles in the normalized coordinates  $\theta_n$  can be found from the rms angles of the Gaussian distribution in the non-normalized coordinates  $\theta_0$  according to the following equation:

$$\theta_n = \theta_0 \sqrt{\beta/\epsilon}, \quad (3.3)$$

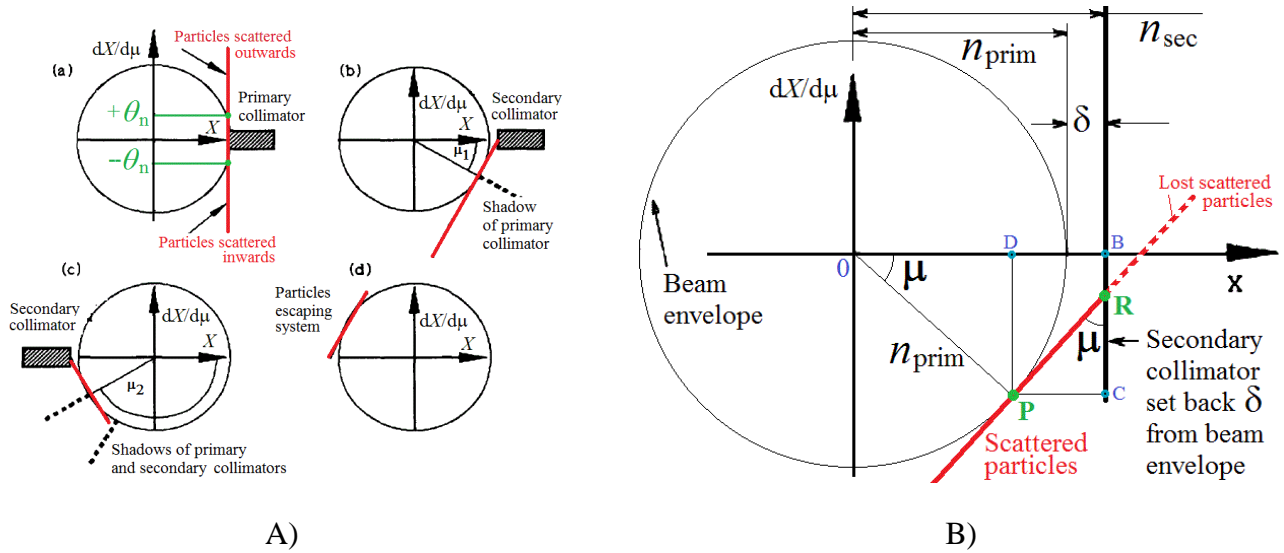


Figure 3.8: Main features of two-stage collimation scheme in normalized phase-space [59]: A) every collimator located at an optimal phase shift; B) details of situation "b" with a non-optimal phase shift.

All scattered particles are located outside of the phase space occupied by the beam envelope. Therefore, they can be intercepted by means of the secondary collimators without influencing the particles inside the beam envelope. The situation "b" in Fig. 3.8,A shows the interception of the

outwards tail of the scattered particles by the first secondary collimator located at an optimal phase shift  $\mu_1=\mu_{\text{opt}}$  ( $0 < \mu_{\text{opt}} < 90^\circ$ ) from the primary collimator. The situation "c" in Fig. 3.8,A shows the interception of the inwards tail of the scattered particles by the second secondary collimator located at an optimal phase shift  $\mu_1=\pi-\mu_{\text{opt}}$  from the primary collimator.

Note that both secondary collimators intercept only tails of the scattered particle distributions, while the dense central part of the distributions shown as the situation "d" in Fig. 3.8,A escapes from the collimation system. Existence of the particles escaping from the two-stage collimation system is caused by the mandatory gap  $\delta$  between the beam envelope and secondary collimators. Therefore, secondary collimators could not intercept all scattered particles and ratio of the intercepted particles to all scattered particles is always less than 100 %.

Figure 3.8,B shows the situation "b" (see Figure 3.8,A for the secondary collimator nearest to the scatterer) in more details for general case of non-optimal phase shift. The scattered particles are spread out along the red line at an angle  $\mu$  equal to the betatron phase advance between the primary and secondary collimators. The secondary collimator is stepped back from the beam envelope to prevent it becoming a new primary collimator. The line segment PR is a locus of the particles which are not intercepted by the first secondary collimator, and its minimum corresponds to the maximum length of outwards tail (red dotted line) intercepted by the first secondary collimator. There is an optimum  $\mu_{\text{opt}}$  for which the length of the line PR reaches its minimum.

A convenient equation for the optimal  $\mu_{\text{opt}}$  has been derived in ref. [60]. Using Figure 3.8,B, the length of the straight-line segment PR designated by  $K$  can be expressed as<sup>7</sup>

$$K = \frac{n_{\text{sec}} - n_{\text{prim}} \cos \mu}{\sin \mu}. \quad (3.4)$$

The function  $K(\mu)$  has minimum value at  $\mu=\mu_{\text{opt}}$ , which is expressed by the following equation:

$$\cos \mu_{\text{opt}} = n_{\text{prim}} / n_{\text{sec}}. \quad (3.5)$$

This equation defines two angles  $\mu_{\text{opt},1}$  and  $\mu_{\text{opt},2}=(\pi-\mu_{\text{opt},1})$ . One secondary collimator should be set at a phase shift  $\mu_{\text{opt},1}$  ( $0 < \mu_{\text{opt},1} < 90^\circ$ ) downstream of the primary collimator, and another secondary collimator should be set at the opposite side of the beam at a phase shift  $(\pi-\mu_{\text{opt},1})$ . Once  $n_{\text{prim}}$  and  $n_{\text{sec}}$  have been chosen,  $\mu_{\text{opt}}$  is deduced. For example, if  $n_1=3$ , and  $n_2=3.5$ , then  $\theta_{\text{opt}}=31^\circ$ , and secondary collimators should be located at phase advances  $31^\circ$  and  $149^\circ$ . The optimal phase advances, the minimal parameter  $K_{\text{opt}}$  is defined by the following equation:

$$K = \sqrt{n_{\text{prim}}^2 - n_{\text{sec}}^2}. \quad (3.6)$$

Thus, the secondary collimators located at optimum  $\mu_{\text{opt}}$  will intercept maximal number of the scattered particles reaching a possible theoretical limit. This optimum depends upon the radius of the beam envelope, which equals the half-aperture of the primary collimator  $n_{\text{prim}}$  (normalized) and the step back  $\delta$  (normalized), which defines the position of the secondary collimator  $n_{\text{sec}}=n_{\text{prim}}+\delta$ .

If for given parameters  $n_{\text{prim}}$  and  $\delta$  both secondary collimators are located at optimal phase shifts from the primary collimator, than both secondary collimators will intercept maximal theoretically

---

<sup>7</sup> With help of 3 relations: 1)  $K=l_{\text{PR}}=l_{\text{PC}}/\sin \mu$ ; 2) where  $l_{\text{PC}}=l_{\text{DB}}=(n_{\text{sec}}-l_{\text{OD}})$ ; 3)  $l_{\text{OD}}=n_{\text{prim}} \cos \mu$ .

possible number of particles, while it will happen during the first passage of the scattered particles through the secondary collimators ( $0 < \mu < 2\pi$ ).

Let's imagine what happens in a practical case when the secondary collimators are located at slightly non-optimal phase shifts. Some portion of scattered particles, which is less than the above theoretical maximum, can be intercepted at the first passage of the scattered particles through the secondary collimators. Let's assume an arbitrary large number of passages (or turns) in cyclic machine. After some number of turns in a machine with non-integer tunes the remains of not-yet-intercepted scattered particles will approach to the secondary collimator at more and more favorable phases allowing an interception of new portions of the scattered particles. This process could continue for indefinite number of turns, and finally, a theoretical limit for maximum number of intercepted particles will be reached.

Thus, a location of the secondary collimators at non-optimal phase shifts leads to the multi-turn collimation process during which small portions of scattered particles are intercepted by secondary collimators. This situation looks to unavoidable in practice, since it may happen either due to physical impossibility to set absorbers at the right location or due to variations of machine optics (and hence phase advances) for different regimes.

Let's remind again that the above considerations are assumed the linear beam dynamics during a larger number of turns. However, the perfect straight lines shown in Figure 3.8 can be distorted and destroyed after some number of turns due to a presence of non-linear fields in a realistic machine.

### **3.3 Preparation for Numerical Simulations of the Collimation System**

#### **3.3.1 Substituting STRUCT code by MADX code**

As was already described in the chapter 1, the original 2SC system installed in Booster had been designed with the STRUCT code [19], which simulated a multi-turn tracking of halo protons in the Booster lattice with their scattering on collimators. Results of the STRUCT code have predicted the beam loss profile around Booster. Protons lost on the machine components were stored to the files for the next step of calculations with the MARS code [20], which performed full-scale Monte Carlo hadronic and electromagnetic shower simulations.

In the 2014 talk [66], some collimation relevant features of the STRUCT code has been considered. The STRUCT code is basically particle tracking code performing the following tasks:

- Importing MAD-8 optics table for lattice generation
- Simulation of lattices with all types of magnets in Booster - bends, combined function magnets, multipoles (Q, S, O,...14-), RF cavities, drifts, etc.
- Implement different types of apertures
- Importing externally generated particle distributions.
- Treating an interaction of protons with material of collimators (some modules of the MARS code were included in STRUCT)
- Exporting coordinates of lost particles for further usage with MARS-code

However, programming style and the status of the STRUCT code by the end of 2014 did not allow its effective usage due to the following reasons [66]:

- the code had been developed and supported by only one person (A. Drozhdin)
- difficulties to use STRUCT code without author guidance (A.D. was retired in 2012)
- some FORTRAN modules have several versions (each for every particular task) resulting in many versions of executables
- some numerical data for particular tasks was written inside source code
- absence of a guide how combine multiple versions of modules to produce executable
- compilation was possible only under UNIX OS

It was concluded that the STRUCT code is obsolete and should be replaced by another particle tracking code. It was decided to use tracking modules of the MADX code [67] as a substitute of the STRUCT code. Such choice has been motivated by several reasons. First, the MADX code developed and supported at CERN has modern tracking routines and recognized world-wide as a kind of industry standard. Second, V. K. had a long time experience in development and usage of MADX. Several other features of the MADX code also made it attractive to be a substitute of the STRUCT code:

- Since the Booster lattice file [68] by 2014 has been already supported in MADX format, therefore there was need for importing MAD-8 lattice file as for STRUCT code;
- Nonlinear tracking of halo particles by MADX is symplectic and was already benchmarked by many users.
- Arbitrary initial particle distributions can be also generated and accepted for tracking
- Most of aperture restrictions (e.g. rectangular, elliptical, racetrack, etc) with offsets are implemented in MADX thin-track module
- output text file with lost particles is available for further usage with MARS
- code extensions for both space-charge and fringe-field effects are available, if needed

Thus, a new pair of codes, MADX & MARS was chosen to simulate proton tracking in the Booster collimators. Since MADX code is not a collimation dedicated code, it has no some features relevant to the simulation of the Booster collimators. Therefore, it was also decided to learn how those features have been implemented in the STRUCT code and to embed some of them into MADX code.

### **3.3.2 Adaptation of MADX code for Booster collimation**

The thin-lens tracking module of MADX has been chosen to be used in collimator simulations. The following STRUCT code features have been implemented with the MADX code:

- Several routines for generation of initial particle distributions have been written using the MADX script language
- Fortran subroutines for simulations of proton scattering on the primary collimator thin-foil implemented in the STRUCT code and originally imported from old versions of MARS code has been adapted and embed into the MADX thin-track module
- The specific for Booster combined-function magnets aperture restrictions with trapezoidal cross-section has been implemented in the MADX thin-track module

#### **3.3.2.1 Generation of the initial particle distributions**

In order to evaluate an efficiency of the two-stage collimation system a numerical tracking of the halo particles should be performed. According advices by N. Mokhov [5, 49, and 69] and V. Lebedev [50], the halo particles should start at the edge of the primary collimators from its upstream side. Figure 3.9 show scheme for a generation of the initial distribution of the halo particles. In the real  $(x,y)$ -phase space the halo particle distribution is a thin strip with a typical thickness of  $\Delta x_{\text{halo}} \sim 10\mu\text{m}$  (halo size), and particle distribution along the  $y$ -axis follows to Gaussian law. Several routines using the MADX script language (or macros) has been written to generate initial particle distributions for a given halo size  $\Delta x_{\text{halo}}$ . Other parameters for a generation of the initial distribution were taken from the Twiss parameters at the locations of the primary collimators.

The starting points of the MADX lattice have to be set at upstream side of the primary collimators. Since the horizontal and vertical primary collimators are located at the different places, two independent simulations have been performed for horizontal and vertical planes. Also two versions of the MADX lattice should be generated from the original MADX lattice file starting at S24. The first lattice started at the horizontal primary collimator is used for simulations in the horizontal plane, and the second lattice started at the vertical primary collimator is used for simulations in the vertical plane.

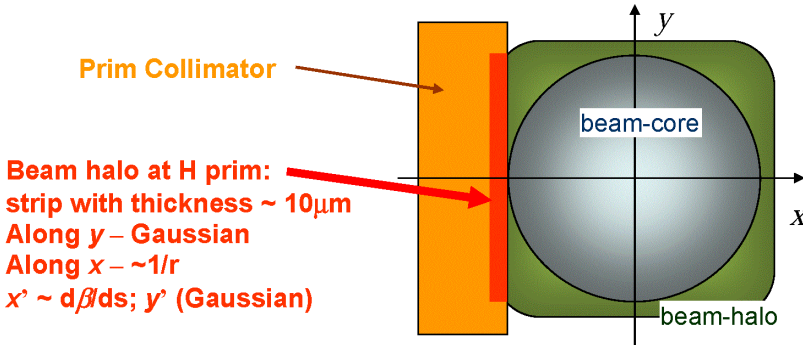


Figure 3.9: Initial particle distributions at upstream edge of the horizontal primary collimators.

Figure 3.10 [70] demonstrates an example of the initial proton distribution at the edge of the horizontal primary collimator with the halo size of  $\Delta x_{\text{halo}} \sim 10\mu\text{m}$ . The plots have been automatically generated by GNUPLOT code using the MADX output files. Nine plots are presented. The first three plots show the particle populations on the transverse phase-spaces  $(x, y)$ ,  $(x, p_x)$ ,  $(y, p_y)$ , and the forth plot shows the phase-space  $(x, y)$  enlarged for a visualization of the halo size of  $\Delta x_{\text{halo}}$ . The next five plots show the projections of the particle distributions along the transverse axes  $x$ ,  $y$ ,  $p_x$ ,  $p_y$ , and along the relative particle energy given by the variable  $p_t$  in the MADX code [67]. Since a monochromatic initial particle distribution is assumed, then  $p_t = 0$  for all particles on the plot "PT-histogram".

### 3.3.2.2 Implementation of the proton scattering on thin-foil

The standard version of the MADX code has no any routines for simulations of the charge particles with matter of the accelerator walls. For simulations of the two-stage collimation system it is necessary to simulate the particle scattering on a thin-foil of the primary collimator. There can be several possible ways for such simulation.

The first and simplest way is to use an analytical formula by Moliere, which well describes the multiple Coulomb scattering of high energy particles interacting with the nuclei in a thin foil. The angular distribution of the scattered particles downstream of the foil is roughly Gaussian for small angles. The rms angle of the projected distribution is given by [71, p.328]:

$$\theta_{\text{rms}}^{\text{plane}} = \theta_0 = \frac{13.6 \text{ MeV}}{\beta c p} z \sqrt{x/X_0} [1 + 0.038 \ln(x/X_0)], \quad (3.7)$$

where  $p$ ,  $\beta c$ , and  $z$  are the momentum, velocity, and charge number of the incident particle, respectively. The parameter  $x/X_0$  is the thickness of the scattering medium in radiation lengths.

Let's consider an example for the scattering of the proton beam ( $z=1$ ) with the kinetic energy of 400 MeV ( $pc=954 \text{ MeV}\cdot\text{c}$ ) on the copper foil with thickness  $d=0.1\text{cm}$ . The copper density is equal to  $\rho=8.96 \text{ g/cm}^3$ , and the radiation length of copper is equal to  $X_0 = 12.86 \text{ g/cm}^2$  [71, p.114]. Then, the parameter  $x$  is equal to  $x=\rho \cdot d=0.896 \text{ g/cm}^2$ . The substitution of numerical values into the eq. 3.7 produces the rms angle  $\theta_0=4.7 \text{ mrad}$ .

The second way is to generate initial particle distributions with help of some special code dedicated for simulation of particle interaction in matter. Then the particle distribution is imported into the particle tracking code. For example, this approach has been implemented for study the collimation system for heavy ion synchrotron SIS100 at GSI, Germany [62], where the FLUKA code is used for simulations of the scattering process in the primary collimators and the MADX code is used for particle

tracking through the accelerator lattice. However, such approach requires the creation and running some additional scripts for transferring the particle coordinates between codes, what can be not so convenient.

```
segm#0001; elem#00000; turn#000000; Ntracks=0010000; el-name <>start>>
```

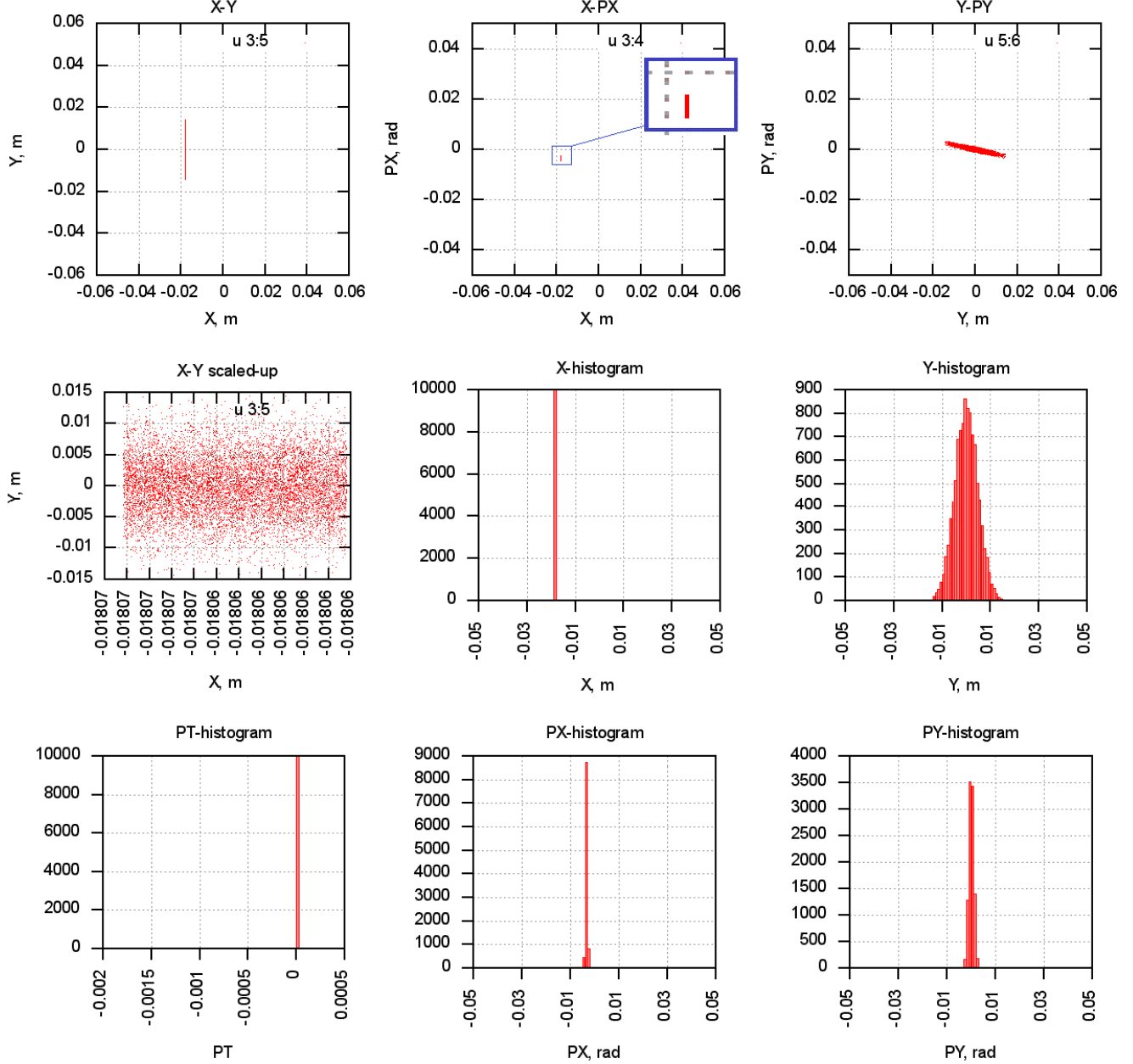


Figure 3.10: Example of the generated particle distribution at "start" of MADX code.

The third way has been implemented in the STRUCT code, which the particle tracking code embeds some relatively simple subroutines from the dedicated particle-matter interaction code. Following to an advice by N.V. Mokhov [49], the package of subroutines TARGB simulating particle-foil interactions has been retrieved from the STRUCT source code. One of the MARS code authors S.I. Striganov has inspected the extracted TARGB source code in order to understand the frames of its applicability [72]. It was concluded that the TARGB source code is based on an old version of the

MARS code. It uses the Monte-Carlo simulations of physical processes causing energy loss and scattering of protons in thin primary collimators. The multiple Coulomb scattering is simulated with the Moliere distribution. The Landau distribution is used for computation of energy loss. Finally, in order to simulate proton interaction with the thin foils of the primary collimators, the TARGB module of the STRUCT code has been transferred to the MADX code and named as "SCATTER" [70].

Figure 3.11 shows some results of simulation test for the "SCATTER" module. The test simulation was formulated by the following way: the incident monochromatic 400 MeV proton ray consisting of  $10^4$  particles hits 1 mm thick copper foil at the normal-angle.

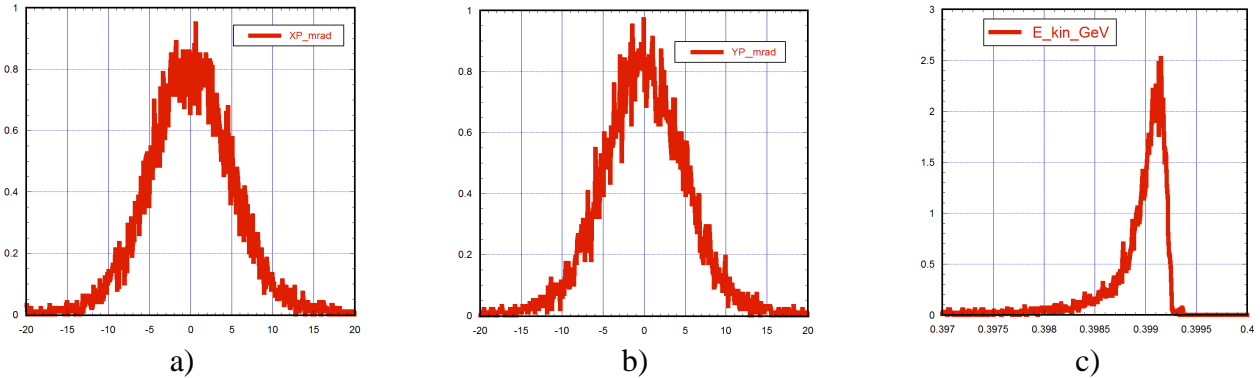


Figure 3.11: Example of the proton distributions simulated by subroutine TARGB: a)  $x'$ -distribution; b)  $y'$ -distribution; c) energy-distribution.

The  $p_x$ -distribution and  $p_y$ -distribution looks quite similar since the scattering process posses an angular spatial isotropy. The half-widths of both distributions are equal about  $\sim 5$ mrad, what looks to be quite consistent with the values of  $\theta_0=4.7$  mrad obtained with the analytical Moliere formulae eq. 3.7 under the same conditions. The energy distribution shown in Fig. 3.11,c has been also tested using the online code PSTAR [73, 74], which calculates the stopping power and range tables for protons in various materials. The average proton energy evaluated with PSTAR is equal to 398.1 MeV, while the mean value of energy-distribution probability by the SCATTER module is equal to 398.6 MeV.

Figure 3.12 [70] shows the proton distribution at the downstream side of the horizontal primary collimator made of the  $0.38\text{ }\mu\text{m}$  thick copper foil. The initial proton distribution was shown in Fig. 3.10.

As results of interaction of the proton beam with the horizontal primary collimator foil, the initial thin-width distributions along the transverse variables  $p_x$  and  $p_y$  have been converted into bell-shaped distribution similar to Gaussian distribution, and the initial monochromatic line  $p_t=0$  has been converted into a kind of Landau distribution which looks like a non-symmetric bell-shaped distribution with a low-energy tail and an abrupt high-energy side, while the distribution is shifted to low-energy direction with  $p_t < 0$ .

The SCATTER module for simulations of the proton beam with thin scattering foil can be used with MADX particle tracking module THIN-TRACK following simple rules. The primary collimator should be described in the MADX lattice as a zero-length ( $L=0$ ) rectangular collimator RCOLLIMATOR with the special aperture type either HPRIMCOLL or VPRIMCOLL for horizontal and vertical primary foil, respectively. The aperture sizes for this element are treated as outer boundaries of particle stopping target, i.e. inversely to conventional rectangular apertures defining internal boundaries of the vacuum pipe. The foil matter, its actual thickness in meters used in particle-matter calculations, and cut-off energy for low energy particles are given by the parameters

PRIM\_COLL\_MATTER, DP\_RELATIVE\_DROP, and MATTER\_THICKNESS\_M, respectively. The example below has been used for the above Fig. 3.12:

```

hprim_10: rcollimator, l=0, APERTYPE=hprimcoll,
           APERTURE={xsize_hprim,ysize_hprim},
           APER_OFFSET={x_hprim_neg_offset,0.0},
           PRIM_COLL_MATTER=copper,
           DP_RELATIVE_DROP=0.9,
           MATTER_THICKNESS_M=0.000381;

```

segm#0002; elem#00004; turn#000001; Ntracks=0009973; el-name <>m\_hprim\_e>

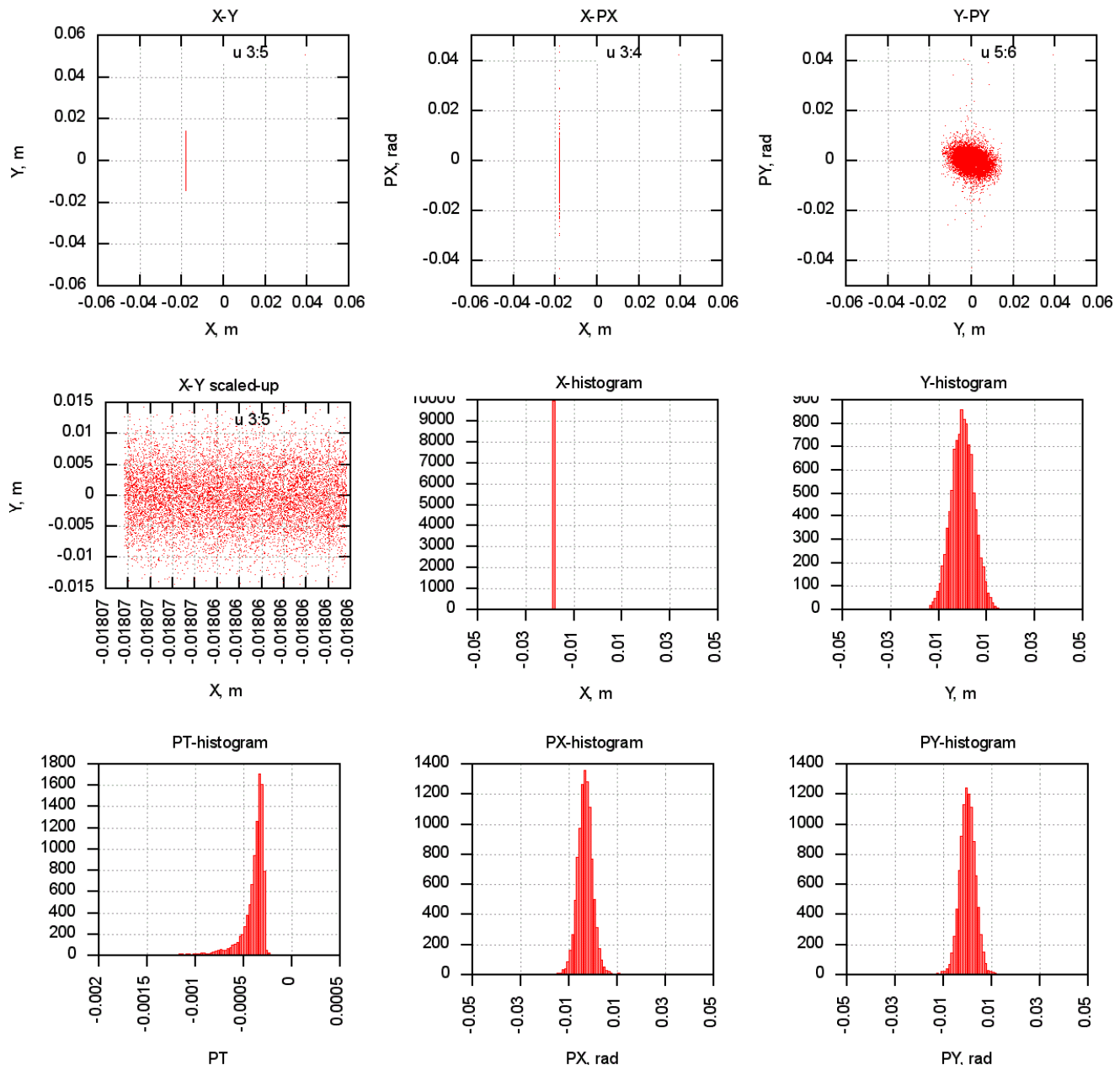


Figure 3.12: Particle distribution after scattering on the horizontal primary collimator with  $0.38 \mu\text{m}$  thick copper foil for the initial proton distribution shown in Fig. 3.10.

### 3.3.2.3 Implementation of the trapezoidal aperture in MADX

Following to the STRUCT code using trapezoidal apertures for boundaries of the Booster gradient magnets, similar aperture has been imbedded into the MADX particle tracking module THIN-TRACK. In order to avoid confusions with a sign for the rotation angle of the trapezoidal aperture, two additional types of the apertures has been introduced: FOCTRAPEZOID and DEFTRAPEZOID. This aperture should be described in the MADX lattice file similar to other standard apertures. For example, the trapezoidal aperture for F magnet is described with the following script [70]:

```
a_hor_foc_trap:= 0.0825; b_ver_foc_trap:= 0.02083;  
tg_alpha_foc_trap:= 0.086;  
FMAG_C: SBEND, APERTYPE= FOCTRAPEZOID,  
APERTURE={a_hor_foc_trap, b_ver_foc_trap, tg_alpha_foc_trap};
```

The detailed description and usage of this aperture is given in the next section.

### 3.3.3 Attaching Regular Apertures to the Booster MADX lattice

The original Booster lattice files have been created for the MAD-8 code, which was a predecessor of MADX. The MAD-8 lattice format has been supported for many years starting from 2000 and the last version in MAD-8 was issued in April of 2013. The MADX version of Booster lattice has been created in 2013 by M. McAteer and C.Y. Tan [68]. All available versions of Booster lattice files both in MAD-8 and MADX formats have been inspected in order to find any information about apertures in Booster. As result, all inspected lattice files do not use aperture restrictions at all.

However, the information about Booster apertures has been comprehensively implemented in the STRUCT lattice files for all Booster elements around the ring. Three types of apertures used in the STRUCT lattice files are the following: circular, rectangular, and trapezoidal aperture. Two first aperture types have been used for most Booster elements and beam pipes. The circular and rectangular apertures are quite basic and exist in most tracking code including MADX.

The trapezoidal aperture is quite specific, and it has been used to define pole shapes of Booster gradient magnets. Figure 3.19,a shows a sketch of the trapezoidal aperture from the STRUCT manual [19], where it is defined as "parallel vertical jaws and horizontal jaws rotated with respect to horizontal plane by angle  $\pm\alpha$ ". Figure 3.19,b shows three variants of trapezoidal aperture against the background with magnet drawings already shown before in Fig. 2.2. Figure 3.19,b also shows the horizontal and vertical half-widths of apertures denoted as  $a$  and  $b$ , respectively.

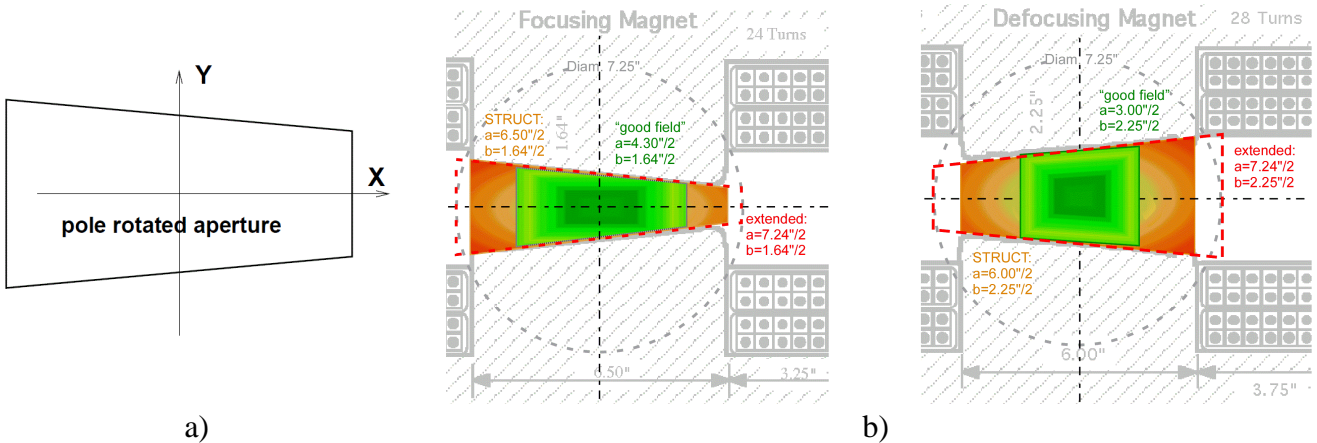


Figure 3.19: Trapezoidal apertures: a) definition in STRUCT manual code [19]; b) magnet cross-sections and the trapezoidal aperture for "good field" area (green), for a regular STRUCT lattice file "LAT92.INP" (brown), and a special STRUCT lattice file<sup>8</sup> with "extended" trapezoidal aperture for a horizontal notching study.

All three variants of the trapezoidal apertures shown in Fig. 3.19,b have different horizontal half-widths  $a$  and the same vertical half-widths  $b$  coinciding with the sizes of pole tips half-gaps equal to  $b=0.82"$  and  $b=1.125"$  for F and D magnets, respectively.

The first trapezoidal aperture in Fig. 3.19,b (green color) shows boundaries of the "good-field" area [4,75] with horizontal half-widths  $a=2.15"$  and  $a=1.5"$  for F and D magnets, respectively. The second aperture shown in Fig. 3.19,b (brown color) is a regular trapezoidal aperture one used in most STRUCT lattice files. The horizontal half-widths of this regular STRUCT apertures are equal to  $a=3.25"$  and  $a=3.00"$  for F and D magnets, respectively. Thus, this aperture is wider than "good-field" aperture by 51% and 100% for F and D magnets, respectively. The third trapezoidal aperture was found

<sup>8</sup> the file name is "LAT92.INP\_2-hor\_notcher\_L12\_0.7GeV\_80Gauss\_p6inch"

in the STRUCT lattice file<sup>9</sup> for a horizontal notching study. It is a special variant of horizontally "extended" trapezoidal aperture with the horizontal half-widths equal to  $a=3.25"$  and  $a=3.00"$  for F and D magnets, respectively.

According to the 1968 NAL design report [2], the initial design of the Booster gradient magnets used an elliptical vacuum chamber located inside the pole tips. The sizes of the vacuum chamber were equal to  $5.5"\times1.65"$  for F magnets, and  $4.0"\times2.25"$  for D magnets. The sizes of "good-field" area were almost the same. The overall transverse sizes of magnets were equal to  $24"\times16"$ . Figure 3.20 shows normalized field gradient for computed pole contours shown in Fig.9-5 of the 1968 design report [2].

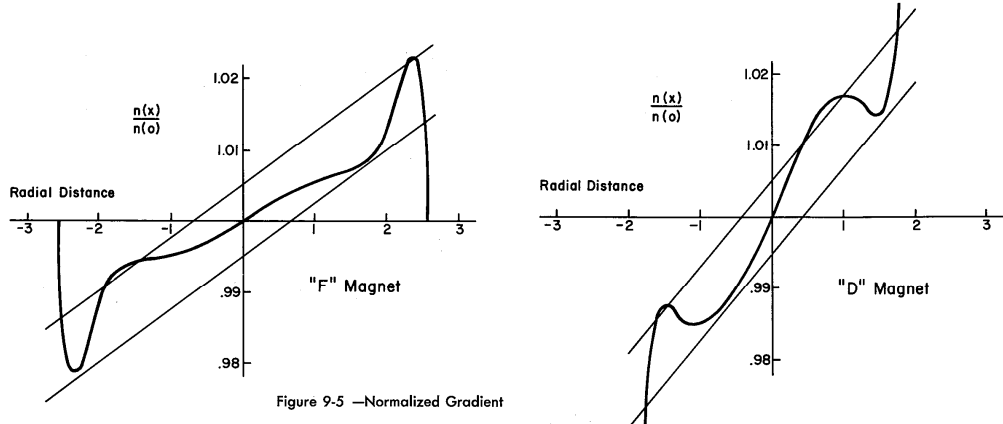


Figure 3.20: Computed normalized gradients in F-magnet and D magnets [2, fig. 9-5].

The present construction with gradient magnets completely enclosed in a stainless-steel vacuum chamber with overall transverse dimensions  $18"\times13"$  has been considered in the report [75] published in 1969. The presented in this report widths of the "good-field" were  $4.25"\times1.64"$  for F magnets, and  $3.0"\times2.25"$  for D magnets. These sizes of the "good-field" coincide with sizes presented in "Booster Rookie book" [4] and shown in Fig 3.19,b. According to ref. [3] the designed pole tips of the Booster magnets were contoured to produce field gradients on the median plane within 1 % design fields over the specified "good field" width.

Figure 3.21 reproduces the plot from the report [75] and shows the normalized median plane gradients, which have been calculated for magnet profiles computed with help of methods using a complex variable transformation theory. The low and high excitation corresponds to the injection and extraction energy, respectively. It was declared [75] that the designed magnetic field on the median plane possesses the requisite dipole, quadrupole, and sextupole characteristics over a finite working region (good-field region). Termination of the good-field region is brought about as sharply as is consistent with leaving the good-field region its desired characteristics within pre-specified tolerances.

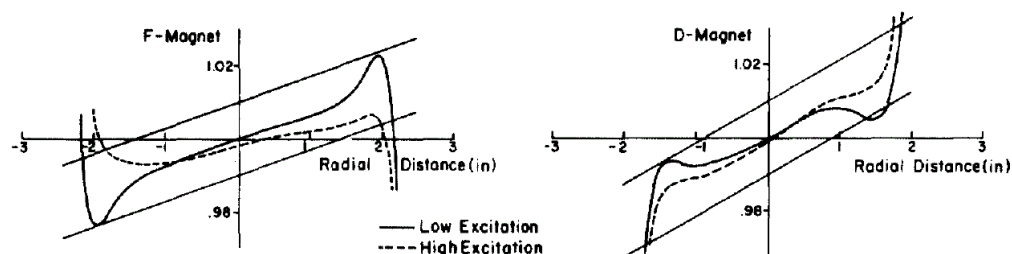


Figure 3.21: Computed magnetic-field gradients for Booster magnets [75, fig.3].

<sup>9</sup> the file name is "LAT92.INP\_2-hor\_notcher\_L12\_0.7GeV\_80Gauss\_p6inch"

The beam dynamic simulations are usually performed within a simulation area, which is usually limited by vacuum chamber walls. In the case of Booster, there are no walls in the horizontal direction, and aperture restriction could be introduced in terms of some physical considerations. For example, it looks to be reasonable to restrict the simulation area horizontally by the horizontal width of the "good-field" area. Such assumption will enable a realistic beam dynamic simulation using known magnetic fields within the simulation area. However, for counting particle losses on imaginary boundaries looks to be not adequate, since particles have a chance to survive moving outside the "good-field" area under action of dominated magnetic field and small unmeasured high-order components.

Some trade-off decision is required. The imaginary horizontal boundaries of the trapezoidal aperture used in the STUCT code coincide with boundaries of the pole tips. Note, that tracking results for particles which -pass outside of the "good-field" area during multiple-turns should be considered as unreliable. However, the particle losses happened during a single pass outside of the "good-field" area looks to be reliable result.

Let's evaluate an importance of the "good-field" aperture restriction and compare it with minimal beam aperture recognized earlier with help of Figure 2.2. Let's assume the 95% normalized emittances of  $12 \text{ mm}\cdot\text{mrad}$  as in the 2004 design report [11]. Then, the un-normalized rms emittance at the injection energy is equal to  $2 \text{ mm}\cdot\text{mrad}$ . The table 3.1 below presents maximum values of the  $\beta$ -functions [2], rms beam sizes, and sizes of the "good field" area.

Table 3.1 maximum  $\beta$ -functions, rms beam sizes, "good field" sizes in inch, mm and  $\sigma_{\text{rms}}$ .

element	$\beta_{\text{hor}} / \beta_{\text{ver}}, \text{ m}$	$\sigma_{\text{rms}}, \text{ mm}$	$3\sigma_{\text{rms}}, \text{ mm}$	sizes of "good field" area		
				$2a / 2b, \text{ inch}$	$a_h / b_v, \text{ mm}$	$a_{\min} / b_{\min}, \text{ in } \sigma_{\text{rms}}$
F magnet	$33.75 / 10.82$	$8.2 / 4.6$	$24.6 / 14.0$	$4.3'' \times 1.64''$	$54.6 / 20.8$	$6.6 / 4.5$
D magnet	$17.30 / 20.47$	$5.9 / 6.4$	$17.6 / 19.2$	$3.0'' \times 2.25''$	$38.1 / 28.6$	$6.5 / 4.5$
Long (RF-cavity)	$7.59 / 20.47$	$3.9 / 6.4$	$11.7 / 19.2$	Diam. $2.25''$	$28.6 / 28.6$	$7.3 / 4.5$

The minimal apertures  $a_{\min}$  and  $b_{\min}$  expressed in the beam-sigma demonstrate most severe aperture restrictions. The minimal horizontal apertures  $a_{\min} > 6.5\sigma_{\text{rms}}$  are quite large, allowing large deviations of the beam central orbit. The minimal vertical apertures are smaller  $a_{\min} = 4.5\sigma_{\text{rms}}$ . This minimum value is reached at the three locations of the Booster periods: 1) at junctions of F magnets with 0.5 m short drift sections between F and D magnets; 2) at junctions of D magnets with the long straight sections; 3) at drift-tubes of RF-stations.

In order to compare the MADX results with the SRUCT results, it was decided to implement the regular STRUCT trapezoidal aperture in the MADX lattices. Circular and rectangular apertures found in the STRUCT code have been transferred into MADX lattice file for the most Booster periods. Note, that MADX uses zero-length apertures which should be normally located at both ends of a uniform beam pipe.

Some apertures found in the STRUCT lattice did not correspond to installed accelerator elements. In most cases it was originated by modifications or replacements of some machine elements which were performed during the last decades, e.g. the long straight section 12 now contains new beam kickers. However, the STRUCT apertures in the collimation area did not correspond to actually installed elements at all. Therefore, new realistic apertures for the collimation area have been inserted in the MADX lattice file for the periods 5, 6, and 7.

### 3.3.4 Apertures in Collimation Area for the Booster MADX lattice

Using both available drawings and ruler measurements in the Booster tunnel, the layout of the Booster periods 5, 6, and 7 containing the collimation system (see its layout in Fig.2.4) has been restored. Figures 3.22, 3.23, and 3.24 show the layouts of the periods 5, 6, and 7, respectively [70].

The gradient magnets shown in these figures are marked by all possible ways used including the labels glued on the magnet surfaces, the designations in STRUCT lattice files, and marks on collimation layout schemes. For example, the defocusing magnet located before long straight section 5 is designated in the STRUCT code as "DMAGU05", which is decoded as "Defocusing MAGnet located at Upstream of the section". The collimation schemes use the abbreviation "4-4 D" for this magnet. Two labels are glued on this magnet at its ends, namely the label "4-04U" for Upstream end and the label "4-04D" for Downstream end. Some leading zeros and lower-case letters have been added to the magnet marks to facilitate understanding.

Figure 3.22,a shows the layout of the period 5 beginning from the center of the short straight section 4 (S04) and ending at the center of the short straight section 4 (S05). The second half of S04 shown in this figure contains the correction package magnet denoted in MADX lattice files as "CPSO4". Note, that the correction packages located in short straight sections S04, S05, and S06 are not shown in Figures 3.22, 3.23, and 3.24. Figure 3.22,a also shows sketches of the trapezoidal apertures and their half-widths for both F and D magnets.

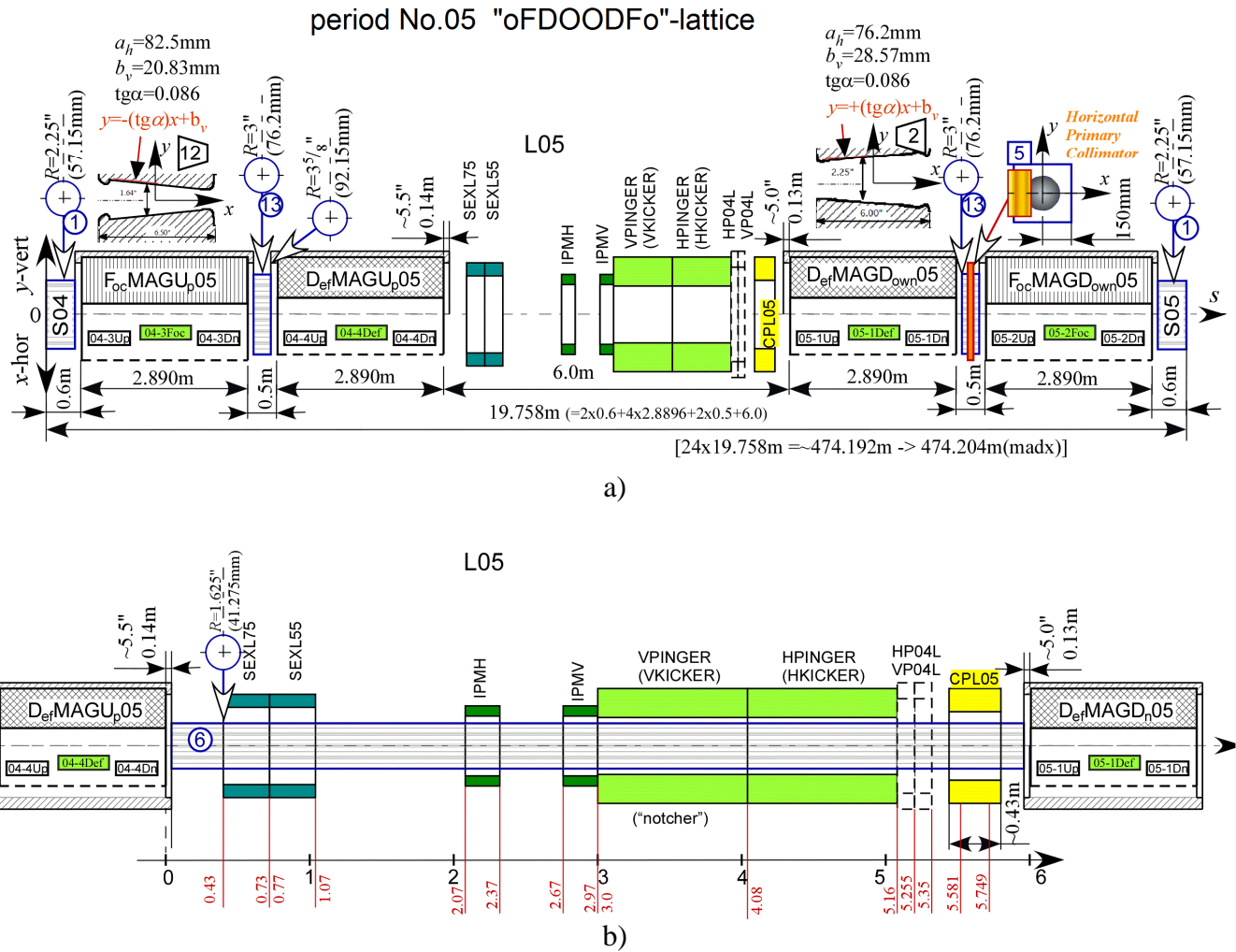


Figure 3.22: Scheme of the period 5: a) layout of the period 5; b) apertures in long straight 5.

The period 5 includes four gradient magnets (two F and two D magnets), the long straight section 5 (L05), which contains sextupole magnets, kickers, the horizontal and the vertical Ion Profile Monitors (IPM), and correction package magnet "CPL05". The horizontal primary collimator is installed in the second downstream 0.5-meter short drift of period 5. The beam aperture in L05 is beam pipe with diameter of 3.25".

Figure 3.23,a shows the layout of the period 6 beginning from the center of S05 and ending at the center of S06. The period 6 contains two secondary collimators located in L06, and the vertical primary collimator located in the first upstream 0.5-meter short drift of period 6.

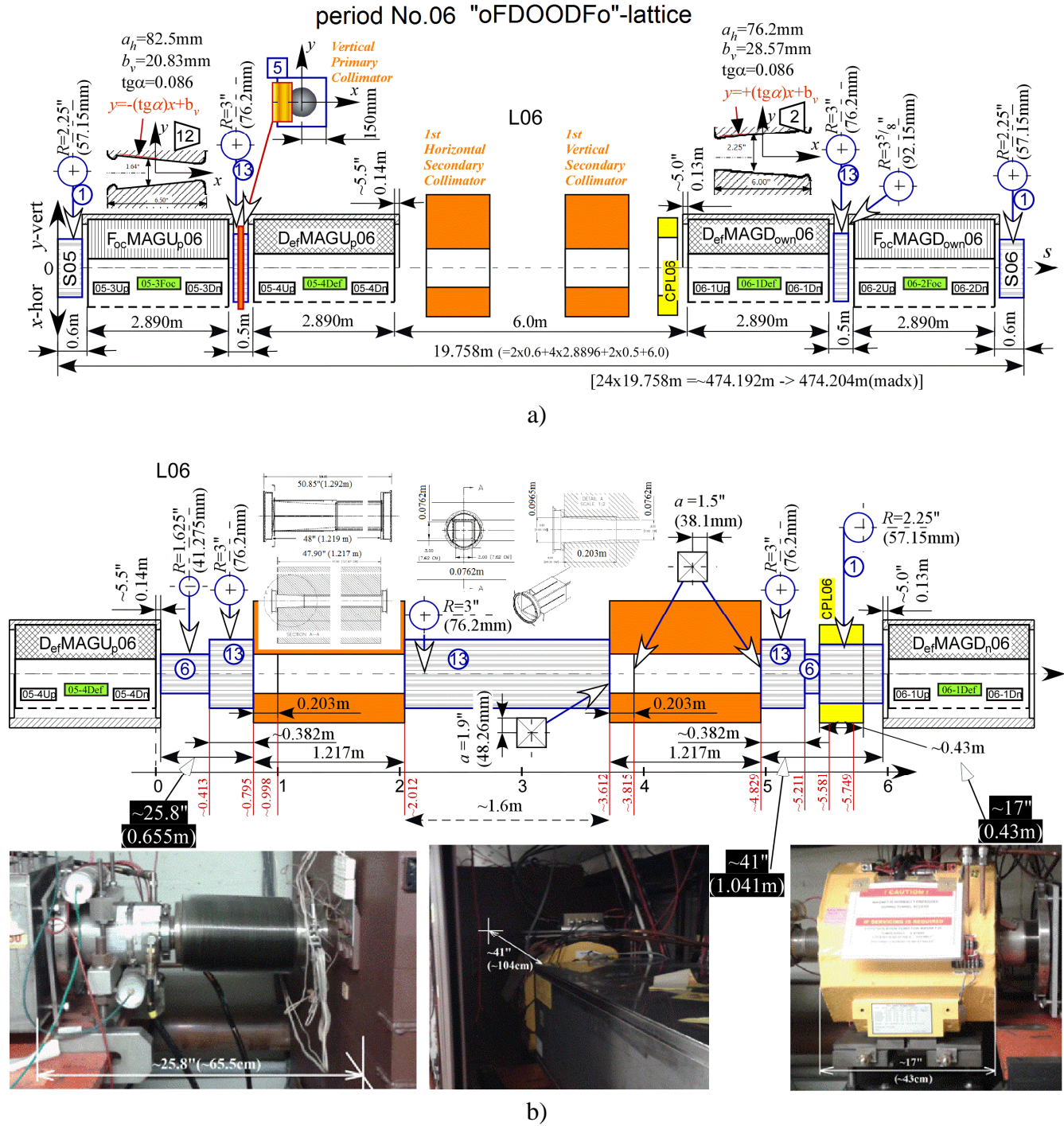


Figure 3.23: Scheme of the period 6: a) layout of the period 6; b) apertures in long straight 6.

Figure 3.23,b shows apertures in L06 for both beam pipes and two secondary collimators. Available drawings and photos are also shown for better illustration. Each secondary collimator with square tapered aperture is represented by 3 zero-length rectangular apertures in the MADX lattice file.

Figure 3.24,a shows the layout of the period 6 The period 6 contains one secondary collimator located in L06. Figure 3.24,b shows apertures for both beam pipes in L06 and the secondary collimator.

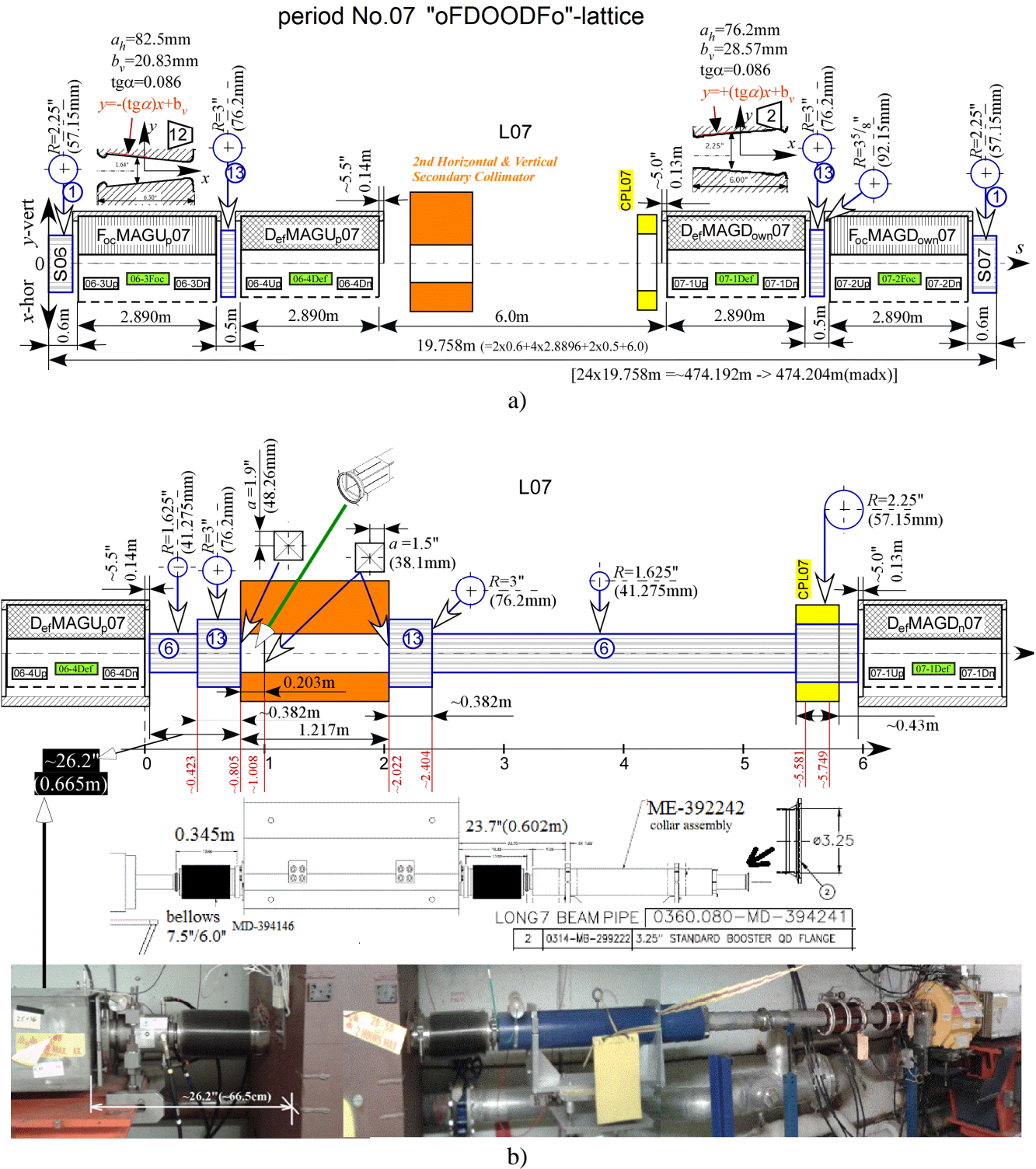


Figure 3.24: Scheme of the period 7: a) layout of the period 7; b) apertures in long straight 7.

### 3.3.5 Non-linear fields in the Booster lattice files

An adequate beam dynamic simulation of real accelerator requires knowledge of magnetic fields within the simulation area. The Booster combined function magnets has been designed to possess the requisite dipole, quadrupole, and sextupole characteristics with precision 1 % over the "good field" width. The boundaries of the 1% error area for computed gradients are shown by two parallel lines in the above Fig.3.20 and Fig 3.21. The behavior of the gradient curves depends on the excitation level due to iron saturation effects. For computed gradients in Fig 3.21 the curves for low and high excitation still remain within 1% error area assuming small shortening of the "good-field" area [75].

Since the computed fields were based on some modeling assumptions for used computer codes [75], they could not predict precisely actual fields for the fabricated magnets. Therefore, the magnetic fields of the Booster magnets have been measured during 1970th by several researches under different conditions and approaches.

The 1973 report [3] edited by E.L. Hubbard reproduce the gradient curves measured by R. Peters. Figure 3.28,a shows these normalized gradient curves for both F and D magnets. The widths of the plot area with small deviations of both curves are in agreement with the sizes of the "good field" area. The measurements of the dc relative gradient for R magnet "F-47" magnet have been presented in the 1974 report by R. Jahala [76]. The measurements have been performed for four excitation levels including the injection and extraction. Figure 3.28,b reproduce the "Fig.3" from that report.

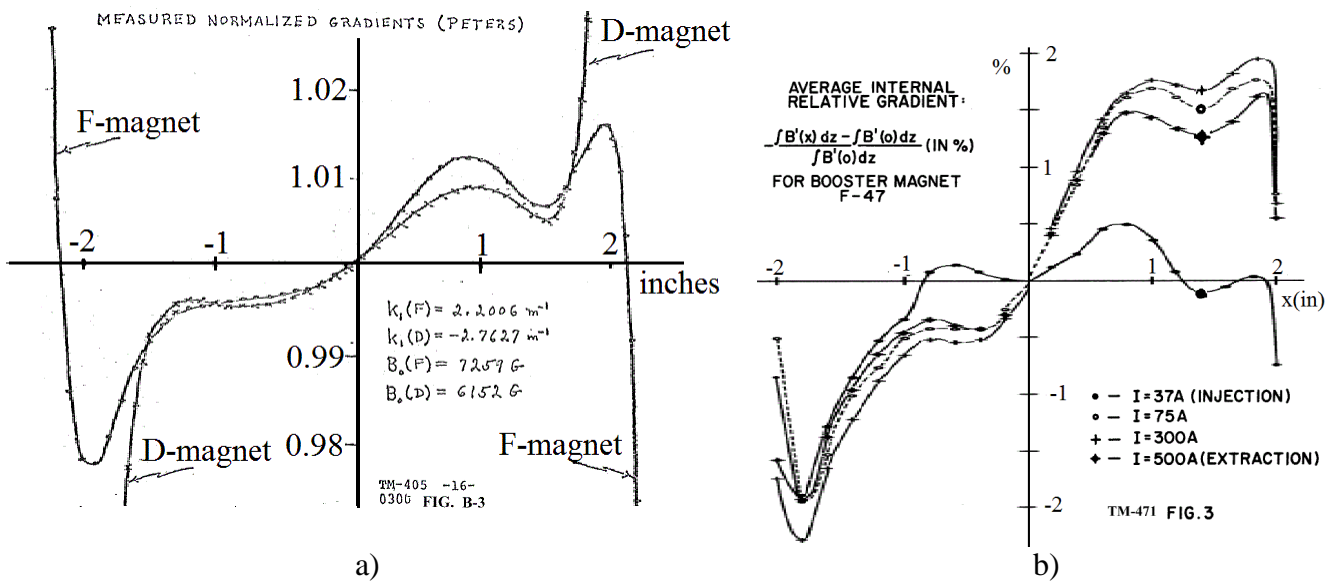


Figure 3.28: Measured normalized gradients in Booster magnets: a) the measurement results by R. Peters reproduced in ref. [3, fig. B-3]; b) The average internal gradient at the various current for F magnet "F-47" [76, fig.3].

The 1976 report [77] by E. Gray contains the ac measurement results made on a spare D magnet D-48, which was connected into the Booster ring and operated in the standard ac cycle. It was concluded that the presented ac measurements are in basic agreement with previous dc measurements. Figure 3.29 reproduces the "Fig.6" from that report.

The field measurement results for the Booster gradient magnets reproduced in Fig. 3.29 have been plotted on a copy of "Fig.9-5" from the accelerator design report [2, fig. 9-5] shown by solid lines. The results of dc measurements for F and D magnets from unpublished 1974 report [78] by R. Yamada

et al have been superposed on the plots (see dots denoted as "R.J. data") together with the ac measurements (see crosses denoted as "Present data" ) by E. Gray.

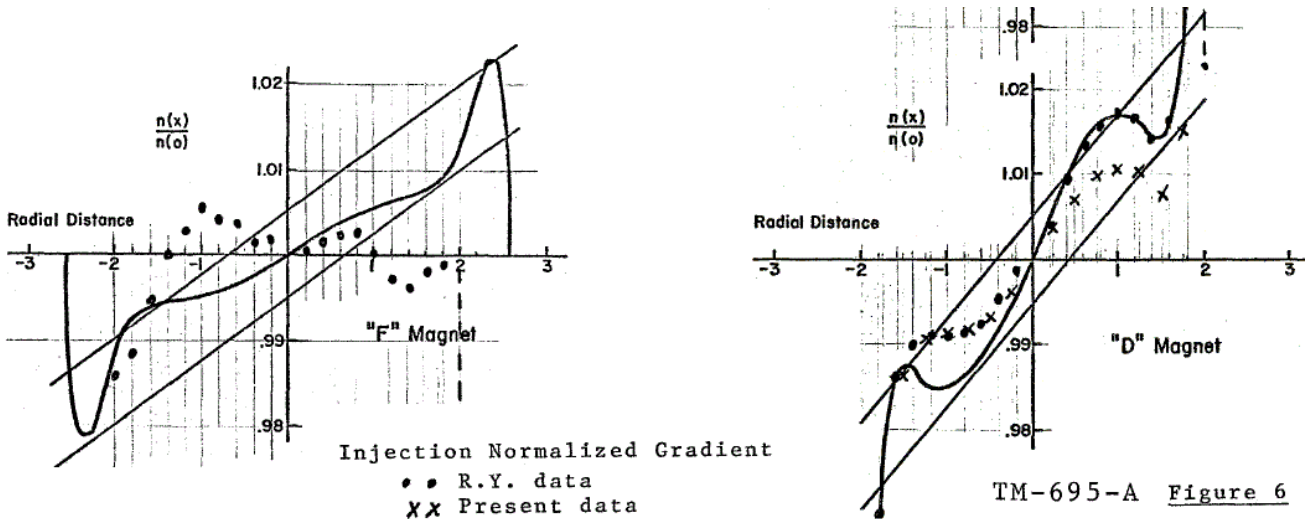


Figure 3.29: The injection normalized gradients for F and D magnets from ref. [77, fig.6].

From the above presented plots one can see that measured magnetic gradient curves in real F and D magnets have quite complicated shapes varying with change of an excitation level. Probably, some other old measurement results could be found. For example, measurements of sextupole components in gradient magnets have been performed in 2003 [79]. However, details of those studies were not published at all.

The Booster lattice files for both MAD-8 and STUCT code contain only quadrupole and sextupole components for the gradient magnets, while both components were set as constants independent of beam energy. Thus, the old results of the magnetic field measurements were not implemented in the beam dynamics codes. Moreover, recently the sextupole components in MADX lattice have been revised because the MADX model could not correctly predict both tunes and chromaticity [80].

Since even sextupole component in the gradient magnets still causes some questions, it looks to be nonsense to implement other high order components existing within a "good field". Thus, the beam dynamics simulations for Booster lattice could not reproduce details of the particle motion depended on high order nonlinearities. It may be reasonable in some cases to neglect the nonlinear components in the case when beam passes through the machine elements only a few times. However, non-linear field components become essential for the multi-turn beam dynamics, when beam passes through the machine elements many times during many turns. Particularly, it is not possible to simulate correctly how linear particle trajectories will be distorted during many turns by nonlinear components existing within a "good field" area. Therefore, an implementation of a collimation system relying on a linear behavior of the particle trajectories during many turns looks to be risky and should be avoided.

For example, the scattered on primary collimator foil halo particles must pass through the existing two-stage collimation system many times during tens and even hundreds turns. According to the design the initial amplitude of the halo particles is equal to  $3\sigma$  and even more after scattering on the primary collimator. It looks to be doubtful that linear trajectories of the scattered particles will be preserved in order they hit the secondary collimators at prescribed coordinates and impact parameters.

### 3.4 Peculiarities of the Booster two-stage collimations system

#### 3.4.2 Analytical evaluations for 2SC in the vertical plane

For our evaluations we need to choose three typical scattering foils relevant for the Booster collimation system near injection energy. Many primary collimator foils of different thickness and made up different materials has been considered and suggested. Since the main purpose of the primary collimator is scattering the halo particles, let's consider two foils to be equivalent, if they provide the same scattering angle given by the Moliere formulae (eq.3.7). For the given energy of the incident proton, two foils are equivalent if the ratio  $x/X_0$  is the same.

Figure 3.30 shows the thickness  $t$  of an equivalent aluminum foils for primary collimators made of different materials vs the energy scale. Some foils have been recommended by the 2004 design with the STRUCT code (violet color). One 381  $\mu\text{m}$  copper foil (pink color) had been installed in 2005 and existed till 2014, and another new 381  $\mu\text{m}$  aluminum foil (green) has been installed in 2015. Also several foils (brown color) have been considered as possible candidates.

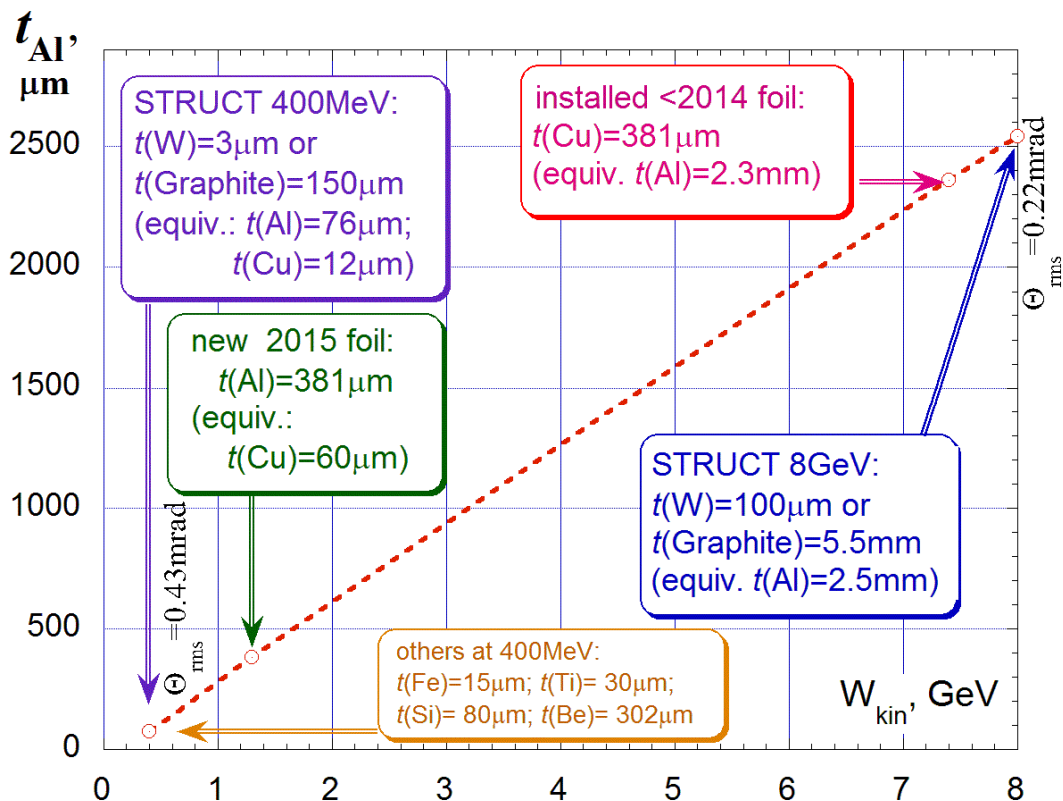


Figure 3.30: Thickness  $d$  of an equivalent aluminum foils for primary collimators made of different materials vs energy scale.

Originally, in our simulations the cooper foils has been used. For example, the thickness of the new 381  $\mu\text{m}$  Al foil has been derived from the optimal  $\sim 50 \mu\text{m}$  copper foil found in our numerical simulations of 2SC system [81, 82]. Therefore, let's use the thickness  $t$  of an equivalent cooper foils instead of the thickness  $t$  of an equivalent aluminum foils shown in Fig. 3.30. Let's consider three variants of the primary collimators foils. All three are the copper foils with different thickness  $t_{\text{Cu}}$ : 400  $\mu\text{m}$ , 50  $\mu\text{m}$  and 10  $\mu\text{m}$ . The first 400  $\mu\text{m}$  foil is close to the foil existed till 2014, the second 50  $\mu\text{m}$

foil is close to the new Al foil installed in 2015, and the thinnest 10  $\mu\text{m}$  foil is very close to the foil recommended by STRUCT design for the injection energy. For 400 MeV proton beam the rms angles calculated with help of the Moliere formulae (eq.3.7) are equal to the following values:

$$\theta_{0,\text{Cu}}^{\text{p:400MeV}} [\text{mrad}] = \begin{cases} 2.88, & t_{\text{Cu}} = 400 \mu\text{m} \\ 0.93, & t_{\text{Cu}} = 50 \mu\text{m} \\ 0.38, & t_{\text{Cu}} = 10 \mu\text{m} \end{cases} . \quad (3.8)$$

Then, for three copper foils the rms angle in the normalized coordinated angle  $\theta_n$  can be calculated with eq. (3.3). With the unnormalized rms emittance of  $\epsilon_{\text{rms}}=2 \cdot 10^{-6} \text{ m}\cdot\text{rad}$  and the vertical  $\beta$ -function at the primary collimator of  $\beta_y=11.85$ , the rms angles in the normalized coordinates  $\theta_n$  for copper foils are equal to

$$\theta_{n,\text{Cu}}^{\text{p:400MeV}} = \begin{cases} 7.05, & t_{\text{Cu}} = 400 \mu\text{m} \\ 2.26, & t_{\text{Cu}} = 50 \mu\text{m} \\ 0.93, & t_{\text{Cu}} = 10 \mu\text{m} \end{cases} . \quad (3.9)$$

Let's assume that the Booster optics is linear and uncoupled. In this case, an evolution of the phase space in the normalized coordinates is described by the rotation matrices. Every particle moves along its invariant circle with radius defined by initial conditions. All particles represented on the normalized coordinates are rotated on the same angle (phase advance)  $\mu$  after a transition from one element to another. Particularly, circles and straight lines represented on the normalized phase-space will preserve their shapes.

Figure 3.31 shows an evolution of the halo protons in the vertical normalized phase space during their passage throughout the Booster elements according to the 2SC scheme for the collimation in the vertical direction, which involves the vertical primary collimator and two secondary collimators "6B" and "7A", while the secondary collimator down not involved in the 2SC and stays in the vertical garage position.

At the initial moment, the halo protons are scattered by the vertical primary collimator "Vprim" located at  $Y=3$  (or  $y=3\sigma$  in the non-normalized coordinates). Scattered protons populate a vertical straight line shown by red. This line touches the  $3\sigma$ -circle only at one point with coordinates  $Y=3\sigma$  and  $Y=0$ . Let's call this point as the center of the red line. This straight line includes particles scattered outwards ( $Y>0$ ) and inwards ( $Y>0$ ).

Let's assume that the angle distribution of the scattered protons is Gaussian with rms angle  $\theta_0$  given by Moliere formula (see eq.3.7). Therefore, in the normalized phase-space scattered protons will populate the straight line with the density distributed according the Gaussian low with rms angle  $\theta_{\text{norm}}$ , which is defined by  $\theta_0$  according to eq.3.3. During evolutions of the normalized phase-space shown in Fig. 3.31, the density of scattered particles along the red straight lines will be preserved.

Let's normalize the total number of particles populated along the straight line by unity (or 100%). The portion of particles located within the line segment  $[p_{\min}, p_{\max}]$  is defined by the following integral:

$$\Xi(\theta_n, p_{\min}, p_{\max}) = \frac{1}{\sqrt{2\pi}\theta_n} \int_{p_{\min}}^{p_{\max}} \exp\left(-\frac{\xi^2}{2\theta_n^2}\right) \cdot d\xi , \quad (3.10)$$

while due to the normalization the values of  $\Xi(\theta_n, -\infty, +\infty)=1$ .

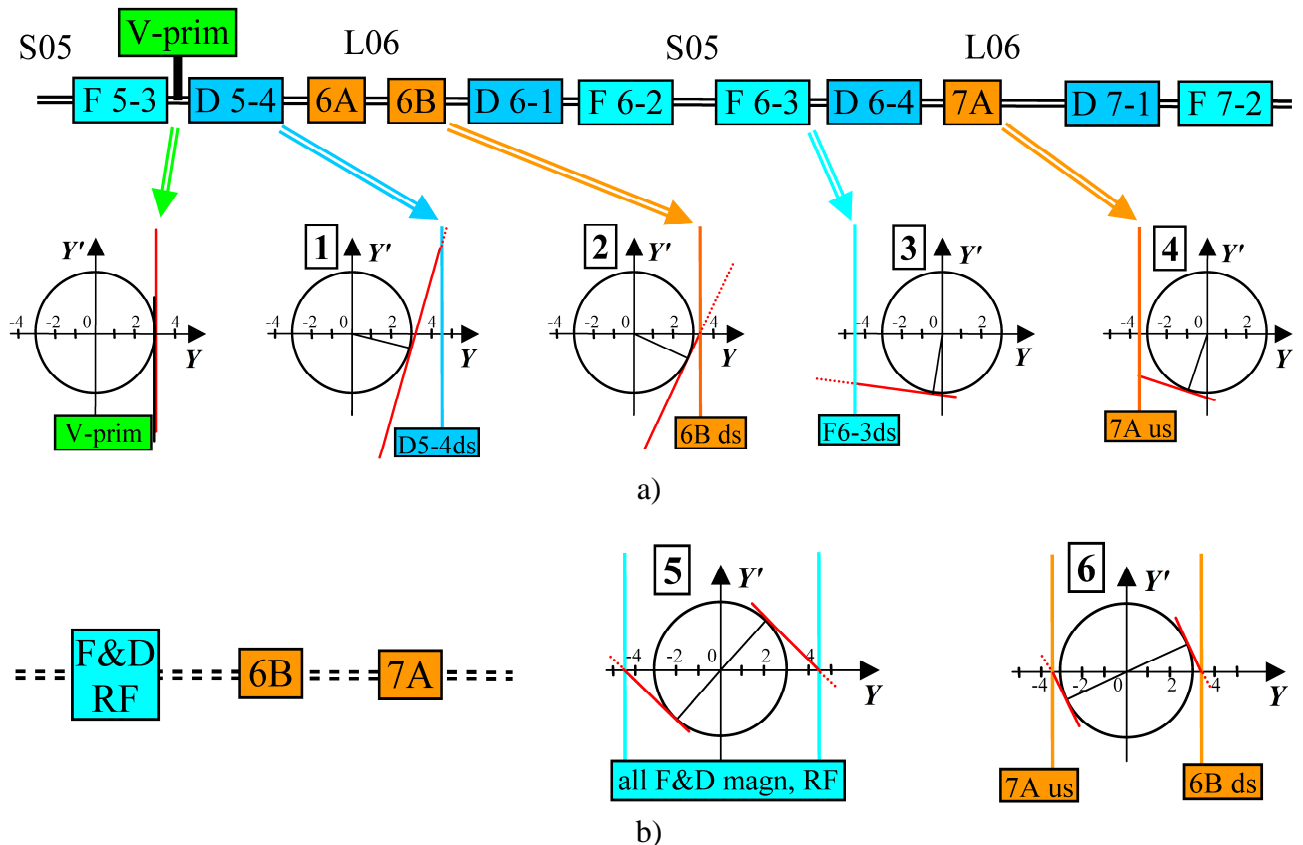


Figure 3.31: Passage of scattered protons throughout the small aperture elements according to the 2SC scheme in the vertical plane: a) the first passage of the 2SC system; b) further and multi-turn passages of all gradient magnets and RF cavities, and all secondary collimators.

During its sequent passage throughout the Booster elements the scattered protons could be intercepted by small aperture restrictions of the Booster elements including the secondary collimators, gradient magnets and the RF cavities (see Table 3.1). This process is defined by the Booster optics, beam energy and emittance, and parameters of the primary collimator. Under assumption of linear and uncoupled optics, the interception process can be evaluated using analytical formulae.

Table 3.2 contains both initial parameters and results of analytical calculations for the Booster elements with small aperture restrictions. The 1st column of the table contains the sequent numbers for diagrams shown in Fig. 3.31. The second column contains names of the elements abbreviated according to the scheme of Booster elements shown on the top of Fig. 3.31. Since the Booster magnets and collimators are optically quite long, the parameters at their upstream (us) and downstream (ds) ends are presented in separate rows of the table.

The Twiss parameters calculated for the Booster lattice file by the MADX code are shown in the columns iii-vii. The column viii contains the vertical aperture half-widths  $b_v$  for gradient magnets and RF cavities. The column ix lists these aperture half-widths calculated for the normalized coordinates. The parameter  $K$  presented in the column x has been calculated with help of eq. 3.4 using phase advances values  $\mu$  given in the column vii, viii and substituting  $n$  values from the column ix instead of  $n_{sec}$ .

Let's consider an evolution of the red straight line shown in Fig. 3.31 for the copper foil with the thickness  $t_{Cu}=400 \mu m$ . This line is rotated by the angle  $\mu=10.82^\circ$  (see column vii of Table 3.2) at the downstream end of the D magnet "D 5-4" shown in the diagram 1. The outward tail of the red line

touches the aperture of the "D 5-4" at the distance  $K=8.34$  (see column x of Table 3.2) from the center of the read line. Therefore, the outward tail of the red line within the distances  $K=[-\infty, 8.34]$  will be intercepted by the aperture of the downstream end of the "D 5-4". The portion of stopped particles in this outward tail is calculated by the function  $\Xi(\theta_n, p_{\min}, p_{\max})$  with the following parameters:  $\theta_n=7.05$  (from eq.3.9 for the 400 $\mu\text{m}$  Cu-foil);  $p_{\min}=+\infty$  and  $p_{\max}=8.34$ . The resulting value of  $\Xi(7.05, 8.34, +\infty)=0.118$  is shown in the column xi of the Table 3.2. Thus, the downstream aperture of the "D 5-4" stops about 11.8% of the scattered particles.

Table 3.2 Calculations of  $K$  and  $\Xi$  values for different thickness of the copper foils  $t_{\text{Cu}}$

No [ <sup>10</sup> ]	Element names	Twiss parameters by MADX					$y=b_v, \text{m}$ [ <sup>11</sup> ]	$Y=n$ [ <sup>12</sup> ]	$K$ eq.(3.4)	$\Xi$ for $t_{\text{Cu}}$ , [ $\mu\text{m}$ ] <sup>13</sup> :		
		S, m	$\beta_v, \text{m}$	$\alpha_v$	$\mu, \text{rad}/2\pi$	$\mu_v, \text{deg}$				400	50	10
i	ii	iii	iv	v	vi	vii	viii	x	xi	xii	xiii	
	V-prim	0	11.85	-2.170	0	0		3				
	D 5-4 us	0.250	12.97	-2.282	0.0032	1.15	0.0286	5.62	130	0	0	0
1	<b>D 5-4 ds</b>	<b>3.139</b>	<b>20.42</b>	<b>0.151</b>	<b>0.0294</b>	<b>10.82</b>	<b>0.0286</b>	<b>4.48</b>	<b>8.34</b>	<b>0.118</b>	<b>0.0001</b>	<b>0</b>
	COL1 us	3.934	20.21	0.111	0.0357	12.85		3.31	1.73			
	COL1 ds	5.152	20.02	0.050	0.0453	16.31		3.32	1.57			
	COL2 us	6.752	19.99	-0.030	0.0581	20.92		3.32	1.45			
2	<b>COL2 ds</b>	<b>7.969</b>	<b>20.13</b>	<b>-0.091</b>	<b>0.0677</b>	<b>24.37</b>		<b>3.32</b>	<b>1.42</b>	<b>0.301</b>	<b>0.265</b>	<b>0.063</b>
	D 6-1 us	9.140	20.42	-0.137	0.0769	27.68	0.0286	4.48	3.92			
	D 6-1 ds	12.029	12.96	2.290	0.1032	37.15	0.0286	5.62	5.35			
	F 6-2 us	12.529	10.79	2.058	0.1099	39.56	0.0208	4.48	3.40			
	F 6-2 ds	15.419	5.342	0.112	0.1769	63.68	0.0208	6.36	5.61			
	F 6-3 us	16.619	5.346	-0.111	0.2130	76.68	0.0208	6.36	5.83			
3	<b>F 6-3 ds</b>	<b>19.509</b>	<b>10.82</b>	<b>-2.056</b>	<b>0.2799</b>	<b>100.76</b>	0.0208	<b>4.47</b>	<b>-5.12</b>	<b>0.234</b>	<b>0.012</b>	<b>0.0</b>
	D 6-4 us	20.008	13.00	-2.290	0.2866	103.17	0.0286	5.61	-6.46			
	D 6-4 ds	22.898	20.48	0.150	0.3128	112.61	0.0286	4.47	-6.09			
4	<b>COL3 us</b>	<b>23.703</b>	<b>20.27</b>	<b>0.110</b>	<b>0.3191</b>	<b>114.87</b>		<b>3.32</b>	<b>-5.05</b>	<b>0.003</b>	<b>0.001</b>	<b>0</b>
	COL3 ds	24.920	20.08	0.049	0.3287	118.33		3.32	5.39			
5	<b>All_RF_D_F</b>					→ "48.2"	0.0286	<b>4.5<sup>[14]</sup></b>	→ "3.35"	<b>0.08</b>	<b>0.056</b>	<b>0</b>
6	<b>N-turns Col2&amp;3</b>					→ "25.4"		<b>3.32</b>	→ "1.42"	<b>0.103</b>	<b>0.196</b>	<b>0.063</b>
7	<b>Escape</b>									<b>0.16</b>	<b>0.47</b>	<b>0.874</b>

Since the secondary collimator "6A" stays in the garage position for considered scheme, the next aperture restriction comes from the secondary collimator "6B". The diagram 2 of the Fig. 3.31 shows the further interception of the outward tail at the downstream end of the collimator "6B". The total portion of the protons stopped by the collimator "6B" is defined by the value of  $\Xi(7.05, 1.42, 8.34)=0.301$ , which is listed in the column xi of the Table 3.2.

Note, that the downstream end of the collimators "6B" is located at the optimum phase advance for the given values of  $n_{\text{prim}}$  and  $n_{\text{sec}}$ . Thus, the collimator "6B" cuts the maximum possible length of the outward tail of the scattered protons. Table 3.3 contains the optimal phase shifts  $\mu_{\text{opt}}$  and minimum  $K_{\text{opt}}$  for secondary collimators & RF-cavities. For the chosen values of the primary collimator location  $n_{\text{prim}}=3$  and the set-backs of the secondary collimators  $\Delta_s=2$  mm, these values have been calculated with help of the eqs. (3.5), (3.6).

<sup>10</sup> Sequent numbers shown in Fig.3.31 and Fig.3.32.

<sup>11</sup> see Table 3.1

<sup>12</sup>  $n = b_v / \sqrt{\epsilon \beta_y}$

<sup>13</sup> using eq.(3.10)

<sup>14</sup> see Table 3.1

Table 3.3 Optimal phase shifts  $\mu_{\text{opt}}$  and minimum  $K_{\text{opt}}$  for secondary collimators & RF-cavities.

element name	Integer values of $Y_{\text{sec}}$ : $[n_{\text{prim}}]$	set-backs of sec. collimators:		$n_{\text{sec}}=[n_{\text{prim}}]+\delta$	eq. 3.5		$K_{\text{opt}}$
		$\Delta_{\delta}$ m	$\delta$		$\mu_{\text{opt}}$ , rad	$\mu_{\text{opt}}$ , deg	
COL2 us	3	0.002	0.32	3.32	0.442	25.4	1.42
COL2 ds	3	0.002	0.32	3.32	0.442	25.4	1.42
COL3 us	3	0.002	0.32	3.32	0.442	25.4	1.42
COL3 ds	3	0.002	0.32	3.32	0.442	25.4	1.42
All_RF_D_F				4.5	0.841	48.2	3.35

The two magnets "D 6-1" and "F 6-2" located at the phase advances  $\mu < 90^\circ$  will not intercept any protons from the outward tail, since their  $K$ -parameters are larger than  $K$ -parameter of the secondary collimator "6B". Therefore, they could not reach the remains of the outward tail after collimator "6B".

However, the downstream end of the magnet "F 6-3" located at the phase advance  $\mu > 90^\circ$  will intercept the inward tail of the scattered protons as it is shown in the diagram 3 of Fig. 3.31. The portion of the stopped particles is equal to  $\Xi(7.05, -\infty, -5.12)=0.234$ .

The diagram 4 of the Fig. 3.31 shows the further interception of the inward tail at the upstream end of the collimator "7A". This collimator located the phase advance  $\mu=(180^\circ-65.13^\circ)$ , which is far from the optimal value  $\mu_{\text{opt},7A}=25.4^\circ$ . Therefore, this collimator cuts the inward tail at  $K=-5.05$ , which is much larger of the minimal value  $K_{\text{opt}}=1.42$  shown in Table 3.3. The portion of the stopped particles is very small to  $\Xi(7.05, -5.12, -5.05)=0.003$ , since the upstream magnet "F 6-3" has already cut the inward tail at the distance  $K=5.12$  from the center of the red line.

After passing the secondary collimator "7A" during the first turn, the scattered protons will pass throughout a sequence of the  $\sim 90$  gradient magnets and  $\sim 20$  RF-cavities located within periods  $8 \div 24$  and  $1 \div 5$ . Each gradient magnet and RF cavity is the aperture restrictions. Thus, the scattered protons will pass many aperture restrictions located at many different phase advances. Let's name this sequence of elements as "All\_RF\_D\_F", and add their data in a separate row of Table 3.2.

One can assume, that some of these gradient magnets and RF cavities are passed at the phase advance which is close to the optimal phase advance  $\mu_{\text{opt}}=48.2^\circ$  shown in Table 3.3 with the name "All\_RF\_D\_F". Therefore, some of these elements could cut the inward tail at the distance  $K_{\text{opt}}=3.35$  from the red line center (see the diagram 5 of the Fig. 3.31). Thus, the portion of the protons stopped by "All\_RF\_D\_F" is close to  $\Xi(7.05, -5.05, -3.35)=0.08$ . Note, that the outward tail is not reachable for "All\_RF\_D\_F", since it was already cut at  $K_{\text{opt}}=1.42$  by the collimator "6B".

The collimation process could be lasted during many turns. Since the tune shift is not equal to an integer number, the scattered protons will pass the machine element at different phases during each sequent turn. One can also assume, that at some turn the scattered protons will arrive to the secondary collimator (either "6B" or "7A") at the phase close to the optimal phase advance  $\mu_{\text{opt}}=25.4^\circ$ , and the inward tail will be cut at the minimum distance  $K_{\text{opt}}=1.42$  from the center of the red line. This event is shown on the diagram 6 of the Fig. 3.31. The portion of the protons stopped by the secondary collimator at some turn is close to  $\Xi(7.05, -3.35, -1.42)=0.103$ .

Finally, the portion of the scattered protons, which escape from the 2SC system is evaluated as  $\Xi(7.05, -1.42, +1.42)=0.16$ . Remind that existence of the escaped particles in 2SC is unavoidable and defined by the mandatory gap  $\delta$  between the  $3\sigma$ -beam envelope and the secondary collimators.

Similar calculations have been performed for two other foils thickness. They are listed in columns xii, xiii of Table 3.2. The calculated values can be used for evaluations of the collimation efficiency. Figure 3.32 contains the numerical examples and graphical illustrations for the calculations of the collimation efficiency for three copper foils considered here.

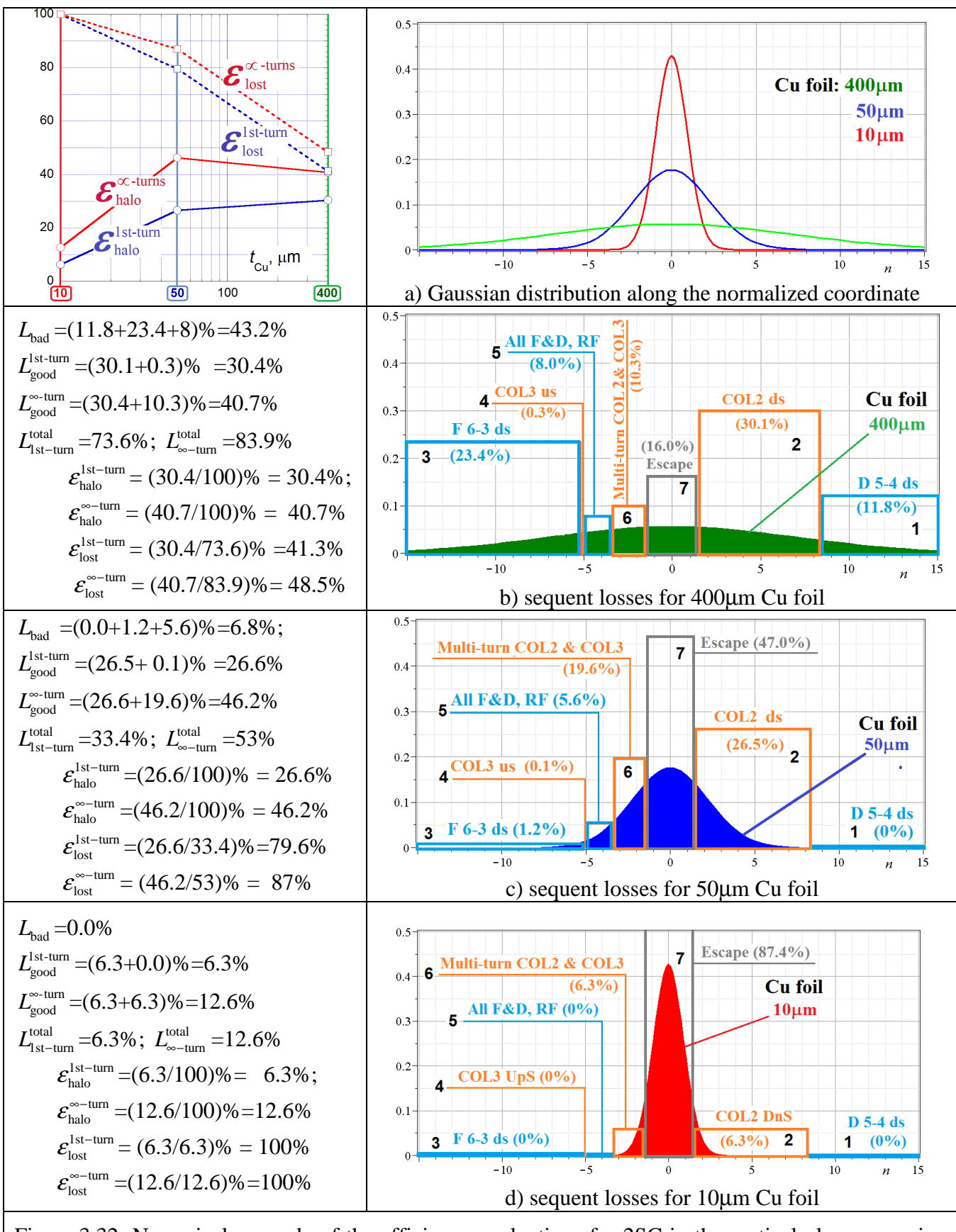


Figure 3.32: Numerical example of the efficiency evaluations for 2SC in the vertical plane assuming linear beam dynamics.

### 3.4.1.1 Definitions of the Collimation Efficiency

The collimation efficiency can be defined in two ways [49, 57, 62, 63, and 64], which will be denoted here as  $\epsilon_{\text{halo}}$  and  $\epsilon_{\text{lost}}$ . It assumed that the halo protons start at the upstream edge of the primary collimator and then pass through the primary collimator foil. Let's denote the number of these halo protons as  $N_{\text{halo}}$ . After scattering on the primary collimator these halo protons may move along machine elements during many turns, while some of them can be lost on the aperture restrictions of the machine elements including the secondary collimators.

Usually, the secondary collimators are well-shielded elements and therefore the beam losses on them could be treated as "useful" (or desirable). All other machine elements have no shielding protection and therefore the beam losses on the must be avoided. Let's denote the total number of lost halo particles as  $N_{\text{lost}}$ , and the total number of the halo particles lost on the secondary collimators  $N_{\text{SecColl}}$ . Then, both collimation efficiencies are given by the following ratios:

$$\epsilon_{\text{halo}} = N_{\text{SecColl}} / N_{\text{halo}}, \quad (3.11)$$

$$\epsilon_{\text{lost}} = N_{\text{SecColl}} / N_{\text{lost}}. \quad (3.12)$$

The first definition of the collimation efficiency  $\epsilon_{\text{halo}}$  has been used in ref. [62, 63, 64], and the second one with  $\epsilon_{\text{lost}}$  has been used in ref. [49, 57, and 62]. Both efficiencies become the same when all halo protons are lost ( $N_{\text{lost}}=N_{\text{halo}}$ ). Let's use both definitions of the collimation efficiency in this report.

### 3.4.1.2 Collimation Efficiencies for analytical evaluations of the vertical 2SC

Let's explain in details calculations of the collimation efficiency for the above analytical consideration of the 2SC in the vertical plane presented in Fig 3.32. Both collimation efficiencies have been calculated after the first turn and for infinite large number of turns, resulting in the following four parameters:  $\epsilon_{\text{halo}}^{\text{1st-turn}}$ ,  $\epsilon_{\text{halo}}^{\infty\text{-turn}}$ ,  $\epsilon_{\text{lost}}^{\text{1st-turn}}$ , and  $\epsilon_{\text{lost}}^{\infty\text{-turn}}$ . The left upper plot presents final results for these four collimation efficiencies at three thickness of copper foil.

Figure 3.32,a shows the Gaussian density distributions along the red straight line for three thicknesses of copper foil. Figures 3.32,b,c,d present sequent beam losses during beam pass throughout of the Booster elements for the foil thickness 400 $\mu\text{m}$ , 50 $\mu\text{m}$ , and 10 $\mu\text{m}$ , respectively. The bar numbers corresponds to the sequent numbers of diagrams in Fig. 3.31 and to numbers in the column i of Table 3.2. The values of the proton portions  $\Xi$  listed in the columns xi+xiid of Table 3.2 are shown in percents for every bar of Fig 3.32,b,c,d.

#### An example with 400 $\mu\text{m}$ Cu foil

First, let's consider the sequent losses for the 400 $\mu\text{m}$  Cu foil shown in Fig 3.32,b. The sum of "bad" (undesirable) losses on apertures of the gradient magnets and on RF-cavities is equal to  $L_{\text{bad}}=43.2\%$ . The sum of "good" beam losses inside of secondary collimators "6B"(or COL2) and "7A" (or COL3) during the first turn are equal  $L_{\text{good}}^{\text{1st-turn}}=30.4\%$ . After infinite number of turns these "good" losses could potentially increase up to  $L_{\text{good}}^{\infty\text{-turn}}=40.7\%$ . The total losses on all machine elements after the 1st turn are equal to  $L_{\text{1st-turn}}^{\text{total}}=L_{\text{bad}}+L_{\text{good}}^{\text{1st-turn}}=73.6\%$ . After infinite number of turns the total losses on all machine elements could reach up to  $L_{\infty\text{-turn}}^{\text{total}}=L_{\text{bad}}+L_{\text{good}}^{\infty\text{-turn}}=83.9\%$ . The number of escaped protons which will continue motion without interactions with any aperture of the machine is equal to  $P_{\text{escape}}^{\infty\text{-turns}}=16.0\%$

(see "Escape" name in Table 3.2). Note, the sum of lost and escaped protons  $L_{\infty\text{-turn}}^{\text{total}} + P_{\text{escape}}^{\infty\text{-turns}} = 99.9\%$  is almost equal to 100%.

All collimation efficiencies for the 400 $\mu\text{m}$  Cu foil are less than 50%, because the "bad" beam losses on unshielded elements with small apertures are too high  $L_{\text{bad}} = 43.2\%$ . These values are quite low and almost the same as for a well-aligned single stage collimation system, which has absorption efficiency about 50% (see Fig.3.3) and is much simple in a practical realization.

If the apertures of the gradient magnets and RF-cavities could be essentially increased, the "bad" beam losses will drop down, i.e.  $L_{\text{bad}} \rightarrow 0$ , and the "bad" losses will be converted into "good" losses happened on the secondary collimators. In such case, the "good" losses could reach up to  $L_{\text{good}}^{\text{1st-turn}} \rightarrow 73.6\%$  and  $L_{\text{good}}^{\infty\text{-turn}} \rightarrow 83.9\%$ . In this case, the collimation efficiencies  $\epsilon_{\text{halo}}$  could reach up to  $\epsilon_{\text{halo}}^{\text{1st-turn}} \rightarrow 73.6\%$  and  $\epsilon_{\text{halo}}^{\infty\text{-turn}} \rightarrow 83.9\%$ . The collimation efficiency  $\epsilon_{\text{lost}}$  could approach to 100%, which actually misleading for our consideration, since such excellent 100%-result masks existence of considerable 16%-fraction of escaped protons.

However, the apertures of the Booster magnets and RF-cavities are considered to be permanent for our study of the existing 2SC system. Therefore, a reduction of "bad" beam losses of these elements can be reached via usage of thinner foils. The calculations of the collimations efficiencies for two other foil thicknesses are similar to the presented above, and details of calculations will be omitted.

### **An example with 50 $\mu\text{m}$ Cu foil**

Figure 3.32,c shows the sequent beam losses for the 50 $\mu\text{m}$  Cu foil, which is 8 times thinner of the considered above 50 $\mu\text{m}$  Cu foil. It is seen, that the density distribution is reduced at the distribution tails and is increased at the distribution center. Therefore, the "bad" losses on the gradient magnets and RF-cavities, which intercept particles located on the tails of distributions, will be essentially reduced to  $L_{\text{bad}} = 6.8\%$  from  $L_{\text{bad}} = 43.2\%$  for 400 $\mu\text{m}$  foil. On the other hand, the portion of escaped protons located near the center of the distribution is increased up to one half ( $P_{\text{escape}}^{\infty\text{-turns}} = 47\%$ ).

As result, there collimations efficiency  $\epsilon_{\text{halo}}$  changes slightly:  $\epsilon_{\text{halo}}^{\text{1st-turn}}$  is reduced to 26.6%, and  $\epsilon_{\text{halo}}^{\infty\text{-turn}}$  is increased to 46.2% from 30.4% and 40.7% for the 50mm foil, respectively. However, the collimation efficiency  $\epsilon_{\text{lost}}$  demonstrates an essential progress and reaches values of  $\epsilon_{\text{lost}}^{\text{1st-turn}} = 79.6\%$  and  $\epsilon_{\text{lost}}^{\infty\text{-turn}} = 87\%$ , which looks quite good, but don not alarm about the large number of escaped protons, which are out of a control of 2SC system in a general case.

### **An example with 10 $\mu\text{m}$ Cu foil**

The situation becomes even more questionable for the case of the thinnest 10 $\mu\text{m}$  copper foil. In this case the "bad" losses disappear at all,  $L_{\text{bad}} = 0\%$ , and the most of the particles escape from the 2SC system ( $P_{\text{escape}}^{\infty\text{-turns}} = 87.4\%$ ). In return, the collimation efficiency  $\epsilon_{\text{halo}}$  is very low, namely  $\epsilon_{\text{halo}}^{\text{1st-turn}} = 6.3\%$  and  $\epsilon_{\text{halo}}^{\infty\text{-turn}} = 12.6\%$ , and it signals about worth situation. However, the collimation efficiency  $\epsilon_{\text{lost}}$  reaches maximum possible values, namely  $\epsilon_{\text{lost}}^{\text{1st-turn}} = 100\%$  and  $\epsilon_{\text{lost}}^{\infty\text{-turn}} = 100\%$ , which declare some favorable situation. The key difference between two definitions of collimation efficiencies is related to different treatments of the escaped particles. The collimation efficiency  $\epsilon_{\text{halo}}$  directly depends on the number of escaped protons, i.e.  $\epsilon_{\text{halo}} = N_{\text{SecColl}} / (N_{\text{lost}} + P_{\text{escape}})$ , while the collimation efficiency  $\epsilon_{\text{lost}} = N_{\text{SecColl}} / N_{\text{lost}}$  simply ignores escaped protons. The meaning of the escaped protons depends on their behavior in a particular machine in view point of the collimation matters.

### 3.4.1.3 Differences between a "steady" machine vs a rapid synchrotron

Let's understand how particles escaped from a 2SC system could behave in a "steady" machine like a hadron collider or storage ring and in a rapid cycling synchrotron like the Fermilab Booster. Note that escaped particles must stay on  $3\sigma$ -beam envelope which sits on the closed orbit.

The relevant features of a steady machine are the following: a) the beam energy is constant; b) the physical and dynamical beam apertures are quite high and approaches to  $7\div 10 \sigma$ ; c) the beam bunches are already formed and preserve their shapes, while circulating for many hours under stationary conditions for closed orbit and beam envelope; d) the emittance grown is minimal, while beam halo size increases with very slow speed within a few micrometers per turn.

In such machine, the escaped particles have good chances to be intercepted by the primary collimator again after many hundreds or even thousands turns. It could be ensured if that physical aperture is sufficiently high and the primary collimator foil is quite thin resulting in a minimal energy drop for scattered particles. Under such conditions the escaped protons could circulate for many turns in a machine without touching aperture restriction.

After a next interaction of the escaped particles with primary collimator foil, some part of the scattered protons could be intercepted by the secondary collimators similar to the first pass. Thus, the initial portion of the escaped protons  $P_{\text{escape}}$  will be reduced again and again with every next pass of 2SC collimation system. In principle, the initial portion of the escaped protons  $P_{\text{escape}}$  could be reduced to 0, while the number of particles lost on the secondary collimators  $N_{\text{SecColl}}$  will be increased. The final value of the collimation efficiency  $\epsilon_{\text{halo}}$  will become high and reach the initial value for  $\epsilon_{\text{lost}}$ .

Such high values of the collimation efficiency could be easily obtained in computer simulations of 2SC systems via multi-turn beam tracking under ideal conditions, which assume a constant both beam energy and ideal magnetic fields. Such ideal simulations can be performed for a very large number of turns and allow multiple passes of scattered protons throughout of the primary collimators, and hence, high values of the collimation efficiency can be simulated. However, a computer model should be adequate to the conditions in a real machine.

For example, the particle tracking with the STRUCT for the Booster 2SC system code has been restricted by 400 turns [43]. The simulations have shown that at the injection energy, an average number of each particle interaction with horizontal and vertical primary collimator was about 1 for both directions, while at the top energy this number increased up to  $\sim 8$  and  $\sim 5$  for horizontal and vertical primary collimator, respectively. These results demonstrate that the above mechanism for increasing the collimation efficiency with help of multiple passing throughout primary collimators does not feasible at the injection energy considered in our studies. Although the assumption about a steady conditions during 400 turns in Booster looks to be a quite doubtful.

Let's consider conditions and peculiarities for 2SC near the injection energy in such specific rapid cycling synchrotron as Fermilab Booster. They are the following: a) the beam energy varies from 0.4 MeV till 8GeV during 20,000-turn Booster circle as shown in Fig. 3.33; b) the beam envelope must shrink inversely to the product of relativistic  $\beta$  and  $\gamma$  due to an adiabatic damping as shown in Fig. 3.33; c) the physical aperture of the beam elements is as small as  $4.5\sigma$ ; d) the beam central orbit varies during cycle and tuned independently for different time points; e) the transverse sizes of the beam bunches vary during acceleration cycle; f) the accelerated bunches could not be stationary, since even correcting magnets are tuned independently for different time points; g) there can be a continuous beam mismatching during accelerating cycle leading to the uncontrollable emittance growth; h) the speed of the emittance growth and an increase of the halo size should be essentially larger than in a steady machine, but they are unknown and not measurable at all.

Various beam physics mechanisms for an emittance growth and the halo formation had been already itemized in the section 3.2.1 Some of them could be simulated with some good precision, but they are not able to predict beam size in existing machine with many unknown conditions and

parameters. Any inclusion of some particular mechanism will generate non-reliable and rather speculative misleading results. Only well understandable, measurable and predictable concepts and mechanisms could be brought into play at design and simulations of a collimation system, since we want to remove uncontrollable beam losses in a controllable way.

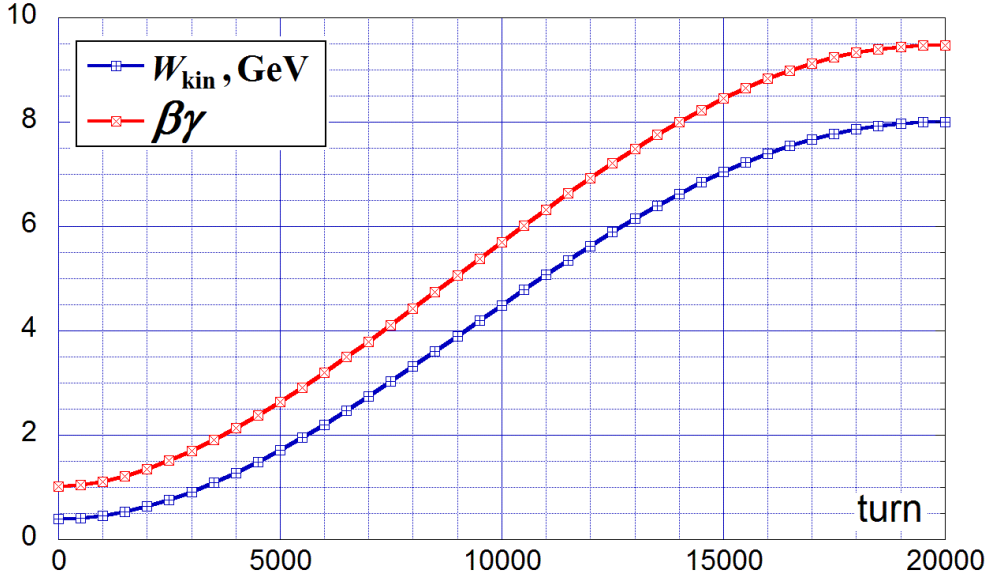


Figure 3.33: Thickness  $d$  of an equivalent aluminum foils for primary collimators made of different materials. Some foils have been recommended by the 2004 design with the STRUCT code. One copper foil had been installed in 2005 and existed till 2014, and another new aluminum foil has been installed in 2015. Also several foils shown in brown frame have been considered as possible candidates.

For example, the adiabatic damping shrinking the beam size is deterministic process, but many other counter processes responsible for an emittance growth are unknown and unpredictable. It could be only concluded that beam size will vary, and the second hit of escaped protons into the thin edge of the primary collimator is improbable. Thus, the above mechanism increasing the collimation efficiency via multi-passing of scattered protons throughout of the primary collimators should be excluded from our considerations for the Booster case. The cited above simulations [43] with the STRUCT code allowing energy variations also showed that the multi-passing process does not happen during at least 400 turns at the injection energy.

The most above peculiarities of operation are not specific for Booster only, they are quite normal for any rapid cycle synchrotron. Therefore, these Booster features should be taken into account at choice of the collimation system type and its design and simulations.

### 3.4.1.4 Summary of reasons for potentially low collimation efficiency

Let's summarize main reasons of potentially low efficiency of the Booster 2SC. The first reason is small apertures of gradient magnets and RF-cavities. They do not allow a usage of a rather thick 400  $\mu\text{m}$  Cu foil reducing the collimation efficiency  $\epsilon_{\text{halo}}$  down to 30÷40%, which could not exceed collimation efficiency of the conventional single stage collimation. The elimination of those aperture restrictions could potentially increase the collimation efficiencies up to ~85%, since the portion of the escaped protons is low as ~15%.

In order to reduce direct beam losses of the apertures of gradient magnets and RF-cavities, the usage of thinner foils looks to be attractive. However, the portion of escaped protons for thinner foils

will be increased dramatically from  $P_{\text{escape}} \sim 50\%$  for the 50  $\mu\text{m}$  Cu foil till  $P_{\text{escape}} \sim 90\%$  for very thin 10  $\mu\text{m}$  Cu foil corresponding to the 2004 design. It could be assumed that due to an emittance growth the escaped particles could hit the secondary collimators. However, such process is similar to a one for conventional single stage collimation and its efficiency should be the same as for single stage collimation. There is no a clear physical mechanism due to which the escaped particles will hit the secondary collimators with enlarged impact parameters as in 2SC scheme. Therefore, a low collimation efficiency  $\epsilon_{\text{halo}} < 15\%$  for very thin 10  $\mu\text{m}$  Cu foil (as the 2004 design) looks to be well-explained, while a high collimation efficiency  $\epsilon_{\text{lost}} \sim 100\%$  looks to be doubtful.

Then, the primary collimator with the 50  $\mu\text{m}$  Cu foil is a compromise between a reduction of beam losses on the aperture restrictions and a reduction of the escaped protons. It could potentially reach the collimation efficiency of  $\epsilon_{\text{halo}} \sim 50\%$ .

The second reason for potentially low efficiency of the Booster 2SC is non-optimal phase locations of the secondary collimators. As shown above (see Table3.3) for the design values  $n_{\text{prim}}=3$  and  $n_{\text{sec}}=3.32$  the optimal phase advances between primary and secondary collimators for 2SC in both planes are equal to  $\mu_{\text{opt},1}=25.4^\circ$  and  $\mu_{\text{opt},2}=(180^\circ-25.4)=154.6^\circ$  for the first and the second secondary collimators.

Figure3.34 shows the phase advances available for locations of the secondary collimators. The available phase advances in the horizontal plane cover the range  $\mu=32^\circ \div 81^\circ$  and  $\mu=130^\circ \div 185^\circ$  in Long straight 6 and 7, respectively. According to the 2004 design (see Table2.2), the first secondary collimator COL1(6A) has been set at the phase advance  $\mu_{6A}=53^\circ$ , and the second secondary collimator COL3(7A) has been set at the phase advance  $\mu_{7A}=143^\circ$ . The phase advances for both horizontal secondary collimators are considerably far from the optimal phases.

The available phase advances in the vertical plane cover the range  $\mu=10^\circ \div 27^\circ$  and  $\mu=113^\circ \div 130^\circ$  in Long straight 6 and 7, respectively. According to the 2004 design (see Table2.2), the first secondary collimator COL2(6B) has been set at the phase advance  $\mu_{6B}=21^\circ$ , and the second secondary collimator COL3(7A) has been set at the phase advance  $\mu_{7A}=124^\circ$ . The phase advance of the vertical collimator 6A is very close to optimal value, but the phase advance of the vertical collimator 7A is considerably far very from the optimal phases.

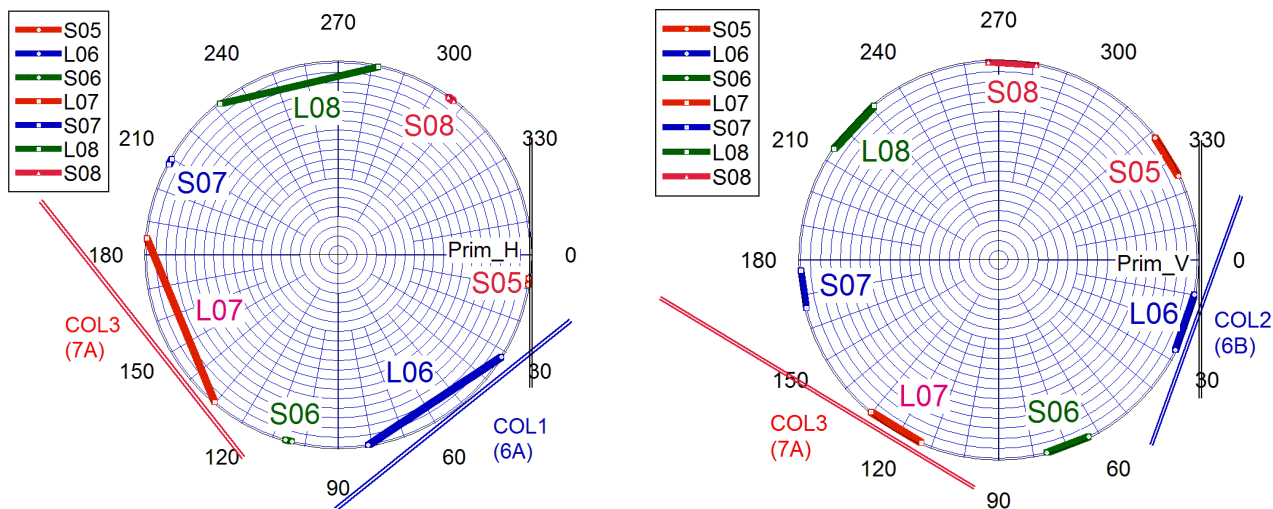


Figure 3.34: Phase advances available for locations of the secondary collimators in periods 5-8 for collimation in the horizontal and vertical planes.

A location of the secondary collimators at non-optimal phase shifts leads to the multi-turn collimation process during which small portions of scattered particles are intercepted by secondary collimators. Then it becomes to be questionable how many turns the scattered particles could be considered remain of the trajectory which is the sum of initial central beam orbit and  $3\sigma$ beam envelope until they will approach to the secondary collimator in an optimal phase. Thus, even for compromised 50  $\mu\text{m}$  Cu foil a stable linear beam dynamics within a Booster aperture during many turn is a necessary condition in order to reach a moderate values of the collimation efficiency  $\epsilon_{\text{halo}} \sim 50\%$ .

The third reason for potentially low efficiency of the Booster 2SC is a large fraction of escaped protons, which are out of any control by the collimation system. Their behavior depends on the operation features of the real machine. In our studies, these escaped protons are considered to be non-controllable losses. We could not suggest any well understandable, measurable and predictable physical concepts and mechanisms which will force these particles to hit the secondary collimators with enlarged impact parameter. Let's remind that the task of the 2SC collimation system is to enlarge the impact parameters of the particles hitting the secondary collimators. More generally, the 2SC collimation system must intercept uncontrolled potentially lost particles in a well-controllable way.

The above analytical consideration clearly demonstrates a potentially low efficiency of the Booster 2SC system in the vertical plane. The analysis for the horizontal plane is so straightforward. Therefore, in the next chapters the results of the numerical simulations for the vertical and the horizontal planes will be presented. Since it is not possible to prove theoretically an existence or an absence some favorable physical mechanisms in a real machine, the experimental studies for 2SC system has been also performed.

## **3.5 Numerical Simulations**

### **3.5.1 New Simulation Approaches**

As it was explained above, since the STRUCT code is not presently maintained at Fermilab, it has been decided to replace it by tracking with MADX, which has been adapted for simulations of the 2SC. A new combination of the MADX and MARS15 codes is used for proton tracking in the Booster with their scattering on collimators [83, 84].

Adaptation of the MADX code included modifications of both a MADX script for the Booster lattice and a MADX source code itself. The apertures for all Booster elements have been inserted into the MADX-lattice using sizes given either in the STRUCT-lattice file or in the engineering drawings. Also, a new trapezoidal aperture for the Booster combined function magnets has been implemented in the MADX source code. The proton out-scattering in absorbers is simulated via a direct use of the MARS code, while proton interactions with foils of the primary collimators is simulated with the TARGB module embedded in the MADX code.

The simulation algorithm includes the following steps:

- a) generation of halo proton distribution at the edge of a primary collimator with an external script;
- b) multi-turn tracking of halo protons using the MADX thin-track module including proton interactions with foils of primary collimators (via TARGB) and recording coordinates of protons lost on lattice apertures;
- c) collection of protons lost on apertures of each absorber and restoration of their coordinates at the front planes of the absorbers using an external script;
- d) tracking protons collected at the previous step through each absorber using its MARS models, where the MARS code perform full Monte Carlo simulations for protons inside of absorbers;
- e) collection of protons out-scattered from absorbers at the back plane of absorbers using an external script;
- f) tracking of out-scattered protons from the back plane of absorbers using MADX and recording lost protons;
- g) post-processing via counting lost protons on lattice elements before and after tracking with MARS code, i.e. with or without out-scattering effects.

### **3.5.2 Absorber Model in MARS Code**

In order to simulate correctly out-scattering of protons in absorbers, a MARS model has been created for 3 identical secondary collimators. The model has been created and supported by I. Tropin and N. Mokhov. Since MARS code use its own coordinate system, some interface for importing and exporting the particle coordinates is needed. Such interface has been created by I. Rakhno. It is similar to interface used for interactions with the STRUCT code, and therefore it uses the STRUCT coordinate system  $(x, x', y, y', p)$ , which is different from the canonical coordinates used in the MADX code. Then an additional interface code for exchange of the STRUCT-style coordinates and MADX coordinates has been written by V.K.

Figure 3.35,a shows the longitudinal section sketch of the secondary collimator with relevant sizes used for implementation of the MARS model. These sizes have been extracted from the absorber drawings presented in Fig 2.20. Figure 3.35,b shows the cross-sections of the MARS model drawn in the internal MARS coordinates. The MARS model is used by MADX as a "black-box". MARS model is centered on the longitudinal axis of the MARS internal coordinate system. All transverse shifts of the real collimators are simulated via virtual shifts of proton coordinates during theirs export / import between MADX and MARS.

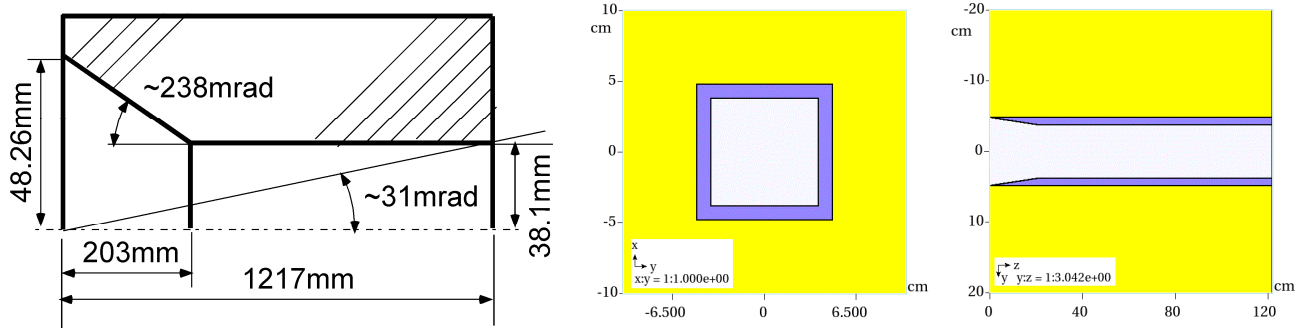


Figure 3.35: The sketch of the secondary collimator cross-section with relevant sizes (a) and the cross-sections of its MARS model (b).

### 3.5.3 Simulations for Single Stage Collimation System

The MARS model has been also used for calculation of the absorption efficiency of a single absorber allowing us to evaluate an efficiency of the existing 1SC system. It is known that there is a strong dependence of the absorption efficiency on angular alignment of the absorber jaw and size of the beam halo [57] (also see Fig.3.3 reproduced from [57]). Figure 3.36 shows a longitudinal section of the absorber having a frontally-tapered square aperture and positions of incident halo rays used in the simulations. The halo rays with negative slopes  $x'<0$  cross the absorber jaw at its tapered front end while the halo rays with  $x'>0$  cross the jaw at its rectangular back end.

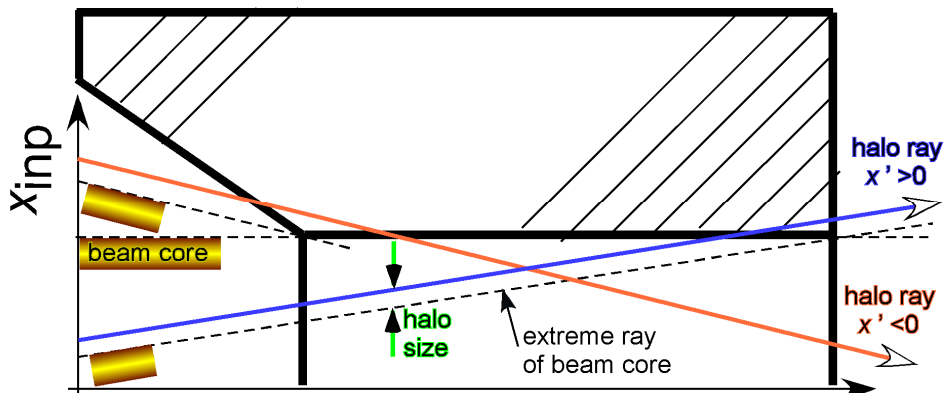


Figure 3.36: Longitudinal section of absorber and positions of halo rays at  $x' > 0$  (blue) and  $x' < 0$  (red).

In simulations, the halo rays consist of  $N_{\text{halo}}=10^4$  protons with identical input coordinates  $(x_{\text{inp}}, x')$ , while  $x_{\text{inp}}$  is explicitly defined by  $x'$  due to an assumption that the beam core (or an envelope) just touches absorber surface without any loss of protons from the beam core. Counting the number of protons lost in absorber  $N_{\text{lost}}$ , the absorption efficiency is defined similar to the collimation efficiency  $\epsilon_{\text{halo}}$  as

$$\epsilon_{\text{abs}} = N_{\text{abs}} / N_{\text{halo}} , \quad (3.12)$$

where  $N_{\text{abs}}$  is a number proton absorbed in the collimator without generating out-scattered protons.

Figure 3.37 shows  $\epsilon_{\text{abs}}$  versus the beam slope  $x'$  at different halo sizes for 400 MeV protons.

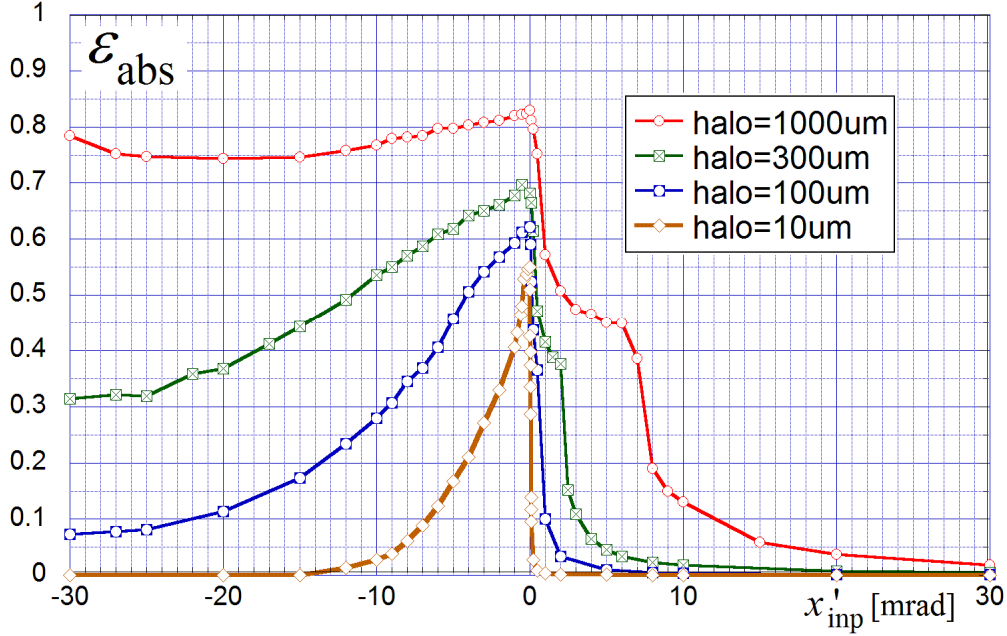


Figure 3.37:  $\epsilon_{\text{abs}}$  vs beam slope  $x'$  at different halo sizes: 10 μm (brown), 100 μm (blue), 300 μm (green), 1mm (red).

The  $\epsilon_{\text{abs}}$ -curves have maximum values at zero  $x'$ , *i.e.* at an ideal angular alignment. The maximum values depend on the halo size and reach 55%, 62%, 68%, and 83% for the halo sizes of 10 μm, 100 μm, 300 μm, and 1mm, respectively. These curves can be also interpreted as dependencies on the impact parameter.

The efficiency  $\epsilon_{\text{abs}}$  for halo rays with negative slopes ( $x' < 0$ ) is considerably higher than for rays with positive slopes ( $x' > 0$ ) since the frontally-tapered aperture increases the effective absorption length for halo rays with  $x' < 0$  in comparison to halo rays with  $x' > 0$ , which cross a relatively sharp non-tapered back end of the jaw. Unfortunately, the absence of tapering for the back end jaws of the Booster absorbers fabricated in ~2003 reduces a range of  $x'$  with a high  $\epsilon_{\text{abs}}$  by a factor ~2. Note, that modern collimators designed at Fermilab in the last decade have "tapers" at both front and back jaws [85].

The above plots could also provide a lower bound of the collimation efficiency for the 2SC system. For this purpose, it is convenient to consider the fraction of non-absorbed particles, *i.e.* the fraction of particles out-scattered back into the vacuum chamber. The figure of merit is the absorption inefficiency, which is defined as

$$\eta_{\text{abs}} = N_{\text{out-scat}} / N_{\text{halo}} \approx 1 - \epsilon_{\text{abs}}, \quad (3.13)$$

where  $N_{\text{out-scat}}$  is a number of out-scattered protons.

Let's assume a well aligned absorber ( $x'_{\text{inp}} \sim 0$ ), then its absorption efficiency  $\epsilon_{\text{abs}}$  should be close to the maximum values of  $\epsilon_{\text{abs}}$ -curves in Figure 3.37. Table 3.4 lists the evaluations the goal values for a 2SC system at different values of the beam halo size. The column ii lists the maximum values of the  $\epsilon_{\text{abs}}$ -curves, and the column iii contains the values of the portion of out-scattered particles. The major purpose of the 2SC system is a reduction of the out-scattered particles.

Let's assume that under considered ideal conditions the 2SC system could reduce the portion of out-scattered protons by 50%. In comparison to a simple conventional single-stage collimation working as a single pass system within the length of absorber, the 2SC system is much complicated and could

reach its maximum efficiency only after many turns requiring a preservation of many initial parameters. Therefore, the above 50% will drop down in a real machine.

Table 3.4 Evaluations of the goal values for the collimation efficiency of 2SC system.

Halo size, $\mu\text{m}$	max $\epsilon_{\text{abs}}$ , %	$\eta_{\text{abs}}$ , %	2SC $\eta_{\text{halo}}$ , %	2SC $\epsilon_{\text{halo}}$
i	ii	iii	iv	v
10	55	(100-55)=45	0.5*45=~23	100-23=77
100	62	38	19	81
300	68	32	16	84
1000	83	17	9	91

With the assumed 50 % reduction, the required collimation inefficiency in the column iv must be two times less than  $\eta_{\text{abs}}$ . The final goal values for the collimation efficiency are listed in column v. They should reach at least 77% even for the smallest 10  $\mu\text{m}$ -halo size. For a halo sizes larger than 100  $\mu\text{m}$  the theoretical collimation efficiency of 2SC must be higher 80%.

### 3.5.4 Simulations for Two Stage Collimation in Vertical Plane

#### 3.5.4.1 Simulation of 2SC in vertical plane with 1D-configuration

There can be several combinations for collimator locations realizing 2SC schemes. The 2SC collimations in horizontal and vertical planes are simulated separately. Let's follow to configurations suggested in the original 2004 design and described in chapter 2.4.2.5 (see Fig. 2.17 and Table 2.2), where for the collimation in the vertical plane used the following combination of collimators: 1) the primary collimator touches the bottom side of the beam core; 2) the first vertical secondary collimator "SV1" (also called as "COL2", "6B") located at the phase shift  $\mu=53^\circ$  touches the beam at bottom side; 3) the second vertical secondary collimator "SHV2" (also called as "COL2", "7A") located at the core at the phase shift  $\mu=143^\circ$  touches the beam at top side.

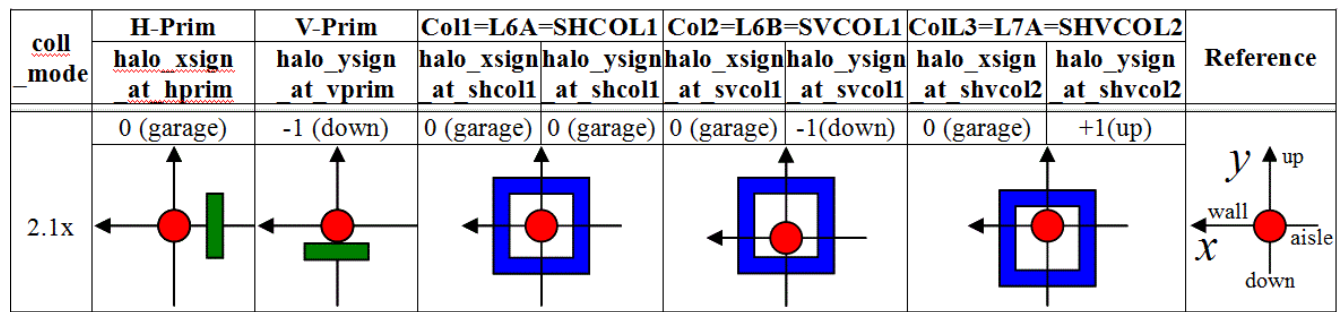


Figure 3.38: The transverse positions of collimators used for simulations of the 2SC in vertical plane for pure 1D-configuration.

The design scheme shown in Fig. 2.17 also involves the secondary collimator "SH1" (also called as "COL1", "6A"), which touches the beam from opposite side than "SV1". In this case, the phase shift of "SH1" is not optimal at all, and its position does not correspond to 2SC principles. This collimator will not intercept the scattered protons at least at the first pass, when it will operate in a conventional single-stage collimation mode. However, after many turns, the phase advance for this collimator could approach to an optimal and this collimator may help to improve the final multi-turn

efficiency of 2SC system. Probably, for the same reasons the horizontal collimator laws could be also involved into the vertical 2SC collimation.

For the first simulations, let's use the pure classical scheme without involving a horizontal jaws and vertical jaws of the collimator "6A". These collimator jaws will be located in garage positions far from the beam core. Let's call this classical configuration as a "pure 1D-configuration". Figure 3.38 shows the transverse positions of collimators used for simulations of the 2SC in vertical plane for a pure 1D-configuration.

In the simulation model for 2SC collimation in the vertical plane, collimators V-prim, 6A and 7A are used. V-prim is placed at the lower edge of the  $3\sigma$ -beam core. The jaws of the 6B and 7A collimators are positioned with a 2mm offset from the  $3\sigma$ -beam core, while the jaw of collimator 6B is located below the beam and the jaw of collimator 7A is located above the beam.

Among other things, the presented simulations with the 2SC system are to define an optimal foil thickness  $t_{\text{PrColl}}$  at 400 MeV. Here, results for 2SC in the vertical plane with copper foils are presented. The simulations have been done using the bundle of MADX and MARS15 codes for halo protons,  $N_{\text{halo}}=10^4$ , distributed along the front edge of the vertical primary collimator.

Figure 3.39 shows the simulation results with MADX tracking only when all protons touching any vacuum walls are considered to be lost, *i.e.* the out-scattering effects are ignored. The results for simulation with the out-scattering effects using both the MADX and MARS codes are shown in Fig 3.40.

Figure 3.39,a shows the total number of lost protons  $N_{\text{lost}}$  around the ring including losses on secondary collimators. Figure 3.39,b shows the total number of protons lost on the secondary collimators  $N_{\text{SecColl}}$ . The 10-turn curve has a maximum at  $t_{\text{PrColl}} \sim 80\mu\text{m}$ , and the 100-turn curve has a maximum at  $t_{\text{PrColl}} \sim 20\mu\text{m}$ . Figure 3.39,c shows the collimations efficiencies  $\epsilon_{\text{halo}}$  and  $\epsilon_{\text{lost}}$ . Let's compare the shown in Fig 3.39 numerically simulated collimation efficiencies  $\epsilon_{\text{halo}}$  and  $\epsilon_{\text{lost}}$  with the analytically derived collimation efficiencies  $\epsilon_{\text{halo}}$  and  $\epsilon_{\text{lost}}$  shown in Fig.3.32. Table 3.5 lists the values for comparison numerical simulations with analytical evaluations.

In general, the results of numerical simulation and results of analytical evaluations are quite close to each other for thick 400  $\mu\text{m}$  foil, and looks to be pretty different for thin 10  $\mu\text{m}$  foil. The difference is originated from different treatments of escaped protons. In analytical evaluations assuming a linear and uncoupled beam dynamics the escaped protons could not be lost. In numerical simulations using the lattice file with some imperfections like sextupole fields in gradient magnets and non-periodic  $\beta$ -functions, the protons escaped from the collimation system after the first passage could be lost after many turns.

To minimize this effect from multi-turn tracking of the escaped protons, let's compare the limiting analytical values of  $L_{\infty-\text{turn}}^{\text{total}}$ ,  $\epsilon_{\text{halo}}^{\infty-\text{turn}}$ , and  $\epsilon_{\text{lost}}^{\infty-\text{turn}}$  with the 10-turn values of the numerical tracking, namely  $L_{10-\text{turn}}^{\text{total}}$ ,  $\epsilon_{\text{halo}}^{10-\text{turn}}$ , and  $\epsilon_{\text{lost}}^{10-\text{turn}}$ . It looks that 10-turns could be enough to collect most of scattered protons on collimators and apertures, and slow effects of lattice imperfections will not appeared so much after 10 turns.

For example, the data in column ii and column iii shows that the maximum losses  $L_{\infty-\text{turn}}^{\text{total}} = 84\%$  and the 10-turns losses  $L_{10-\text{turns}}^{\text{total}} = 97\%$  for 400  $\mu\text{m}$  are close and small 13%-difference, probably, related to multi-turn losses of escaped protons could contribute much in a result difference. Therefore, the maximal analytical efficiencies  $\epsilon_{\text{halo}}^{\infty-\text{turn}} = 41\%$  and  $\epsilon_{\text{lost}}^{\infty-\text{turn}} = 49\%$  are very close to the numerical efficiencies after 10 turns  $\epsilon_{\text{halo}}^{10-\text{turn}} = 45\%$  and  $\epsilon_{\text{lost}}^{10-\text{turn}} = 43\%$ .

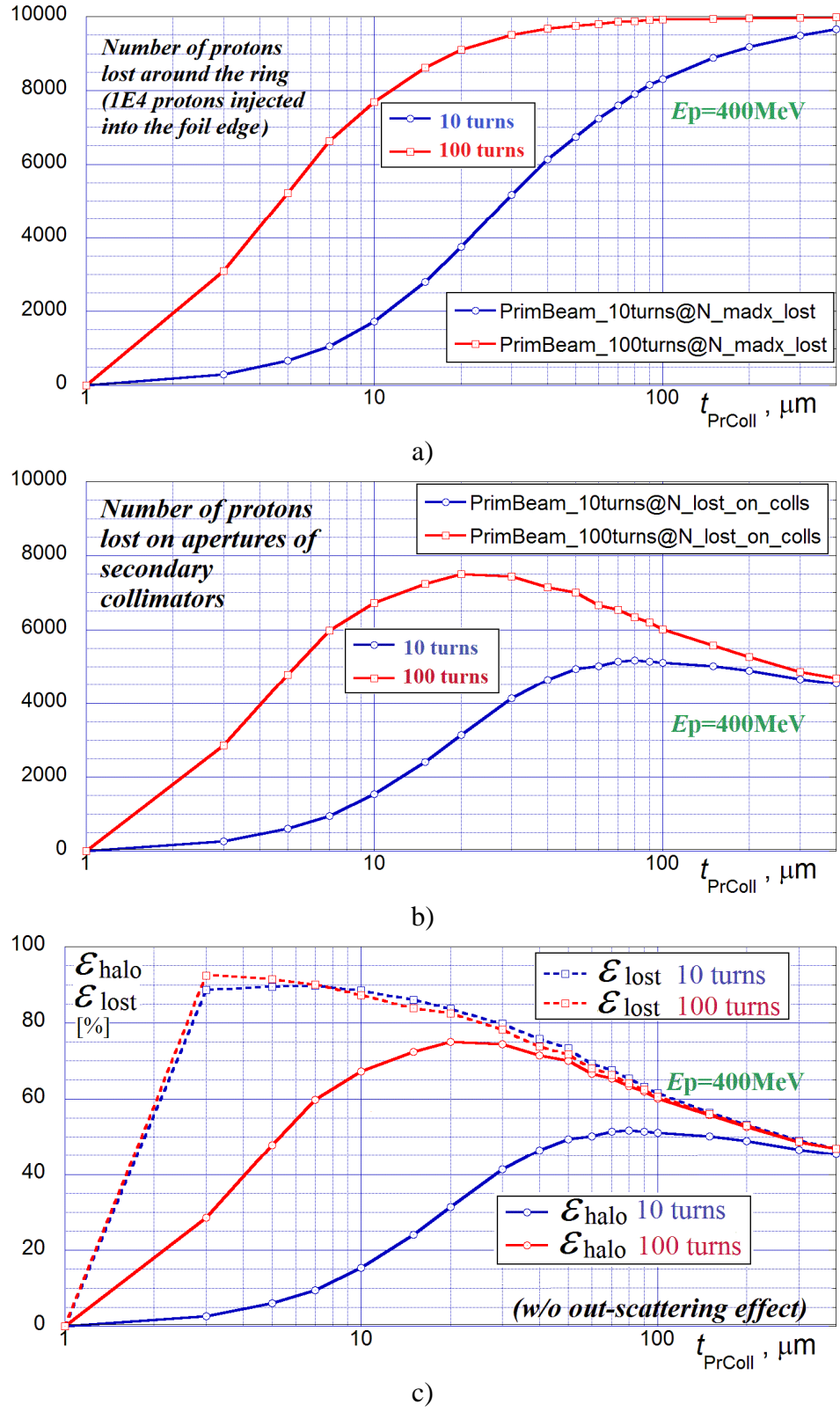


Figure 3.39: The simulation results with MADX tracking and without out-scattering effects after 10 (blue) and 100 turns (red) for the 2SC in vertical plane for pure 1D-configuration: a)  $N_{\text{lost}}$  vs  $t_{\text{PrColl}}$ ; b)  $N_{\text{SecColl}}$  vs  $t_{\text{PrColl}}$ ; c)  $\mathcal{E}_{\text{halo}}$  and  $\mathcal{E}_{\text{lost}}$  vs  $t_{\text{PrColl}}$ .

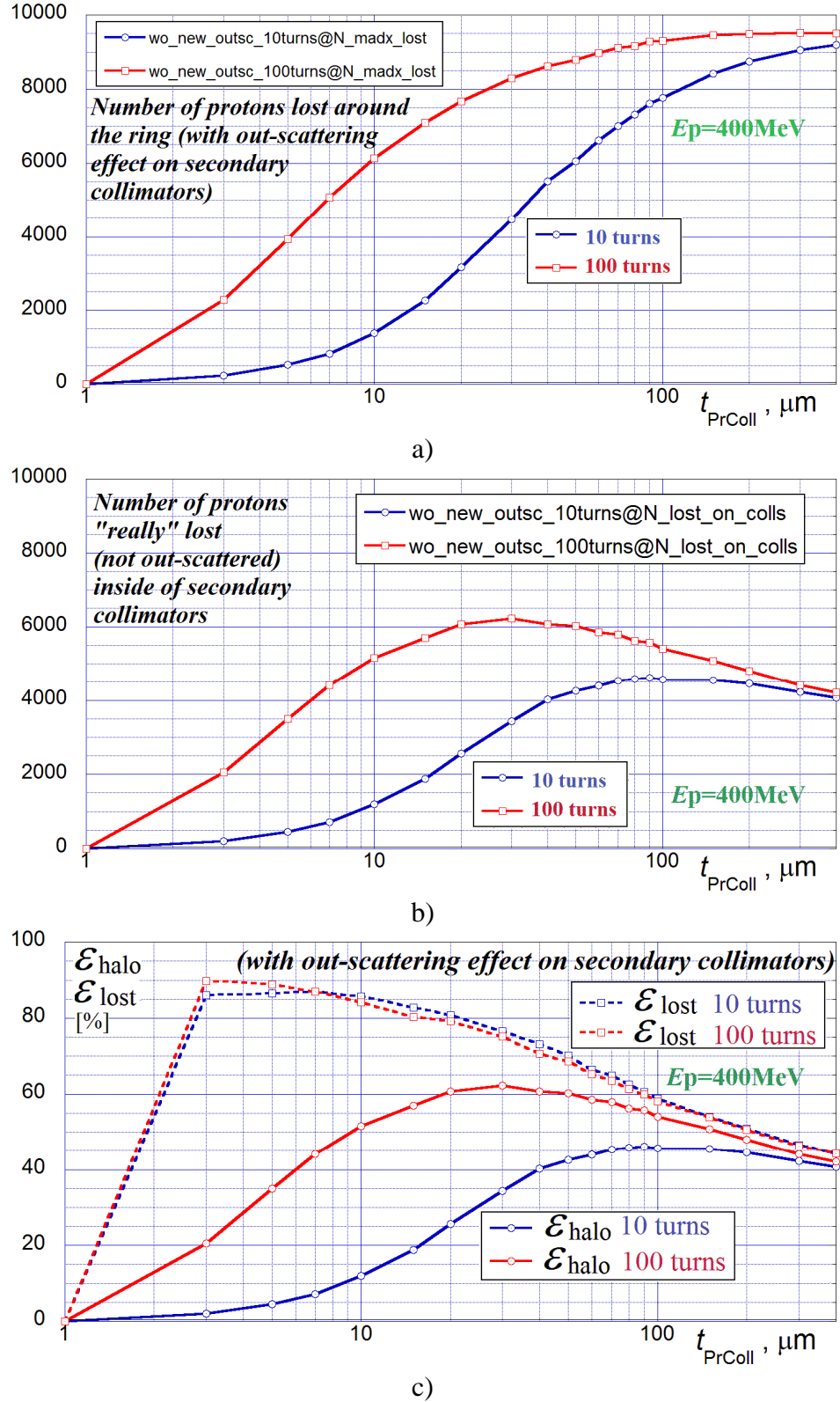


Figure 3.40: The simulation results by MADX and MARS tracking with the out-scattering effects after 10 (blue) and 100 turns (red) for the 2SC in vertical plane for pure 1D-configuration: a)  $N_{\text{lost}}$  vs  $t_{\text{PrColl}}$ ; b)  $N_{\text{SecColl}}$  vs  $t_{\text{PrColl}}$ ; c)  $\mathcal{E}_{\text{halo}}$  and  $\mathcal{E}_{\text{lost}}$  vs  $t_{\text{PrColl}}$ .

Table 3.5 Comparison numerical simulations with analytical evaluations for vertical 2SC

$t_{\text{PrColl}}$ , $\mu\text{m}$	analytical $L_{\text{1st-turn}}^{\text{total}} \div L_{\infty-\text{turn}}^{\text{total}}$	numerical $L_{\text{10-turn}}^{\text{total}} \div L_{\text{100-turn}}^{\text{total}}$	analytical $\mathcal{E}_{\text{halo}}^{\text{1st-turn}} \div \mathcal{E}_{\text{halo}}^{\infty-\text{turn}}$	numerical $\mathcal{E}_{\text{halo}}^{\text{10-turn}} \div \mathcal{E}_{\text{halo}}^{\text{100-turn}}$	analytical $\mathcal{E}_{\text{lost}}^{\text{1st-turn}} \div \mathcal{E}_{\text{lost}}^{\infty-\text{turn}}$	numerical $\mathcal{E}_{\text{lost}}^{\text{10-turn}} \div \mathcal{E}_{\text{lost}}^{\text{100-turn}}$
i	ii	iii	iv	v	vi	vii
10	6÷13 %	17÷77 %	6.3÷13 %	15÷65 %	100÷100 %	87 %
50	33÷53 %	67÷97 %	27÷46 %	50÷70 %	80÷87 %	67÷68 %
400	74÷84 %	97÷100 %	30÷41 %	45÷47 %	43÷49 %	43÷47 %

Note, that the total losses  $L_{\infty-\text{turn}}^{\text{total}}$  and  $L_{\text{10-turns}}^{\text{total}}$ , and collimation efficiencies  $\mathcal{E}_{\text{halo}}^{\infty-\text{turn}}$  and  $\mathcal{E}_{\text{halo}}^{\text{10-turn}}$  are very close to each other for all foil thickness, while  $\mathcal{E}_{\text{lost}}^{\infty-\text{turn}}$  and  $\mathcal{E}_{\text{lost}}^{\text{10-turn}}$  are quite different for 10  $\mu\text{m}$  and 50  $\mu\text{m}$ . Thus, the collimation efficiency  $\mathcal{E}_{\text{halo}}$  provides well-predictable and understandable results based on usage of clear linear dynamics. Therefore, it will be used as figure of merit of the collimations system.

In contrary, as it was discussed above, the collimation efficiency  $\mathcal{E}_{\text{lost}}$  ignores escaped protons and may provide misleading results for our studies. Nevertheless, the collimation efficiency  $\mathcal{E}_{\text{lost}}$  will be shown on next plots for illustrations.

Now let's consider the simulation results shown in Fig. 3.40. These simulations take into account the out-scattering effect in absorbers and only absorbed protons  $N_{\text{SecColl}}$  are included into  $N_{\text{lost}}$ . The out-scattered protons are ignored in the presented counting of the collimation efficiency, since their behavior is uncontrollable. Figure 3.40,a shows the total number of protons lost around the ring  $N_{\text{lost}}$  versus  $t_{\text{PrColl}}$ . Figure 3.40,b shows dependence of  $N_{\text{SecColl}}$  on  $t_{\text{PrColl}}$ . The 10-turn curve has a maximum at  $t_{\text{PrColl}} \sim 90 \mu\text{m}$ , and the 100-turn curve has a maximum at  $t_{\text{PrColl}} \sim 30 \mu\text{m}$ .

Figure 3.40,c shows both collimation efficiencies as a function of the foil thickness  $t_{\text{PrColl}}$ . The  $\mathcal{E}_{\text{lost}}$ -curves at 10 and 100 are overlapped, *i.e.*  $\mathcal{E}_{\text{lost}}$  does not depend on number of turns if it  $> 10$ .  $\mathcal{E}_{\text{lost}}$  have maximum values  $\mathcal{E}_{\text{lost}} \sim 90\%$  at  $t_{\text{PrColl}} < 10 \mu\text{m}$ . However, less than a half of halo protons are lost on absorbers after 100 turns (see Fig. 3.40,b), and the efficiency  $\mathcal{E}_{\text{halo}} < 50\%$  at  $t_{\text{PrColl}} < 10 \mu\text{m}$ .

Our simulation model assumes non-variable parameters of a Booster like storage ring. On the other hand, trajectories of scattered halo particles in the Booster can be essentially distorted due to variations of beam energy and central orbit, and other fluctuating parameters. It is not known how many turns can be considered as "frozen". Let's assume that several tens of turns have "frozen" conditions. The optimal thickness of Cu foil for several tens of turns is around 50  $\mu\text{m}$ . Therefore, following our simulation results and to ensure the mechanical rigidity of the primary foils construction, an equivalent Al foil with thickness of 380  $\mu\text{m}$  has been installed in 2015 [45].

Presented results suggest [84]: a) if "frozen" conditions in the Booster exist for more than 100 turns, then the 2SC efficiency  $\mathcal{E}_{\text{halo}} > 60\%$ ; b) if the beam halo size is small  $\leq 10 \mu\text{m}$ , the absorption efficiency of 1SC, is also small  $\mathcal{E}_{\text{abs}} < 55\%$ ; c) Under the above conditions "a" & "b" the 2SC system could be more effective than the 1SC system with 10 %.

However, it looks to be too optimistic hope that the "frozen" condition could be preserved over 100 turns. Moreover, the simulated turn-by-turn accumulation of  $\mathcal{E}_{\text{halo}}$  relies on the initially escaped protons, which could be intercepted by secondary collimators after many turns, if their amplitudes are increased due to some imperfections, *e.g.*, non-linear fields and distorted  $\beta$ -functions. This process is uncontrollable and its parameters look to be unpredictable. Therefore, the reliable values of the collimation efficiency for the Booster 2SC system could be simulated maximum within several tens of turns. This means that the collimation efficiency that the Booster 2SC system is about  $\mathcal{E}_{\text{halo}} \sim 45\%$ . This value is lower than the absorption efficiency of single well-aligned secondary collimator operating in a conventional 1SC mode.

### 3.5.4.2 Simulation of 2SC in vertical plane with full 2D-configuration

In previous paragraph the simulation results for pure classical 2SC schemes has been presented. Here, we present the simulation results for the 2004 design scheme (see Fig. 2.17) which involve all three secondary collimators, while use all available vertical and horizontal jaws. Figure 3.41 shows the transverse positions of collimators used. Let's name this configuration as "a full 2D-configuration".

coll mode	H-Prim	V-Prim	Col1=L6A=SHCOL1	Col2=L6B=SVCOL1	Col3=L7A=SHVCOL2	Reference			
	halo_xsign at hprim	halo_ysign at vprim	halo_xsign at shcoll	halo_ysign at shcoll	halo_xsign at svcoll				
2.5x	0 (garage)	-1 (down)	+1 (wall)	+1(up)	-1(aisle)	-1(down)	-1(aisle)	+1(up)	

Figure 3.41: The transverse positions of collimators used for simulations of the 2SC in vertical plane for full 2D-configuration, corresponding to the 2004 design with using all vertical and horizontal jaws of all three secondary collimators.

Figure 3.42 shows the simulation results for the 2SC in vertical plane for full 2D-configuration, while the out-scattering effects are included via usage the MARS code. The dependencies on the thickness of the copper primary collimator  $t_{\text{PrColl}}$  are shown for both collimation efficiencies  $\epsilon_{\text{halo}}$  and  $\epsilon_{\text{lost}}$ . The vertical black lines illustrate the foil thicknesses corresponding to the 2004 design, to the old foil existed till 2014, and new foil installed in 2015.

The collimation efficiency  $\epsilon_{\text{lost}}$  demonstrate the best values for the thinnest  $\sim 12 \mu\text{m}$  foil. However, these values are misleading since proton losses<sup>15</sup> are too low, e.g.  $\sim 25\%$  after 100 turns and  $\sim 65\%$ . Such multi-turn accumulation of the beam losses is related to the losses of the initially escaped protons.

The collimation efficiency  $\epsilon_{\text{halo}}$  for the thinnest  $\sim 12 \mu\text{m}$  foil is rather small after 10 turns and could reach up to 65 % during uncontrollable and conditional multi-turn interception of the initially escaped protons. The collimation efficiency  $\epsilon_{\text{halo}}$  for the thickest  $\sim 400 \mu\text{m}$  foil (old foil before 2014) is equal to  $\epsilon_{\text{halo}} = 60\%$ , while it is the same for 10 and 100 turns, since scattered protons are mainly lost under deterministic conditions of linear dynamics during the first pass.

The collimation efficiency  $\epsilon_{\text{halo}}$  for the new  $380 \mu\text{m}$  Al foil equivalent to  $\sim 50 \mu\text{m}$  Cu foil is between maximum values for 10-turn  $\epsilon_{\text{halo}}$ -curve and 100-turn  $\epsilon_{\text{halo}}$ -curve. It could reach  $\epsilon_{\text{halo}} = 57\%$  after 10 turns and  $\epsilon_{\text{halo}} = 75\%$  after 100 turns. However, the value of  $\epsilon_{\text{halo}} = 57\%$  after 10 turns is considered to be reliable, while the value  $\epsilon_{\text{halo}} = 75\%$  after 100 turns is doubtful, because it is relying on a hope about a stable almost linear beam dynamics within the Booster aperture.

Figure 3.43 shows the loss distribution after 100 turns along of 16 selected intervals. These losses include the losses of the out-scattered protons, which were tracked with MADX after tracking MARS tracking within every secondary collimator. The schematic layout of the collimation system shown below explains locations of these 16 intervals.

Considerable losses happens within  $\sim 25 \text{ m}$  region on the intervals with numbers 7 (D magnet in front of absorber 6A), 8 (absorber 6A), 9 (pipes between absorbers 6A and 6B), 10 (absorber 6B), 11 (four gradient magnets around short 6), 12 (absorber 7A), and 13 (beam pipes on Long 7 behind absorber 7A), while losses in intervals 8, 10, 12 are useful, while losses of the rest intervals are worse.

<sup>15</sup> Number of losst particles could be directly derived from the  $\epsilon_{\text{halo}}$ -curves.

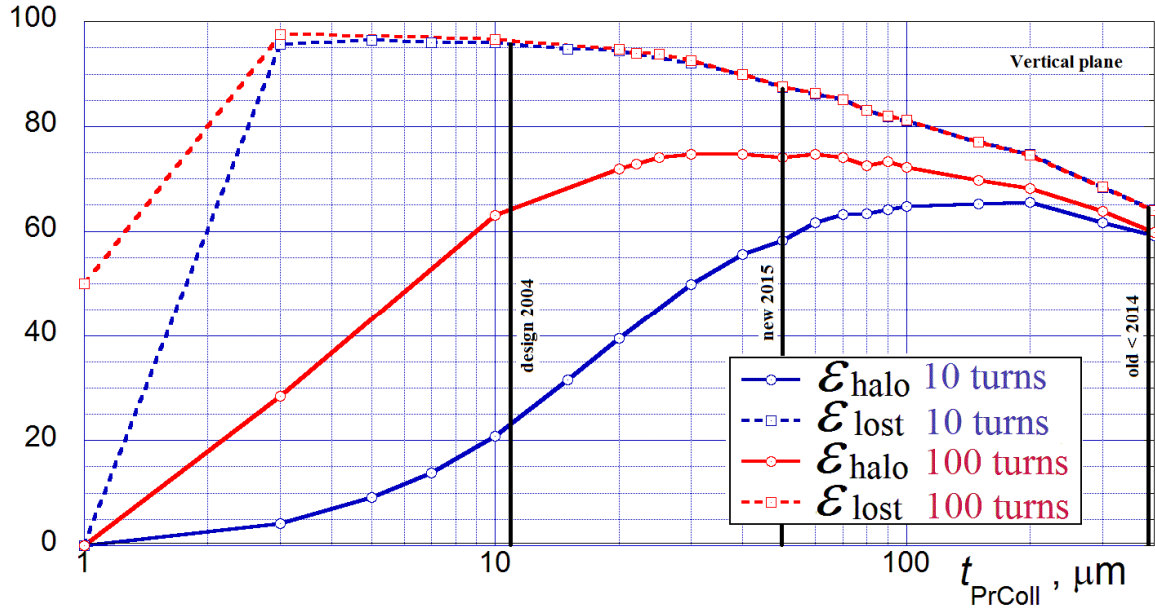


Figure 3.42: The collimation efficiencies  $\epsilon_{\text{halo}}$  and  $\epsilon_{\text{lost}}$  vs the thickness of copper primary collimator  $t_{\text{PrColl}}$  for the 2SC in vertical plane for full 2D-configuration after 10 (blue) and 100 turns (red) with accounting for the out-scattering effects.

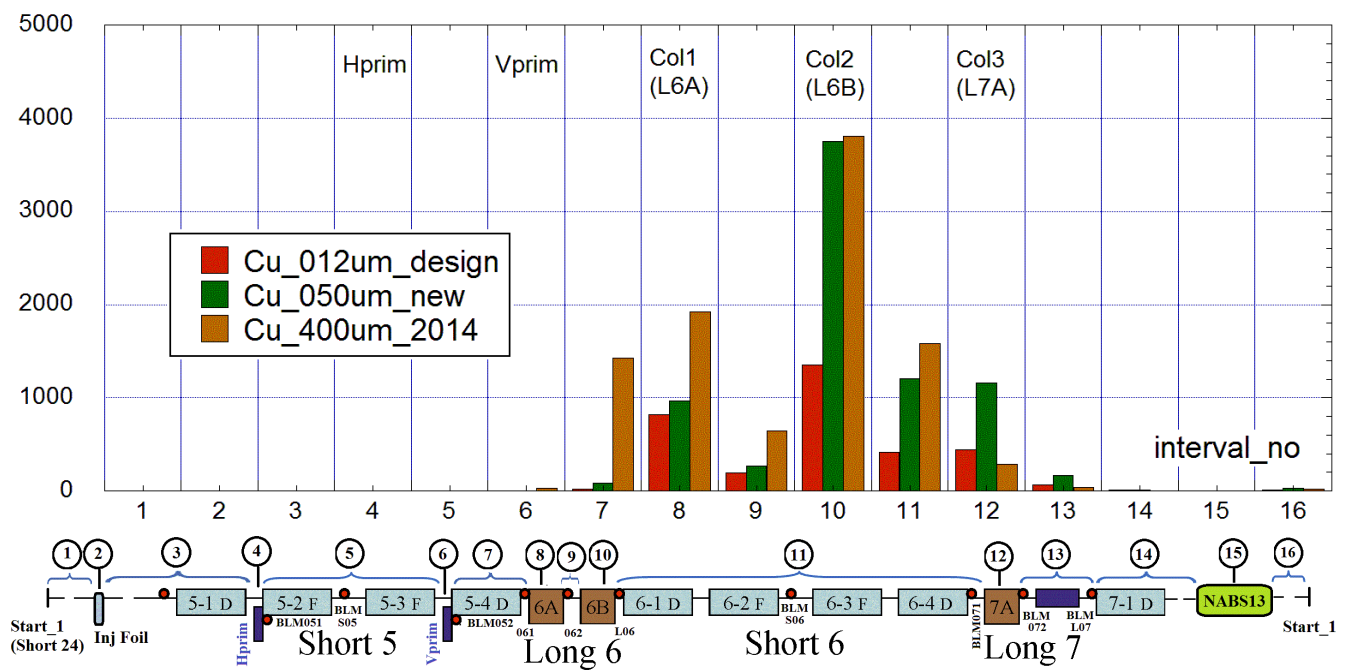
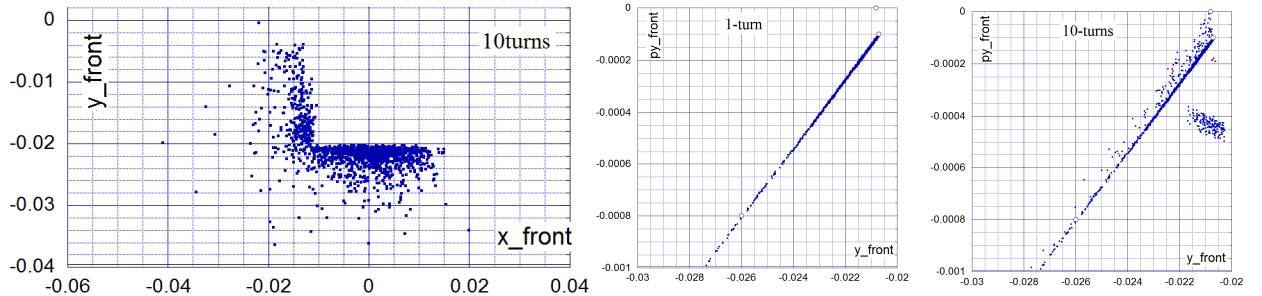
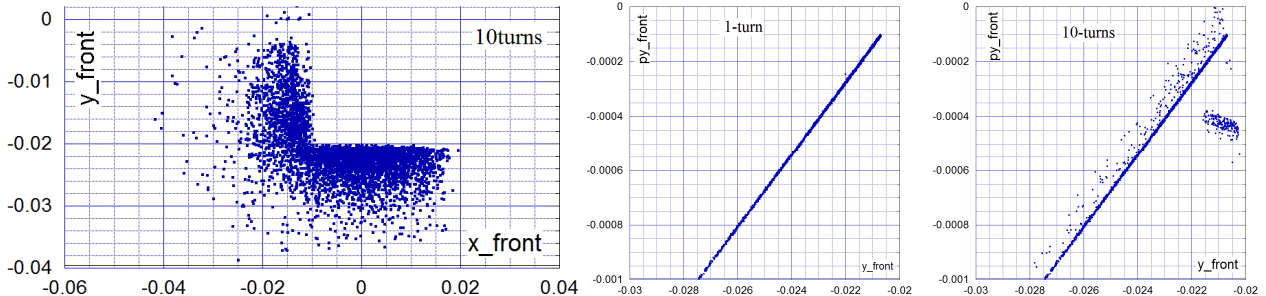


Figure 3.43: The loss distribution for the 2SC in vertical plane for full 2D-configuration after 100 turns along of 16 selected intervals shown below in schematic layout of the collimation system.

Figure 3.44 shows the phase spaces ( $x, y$ ) and ( $y, y'$ ) of the lost particles at the front of COL2 (6B) for the 12  $\mu\text{m}$  and 50  $\mu\text{m}$  (b) primary collimator foils, while the ( $y, y'$ ) is shown twice after the first pass and after 10 turns.



a) the  $12 \mu\text{m}$  Cu primary collimator foil



b) the  $50 \mu\text{m}$  Cu primary collimator foil

Figure 3.44: Phase spaces of the lost particles lost at the front of COL2 (6B) for simulations of the 2SC in vertical plane for full 2D-configuration.

It can be seen that lost protons are located far from the boundaries of the collimator jaws for the  $50 \mu\text{m}$  foil than for the  $12 \mu\text{m}$ , *i.e.* the impact parameter for the thicker foil is higher. In the phase space ( $y$ ,  $y'$ ) the particles are located along the thin lines, *i.e.* the coordinates  $y$  and  $y'$  are strongly connected between each other in order to hit in the same point of the absorber. After 10 turns the thin line is smeared, while some additional target spot is appeared. It looks like precise and fine hitting of the target, which could be easily simulated numerically, but probably could be destroyed in a real machine.

Figure 3.44 shows the distributions of the lost particles along the vertical direction. The distribution is considerably wider for the  $50 \mu\text{m}$  foil (a) than for the  $12 \mu\text{m}$  foil. The dependence on an error of the vertical position shown in Figure 3.44,c for the  $12 \mu\text{m}$  foil demonstrates a high sensitivity, e.g. 20 % of particles will fail to hit absorber at position error of  $600 \mu\text{m}$ .

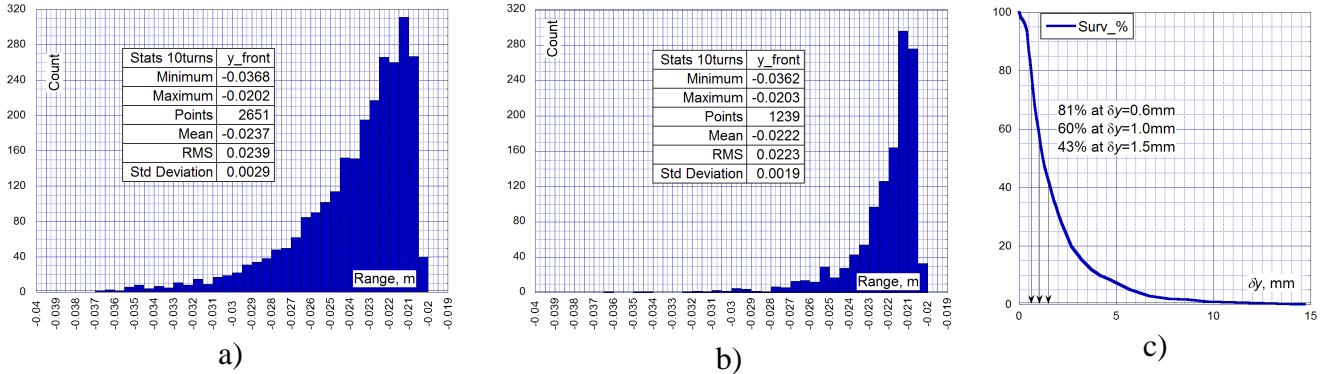


Figure 3.45: Distribution of the lost particles at the front of COL2 (6B) for simulations of the 2SC in vertical plane for full 2D-configuration: a) the distribution for  $50 \mu\text{m}$  Cu foil; b) the distribution for  $12 \mu\text{m}$  Cu foil; c) dependence on an error of the vertical position of the collimator jaw.

Figure 3.46,a shows the accumulations of the collimation efficiency  $\epsilon_{\text{halo}}$  during 300 turns. It is seen that for the thick 400  $\mu\text{m}$  cooper foil (equivalent of old foil existed before 2014) the final efficiency  $\epsilon_{\text{halo}} \sim 60\%$  is reached during the first pass. The new 50  $\mu\text{m}$  copper foil (equivalent of new 380  $\mu\text{m}$  Al foil) reaches the efficiency  $\epsilon_{\text{halo}} \sim 40\%$  after the first pass and then  $\epsilon_{\text{halo}}$  is monotonically increased reaching its final value  $\epsilon_{\text{halo}} \sim 75\%$  during 100 turns. For the thinnest 12  $\mu\text{m}$  copper foil (equivalent of 2004 design) the first pass efficiency is very low  $\epsilon_{\text{halo}} \sim 75\%$ . Then, the efficiency slowly approaches to the efficiency of new 50  $\mu\text{m}$  copper foil and reaches  $\epsilon_{\text{halo}} \sim 75\%$  by 250 turn. Remind again, that this turn-by-turn efficiency accumulation process is mainly related to the losses of the initially escaped from 2SC system protons. These losses are driven by the non-linear fields and other imperfections, which depend on regime of the Booster operations.

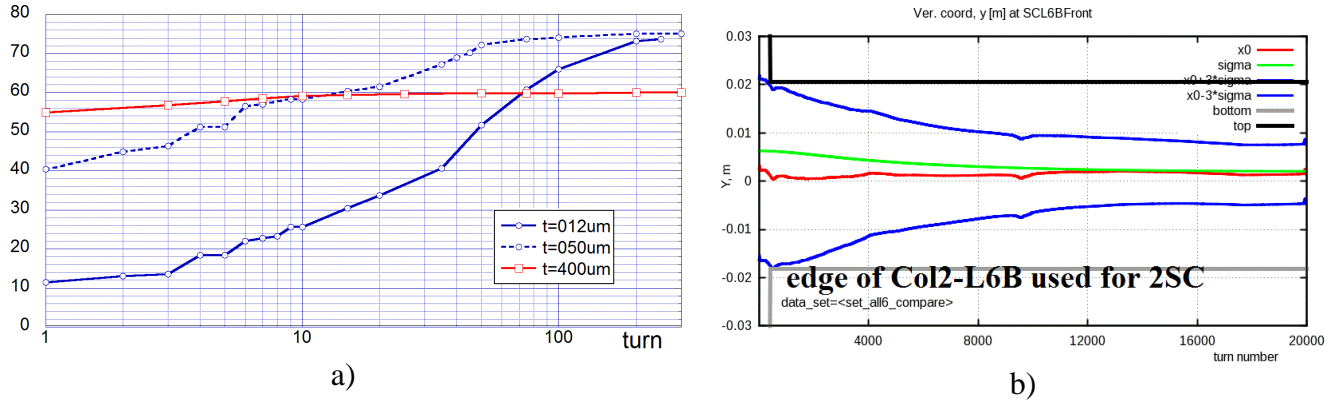


Figure 3.46: On a feasibility of ideal simulation conditions: a) accumulations of the collimation efficiency during 300 turns for simulations of the 2SC in vertical plane for full 2D-configuration; b) ideal  $3\sigma$ -beam envelope around measured closed orbit with shown edge of the collimator COL2 (6B).

Figure 3.46,b shows the ideal (damping as  $\sim 1/\beta\gamma$ )  $3\sigma$ -beam envelope on the top of measured closed orbit and edge of the collimator COL2 (6B). For effective turn-by-turn accumulation of collimation efficiency  $\epsilon_{\text{halo}}$  routinely obtained via numerical simulations, it is necessary to preserve the trajectories on the top of the beam envelope during several tens of turns. Probably, for unsteady machine like the Booster such requirement looks to doubtful and could not to serve as a background idea for the design of 2SC system

### 3.5.5 Simulations for Two Stage Collimation in Horizontal Plane

The 2004 design scheme (see Fig. 2.17) involving all three secondary collimators and using all available vertical and horizontal jaws has been also used for the simulations of the 2SC in the horizontal direction. Figure 3.47 shows the transverse positions of collimators used. Let's name this configuration as "a full 2D-configuration". The positions of all secondary collimators relatively the beam are the same as for 2SC in the vertical direction shown in Fig. 3.41, and only positions of the primary collimators are different. Now, the vertical primary collimator is located in a garage position, and the horizontal primary collimator touch the beam core from the wall side.

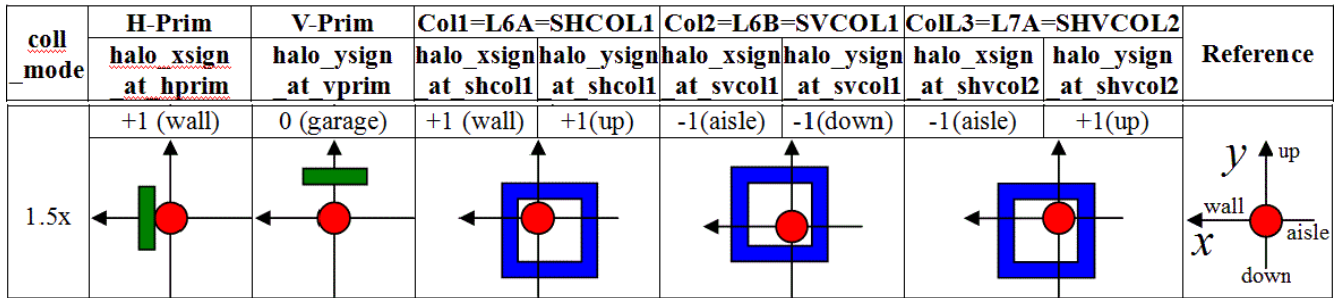


Figure 3.47: The transverse positions of collimators used for simulations of the 2SC in horizontal plane for full 2D-configuration, corresponding to the 2004 design with using all vertical and horizontal jaws of all three secondary collimators.

Figure 3.48 shows the simulation results for the 2SC in horizontal plane for the full 2D-configuration, while the out-scattering effects are included via usage the MARS code. The dependencies on the thickness of the copper primary collimator  $t_{\text{PrColl}}$  are shown for both collimation efficiencies  $\epsilon_{\text{halo}}$  and  $\epsilon_{\text{lost}}$ .

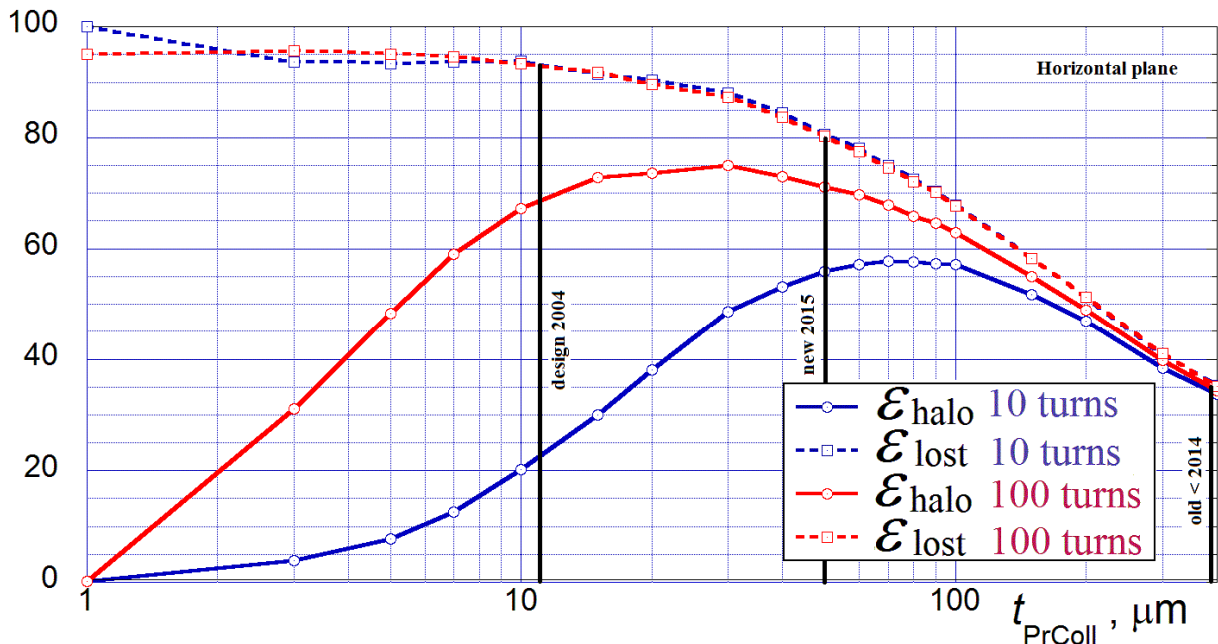


Figure 3.48: The collimation efficiencies  $\epsilon_{\text{halo}}$  and  $\epsilon_{\text{lost}}$  vs the thickness of copper primary collimator  $t_{\text{PrColl}}$  for the 2SC in horizontal plane for full 2D-configuration after 10 (blue) and 100 turns (red) with accounting for the out-scattering effects.

The vertical black lines illustrate the foil thicknesses corresponding to the 2004 design, to the old foil existed till 2014, and new foil installed in 2015. The collimation efficiency  $\epsilon_{\text{lost}}$  demonstrate the best values for the thinnest  $\sim 12 \mu\text{m}$  foil. However, these values are misleading since proton losses<sup>16</sup> are too low, e.g.  $\sim 25\%$  after 100 turns and  $\sim 65\%$ . Such multi-turn accumulation of the beam losses is related to the losses of the initially escaped protons.

The collimation efficiency  $\epsilon_{\text{halo}}$  for the thinnest  $\sim 12 \mu\text{m}$  foil is rather small after 10 turns and could reach up to 70 % during uncontrollable and conditional multi-turn interception of the initially escaped protons. The collimation efficiency  $\epsilon_{\text{halo}}$  for the thickest  $\sim 400 \mu\text{m}$  foil (old foil before 2014) is very low  $\epsilon_{\text{halo}}=35\%$ , while it is the same for 10 and 100 turns, since scattered protons are mainly lost under deterministic conditions of linear dynamics during the first pass.

The collimation efficiency  $\epsilon_{\text{halo}}$  for the new  $380 \mu\text{m}$  Al foil equivalent to  $\sim 50 \mu\text{m}$  Cu foil is between maximum values for 10-turn  $\epsilon_{\text{halo}}$ -curve and 100-turn  $\epsilon_{\text{halo}}$ -curve. It could reach  $\epsilon_{\text{halo}}=55\%$  after 10 turns and  $\epsilon_{\text{halo}}=70\%$  after 100 turns. However, the value of  $\epsilon_{\text{halo}}=55\%$  after 10 turn is considered to be reliable, while the value  $\epsilon_{\text{halo}}=70\%$  after 100 turns is doubtful, because it is relying on a hope about a stable almost linear beam dynamics within the Booster aperture.

Figure 3.49 shows the loss distribution after 100 turns along of 16 selected intervals. These losses include the losses of the out-scattered protons, which were tracked with MADX after tracking MARS tracking within every secondary collimator. The schematic layout of the collimation system shown below explains locations of these 16 intervals.

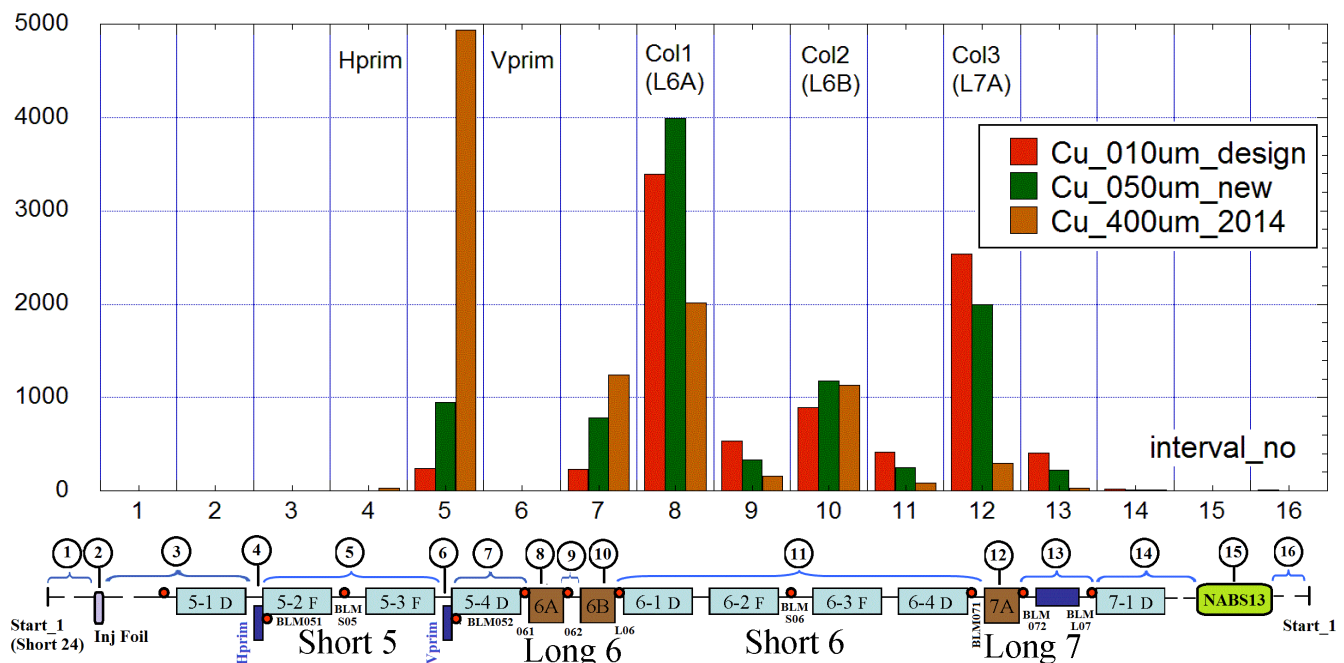


Figure 3.49: The loss distribution for the 2SC in horizontal plane for full 2D-configuration after 100 turns along of 16 selected intervals shown below in schematic layout of the collimation system.

Considerable losses happens within  $\sim 30 \text{ m}$  region on the intervals with numbers 5 (two F magnets at Short 5) 7 (D magnet in front of 6A), 8 (absorber 6A), 9 (pipes between 6A and 6B), 10 (absorber 6B), 11 (four gradient magnets near Short 6), 12 (absorber 7A), and 13 (pipes on Long 7 behind 7A), while losses in intervals 8, 10, 12 are useful, while losses of the rest intervals are worse. We don not see an essential difference between results for 2SC in the horizontal and vertical planes.

<sup>16</sup> Number of losst particles could be directly derived from the  $\epsilon_{\text{halo}}$ -curves.

## 4. Alternative Scheme with Thick Primary Collimator

From our analytical evaluations and numerical simulations of the Booster 2SC system it is clear that main limiting factor for the collimation efficiency is the aperture restrictions in gradient magnets near the collimation region. Therefore, an alternative scheme when the primary collimators are in front of the secondary collimators in long straight section 6 has been suggested. The results of numerical simulation have showed promising results. The proposal of an alternative scheme for the Booster 2SC system has been presented by V. Kapin in February, 2017 [86].

Simulation technique has been based on already developed approach and software for the existing 2SC system. Figure 4.1 shows stimulation layout for the new alternative version of the 2SC system. It has a minimal difference from the layout of the existing 2SC system shown in Fig. 2.4. Presently, the distance between absorbers 6A and 6B is about 1.6 m (see Fig. 3.23). Firstly, in order to have more space for the primary collimators, the absorber 6A is supposed to be shifted by 1 m close to the absorber 6B reducing the distance between absorbers 6A and 6B to 0.6 m. Secondly, both primary collimators has been moved in Long 6 and set at the longitudinal position corresponding to the previous position of the absorber 6A front end.

According to the sketch in Figure 4.1, the positions of the horizontal and vertical primary collimators are quite different, but for numerical simulations it was assumed that they are located approximately at the same position.

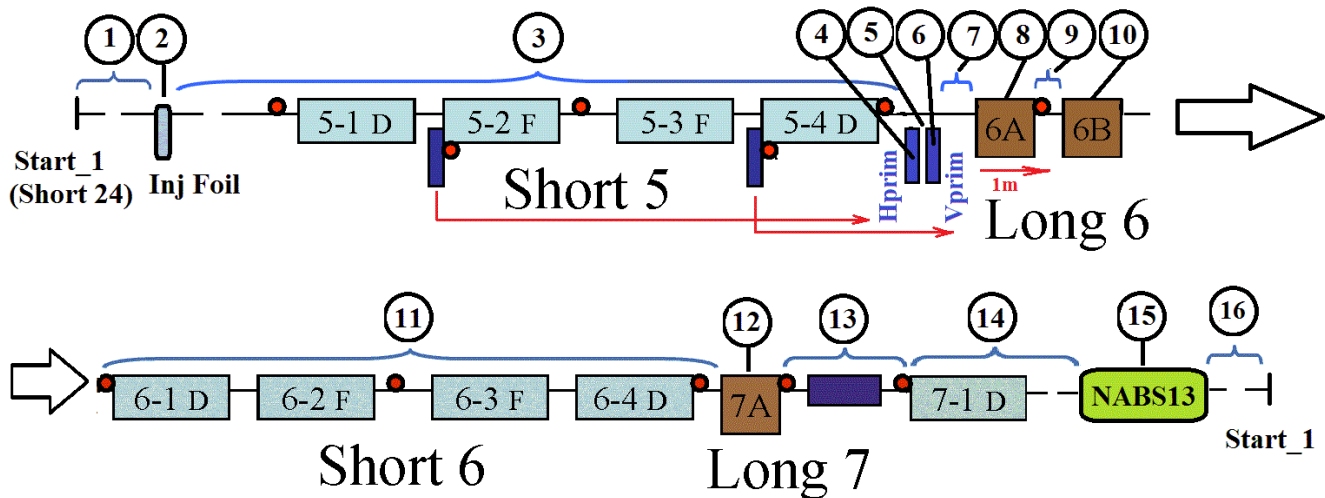


Figure 4.1: The layout of the new 2SC system used in simulations. The new locations of 16 intervals for the loss distribution plots are also presented.

Figure 4.2 shows the simulation results with MADX and MARS codes for the new alternative 2SC scheme after only single pass. In this chapter, the plots for collimation in the horizontal plane will be presented. The plots for collimation in the vertical plane are very similar even quantitatively and therefore they will be omitted.

In these calculations, only losses on the secondary collimators are considered to be useful similar to assumptions used before for the existing 2SC system. It is seen that for a quite this copper scatterer  $\sim 1\text{cm}$  up to 95% of particles lost during the first turn. The collimation efficiency achieves its maximum value  $\epsilon_{\text{halo}}=75\%$  at the thickness of 4mm. Thus, the new 2SC system has the same value of the maximum collimation efficiency  $\epsilon_{\text{halo}}=75\%$  as existing 2SC system. However, this value is reached by the new system during a single pass throughout the collimation region, while for the existing 2SC system the maximum values of  $\epsilon_{\text{halo}}=75\%$  is theoretical limit achievable after 100 turns.

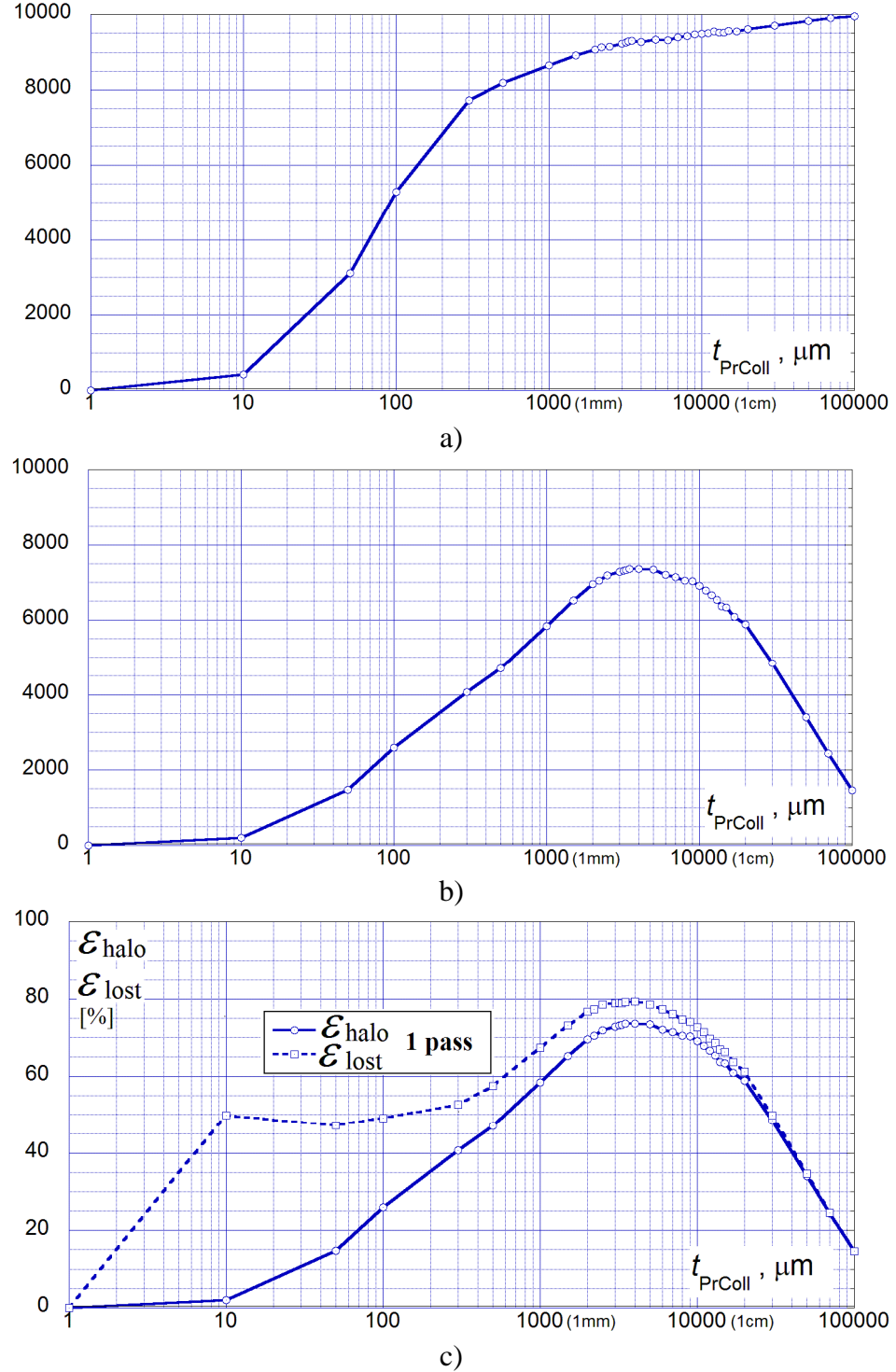


Figure 4.2: The simulation results for the new alternative 2SC scheme after 1 turn by MADX and MARS tracking with the out-scattering effects and copper primary collimator: a)  $N_{\text{lost}}$  vs  $t_{\text{PrColl}}$ ; b)  $N_{\text{SecColl}}$  vs  $t_{\text{PrColl}}$ ; c)  $\mathcal{E}_{\text{halo}}$  and  $\mathcal{E}_{\text{lost}}$  vs  $t_{\text{PrColl}}$ .

Thus, the new 2SC system could have the same maximum value of the collimation efficiency as existing system, and it does not require a stable multi-turn optics as existing system. Moreover, the new system could reach even higher collimation efficiency, if some modification can be performed.

Let's outlook some possible improvements of the new 2SC system. Figure 4.3 shows losses on primary collimator and sum of losses on primary and all secondary collimators. In initial simulation

model for the new 2SC system, the primary collimators have no any radiation shielding and beam losses on the primary collimator are considered to be undesirable. Let's assume that primary collimators may have some shielding. Then, the beam losses on the primary collimator could be treated as "useful" in computations of the collimation efficiency.

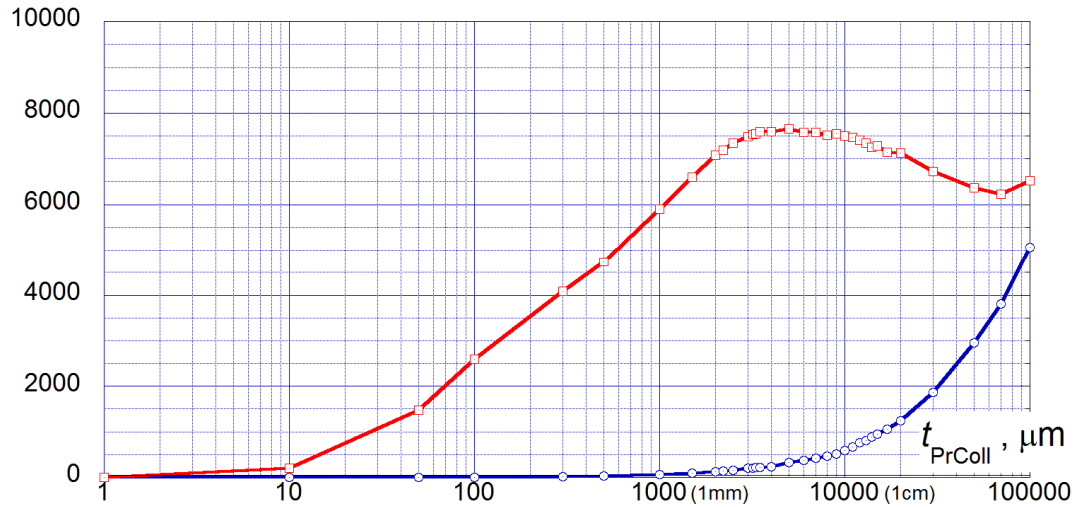


Figure 4.3: Losses on primary collimator (blue) and sum of losses on primary and three secondary collimators (red) for the new alternative 2SC scheme vs the primary foil thickness  $t_{\text{PrColl}}$ .

Figure 4.4 shows improved collimation efficiency for the new 2SC system with a shielded primary collimator. The  $\epsilon_{\text{halo}}$ -curve for non-shielded primary collimator is also shown for reference. The  $\epsilon_{\text{halo}}$ -curve for non-shielded primary collimator is the same as the  $\epsilon_{\text{halo}}$ -curve shown in Figure 4.2,c.

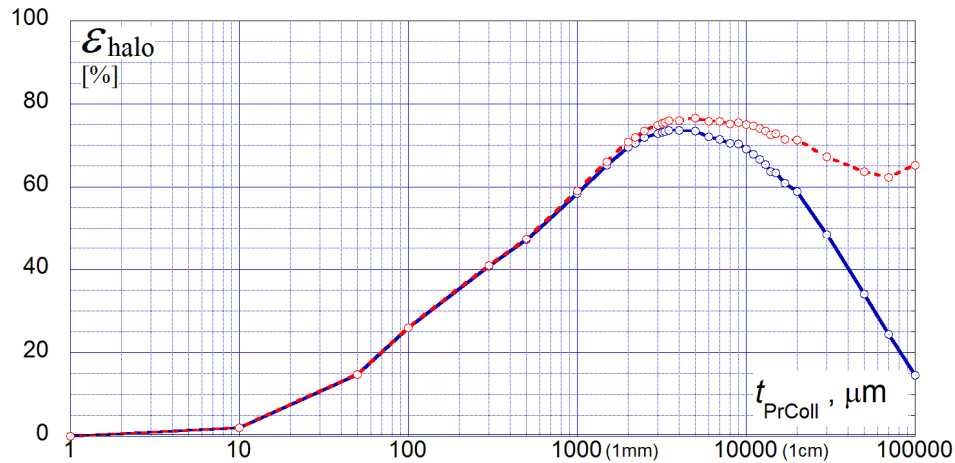


Figure 4.4: The collimation efficiency  $\epsilon_{\text{halo}}$  vs  $t_{\text{PrColl}}$  for the case of well-shielded primary collimator (red) and for the case of non-shielded primary collimator (blue).

In existing 2SC collimation system all beam pipes connecting absorbers are non-shielded (see Fig.3.23 and Fig. 3.24). However, there are can be large beam losses on them in the new 2SC system. Figure 4.5 shows losses on non-shielded intervals (Fig. 4.1) between collimators: a) the interval no. 6 covers the vacuum enclosure of the vertical primary collimator located downstream from the horizontal primary collimator; b) the interval no. 7 covers beam pipe between primary collimators and the

absorber 6A; c) the interval no.9 covers the beam pipe between the absorbers 6A and 7A; d) the interval no.11 covers a long region between absorbers 6B and 7A, which contains 4 gradient magnets, beam pipes and corrector packages. The very high beam losses exists in intervals 7 and 11.

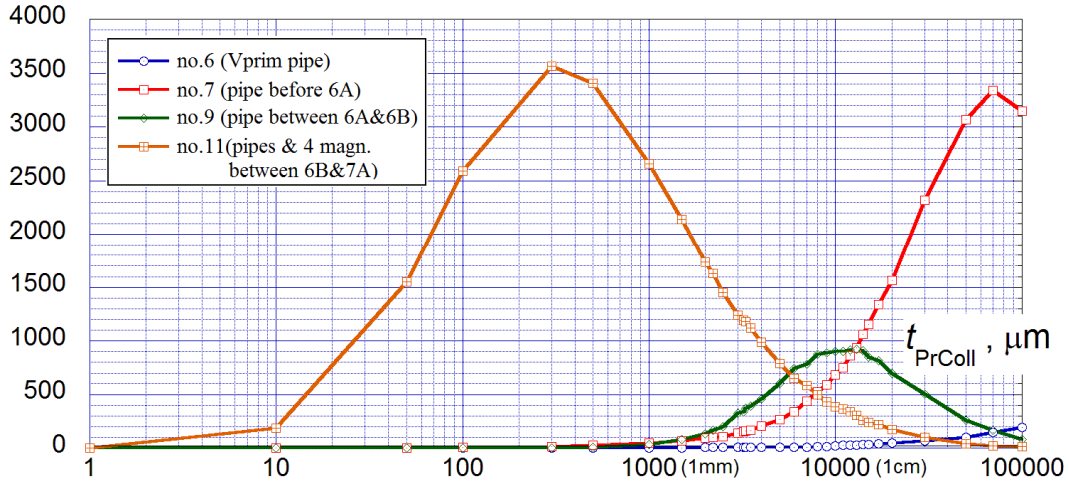


Figure 4.5: Losses on unshielded beam pipes and magnets within the shown in Fig. 4.1 intervals 6, 7, 9, 11 vs the primary foil thickness  $t_{\text{PrColl}}$ .

Let's imagine that existing 6" beam pipes in the collimation area are replaced by the enlarged pipes in order to minimize beam losses on their apertures. In our simulations, the beam pipes with 1 m-diameter are used. In reality, it will be enough to use a well-shielded  $\sim 15 \div 20$ " pipes. Thus, the beam losses in the shielded beam pipes could be counted as useful. Figure 4.6 shows the dependencies  $\varepsilon_{\text{halo}}$  vs  $t_{\text{PrColl}}$  for enlarged beam pipes and for existing 6" pipes.

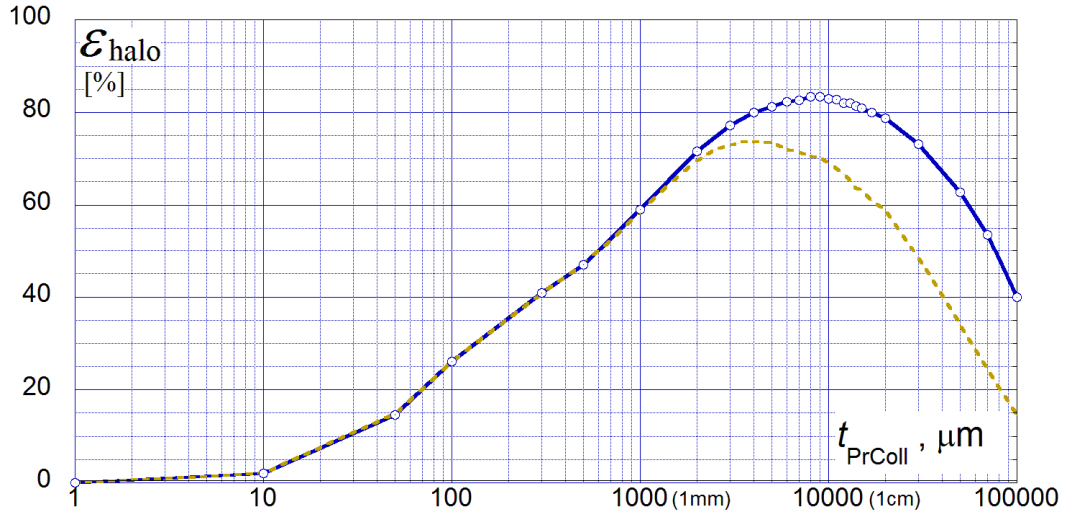


Figure 4.6: The collimation efficiency  $\varepsilon_{\text{halo}}$  vs  $t_{\text{PrColl}}$  for enlarged beam pipes between collimators (blue) and for existing 6" pipes (brown)

The maximum value of  $\varepsilon_{\text{halo}}$  reaches 83% and the optimal thickness of the primary collimator  $t_{\text{PrColl}}$  is shifted from 4mm to  $\sim 8$ mm. Figure 4.7 shows a further improvement of the collimation efficiency, if the primary collimator enclosure will be also well shielded. In this case, the

collimation efficiency is higher 90% in a wide range of the primary collimator thickness  $t_{\text{PrColl}} = 1 \div 10 \text{ cm}$ , while the maximum value of  $\epsilon_{\text{halo}}$  is about 93 % at  $t_{\text{PrColl}} = 5 \text{ cm}$ .

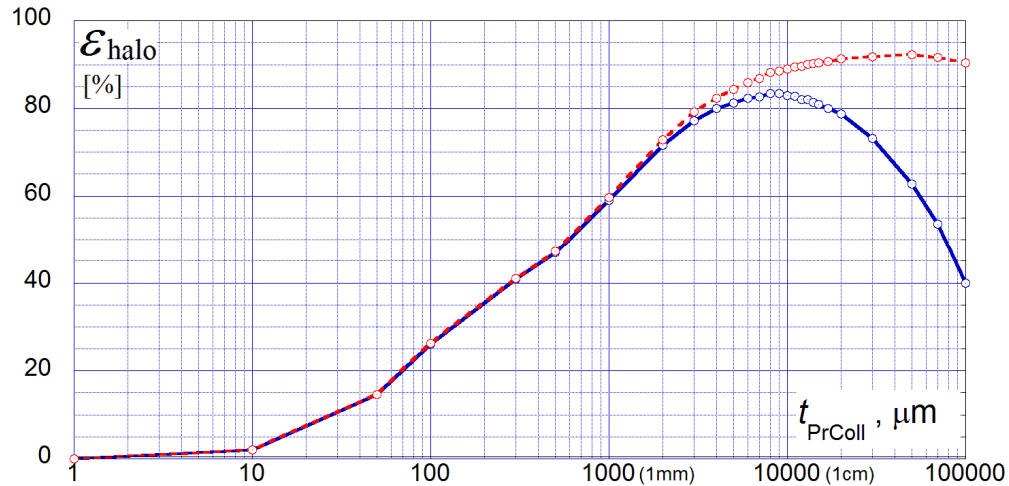


Figure 4.7: The collimation efficiency  $\epsilon_{\text{halo}}$  vs  $t_{\text{PrColl}}$  for enlarged beam pipes between collimators (blue) and for well-shielded primary collimators (red)

Figure 4.8 shows particle losses on beam pipes and magnets for the case of enlarged diameters of the inter-collimator beam-pipes. In comparison with the case with existing 6"-pipes shown in Fig. 4.5 the beam loss curves on the intervals no. 7 and no. 9 have essentially reduced maximum values, while the beam loss curve on the interval no. 11 is not changed. Let's consider the range of the primary collimator thickness  $t_{\text{PrColl}} = 1 \div 10 \text{ cm}$  with high values of  $\epsilon_{\text{halo}}$ . In this range of the thickness  $t_{\text{PrColl}}$ , the losses on the interval no. 11 are decreasing from 4% till 0% with an increase of the primary collimator thickness  $t_{\text{PrColl}}$ . Thus, the beam losses on all inter-collimator beam-pipes are less 5% in the range of the primary collimator thickness  $t_{\text{PrColl}} = 1 \div 5 \text{ cm}$ , while the collimation efficiency is higher 90%.

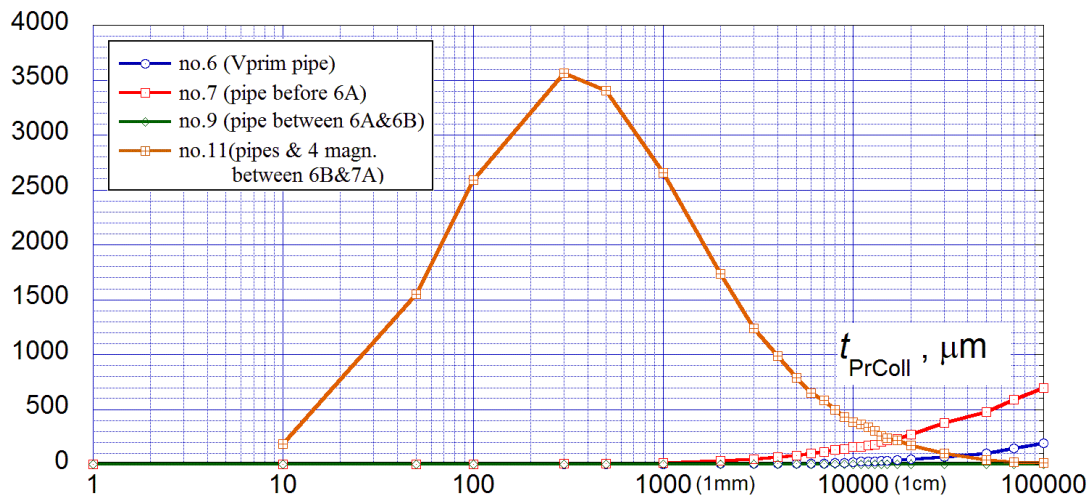


Figure 4.8: Losses on beam pipes and magnets vs the primary foil thickness  $t_{\text{PrColl}}$  within the shown in Fig. 4.1 intervals 6, 7, 9, and 11 for the case of enlarged diameters of the inter-collimator beam-pipes.

Figure 4.9 shows the number of lost particles and the absorption efficiency  $\epsilon_{\text{abs}}$  vs  $t_{\text{PrColl}}$  for every absorber. In the range of  $t_{\text{PrColl}} = 1 \div 5 \text{ cm}$ , the absorbers 6A and 6B have high values of  $\epsilon_{\text{abs}} > 94\%$ ,

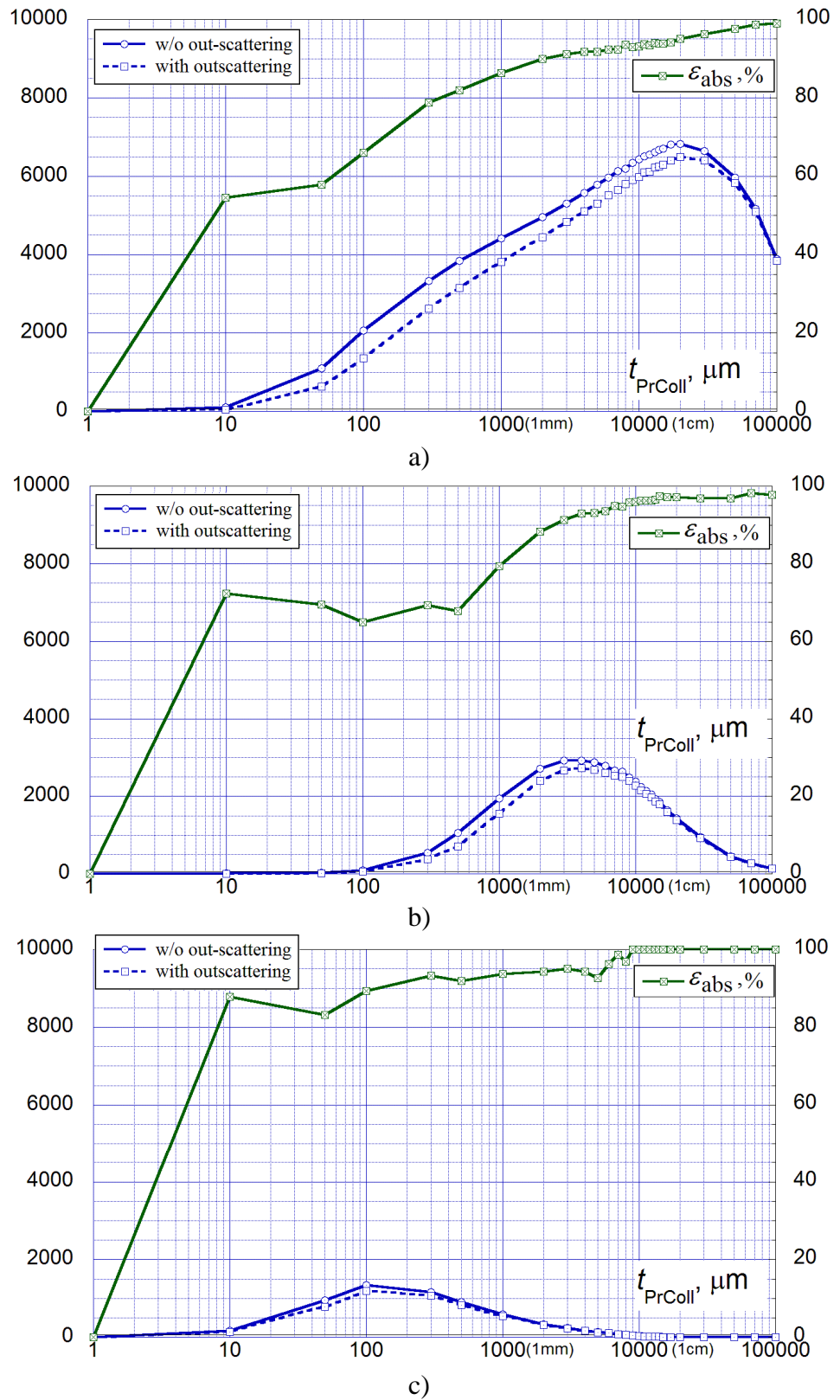


Figure 4.9: The number of lost particles without and with out-scattering effect (the left scale) and the absorption efficiency  $\varepsilon_{\text{abs}}$  (the right scale) vs  $t_{\text{PrColl}}$  for the new alternative 2SC scheme with enlarged beam pipes between collimators: a) collimator "6A"; b) collimator "6B"; c) collimator "7A".

and the beam losses on the collimator 7A are very small. The above results suggest, that in the range of the primary collimator thickness  $t_{\text{PrColl}} = 1 \div 5 \text{ cm}$ , the third absorber 7A and the pipes and magnets between 6B and 7A (interval no 11) could be excluded from the collimation system, since the beam losses on their walls are negligible.

Figure 4.10 shows the distribution of the beam losses for the new 2SC system using the primary collimator with the thickness  $t_{\text{PrColl}} = 3 \text{ cm}$ . Remind, the collimation in the horizontal plane after a single turn is considered. The most of beam loss will happen on the secondary collimators 6A and 6B and the primary collimator. The losses on the third absorber and Booster elements between absorbers 6B and 7A are small.

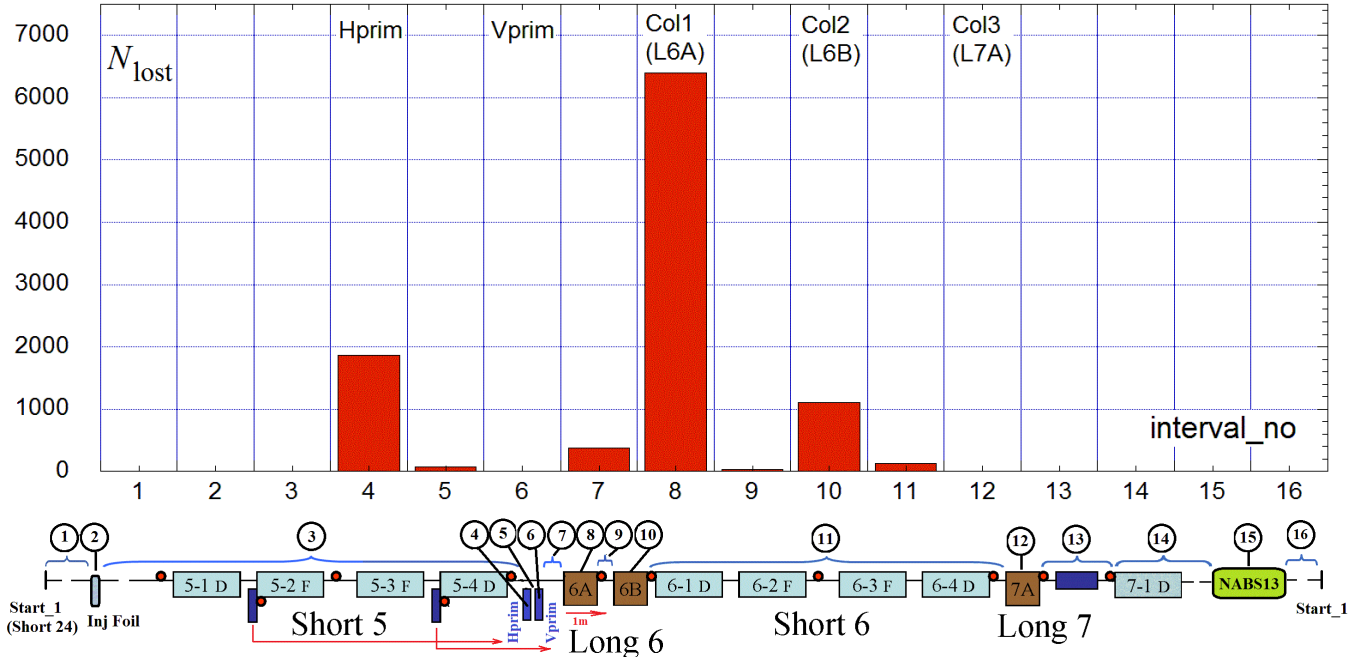


Figure 4.10: The beam loss distribution for the new 2SC in horizontal plane with  $t_{\text{PrColl}} = 3 \text{ cm}$  after single turn along of 16 selected intervals shown below in schematic layout of the new collimation system.

Thus, the final layout of a new 2SC system consists of a thick primary foil, *e.g.* the copper with thickness of  $t_{\text{PrColl}} = 1 \div 5 \text{ cm}$ , and only two vertical and horizontal absorbers 6A and 6B all located within a single long straight section. The total length of the new 2SC system will not exceed  $\sim 4 \text{ m}$ , corresponding to the total length presently occupied by two 1.2 m absorbers with the 1.6 m long beam pipe between the absorbers located in the long straight section 6 (see Fig.3.23).

The mechanical layout of the new 2SC system could be similar to the collimation system used in Rutherford Appleton Laboratory on the ISIS facility (former name SNS) [87] (see figures in Appendix A). The collimation system of the 800 MeV, 50 Hz rapid cycling synchrotron is installed in a 5 m drift section and localizes losses to this region. The system uses 10 movable beam collectors (3 primary and 7 secondary). All construction is located inside a common vacuum vessel.

Thus, the new collimation unit will consist of 4 m long well-shielded vacuum vessel containing two movable primary collimators at its upstream end and the  $\sim 1 \text{ m}$  long movable secondary horizontal and vertical collimation jaws at its downstream end. The vacuum chamber between primary and secondary collimators on the length of  $\sim 1.5 \text{ m}$  should have a quite large diameter to ensure a free drift of scattered protons from the primary collimators to the front edges of the secondary jaws. Such collimation unit can be located at some empty long section, *e.g.* long 8 or long 10.

## ***Conclusion and outlook***

Existing 2SC is difficult for implementation in Booster, since it requires to control and to preserve the halo position at  $3\sigma$  during approximately  $\sim 100$  turns. The new “thick-foil” 2SC is optically easier, because it could reach the same efficiency ( $\sim 75\%$ ) as existing 2SC in a single pass. The collimation efficiency of a new 2SC can reach up to 92%, if beam pipes between secondary collimators and around the primary collimator will be enlarged and well protected.

Assuming the collimation efficiencies of the existing 2SC system  $\varepsilon_{\text{halo}}^{\text{10-turn}} \sim 65\%$  and  $\varepsilon_{\text{halo}}^{\text{100-turn}} \sim 75\%$  and the beam losses to be proportional to the collimation inefficiency  $\eta_{\text{halo}} = 1 - \varepsilon_{\text{halo}}$ , a new collimation unit with collimation efficiency  $\varepsilon_{\text{halo}}^{\text{new}} \sim 90\%$  could reduce the beam losses by a factor 2÷4.

The new 2SC unit may be easily duplicated, if it will demonstrate good operational results. The following staged plans could be suggested. At the first stage the new collimation system could be installed in Long 8. Several questions should be answered:

a) if the new collimation unit could effectively intercept the halo particles at the same level as existing absorbers operating in conventional 1SC mode, but without creation an excessive residual radiation in surrounding area similar to existing absorbers;

b) if the new system operating together with existing absorbers could share (or redistribute) their beam losses and reduce the maximum residual radiation in the collimation area;

b) if the new system operating together with existing absorbers could reduce the radiation levels in remote areas like the RF-cavities.

At the second stage, if the above questions are answered positively, the new collimation units could be duplicated and installed either in another empty long section or even replace some of existing absorbers.

Finally, it may be necessary to use up to four new collimation units in order to effectively protect RF area, if we assume that the halo particles have fast growth rates, which enable them to avoid a single collimation unit and directly hit the apertures of RF-cavities.

## 5. Experimental Studies of the 2SC in Booster

### 5.1 Beam Instrumentation in Collimation Region

Figure 5.1 shows layout of the Booster collimation region and location of beam diagnostic. Near the primary and secondary collimators beam position monitors (BPM), beam loss monitors (BLM) and fast loss monitors created and supported by R.J. Tesarek (FLM) [88,89] are used to evaluate the beam position, radiation rate and when the collimators intercept the beam tails.

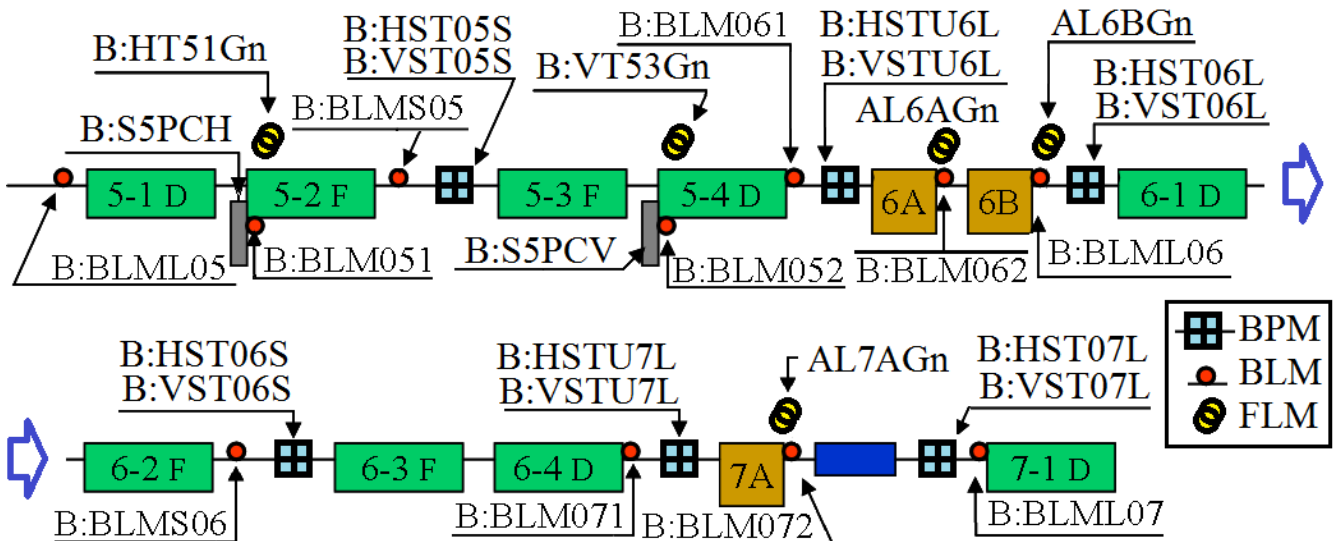


Figure 5.1: Layout beam instrumentations in vicinity of 2SC system in periods 5,6 and 7.

The primary collimators are movable thin scattering foils. The absorbers are movable steel cubes with square beam apertures. According to the 2004 original 2SC design [9,11] protons within  $3\sigma$  are considered to be the beam core and the normalized 95%-emittance equal to  $12\pi \text{ mm-mrad}$ .

In 2015, improvements were made to realize the original design of the 2SC. These improvements include: design and installation of  $380 \mu\text{m}$  thick aluminum primary collimators [45,84] and improvements in the accuracy and reliability of the absorber motion. The further descriptions of these improvements can be found in Appendices B and C.

The purpose of the 2SC system is to localize proton losses at the secondary collimators, reducing irradiation of the rest of the machine to the acceptable levels. The collimation system should interact only with halo protons which are considered to be lost later in the accelerating cycle while preserving the beam transmission efficiency.

## 5.2 Collimation Tests with Booster Beam for the Vertical Plane

For collimation in the vertical plane, collimators V-prim, 6B and 7A are used. V-prim is placed at the lower edge of the beam core. The jaws of the 6B and 7A collimators are positioned with a 2mm offset from the beam core, while the jaw of collimator 6B is located below the beam and the jaw of collimator 7A is located above the beam.

The beam tests with 2SC collimation system in the vertical plane described below have been performed on June 29, 2016 from 2pm till 6pm. The knowledge of the exact study time is useful for any later off-line analysis and data acquisition with Lumberjack data-logger (e.g., ACNET application D44). Some additional details of this study can be found in ref. [83, 90].

### 5.2.1 Initial Configuration of Collimators

In the studies presented here, we consider only vertical collimation. The horizontal positions of collimators were unchanged during the study. Figure 5.2 shows the vertical collimator positions relative to the beam for conventional single-stage collimation (1SC) routinely used for the beam collimation in Booster. Note that all three absorbers are used in the 1SC mode, while the primary collimators are out of beam, i.e. in their garage position. Note, the collimator positions shown in Fig. 5.2 are the initial and final position for our study of the 2SC system. Each collimator touches the beam from one side.

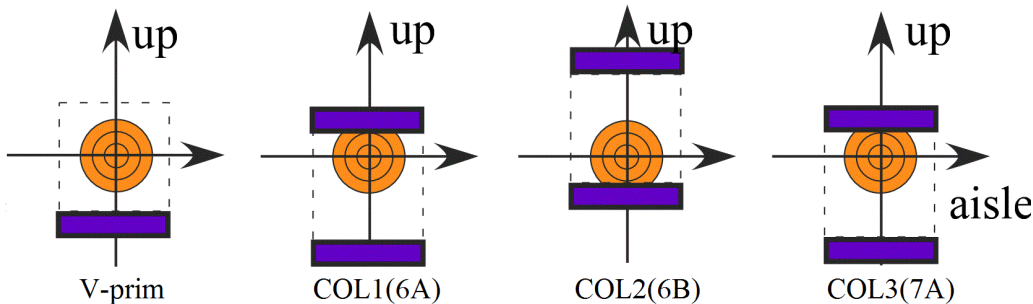


Figure 5.2: Transverse vertical positions of collimator jaws at 1SC.

### 5.2.2 Pre-study for the beam orbits preparations

Preparatory to the test, the vertical beam position throughout the entire accelerating cycle was arranged in such way that all collimators touch the beam at the beginning of the cycle (approximately 300 turns). During these studies, the vertical beam position at the collimators was observed to vary no more than 0.5mm from cycle to cycle.

Data from BPM obtained via ACNET application B38 allows to understand the beam orbits in vicinity of Booster collimation region. Figure 5.3 shows the "mean $\pm$ rms" values of the beam orbits at three different vertical BPMs vs the turn number. The mean and rms values has been obtained from post-processing of 5 pairs measurements, which were taken at 5 particular states of collimator configurations during full  $\sim 2.5$  hr collimation study. Since rms-values are shown at every turn, the resulting "mean $\pm$ rms" looks as a thick brush-painted curve with the thickness of double rms-value.

Figure 5.4 shows the dependencies on turn number throughout full Booster cycle for the mean beam orbit  $y_c$  (red curve), the vertical beam  $\sigma$ -size  $\sigma_y$  (green curve), the boundaries of the beam envelopes given by two curves  $y_c+3\sigma_y$  and  $y_c-3\sigma_y$ . The beam orbit has been restored using data from neighbor BPMs. It is assumed that the beam  $\sigma_y$ -size is dumped with increase of beam energy according to ideal law  $\sim 1/\beta\gamma$ , where  $\beta$  and  $\gamma$  are relative beam velocity and Lorenz factor, respectively.

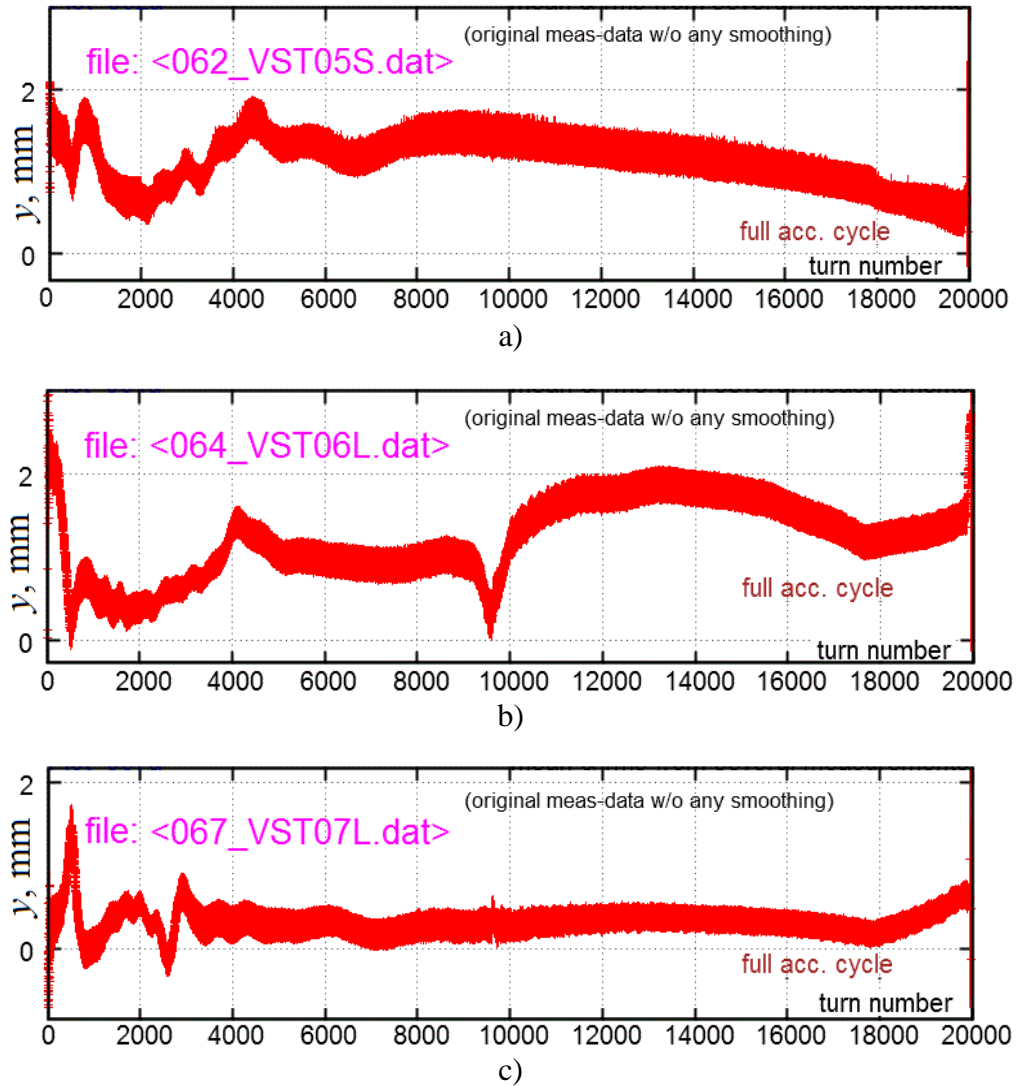


Figure 5.3: Beam Orbits *vs* the Booster turn number for 3 different vertical BPMs: a) BPM located at Short-5 (its ACNET name is B:VST05S); b) BPM located downstream of Long-6 (B:VST06L); c) BPM located downstream of Long-7 (B:VST07L).

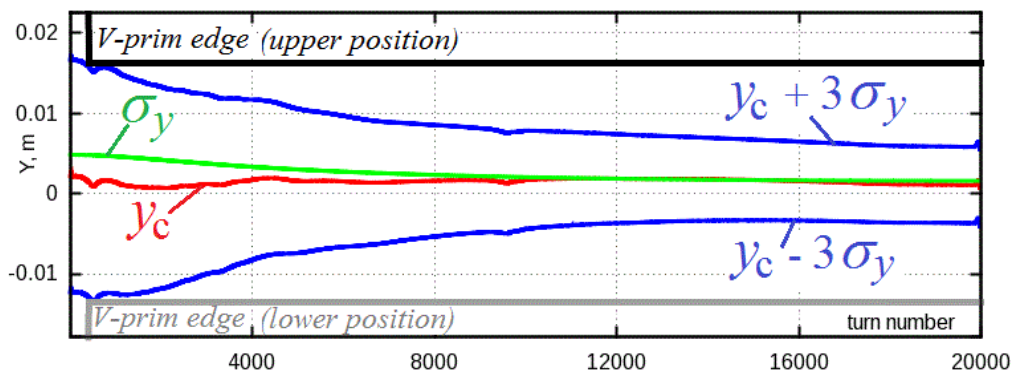


Figure 5.4: Normalized BLMs values summed over 64 BLMs around the ring at the different time points.

Figure 5.4 also shows two possible vertical positions of V-prim edges touching beam are shown (black and grey), since the beam can be touched by V-prim at the top or bottom. These two positions are defined by maximal and minimal values of beam envelopes over the full Booster cycle (20,000 turns) excluding the first 300 turns where BPM-readings are not reliable for not yet bunched beam. During presented vertical collimation study the V-prim touched the beam from the bottom denoted as "lower position" (grey).

### 5.2.3 Collimation Test Steps and 2SC Configurations Realized

Beam losses measured via BLMs (ACNET application B136) were recorded around the booster both before, during and after the 2SC tests for comparison, while both BLMs and FLMs data are available off-line via ACNET application D44.

Below is an outline of the collimation optimization procedure.

- 1) Move COL1(6A) vertically up (out of the beam) to garage position;
- 2) Move COL3(7A) vertically up (out of the beam) to garage position;
- 3) Move V-prim vertically up (to touch the beam edge) and optimize its position (up & down);
- 4) Move COL2(6B) vertically down (out of beam), then move it vertically up (into beam), and finally move it down (out of beam) by ~2mm. As results, 6B intercept (touch) scattered beam from the bottom side of beam;
- 5) Move COL3(7A) vertically down from garage position to the beam until it touches the beam, then move it up (away from the beam) by ~2mm (UP). As results, 6B intercept (touch) scattered beam from the top side of beam;
- 6-7) Move COL3(7A) applying small position adjustments trying to ensure possible re-optimizations while monitoring booster efficiency;
- 8) Move V-prim vertically up and down trying to re-optimize its position;
- 9) Move all collimators one-by-one to initial 1SC positions.

Let's note: a) after step "2" the configuration of collimators corresponds to 1SC mode with single absorber, namely with COL2(6B); b) steps "5", "6", and "7" result in three versions with slightly different collimator positions, each of which corresponds to 2SC mode involving V-prim and two absorbers COL2(6B) and COL3(7A).

Figure 5.5 shows snap-shot of the ACNET window with four FLM-signals (gate No.1) and vertical positions of four collimators. The FLM-signal and position for V-prim are ACNET-variables named as B:VT53G1 and B:S5PCV, respectively. The FLM-signal and position for absorber 6A (COL1) are named as B:AL6AG1 and B:BCOL1V, respectively. The FLM-signal and position for absorber 6B (COL2) are named as B:AL6BG1 and B:BCOL2V, respectively. The FLM-signal and position for absorber 7A (COL3) are named as B:AL7AG1 and B:BCOL3V, respectively. An increase in FLM rate (gated for 100  $\mu$ s around injection, i.e. gate No.1) indicates when collimator is touching the beam core. More details about FLMs can be found in Appendix E.

Figure 5.6 shows the configuration of the 2SC system at optimization. Absorbers only touch the beam core, while V-prim intercepts the beam.

Figure 5.7 shows the collimator positions and booster beam transmission efficiency as a function of time during the study. The letters indicate points when the losses from the BLMs were recorded around the booster. Points A, B and L indicate routine 1SC with all 3 absorbers used. Points C and D indicate 1SC with a single absorber (6B). Points J-K represents the optimized 2SC.

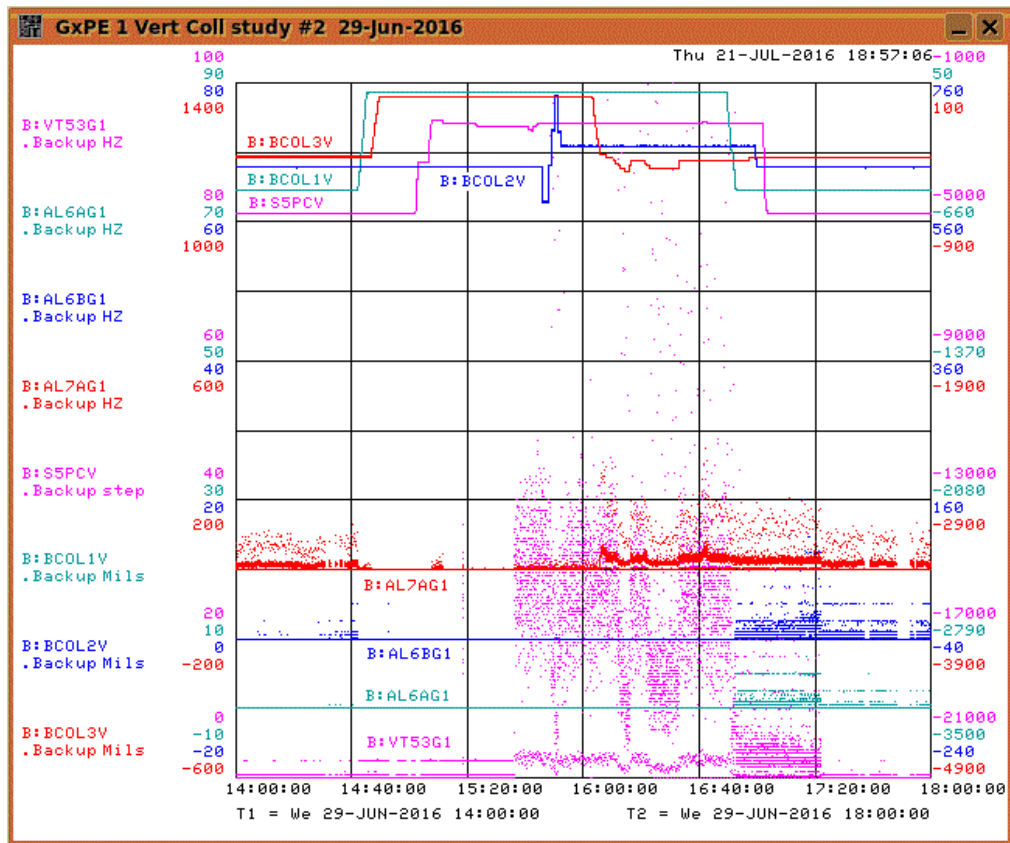


Figure 5.5: ACNET window with FLM-signals and vertical positions of collimators during study.

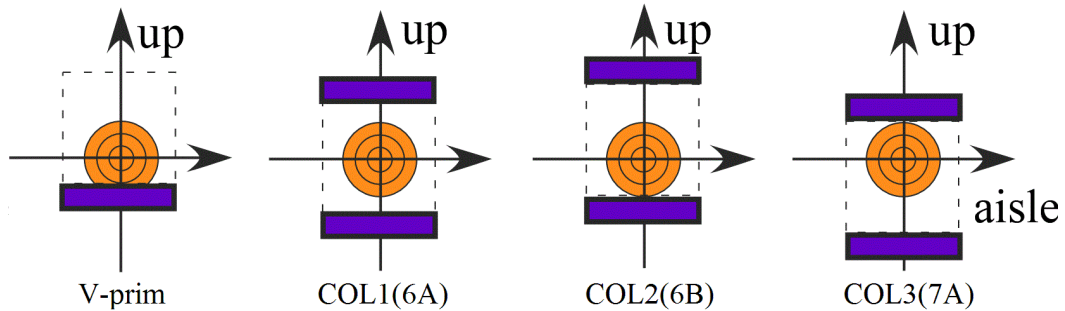


Figure 5.6: Transverse vertical positions of collimator jaws at 2SC.

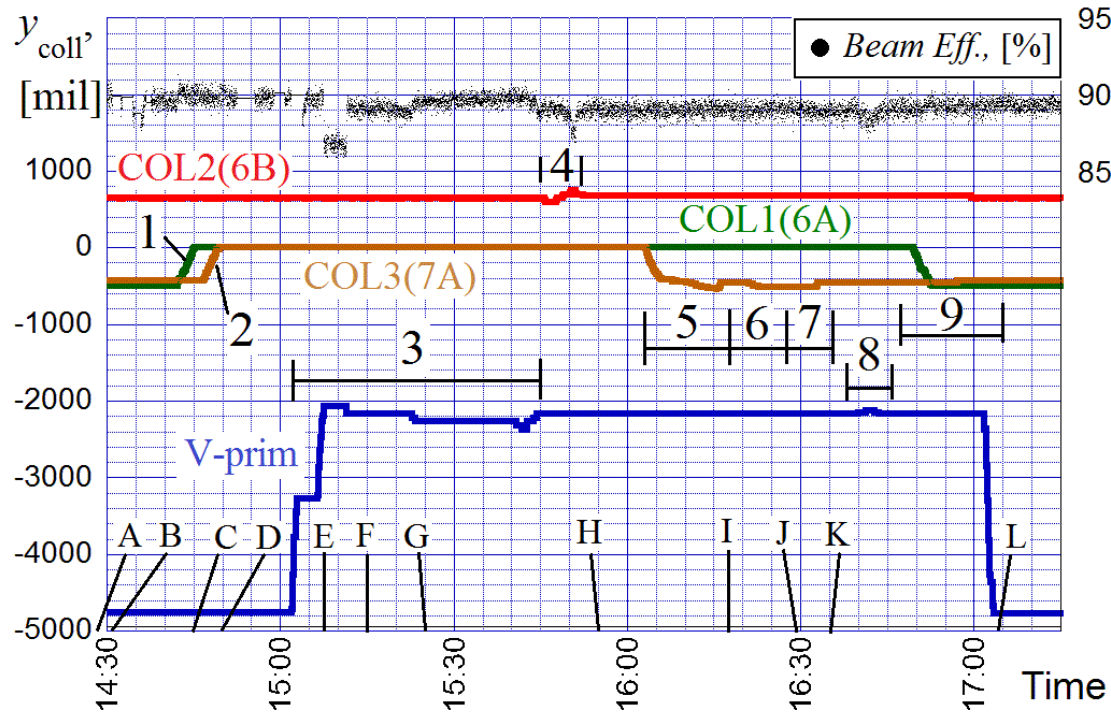


Figure 5.7: Vertical collimator positions (left scale) and the Booster beam transfer efficiency (right scale) vs time.

#### 5.2.4 Post-processing Beam Loss Data

Data from BLM around the Booster have been collected using ACNET applications B136 and B88. Since data exporting from B88 did not work at the study time, the special code developed by V.K. has been used as a substitute of B88. Technically, it is the LINUX executable "B88.exe" directly reading the ACNET variables assigned to BLMs.

Usage of two BLM applications allow us to post-process the BLM signals accumulated at different time-scales: 1) relatively short  $\sim$ 66ms by averaging of BLM signals from B136 during the one Booster cycle ( $\sim$ 66ms); b) relatively long  $\sim$ 1÷2min by B88 during many hundreds of Booster cycles.

In order to have a single figure of merit for beam losses for every particular collimation conditions, sums of BLM signals over several Booster BLMs has been introduced. Such sums can include several different sets of BLMs, *e.g.* sums of all 64 BLMs available for B88 at study time, sums of 48 BLMs regularly located in Short and Long sections of 24 Booster periods.

Figure 5.8 shows the BLM readings as sums of all 64 BLMs around the Booster normalized to give fractions of the radiation trip points (alarm values). Figure 5.9 shows the absolute values of the BLM readings (without normalization) as the sums of all 64 BLMs around the Booster.

The heights of vertical bars shown in Fig. 5.8 and Fig. 5.9 allow us to compare the effectiveness of 2SC and 1SC modes. For example, the normalized BLMs sum (Fig. 5.8) for the 1SC with single absorber (point D) is 5.6, while for the optimized 2SC (point J) is 4.8. It can be concluded that the optimized 2SC reduces the BLMs sum by 14% in comparison to the 1SC with single absorber. Details of such improvement are illustrated in Fig. 5.10, which shows normalized BLMs values around the ring.

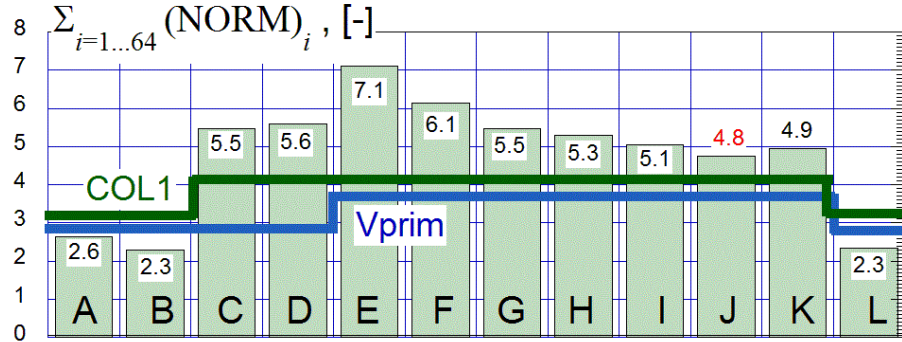


Figure 5.8: Normalized BLMs values summed over 64 BLMs around the ring at the different time points.

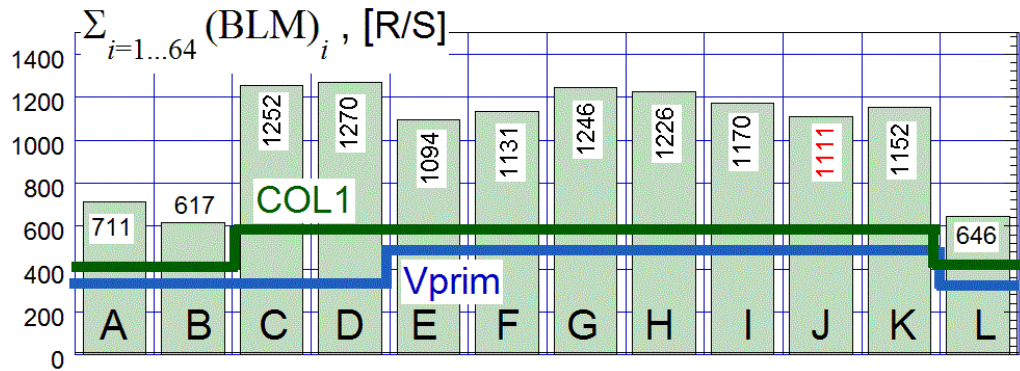


Figure 5.9: Absolute BLMs values summed over 64 BLMs around the ring at the different time points.

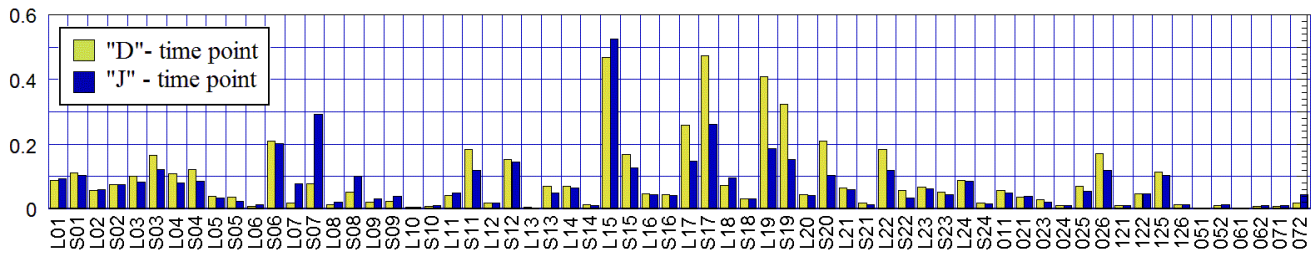


Figure 5.10: Normalized BLMs values around the ring for time points "D" and "J".

One can see the radiation is reduced at BLMs in Booster sections S03, L04, S04, S11, S15, L17, S17, L19, S2, and L22. However, the radiation is increased in sections S07 and L15. Note, that L15 contains an RF cavity which represents an aperture restriction.

On the other hand, the BLMs sum for routine 1SC with three absorbers (point B) is equal to 2.3, which is about twice lower than one for the optimized 2SC (points J or K). Figures 5.11 and 5.12 show the screen snapshots of data available in the Fermilab Main Control Room for the time points B and K.

The above plots clearly demonstrate that the optimized 2SC has increased radiation levels for most BLMs around the Booster and is less effective than the routine 1SC using all 3 absorbers. Additional details of these studies may be found in ref. [83].

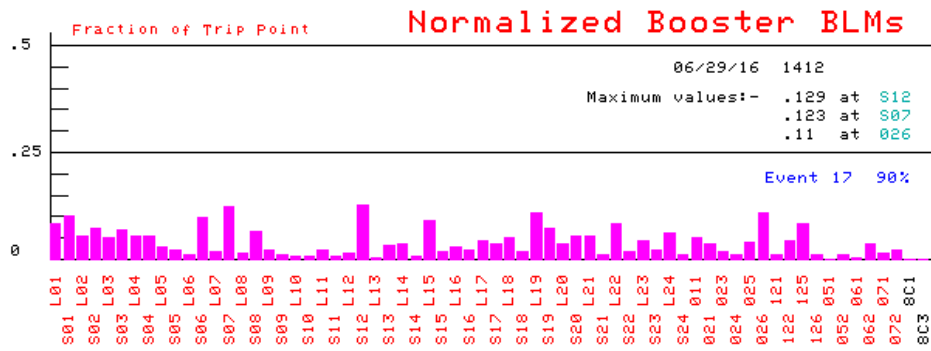


Figure 5.11: The fraction of trip points for time point "B" (1SC with 3 absorbers).

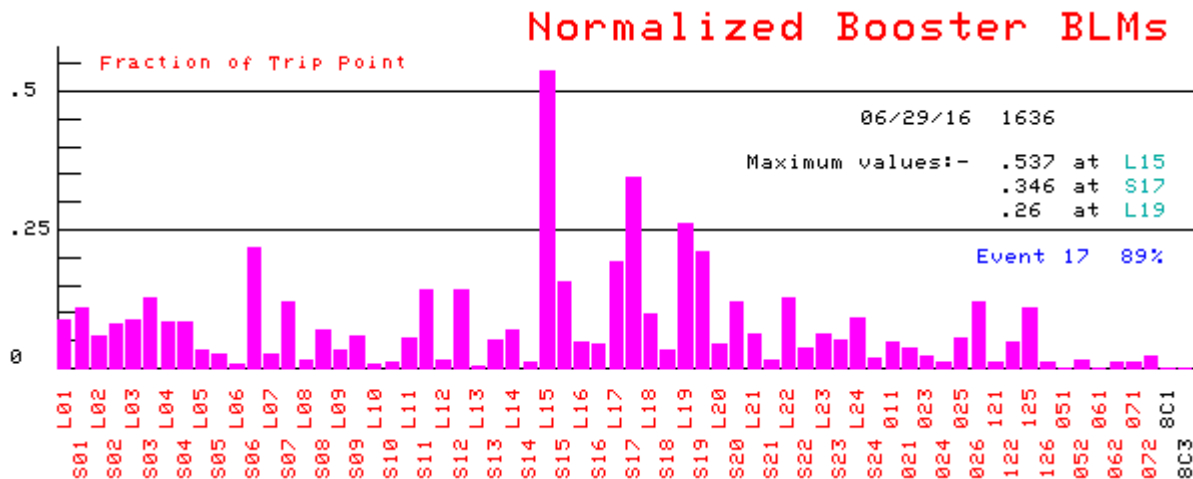


Figure 5.12: The fraction of trip points for time point "K" (optimized 2SC with 2 absorbers).

### **5.2.5 Conclusions for Vertical Collimation Study**

The results of the tests for the Booster collimation system in the vertical plane presented here suggest the following conclusions:

- 1) the beam orbit patterns within accelerating cycle were stable within 0.5 mm during all test time (~2.5hr);
  - 2) the vertical 2SC is operational and showed an improvement by 14% compared to 1SC using a single absorber;
  - 3) compared with vertical routine 1SC, the 2SC mode is less effective by a factor of ~2.

Thus, the beam test with 2SC system operating in the vertical plane did not show any advantages of 2SC mode of operation in a comparison with the conventional single stage operation involving three absorbers.

### 5.3 Collimation Tests with Booster Beam in Horizontal Plane

The beam tests with 2SC system in the horizontal plane described below have been performed on March 2, 2017 from 12:30pm till 16:30pm. Table 5.1 lists and illustrate every of 14 steps for this study reported in ref [91]. The names in the second column denote time points used in the below plots.

Table 5.1 Transverse positions and study steps for 2-Mar-2017 beam study of the horizontal 2SC.

No	ti-me	Step No&name	H-Prim	Col1=L6A (SHCOL1)	Col2=L6B (SVCOL1)	Col3=L7A (SHVCOL2)	Comments
1	A	Record BLM/BPM/ColPos (110325.xls/*_kap03_01n.txt) at usual col-positions (1-stage used in 2016)					Top/Up Wall Inside Down/Bottom Aisle Out
2	A1	move Col2 to garage (->W)					
3		move Col3 to garage (->A)					move all SecCols to garage; <b>STOP BEAM</b> for Hprim motion);
4	B	rec. BLM/BPM (111822/041)					<b>4=1SC with 1 sec.col!</b> <b>4b=all SC - garage!</b>
4a	B1	move Hprim to Wall-garage					
4b	C	move Col1 to garage (->A)					
4c	C1	continue move Col1 (->Aisle) to touch beam from Wall-side					setup the major sec. collimator (=COL1) to touch beam and then optimize H-prim
5	C2	move Hprim (->Aisle) to touch beam from Wall-side					
6:	C3	re-optimize Col1:					"6b=7"= <b>2SC with single major Sec.coll (Col1)</b> (7: 116313/07n)
6a		adjust Col1 to beam (->Aisle)					
6b		retract Col1 from beam(->W)					
7	D	Record BLM/BPM					
8a	D1	move Col3 to beam (->Wall)					
8b	D2	Record BLM/BPM					(8b:117504/08n) retract to ->A
9:		Optimize Col3 at beam core					$\delta x = +1\text{mm} = 40\text{mils}$
9a		Col3 further in beam (->W)					<b>9c=2SC with 2 SC!</b>
9b		retract Col3 from beam(->A)					(9c:118348.xls/09n)
9c	E	Record BLM/BPM					
10		re-optimize (play) Hprim					
10		re-optimize (play with) Col1					<b>10a=re-optimized 2SC with 2 sec.col!</b>
a	F	Record BLM/BPM (_11590.xls/*_10An.txt)					
11	F1	"Surround" beam by Col2: move to touch beam (->A) then retract from beam (->W)					after approach Col2 to beam retract it by $\delta x = +1\text{mm} = 40\text{mils}$ ;
12	G	Record BLM/BPM (_120882.xls/*_12n.txt)					<b>12=2SC with 3 sec.col!</b>
For info		final positions for horizontal 2-stage collimation (while keeping 1SC in vertical plane)					2004 A.D.'s design for 2-stage hor. collimation modified as following: <i>Col2 from opposite side - enhancing Coll1</i>
13	G1	Return all collims to ini. 1SC: a)H <sub>prim</sub> b)Col1 c)Col2 d)Col3	move to Aisle garage	move to Wall	small move into beam (->Wall)	small move to (Wall Aisle)	14: *_122709.xls/ _14n.txt
14	H	Record BLM/BPM	<b>BEAM STOP</b>				

### 5.3.1 Initial Configuration of Collimators

In the studies presented here, we consider only horizontal collimation. The vertical positions of collimators were unchanged during the study. The collimator positions relative to the beam for conventional single-stage collimation (1SC) routinely used for the beam collimation in Booster are shown in Table 5.1 at the step no. 1 (the time point "A"). Note that all three absorbers are used in the 1SC mode in both planes, while the primary collimators are out of beam, i.e. in their garage position. For our study the collimator positions shown at the step no. 1 are the initial and the final positions. During study all collimators are moved only in the horizontal plane, while the preserve their vertical positions and continue to collimate in 1SC mode fro vertical plane.

### 5.3.2 Details of the Collimator motion in the Horizontal Plane

Figure 5.13 shows the horizontal positions of the colimators during the full study with labeling of the study steps and study points. The time point marked by only capital letters (A, B, D-H) are times when a full set of measurement with BLMs (ACNET applications B136, B88) and BPMs (B88) has been performed. The time points marked by additional number are additional time points with only B88 data measured.

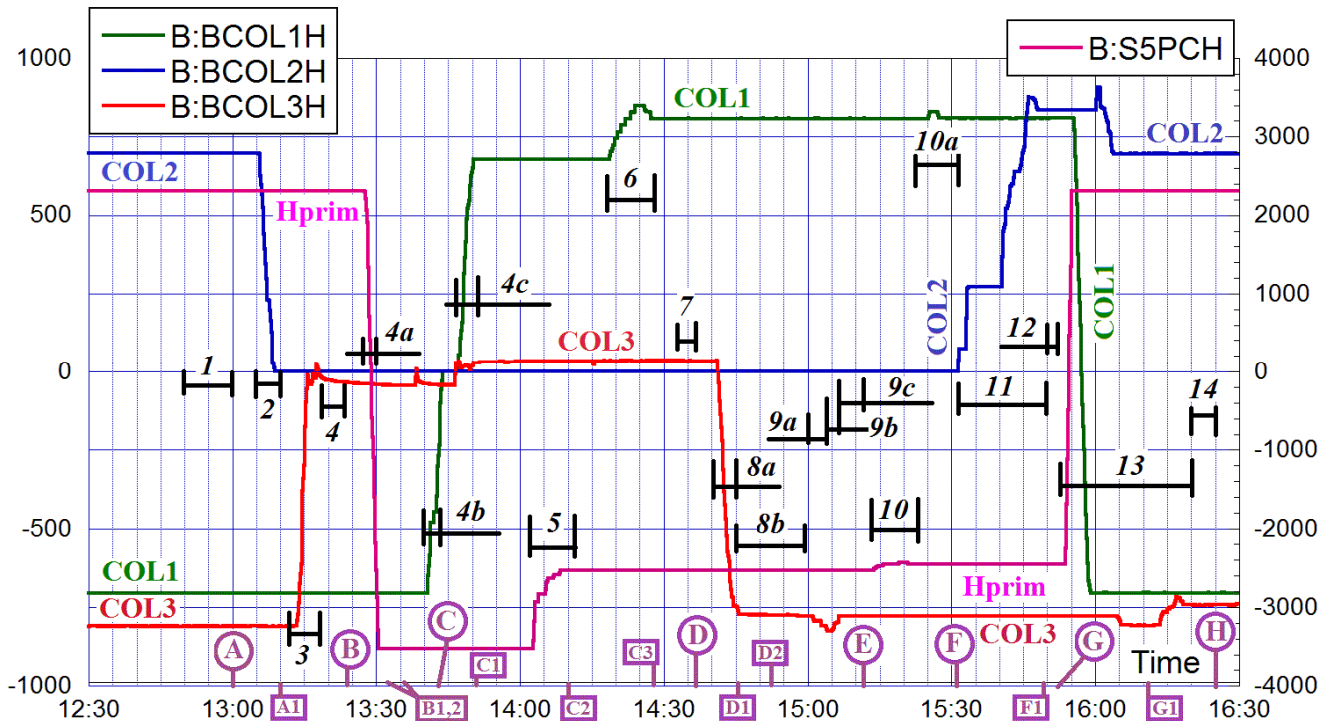


Figure 5.13: Horizontal positions of the secondary collimators (left scale) and primary collimators with labels for study steps and time points.

During study there were some fluctuations in the Booster beam intensity. Figure shows the variations of the beam transmission efficiency "B:BEFF17", the beam charge at the beginning and the end of accelerating cycle "B:CHG1" and "B:CHG2", respectively. The additional time points "D2", "F1", and "G1" located near the times with unstable beam currents has been exluded from a further analysis.

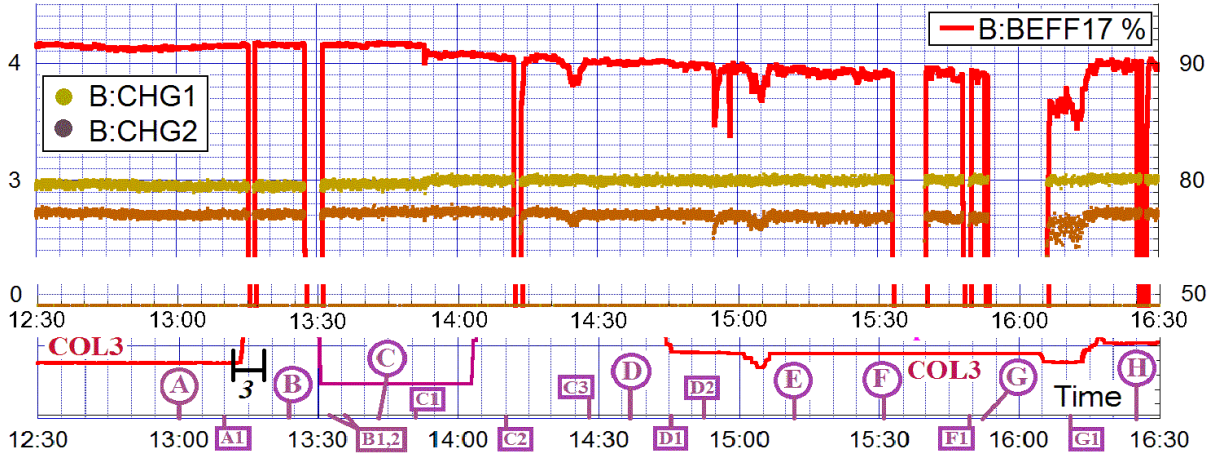


Figure 5.14: Beam intensity fluctuations during study.

### 5.3.3 Realized Configurations for 2SC Horizontal Collimation

For easy understanding of the configurations realized during the study, the time points with their short description are listed in the Table 5.2. Several different configurations for 2SC collimation has been realized and even repeated during study: 1) the 2SC using single secondary collimator; 2) 2SC using two secondary collimators; 3) the 2SC using three secondary collimators.

Table 5.2 Time points and their description

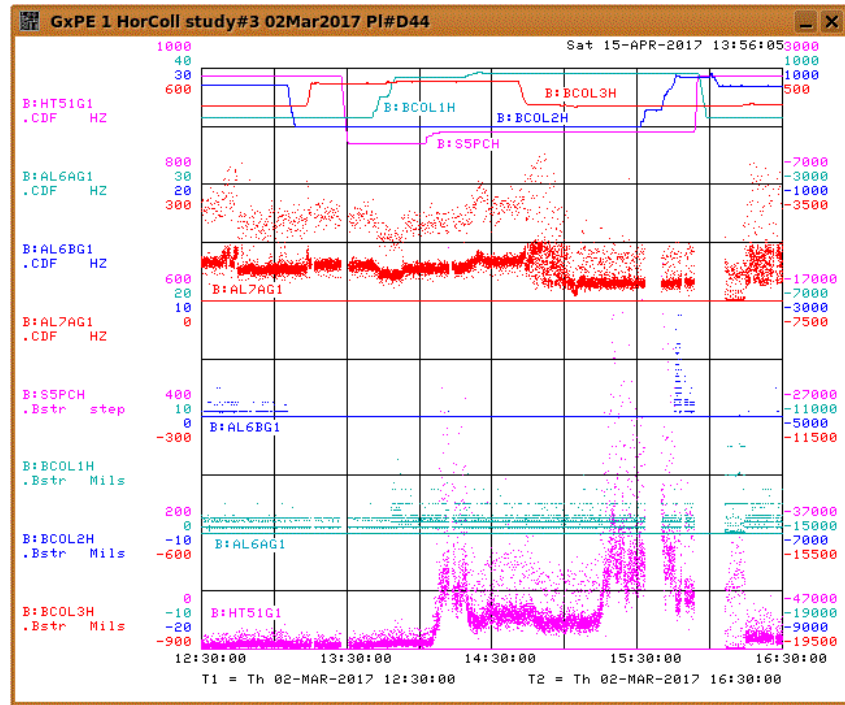
A	usual 1SC (routinely ~2016)	C3	COL1 is re-optimized => "2SC with single sec. col."
A1	COL2 in GRG (garage)	D	(=C3) "2SC with single sec. col."
B	COL3 in GRG	D1	COL3 at beam aisle-side => "2SC with two sec.col."
B1	Hprim in Wall-GRG	E	COL3 is re-optimized => "2SC with 2 sec.col. re-opt"
C	COL1 in GRG (all hor. GRG)	F	Hpr & COL1 re-opt. => "2SC with 2 sec.col., all re-opt"
C1	COL1 at beam Wall-side	G	COL2 at beam W-side => "2SC with 3 sec. cols"
C2	Hprim at beam Wall-side	H	back to initial 1SC (=A)

Figure 5.15 shows the typical screens during tuning the collimations system. The fast loss monitors are used to see changes in the beam losses after change of the collimator position. The locations of FLMs have been shown Fig. 5.1 Since the colimation near the injection energy is studied, the Gate no.1 of FLMs is used.

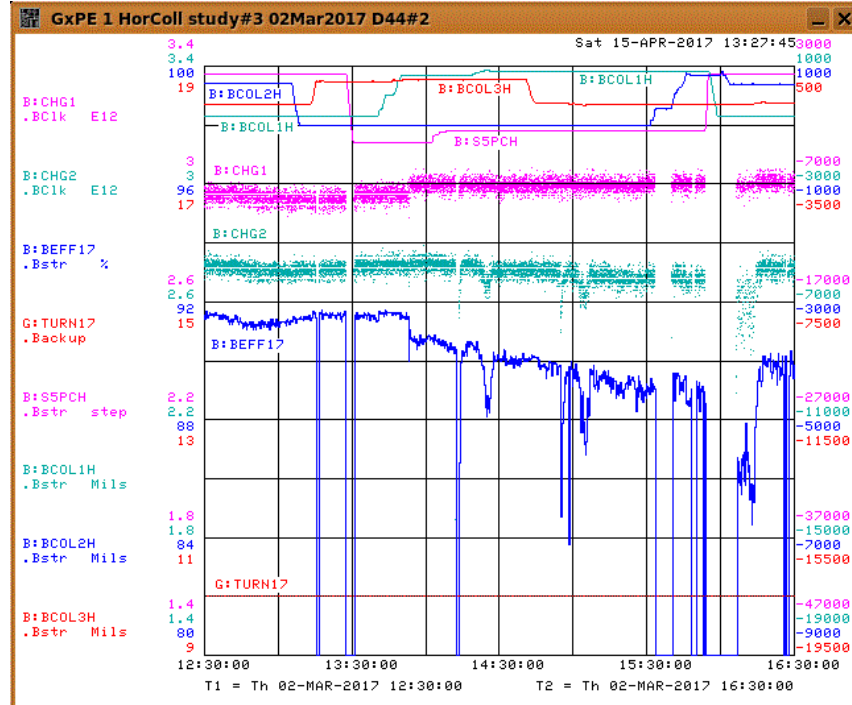
### 5.3.4. Post-Processing Beam Loss Data Study Results

The comprehensive details of this study with cross-checking of available data can be found in ref [91]. In order to have a single figure of merit for beam losses for every particular collimation conditions, several sums of BLM signals over several Booster BLMs has been introduced. Such sums can include several different sets of BLMs, *e.g.* sum of all 64 BLMs available for B88 at study time, sum of 48 BLMs regularly located in Short and Long sections of 24 Booster periods, sum of 11 BLMs located in the collimation region, sum of 24 BLMs regularly located in the short and long sections of the 11 periods with RF-cavities.

BLM loss patterns around the Booster for 2SC have been compared to 1SC at 3 time scales: 1) via averaging over many Booster cycles (B88); 2) via averaging over one cycle (B136 data); 3) at time after injection before notching (B136 data). Conclusions were consistent between 3 scales [91].



a)



b)

Figure 5.15: Typical screens during studies: a) tuning of the 2SC system with help FLMs; b) basic parameters to be controlled.

Figure 5.16 shows several sums of absolute BLM values. These sums have been corrected for a compensation of the intensity drops during study. The corrections have improved the results for 2SC.

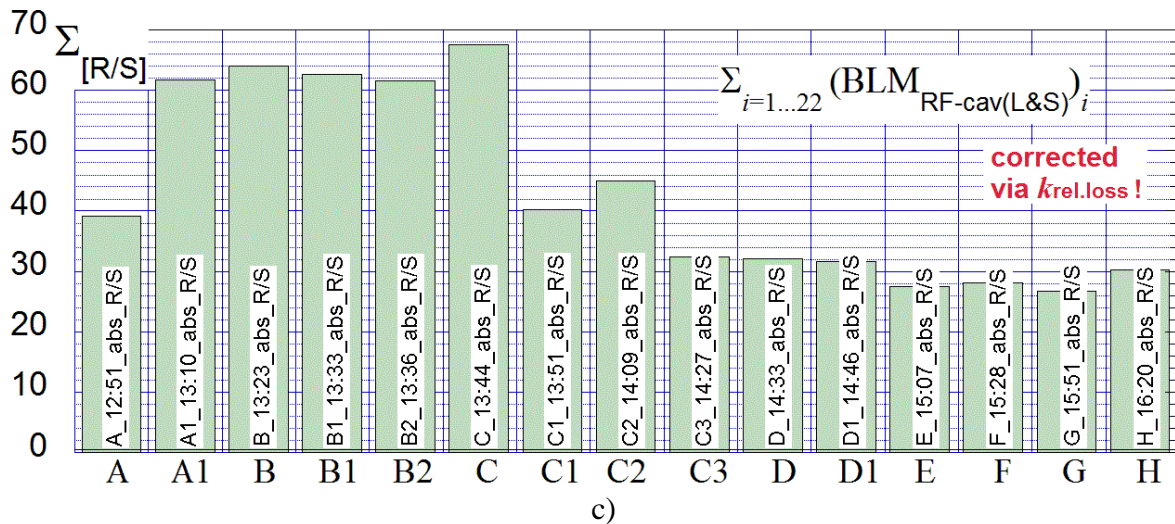
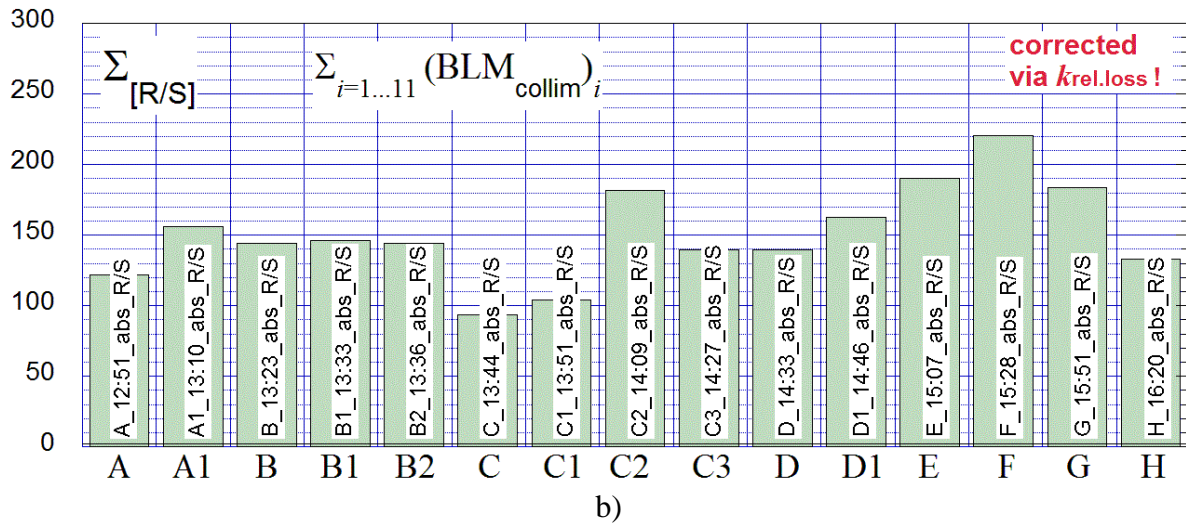
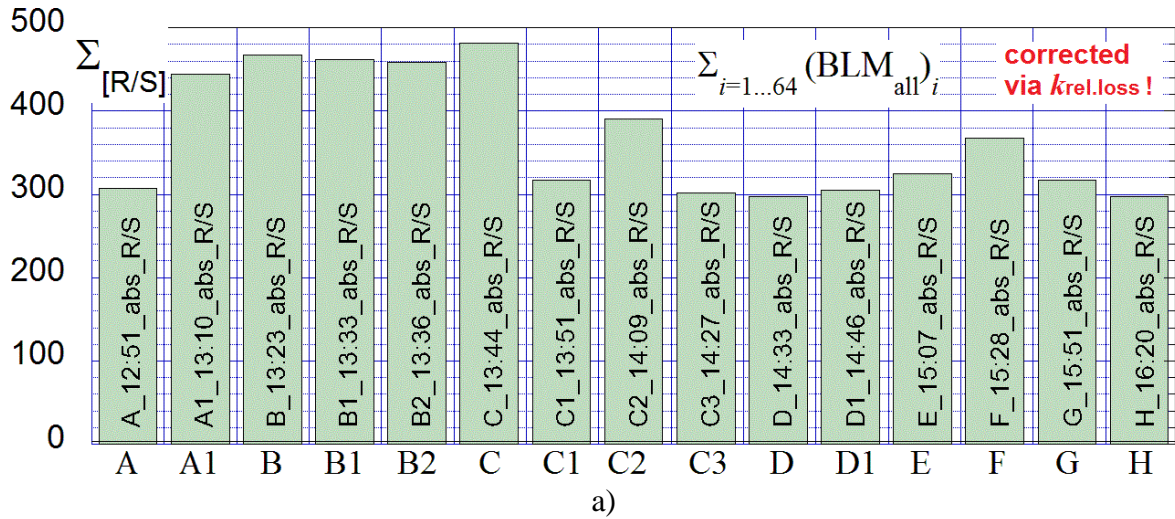


Figure 5.16: Absolute BLM values summed over several BLMs: a) 64 BLMs around the ring; b) 11 BLMs located in the collimation area; c) 22 BLMs located in the periods with RF-cavities.

The height of every vertical bar shown in Fig. 5.16 corresponds to radiation levels due to the beam losses for a particular collimation mode realized during study. It allows us to compare the effectiveness of 2SC and 1SC modes. The height of the bars "A" and "H" characterize the radiation levels for 1SC mode. The 2SC scheme with single secondary collimator was realized at the time points "C3" and "D". The 2SC schemes with two secondary collimators were been realized in three variants at times "D1", "E", and "F". The 2SC scheme with three secondary collimators has been exploited at the time point "G".

Let's analyse Fig. 5.16,a with the 64-BLM sums. These sums taken over all existing BLMs demonstrate equal radiation levels for 1SC modes at the beginning of study ("A") and at end of study ("H"). There is no any time point with sum radiation lower than for these 1SC modes. This means that there is no any 2SC mode with the total 64-BLM signal better than for 1SC modes. It can be concluded that 2SC collimation in the horizontal direction is less effective than the conventional 1SC mode.

Let's consider Fig. 5.16,b with the 11-BLM sums in the collimation area. The radiation levels for all 2SC versions are higher than for 1SC at "A" and "H". Fig. 5.16,c with the 22-BLMs sums in region with RF-cavities shows small less than 10% decrease in radiation level for 2SC modes in comparison to 1SC mode.

It looks that this decrease depends on number of the secondary collimators involved in to 2SC scheme. One can suspect that an equavalent phase length of the collimation system is increased with number of the used collimators including the primary collimators. The collimation system covering a longer phase range may more effectively protect the remote area with RF-cavities in exchange of higher radiation levels at the collimation area.

### 5.3.5 Conclusions for Horizontal Collimation Study

Several two-stage collimation (2SC) schemes in horizontal plane using one, two and three secondary collimators has been implemented during the collimation study on 2-Mar-2017. BLM loss patterns around the Booster for 2SC have been compared to 1SC at 3 time scales (conclusions are consistent between them)

Analysis at three different time scales has demonstrated worse collimation efficiency for 2SC vs 1SC. Some tiny (<10%) reduction of losses has been detected over whole RF-area (periods 14-24) using some heuristical correction.

## 6. Conclusion

One of 22 PIP tasks is a possible upgrade of the Booster collimation system installed in 2004 and is operating in the conventional single stage collimation mode, which was still ensuring a significant reduction in Booster activation. The growth of the Booster proton flux during the last decade leads to an increase of the residual radiation in the collimation area.

The Booster collimation system has been designed as a two-stage collimation (2SC) system, which should be able to reduce residual activation in the collimation area due to suppressing the portion of protons out-scattered from the secondary collimators. New efforts for an implementation of 2SC system in the Booster operation have been started in autumn of 2014. This report finalizes both theoretical and experimental studies performed for the Booster 2SC system.

The presented review of the original 2001-2004 design of 2SC has revealed that the design purpose for 2SC was formulated very softly, assuming 99%-beam loss over up to 25÷50 m region in periods 6, 7 and immediately downstream. However, the existing collimation system operating in 1SC mode also localize the high activation area within 25 m long collimation region. Therefore, the aim of 2SC system has been reformulated. This 2SC system must localize beam losses inside of three 1.2 m-long secondary collimators and reduce the residual activation in the collimation area in comparison to the 1SC mode used in Booster operations.

New software using the MADX and MARS code has been prepared. The results of numerical simulations for 2SC in both horizontal and vertical planes did not show advantages of the 2SC mode in comparison to conventional 1SC mode, for which the absorption efficiency of the secondary collimators has been calculated with MARS code. In order to achieve high collimation efficiency, the numerical simulations require preserving the halo position under unchangeable conditions during up to 100 turns and more. It looks that such condition could not be supported in Booster.

The presented analytical evaluations for 2SC in the vertical plane have defined peculiarities of the Booster collimation system and have explained reasons for its potentially low collimation efficiency. These evaluations also provided insight on possible tricks increasing the resulting collimation efficiency during multi-turn simulations in the lattice with imperfections.

Two major experimental beam studies for the collimation in horizontal and vertical planes have been performed. Several configuration of 2SC has been realized. The sum of many BLMs reading located around the Booster was used as figure of merit to compare 1SC with 2SC. The experimental results did not show any advantages of 2SC operation mode in comparison to 1SC mode. Such results are in agreement with our theoretical prediction about low collimation efficiency due to the Booster peculiarities.

Since the simulation results and experimental studies did not show advantages of 2SC in comparison with 1SC for existing configuration, we have numerically simulated a new configuration of 2SC system using a rather thick foil relocated into the long straight section before of the first secondary collimator. The results of numerical simulations for new proposed 2SC system showed that it is the single pass collimation system and it does not depend on multi-turn behavior of Booster optics. A possible configuration of new 2SC system is discussed and a two-stage plan for updating the Booster collimation system is proposed.

## **Acknowledgements**

The authors would like to thank C.I. Briegel, M.A. Coburn, B.D. Hartsell, J.F. Ostiguy, V.S. Pronskikh, M.H. Slabaugh, I.L. Rakhno, C.Y. Tan for their help, technical support, useful discussion, and kind explanations.

## References

- [1] "Concepts Rookie Book", December 3, 2013;  
[http://operations.fnal.gov/rookie\\_books/concepts.pdf](http://operations.fnal.gov/rookie_books/concepts.pdf)
- [2] "Design Report National Accelerator Laboratory", Second Printing, July 1968
- [3] E.L. Hubbard et al., "Booster Synchrotron", Fermilab-TM-405 (1973).
- [4] "Booster Rookie Book", version v4.1, Revised: April 8, 2009  
[http://operations.fnal.gov/rookie\\_books/Booster\\_V4.1.pdf](http://operations.fnal.gov/rookie_books/Booster_V4.1.pdf)
- [5] N.V. Mokhov, "Beam Collimation at Hadron Colliders", AIP Conf. Proc. No.693, pp. 14-19, 2003.
- [6] A. Drozhdin, P. Kasper, O. Krivosheev, J. Lackey, N. Mokhov, M. Popovic, R. Webber, "Beam Loss, Residual Radiation, and Collimation and Shielding in the Fermilab Booster", PAC'2001, Chicago, USA, . p.2569, published at JACoW-web site<sup>17</sup>.
- [7] R.C. Webber, "Fermilab Booster Operational Status: Beam Loss and Collimation", AIP Conf. Proc. No.642 (2002) 167-169; Fermilab-Conf-02/106-E June 2002.
- [8] N. Mokhov, "Booster Integrated Collimators/Shielding", review talk on March 17, 2003, Beams-doc-654-v1, 2003.
- [9] N.V. Mokhov, A. Drozhdin, P.H. Kasper, J.R. Lackey, E.J. Prebys, R.C. Webber, "Fermilab Booster Collimation and Shielding", PAC'2003, Portland, USA, p.1503 (publ. JACoW); also published as FERMILAB-Conf-03/087 in May of 2003.
- [10] E. Prebys, C. Ankenbrandt, W. Chou, A. Drozhdin, P.H. Kasper, J.R. Lackey, N.V. Mokhov, W.A. Pellico, R. Tomlin, R.C. Webber, "Increasing the Intensity of the Fermilab Booster", PAC'2003, May 12-16, Portland, USA, p.2936; (publ. JACoW).
- [11] A. Drozhdin, P. Kasper, J. Lackey, N. Mokhov, E. Prebys, M. Syphers, D. Still, T. Sullivan, "Commissioning of the Beam Collimation System at the Fermilab Booster", Beams Document Database<sup>18</sup>: Beams-doc-1223-v1, Fermilab, 25 Jun 2004.
- [12] E.J. Prebys, P. Adamson, S. Childress, P.F. Derwent, S. Holmes, I. Kourbanis, V. Lebedev, W. Pellico, A. Romanenko, V. Shiltsev, E. Stern, A. Valishev, R. Zwaska, "Long Term Plans to Increase Fermilab's Proton Intensity to Meet the Needs of the Long Baseline Neutrino Program", IPAC'16, Busan, Korea, p. 1010 (2016); (publ. JACoW).
- [13] W. Pellico et al., "Proton Task Force Report", Beams-doc-3660-v4, 24 Aug 2010.
- [14] B. Webber, W. Pellico, V. Lebedev, and D. McGinnis, "Proton Source Improvement Plan", Beams-doc-3781-v2, Fermilab, 2011.
- [15] F.G. Garcia, K. Gollwitzer,W. Pellico, E. Peoples, B. Zwaska, "PIP Design Handbook", Beams-doc-4053-v4, Fermilab, 2012.
- [16] W. Pellico, K.A. Domann, F.G. Garcia, K.E. Gollwitzer, K. Seiya, R.M. Zwaska et al., "FNAL - the Proton Improvement Plan (PIP)", IPAC'14, Germany, p.3409 (2014); (publ. JACoW).
- [17] S. Nagaitsev, "AD All-hand meeting", April 18, 2017  
<https://indico.fnal.gov/conferenceDisplay.py?confId=14343>
- [18] Proton Improvement Plan-II, Web-page: <http://pip2.fnal.gov/>.
- [19] I.S. Baishev, A.I. Drozhdin, N.V. Mokhov, X. Yang, "STRUCT Program User's Reference Manual", SSCL-MAN-0034 (1994).
- [20] N.V. Mokhov, "The Mars Code System User's Guide", Fermilab-FN-628 (1995); MARS website: <http://mars.fnal.gov>

<sup>17</sup> Joint Accelerator Conferences Web-site "<http://www.jacow.org>"

<sup>18</sup> Fermilab's Accelerator Division Document Databases Web-site: "<https://beamdocs.fnal.gov>"

- [21] E. Prebys, "Collimator System", slide no.35 in the talk "The Fermilab Accelerator Complex: Status and Challenges", Aug 15, 2002, at E. Prebys's Web-site, in "Complete talk archive"<sup>19</sup>, file "pizza\_talk\_20020815.ppt".
- [22] E. Prebys, "Collimator System", slide no.36 in May 2, 2002 talk, ibid.: "spitl\_20020502.ppt".
- [23] E. Prebys, "Booster Collimator Shielding", Dec. 2, 2002, ibid.: "collimator\_20021202.ppt".
- [24] E. Prebys, "Collimator Meeting", Jan. 7, 2003, ibid.: "collimator\_meeting\_20030107.ppt".
- [25] E. Prebys, "Booster Collimation System", page 15 in the talk on Feb. 3, 2003, ibid.: "booster\_ACC\_20030204.PDF".
- [26] E. Prebys, "Collimation System", slide 3, March 8, 2003, ibid.: "review\_figures 8Mar2003.ppt".
- [27] L.M. Bartoszek, "The Design of the Booster Collimator Shielding", documents on Web-page of "Bartoszek Engineering"<sup>20</sup>, updated on 3/13/2003.
- [28] E. Prebys, "Booster Collimation System", slides 24 & 25 in the talk at Accelerator Technology Seminar, March 18, 2003, at the E. Prebys's Web-site: "seminar\_20030318.ppt".
- [29] E. Prebys, "Collimator Project", slide 3, April 18, 2003, ibid.: "protonsource\_20030418.ppt".
- [30] E. Prebys, "Shutdown Schedule", slide 1, Aug 8, 2003, ibid.: " proton\_20030808.ppt".
- [31] E. Prebys, "Proton Source Startup", the slides no. 2, 4, 5, talk on 23 Oct. 2003, ibid.: the file "proton\_startup\_20031023.ppt"
- [32] E. Prebys, "Toward a Proton Plan", slides no.18, 22, 33, talk at PAC Meeting, 12 Dec. 2003, ibid.: the file "PAC\_20031212.ppt".
- [33] E. Prebys, talk 25 Jan. 2004, ibid.: the file " plan\_20040125.ppt".
- [34] E. Prebys, "Proton Source Status and Plans", slides no.10, 11, 16, 17, 19, talk at UEC Meeting, 21 Feb. 2004, ibid.: the file " uec\_20040221.ppt".
- [35] E. Prebys, "Reasons for Optimism", slide no.4, talk at AAC Review, 10 May. 2004, ibid.: the file "protonsource\_20040507.ppt".
- [36] E. Prebys, "Proton Economics and Proton Plan - Update", slides no.5, 9, 10, 11, 15, 32, talk at PAC, 20 June 2004, ibid.: the file "pac\_aspen\_20040620.ppt".
- [37] E. Prebys, "Proton Source", talk on 25 June 2004, ibid.: the file "protonsource\_20040625.ppt".
- [38] E. Prebys, "Booster Status", slides 2, 5, 12, talk at "BooNe" meeting, 8 July 2004, ibid.: the file "boone\_20040708.ppt".
- [39] E. Prebys, "Proton Plan", slides 8, 13, 14, 15, 19, 25, 37, 42, 43, talk on 21 Sep 2004, ibid.: the file "protonplan\_20040921.ppt".
- [40] T. Sullivan, D. Still, "Booster Collimator Overview", talk on 24 June 2004, Beams-doc-1220-v1, Fermilab, 2004
- [41] T. Sullivan, W. Pellico, "Booster Collimators", talk on 30 March 2005 for DOE Review of Tevatron Operations at FNAL, March, 29-31, 2005, Fermilab, 2005 (unpublished).
- [42] N. Mokhov, "Booster Collimation and Shielding", talk at Proton Source Workshop on December 7-8, 2010, Beams-doc-3734-v2, 2010.
- [43] A. Drozhdin, P. Kasper, J. Lackey, N. Mokhov E. Prebys, "Beam Collimation in the Fermilab Booster", March 12, 2004, unpublished, the file "pap\_collim2003.pdf", directory "BOOSTER".
- [44] A.K. Triplett, Powrpoint Presentaion with photos of the booster Collimation area, Jan. 14, 2015
- [45] R.J. Tesarek, B. Hartsell, V. Kapin, N.V. Mokhov, "Calculations of Power Deposited in the Booster Primary Collimators", Beams-doc-4998, Fermilab, 2015.
- [46] F.G.G. Garcia, W. Pellico, "FNAL Proton Source High Intensity Operations and Beam Loss Control", HB'2012, Beijing, China, p.320 (2012); (publ. JACoW).
- [47] F.G.G. Garcia, W. Pellico, "Current and Planned High Proton Flux Operations at the FNAL Booster", HB'2012, Beijing, China, p.378 (2012); (publ. JACoW).

<sup>19</sup> E. Prebys's "Complete talk archive" at web-page: "<http://home.fnal.gov/~prebys/talks/>"

<sup>20</sup> <http://bartoszekeng.com/boostershield/boostershield.htm>

- [48] K. Seiya, S. Chaurize, C. Drennan, W. Pellico, A.K. Triplett, A. Waller, “Development of Cogging at the Fermilab Booster”, IPAC’14, Dresden, Germany, p.2109 (2014).
- [49] N.V. Mokhov, private communications.
- [50] V.A. Lebedev, private communications.
- [51] M. Reiser, “Theory and Design of Charged Particle Beams”, Sec. edition, 2008 by Wiley-VCH.
- [52] I. Strasik, “Machine Protection”, Lecture at CERN Accelerator School, Prague, Czech Republic, Sept, 2014, <http://cas.web.cern.ch/cas/CzechRepublic2014/Lectures/Strasik.pdf>
- [53] V. Kapin and F. Schmidt, Examples for MADX code: examples 1, 3 for PTC-TRACK module, 2007, [http://madx.web.cern.ch/madx/madX/examples/ptc\\_track/](http://madx.web.cern.ch/madx/madX/examples/ptc_track/)
- [54] L.C. Teng, “Beam “Abort” System for the Main Ring”, National Accelerator Laboratory<sup>21</sup> report, FN-195 (0451), October 9, 1969.
- [55] L.C. Teng, “Design Concept for the beam Scrapper System of the Main Ring”, National Accelerator Laboratory<sup>22</sup> report, FN-196 (0452), October 17, 1969.
- [56] P.J. Bryant, N Galante, E. Klein, T.Taylor, “On the alignment design and of collimators”, CERN report SL/93-15(AP), Fenruary, 1993.
- [57] M. Seidel, “The proton Collimation System of HERA”, report DESY 94-103, DESY (1994).
- [58] A. Drozhdin, N. Mokhov, R. Soundranayagam, J.Tompkins, “Toward Design of the Collider Beam Collimation System”, preprint SSCL-555, SSCL, Dallas, February, 1994.
- [59] P.J. Bryant, “Collimation insertions”, Proc. CERN Accelerator School: 5th General Acc. Physics, Sept. 1992, report CERN-94-01, Vol. 1, pp. 174-187
- [60] T. Trenkler and J.B.Jeanneret, “The principles of Two Stage Betatron and Momentum Collimation in Circular Accelerators”, Particle Accelerators, Vol.50, pp.287-311, 1985 by OPA.
- [61] I. Strasik et. al, “Halo Collimation of Proton and Ion Beams in FAIR Synchrotron SIS 100”, talk at CERN on Jan 27 2014, "<https://indico.cern.ch/event/296501/>".
- [62] I. Strašík, I. Prokhorov and O. Boine-Frankenheim, “Beam halo collimation in heavy ion synchrotrons”, Phys. Rev. ST Accel. Beams 18, 081001 (2015).
- [63] L. Burnod, J.P. Jeanneret, “Beam losses and collimation in the LHC: A quantitative approach”, report CERN SL/91-39, CERN (1991), p.20.
- [64] S. Cousineau, D. Davino, N. Catalan-Lasheras, J. Holmes, “SNS Beam-in-Gap Cleaning and Collimation”, PAC’2002, Paris, France, p.1019; (publ. JACoW).
- [65] C.Y. Tan and W. Pellico, “Collimator effort”, talk at the Booster collimation meeting, Dec.17, 2014 (unpublished).
- [66] V. Kapin, “Booster Collimator Efforts: on Simulations/Optics Modeling Software”, talk at the Booster collimation meeting, Dec.17, 2014 (unpublished).
- [67] MADX website: <http://mad.home.cern.ch/mad/>
- [68] C.Y. Tan and K. Seiya, [https://cdcvfs.fnal.gov/redmine/projects/booster\\_madx\\_lattice\\_files](https://cdcvfs.fnal.gov/redmine/projects/booster_madx_lattice_files)
- [69] N.V. Mokhov, V.I. Balbekov, “3.3.2.1 Protons” “Handbook of Accelerator Physics and Engineering”, pp.214-217, 1999 by World Scientific Publishing Co. Ptr. Ltd
- [70] V. Kapin, “Booster Collimator: Simulation with MADX”, talk at PIP Status Report Meeting on 22 April 2015, Beams-doc-4812-v1, Fermilab, 2015.
- [71] J. Beringer et al. (Particle Data Group), Phys. Rev. D86 (2012) 010001, <http://pdg.lbl.gov>.
- [72] S.I. Striganov, private communication, 2015.
- [73] PSTAR program, <http://physics.nist.gov/PhysRefData/Star/Text/PSTAR.html>.
- [74] V.S. Pronskikh, private communication, 2014.
- [75] R. Billinge, S.C. Snowdon, and A. van Steenbergen, “The Design of the NAL Booster”, PAC’1969, p.969, 1969 (publ. JACoW).

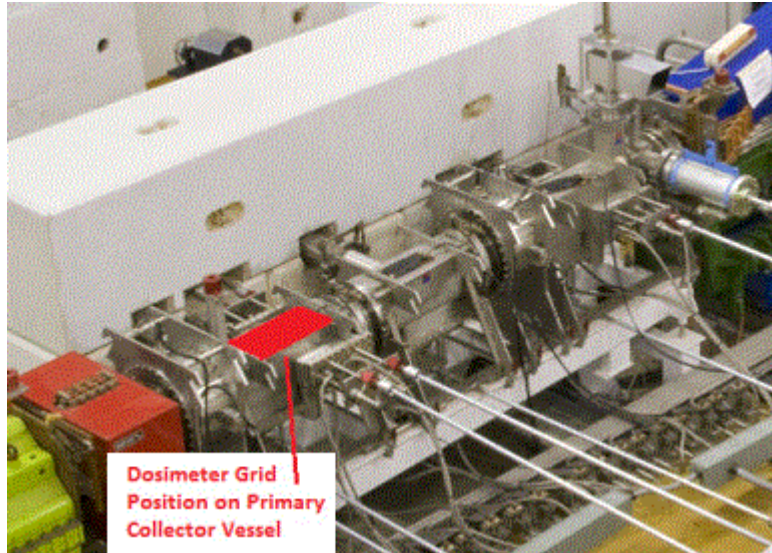
<sup>21</sup> presently Fermi National Accelerator Laboratory (FNAL or Fermilab)

<sup>22</sup> presently Fermi National Accelerator Laboratory (FNAL or Fermilab)

- [76] R. Juhala, “Field Measurements on a Booster Synchrotron F-Magnet”, Fermilab report TM-471, 1974.
- [77] E. Gray, “Booster Magnet D-48 Field Measurement”, Fermilab report TM-695, 1976.
- [78] R. Yamada, J. Pachnik, and P. Price, “Magnetic Field Measurements on Booster Synchrotron Magnets”, April 5, 1974 (unpublished).
- [79] A. Drozhdin, J. DiMarco, R. Tomlin, “Fermilab Booster Magnets Sextupole Components”, unpublished, 31 Oct, 2003.
- [80] C.Y. Tan, K. Seiya, A.K. Triplett, L.R. Prost, “Optics Corrections with LOCO in the Fermilab Booster”, IPAC2016, Korea, 2016
- [81] V.Kapin, “Booster Collimation Update”, talk at PIP Meeting on Aug 12, 2015, Beams-doc-4920-v1, Fermilab, 2015.
- [82] K. Seiya, C.M. Bhat, D.E. Johnson, V.V. Kapin, W. Pellico, C.-Y. Tan, R. Tesarek, “Beam Studies for the Proton Improvement Plan (PIP) - Reducing Beam Loss at the Fermilab Booster”, IPAC’15, Richmond, USA, p.4027 (2015); (publ. JACoW).
- [83] V. Kapin, “Booster Collimation: 2-stage vs 1-stage”, PIP Status Report Meeting on 24-Aug-2016, Beams-doc-5222-v2, Fermilab, 2016.
- [84] V.V. Kapin, V.A. Lebedev, N.V. Mokhov, S.I. Striganov, I.S. Tropin, “Numerical Simulations of Collimation Efficiency for Beam Collimation System in the Fermilab Booster”, NAPAC-2016, Pre-Release-02; Web-prerelease: <http://vrws.de/napac2016/papers/wepoa20.pdf>
- [85] V. Sidorov, private communications, 2016.
- [86] V. Kapin, “A proposal for upgrade of Booster collimations system”, talk at PIP general meeting on Feb.22, 2017, Beams-doc-5340-v1, Fermilab, 2017.
- [87] H.V. Smith, D.J. Adams, B. Jones, C.M. Warsop, “Activation Models of the ISIS Collectors”, IPAC’14, Dresden, Germany, p.893 (2014); (publ. JACoW).
- [88] R.J. Tesarek, “Booster Fast Loss Monitors”, Beams-doc-4797-v3, Fermilab, 2015.
- [89] C. Ornelas and R.J. Tesarek, “Booster Fast Loss Monitor Construction”, Beams-doc-4993-v1, Fermilab, 2015.
- [90] V.V. Kapin, S. Chaurize, N.V. Mokhov, W. Pellico, M. Slabaugh, T. Sullivan, R. Tesarek, A.K. Triplett, “Experimental Studies of Beam Collimation System in the Fermilab Booster”, NAPAC-2016, Pre-Release-02; Web: <http://vrws.de/napac2016/papers/wepoa18.pdf>
- [91] V. Kapin, R.J. Tesarek, S. Chaurize, T. Sullivan, K. Triplett, “Collimation in Booster: Experimental Results for Horizontal Plane”, PIP Status Report Meeting on 19-Apr-2017, Beams-doc-5371-v1, Fermilab, 2017.
- [92] R.J. Tesarek, V. Kapin, T. Sullivan, “Booster Collimator Motion Measurements (6/17/2015)”, Beams-doc-4882-v2, Fermilab, July 9, 2015.
- [93] R.J. Tesarek, “Secondary Collimator Motion Studies: Analysis of the Data”, Beams-doc-4905-v2, Fermilab, Aug 5, 2015.
- [94] M. Slabaugh, “Possible measures to improve mechanics of collimators”, Beams-doc-4906-v1, Fermilab, Aug 5, 2015.
- [95] V. Kapin, “Secondary Collimators Motion Tests done on 23-Jul-2015”, Beams-doc-4907-v5, Fermilab, Aug 5, 2015.

## Appendix A. RAL Collimation Scheme

Figure A.1 shows the collimation system of ISIS-SNS rapid cycling synchrotron [87]



Elevation View of the Collectors in Super-Period 1

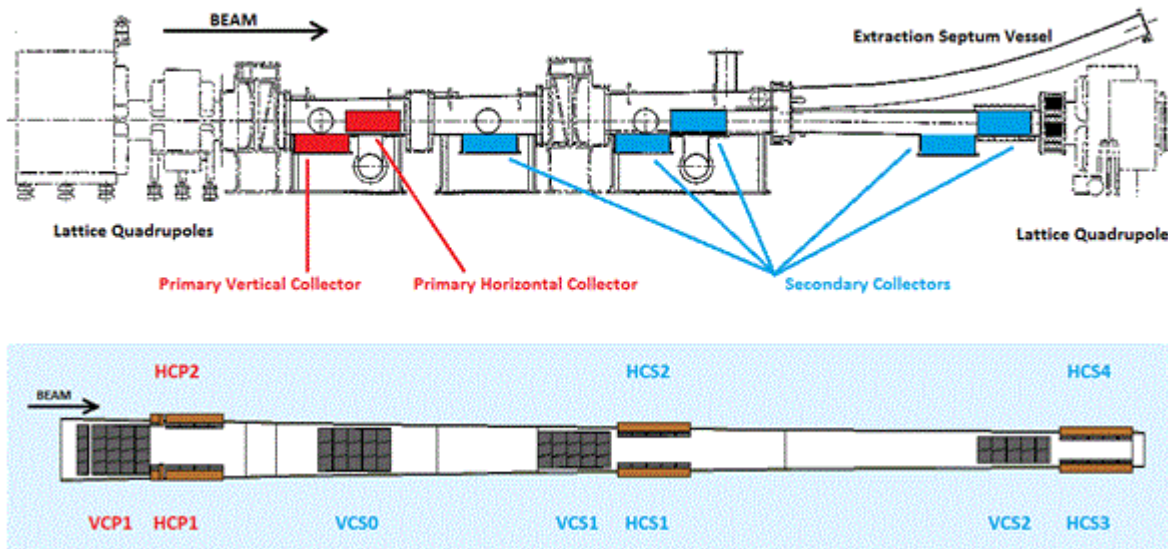


Figure A.1: ISIS-SNS collimation system ([87], IPAC-2014): a) photo of the ISIS collimators; b) elevation view of the primary and secondary collimators and schematic plan of the Fluka model for the collimators system.

## Appendix B Installation of new optimal primary foils

2004 design [9,11]: at 400 MeV 0.15mm graphite (~0.012mm copper);  
Instead, till 2015: 0.381 mm copper installed;

Our simulations [84]: Cu foil for several tens of turns ~ 50 mm

For the mechanical rigidity of the primary foils construction – equivalent Al foil with thickness of 380  $\mu\text{m}$  has been installed [45].

### The first 2014 rejected version of the 381 $\mu\text{m}$ Al primary collimators [81]

A pair of new aluminium Prim-Colls are already fabricated and is ready for installation:

- ❖ All sizes are the same as for existing Cu heat sink (complicated shape) to keep similar manufacturing technology; (heat transfer calculations for Al might be necessary "?")
- ❖ Al foil part has the thickness ~ 381mkm which is equivalent to ~60mkm of Cu foil (left figure)
- ❖ A thinner foils ~300mkm is difficult to fabricate (one was broken during manufacturing – see right figure)
- ❖ Another possible materials are carbon and beryllium (require special investigations)

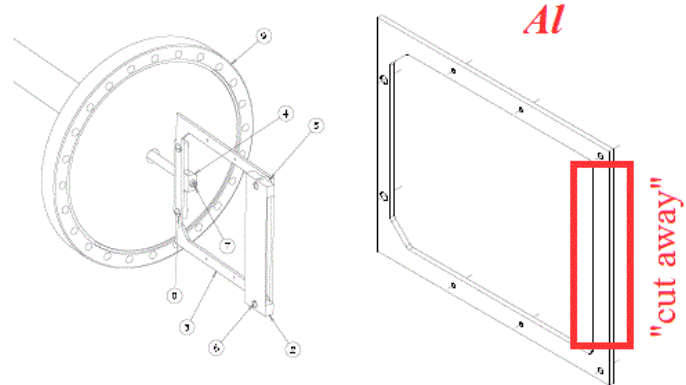


Figure X.03: [20150924\\_Primary\\_Collimator\\_Plans.doc](#)

Figure B.01: Pair of Aluminium primary collimators with heat sink [81].

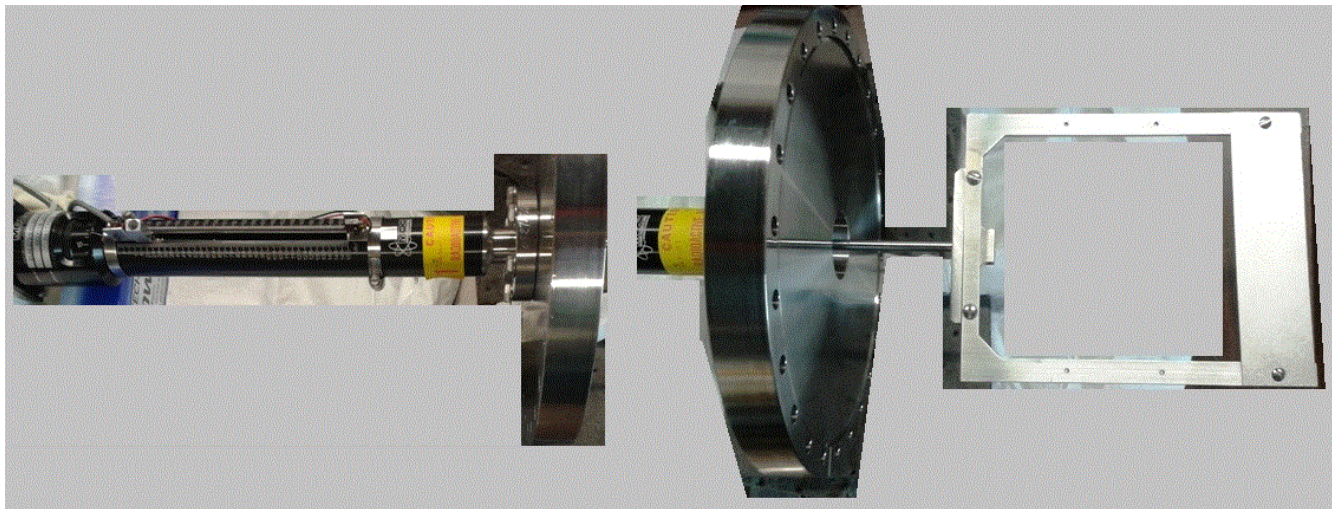


Figure B.01: Primary collimator assembly with installed plane 380  $\mu\text{m}$  Al foil [45].

## **Appendix C. Collimator Motion Applications and Studies**

The measurements of the secondary collimator motions have been performed on 17-June- 2015 and on 23-July-2015. The measured data analysis has been done by R.J. Tesarek [92, 93]. Overview of possible measures to improve mechanics of collimators has been presented by M. Slabaugh [94]. Examples of the raw data saved during measurements and obtained off-line later with help of the ACNET application D44 application can be found in the prepot by V.Kapin [95].

The results of the collimator motion tests have has been summarized at the 12-Aug-2015 PIP [81]:

- Primary collimators moves reliably (tested by Salah & V.Kapin)
- Secondary collimators tests on 23-Jul & 11-Aug have showed some problems for all 3 collimators: vertical motion for all 3 collimators and horizontal motion for 2nd collimator.
- Several meetings and discussions (see Beam-Doc DB [92, 93, 94]); team including M. Coburn (controls), M. Slabaugh (mechanics) and R.J. Tesarek; support from S. Chaurize and T. Sullivand at all studies.

## **Appendix D Beam Instrumentation and ACNET Applications**

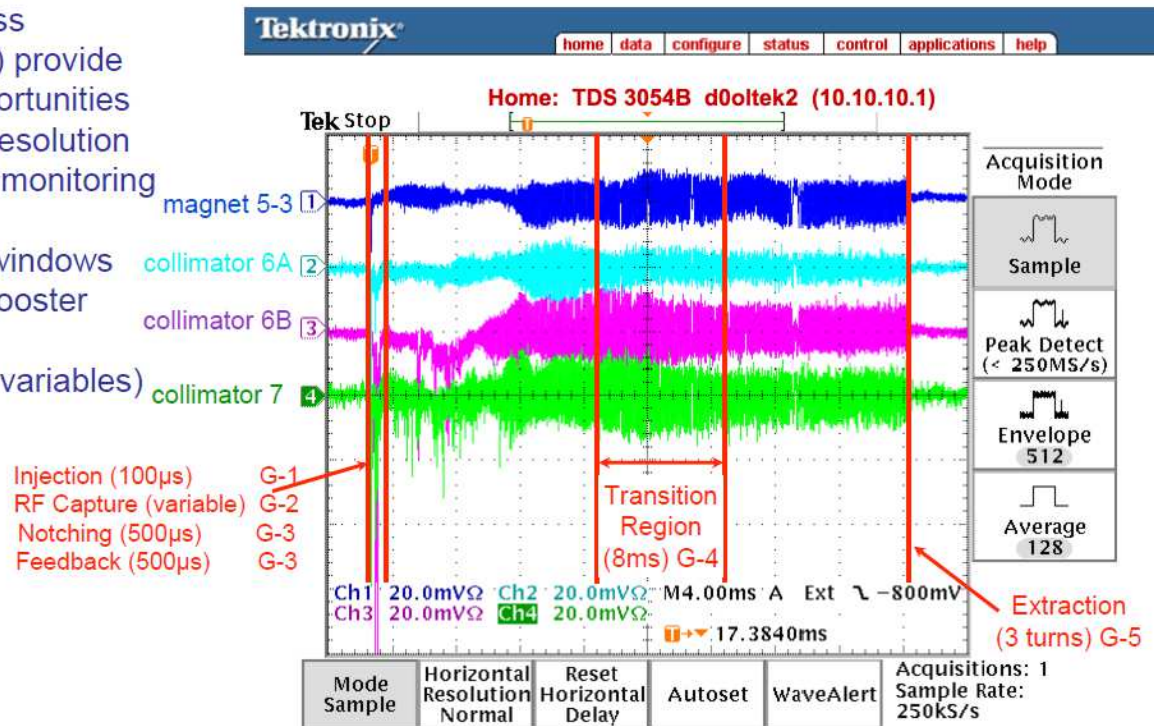
## Appendix E The Fast Loss Monitors (FLM)

The fast loss monitors (FLM) has been created and supported by R.J. Tesarek [88, 89].

### Booster losses: FLM for full booster cycle

Rick's FLMs

(Fast Loss Monitors) provide new opportunities for high resolution (ns) loss monitoring and in specific windows During Booster cycle (ACNET variables)



For collimation tuning FLMs gate G-1 (Injection) is used !

## **Appendix F Software Developed for Post-Processing of Study Results**